DEVELOPMENT OF MRI TECHNIQUES FOR EXPERIMENTAL MODELS OF CARDIOVASCULAR DISEASE

Thesis submitted by

Thomas A. Roberts

MSci, MRes.

March 2014

For the degree of Doctor of Philosophy.

University College London, UK.

Centre for Advanced Biomedical Imaging (CABI)
Paul O'Gorman Building
72 Huntley Street
London
WC1E 6DD

Centre for Mathematics, Physics and Engineering in the Life Sciences and Experimental Biology (CoMPLEX)
Gower Street
London
WC1E 6BT

Declaration

I, Thomas A. Roberts, confirm that the worked presented in this thesis is my own. Where information has been derived from other sources, I confirm that this has been indicated in the thesis. The work is based on research that was conducted by me during the period from October 2011 to August 2014 at the Centre for Advanced Biomedical Imaging (CABI) within University College London.

Thomas Anthony Roberts

March 2014

Abstract

Cardiovascular diseases (CVDs) – including stroke and heart failure – are the leading cause of death worldwide. More people die from CVDs each year than any other cause. Magnetic resonance imaging (MRI) is a powerful technique which is now routinely used for imaging these diseases as it offers high-resolution anatomical detail, exquisite soft-tissue contrast and assessment of function such as tissue water content, oxygenation, metabolism, vascular blood flow and microvascular perfusion. This thesis focuses on the development of MRI techniques for use in pre-clinical animal models of cardiovascular diseases, with a focus on stroke and heart disease.

Firstly, in chapter 3, the continued development of an in-house MRI sequence known as extravascular convectography (EVAC) for measuring the flow of interstitial fluid is described. A series of phantom experiments were conducted to assess the sensitivity of the sequence to slow flowing fluid. Next, an *in vivo* repeatability and reproducibility study was conducted before finally the technique was applied to a rat model of stroke.

In chapter 4, a pair of studies was carried out using recently established, advanced cardiac imaging techniques. In the first study, CINE and late gadolinium-enhanced inversion recovery (LGE IR) imaging were used to assess cardiac structure and function in a Prox1-deficient genetic mouse model of dilated cardiomyopathy. In the second part of the chapter, a multi-parametric MRI study – incorporating CINE, LGE IR, arterial spin labeling and T2-mapping – was conducted in a mouse model of reperfused myocardial infarction to assess the extent of area-at-risk and compare with gold-standard histological staining.

Finally, in chapter 5, the development of a retrospective high-temporal resolution (HTR) CINE MRI sequence for assessing cardiac diastolic function is described and compared with pulsed wave Doppler ultrasound, which is the currently-accepted standard for measuring diastolic function. The HTR-CINE sequence was established, validated and optimised in phantoms and naïve mouse hearts. Repeatability studies were then carried out to ensure the robustness of the technique before application to a mouse model of myocardial infarction.

The overall aim of the research in this thesis is the development of MRI techniques for application to experimental models of cardiovascular disease.

Acknowledgements

Firstly, I would like to express my sincerest gratitude to my supervisors Prof. Mark Lythgoe, Prof. Pete Scambler and Dr. Daniel Stuckey for their support and advice throughout the course of my PhD. More specifically, I would like to thank my primary supervisor Mark for giving me the opportunity to work in CABI in the first instance, for his continued enthusiasm, advice and critique of my work and for cultivating a laboratory environment that is both easy-going and highly motivating. I would like to thank my secondary supervisor Pete for his ongoing encouragement and for keeping me focused throughout my PhD. And, I would like to thank Daniel for coming onboard halfway through my PhD when he steered me through a tricky second year into a highly productive final year, for his scientific advice, enthusiasm and his generosity with his own time. Lastly, I also wish to thank Dr. Simon Walker-Samuel for giving me the opportunity to work on the EVAC project, for his insightful scientific input and for giving me a research associate position!

I would also like to extend my thanks to the staff in CoMPLEX for accepting me onto the PhD program where my time at UCL began. I would like to thank Dr. Guy Moss, Dr. Lewis Griffin and Prof. Alan Johnston for a brilliant MRes year in which I was exposed to all kinds of wonderful science, which made choosing a PhD excruciatingly difficult.

I would like to acknowledge all of my external collaborators in the Oxford Cardiovascular Science and the Hatter Cardiovascular Institute, specifically Prof. Paul Riley, Dr. Louisa Petchey, Dr Catherine Risebro, Dr. Derek Hausenloy and Dr. Rachel Dongworth.

I would like to acknowledge the support of the EPSRC and the British Heart Foundation, which funded me during my time at UCL. I am extremely grateful for their sponsorship.

Finally, I would like to thank a bunch of my nearest and dearest colleagues within and outside of CABI: Rajiv Ramasawmy for our circular discussions on almost everything scientific, Adrienne Campbell-Washburn for her patience and for taking me under her wing very early on, Anthony Price for his endless knowledge of MR physics, Bernard Siow and Jack Wells for all their technical support, Valerie Taylor for her surgical knowhow, Fran Norris for her dab hand at manuscript writing, Holly Holmes for putting up with me cursing at MATLAB, Laurence Jackson for the tea and biscuits, Rupy, Oz, Morium, Miguel, Niral, Izzy, Manil, Simon R, James O'C, Nick, Ma Da, Yichao, Arun, Yanan, Jed, Sonja, Nicky and last, but certainly not least, Siân.

Publications arising from this PhD

Papers

Helen Carnaghan, **Thomas A. Roberts**, Dawn Savery, Francesca C. Norris, Conor J. McCann, Andrew J. Copp, Peter J. Scambler, Mark F. Lythgoe, Nicholas D. Greene, Paolo De Coppi, Alan J. Burns, Agostino Pierro, Simon Eaton. *Novel exomphalos genetic mouse model: The importance of accurate phenotypic classification*. Journal of Pediatric Surgery 48.10 (2013): 2036-2042.

Louisa K. Petchey, Catherine A. Risebro, Joaquim M. Vieira, **Thomas A. Roberts**, John B. Bryson, Linda Greensmith, Mark F. Lythgoe, Paul R. Riley. *Loss of Prox1 in striated muscle causes slow to fast skeletal muscle fiber conversion and dilated cardiomyopathy*. Proceedings of the National Academy of Sciences 111.26 (2014): 9515-9520.

Thomas A. Roberts*, Francesca C. Norris*, Helen Carnaghan, Dawn Savery, Jack A. Wells, Bernard Siow, Peter J. Scambler, Agostino Pierro, Paolo De Coppi, Simon Eaton, Mark F. Lythgoe. *In amnio MRI of mouse embryos*. PLOS ONE 9(10), (2014) e109143.

Simon Walker-Samuel, **Thomas A. Roberts**, Rajiv Ramasawmy, Jake Burrell, S. Peter Johnson, Jack A. Wells, Bernard Siow, Simon Richardson, Miguel Gonçalves, Douglas Pendsé, Simon P. Robinson, R. Barbara Pedley, Mark F. Lythgoe. *Imaging tumor interstitial fluid dynamics with MRI*. Under review.

Rachel. K. Dongworth, Adrienne. E. Campbell-Washburn, **Thomas. A. Roberts**, Derek. M. Yellon, Mark. F. Lythgoe, Derek J. Hausenloy. *Cardiac arterial spin labeling MRI as a novel approach for in vivo quantification of the area-at-risk.* In preparation.

Thomas A. Roberts, Anthony N. Price, Valerie Taylor, Anna Davies, Daniel J. Stuckey*, Mark F. Lythgoe*. *Assessing diastolic function with retrospective high temporal resolution CINE MRI: a comparison with current-standard pulsed wave Doppler ultrasound*. In preparation.

Conference Abstracts

Thomas A. Roberts*, Francesca C. Norris*, Helen Carnaghan, Jack A. Wells, Bernard Siow, Peter J. Scambler, Agostino Pierro, Simon Eaton, Mark F. Lythgoe. *In amnio MRI imaging for the identification of abdominal pathologies*. Proceedings of the ISMRM annual meeting EP11(2012): 4145.

Thomas A. Roberts, Adrienne E. Campbell-Washburn, Rachel K. Dongworth, David L. Thomas, Anthony N. Price, Peter J. Scambler, Derek J. Hausenloy, Mark F. Lythgoe. *Multi-parametric MRI of myocardial infarction in mice at 9.4T*. British Chapter ISMRM annual meeting (2013).

Rachel K. Dongworth, Adrienne E. Campbell-Washburn, **Thomas A. Roberts**, Derek M. Yellon, Mark F. Lythgoe, Derek J. Hausenloy. *T2-mapping cardiac magnetic resonance imaging for assessing area-at-risk in a murine model of myocardial ischaemia-reperfusion injury.* BAS/BSCR 2013 Spring Meeting, P225 (2013).

Adrienne E. Campbell-Washburn, Rachel K. Dongworth, **Thomas A. Robert**s, Anthony N. Price, David L. Thomas, Roger J. Ordidge, Derek M. Yellon, Derek J. Hausenloy, Mark F. Lythgoe. *Multi-parametric MRI assessment of myocardial ischemia-reperfusion injury in mice*. Proceedings of the ISMRM annual meeting TP10(2014): 2426.

Rajiv Ramasawmy*, **Thomas A. Roberts***, Bernard Siow, Sean Peter Johnson, Jack A. Wells, Alan Bainbridge, Rosamund Barbara Pedley, Mark F. Lythgoe, Simon Walker-Samuel. *1 Tesla Bench-top MRI of a Mouse Model of Colorectal Carcinoma Metastasis in the Liver: Comparison with 9.4 Tesla*. Proceedings of the ISMRM annual meeting TP01(2014): 1153.

Thomas A. Roberts, Anthony N. Price, Valerie Taylor, Peter J. Scambler, Daniel J. Stuckey, Mark F. Lythgoe. *Assessment of diastolic function in mouse hearts: high temporal resolution retrospectively-gated CINE MRI vs. ultrasound.* British Chapter ISMRM annual meeting (2014).

Thomas A. Roberts, Anthony N. Price, Anna L. David, Valerie Taylor, Daniel J. Stuckey, Mark F. Lythgoe. *Assessing Diastolic Function in Mouse Hearts: High-temporal resolution CINE MRI vs. Ultrasound*. Proceedings of the ISMRM annual meeting TP(2015): 2713.

* denotes joint authors.

Contents

List of Figures

List of Tables

List of Acronyms

AAR Area-at-risk

ADC Apparent diffusion coefficient

AMPA α-Amino-3-hydroxy-5-methyl-4-isoxazolepropionic acid

ASL Arterial spin labelling

ATP Adenosine triphosphate

au Arbitrary units

BARI Bypass Angioplasty Revascularization Investigation Myocardial Jeopardy Index

bpm breaths/beats per minute

CABI Centre for Advanced Biomedical Imaging

CCA Common carotid artery

CHD Coronary heart disease

CINE Cinematic

CT X-ray computed tomography

CVD Cardiovascular disease

DIR Double inversion recovery

DPI Dots per inch

DTI Diffusion tensor imaging

DWI Diffusion weighted imaging

ECA External carotid artery

ECG Electrocardiography

ED End diastole

EDV End diastolic volume

EPI Echo planar imaging

ES End systole

ESP Echo spacing

ESV End systolic volume

ETE Effective echo time

ETL Echo train length

EVAC Extravascular convectography

FAIR Flow sensitive alternating inversion recovery

FFT Fast Fourier transform

FLASH Fast low angle shot

FOV Field of view

Gd-DTPA Gadolinium diethylenetriaminepentaacetic acid

HFpEF Heart failure preserved ejection fraction

HFrEF Heart failure reduced ejection fraction

HTR High temporal resolution

ICA Internal carotid artery

ICP Intra cranial pressure

IFP Interstitial fluid pressure

IR Inversion recovery

IS Infarct size

k-line Phase encode line within k-space

LA Left atrium

LAD Lower anterior descending

LGE Late gadolinium enhancement

LV Left ventricle

LVM Left ventricular mass

MBF Myocardial blood flow

MBFd Myocardial blood flow deficit

MCA Middle cerebral artery

MCAO Middle cerebral artery occlusion

MRI Magnetic resonance imaging

NF Number of frames

NICE National Institute for Health and Care Excellence

NMDA N-methyl-D-aspartate

NMR Nuclear magnetic resonance

NSTEMI Non-ST segment myocardial infarction

PE Phase encode

PFA Paraformaldehyde

PWI Perfusion weighted imaging

RA Right atrium

RF Radiofrequency

RO Readout

RV Right ventricle

SERCA Sarcoplasmic reticulum calcium ATPase

SNR Signal-to-noise ratio

SPECT Single-photon emission tomography

STEMI ST segment myocardial infarction

SV Stroke volume

T1 T1 relaxation time

T1w T1 weighted

T2 T2 relaxation time

T2* T2 star relaxation time

T2e Elevated T2

T2w T2 weighted

TE Echo time

TI Inversion time

t-PA Tissue plasminogen activator

TR Repetition time

TTC 2,3,5-triphenylterazoliumchloride

VENC Velocity encoding value

CHAPTER 1: AN OVERVIEW OF CARDIOVASCULAR DISEASES

The cardiovascular diseases (CVDs) of myocardial infarction and stroke are the two most deadly diseases in the world, costing hundreds of billions of dollars each year. Imaging is playing an increasingly prevalent role in the diagnosis, management, treatment and understanding of CVDs. In this chapter, myocardial infarction and stroke are briefly discussed including the aetiologies and pathological processes involved in these diseases, how they are commonly imaged in the clinic and how the diseases are recreated in pre-clinical animal models, for use in the studies contained in the rest of this thesis.

1.1 Introduction

Cardiovascular disease (CVD) is the leading cause of death and disability worldwide. In 2012, 17.5 million people died from CVDs according to statistics from the World Health Organization [1], equivalent to 30% of all deaths. By 2030, this figure is projected to rise to more than 23.3 million people [2]. While typically considered a disease of the developed world, CVD is becoming increasingly prevalent in developing countries as well [3].

The economic burden of CVD is enormous. In 2010, the total cost of CVDs in the United States was estimated to be $273 billion [4]. In Europe, expenditure is similarly high: recent estimates from 2012 put the cost of CVD to the European Union at €196 billion ($257 billion) [5]. In the United States, these costs have increased at an annual rate of approximately 6% per year [6], and they are set to continue rising. By 2030, CVD expenditure in the United States is projected to triple, reaching $818 billion [7].

CVDs are a broad group of diseases that includes diseases of the heart, vascular diseases of the brain and diseases of blood vessels. Atherosclerosis, which is the formation of plaques inside blood vessels due to the build-up of fat, cholesterol and calcium, underlies many ischaemic CVDs such as coronary artery disease, cerebrovascular disease and peripheral vascular diseases. Other CVDs include rheumatic heart disease where the heart valves are damaged by inflammation following rheumatic fever; congenital heart disease caused by malformations present at birth; cardiomyopathies which cause thickening of the myocardium; and vascular diseases such as deep vein thrombosis and pulmonary embolism.

Inevitably, as the global burden of CVDs continues to increase, the need to assess and treat these diseases grows as well. In response, the role of non-invasive imaging has become increasingly important for diagnosis, assessment of prognosis and the understanding of the basic mechanisms of disease. This thesis is focussed on magnetic resonance imaging (MRI) of CVDs, in particular pre-clinical studies using mouse and rat models of human disease. Owing to its excellent soft tissue contrast and use of non-ionising radiation to generate images, MRI has emerged as a versatile technique for assessing structure, function, tissue status and the effects of therapeutic drugs. Pre-clinical animal models of CVD are extremely valuable because they permit in-depth, repeatable studies. This allows for the thorough development of experimental therapies, imaging biomarkers and improvements in our understanding of basic mechanisms of disease, which can then inform or be translated into human medical research.

For the rest of this chapter, two of the most prevalent forms of CVD will be described in greater detail, specifically stroke and myocardial infarction, which are central to the MRI studies in this thesis.

1.2 Stroke and myocardial infarction

Myocardial infarction, also known as heart attack, and stroke, also known as brain attack, are the two most deadly forms of CVD, both frequently caused by blood vessel ischaemia following atherosclerosis, which is a pathological process characterised by the formation of fatty, atherosclerotic plaques (or thrombi) that restrict, and potentially block, the flow of blood through arteries [8-12].

Myocardial infarction is the leading cause of death worldwide causing 7.4 million deaths in 2012 [1]. This is closely followed by stroke, the second leading cause of death worldwide, which resulted in 6.7 million deaths in 2012 [1]. The costs of these two diseases to the United States in 2010 were $109 billion and $54 billion [7], respectively, while in the European Union in 2012 the costs were €60 billion ($79 billion) and €38 billion ($50 billion), respectively [5].

1.2.1 Aetiology of stroke

The primary cause of stroke is ischaemia where the blood supply to the brain becomes blocked following thrombus formation. Ischaemia accounts for 85% of stroke cases, while the remaining 15% of cases are caused by haemorrhagic stroke following blood vessel rupture [13]. The animal model of stroke studied in this thesis is an ischaemic injury model, therefore only ischaemic stroke will be described in the rest of this chapter.

1.2.2 Pathophysiology of ischaemic stroke

A series of cellular and molecular processes follows the blockage of a blood vessel, known as the ischaemic cascade [14]. In stroke, this cascade leads to neuronal death and ultimately brain damage. In the central region of the tissue normally perfused by the blocked vessel, known as the ischaemic core, the primary mechanism of cell death is energy failure. In the absence of oxygen and glucose, the neurons cannot generate the adenosine triphosphate (ATP) required by the sodium-potassium pumps to maintain neuronal membrane

homeostasis. As a result, cytoplasmic accumulation of sodium and calcium ions leads to neuronal swelling, loss of membrane integrity and cell dissolution.

Surrounding the ischaemic core is the ischaemic penumbra. In this region perfusion is reduced and tissue is hypoxic, but not to the extent that ATP generation is completely inhibited. Neurons in the penumbra may remain viable for extended periods (hours) following ischaemic injury, but become vulnerable to numerous pathogenic events which may disrupt their weak metabolic balance, described at length by Lo et al (2003) and Moskowitz et al. (2010) [15, 16]. One major factor contributing to penumbra cell death is excitotoxicity where an overabundance of glutamate accumulates in the extracellular space over stimulating α-Amino-3-hydroxy-5-methyl-4-isoxazolepropionic acid (AMPA) and N-methyl-D-aspartate (NMDA) receptors, thus enhancing the influx of sodium, calcium and water. Without intervention, the ischaemic core will gradually increase in size and become irreversibly infarcted as the neurons in the ischaemic penumbra succumb to the effects of reduced perfusion.

1.2.3 Stroke in the clinical setting – imaging and treatment

Rapid diagnosis and treatment of acute stroke is crucial for patient outcome. The National Institute for Health and Care Excellence (NICE) guidelines state that a patient with acute stroke should be imaged immediately [17]. Stroke is routinely imaged using magnetic resonance imaging (MRI) and X-ray computed tomography (CT). CT is the more widely used modality for immediate diagnosis owing to faster scan times [18], however, MRI is the most widely used for assessment of the ischaemic penumbra [19]. The dual use of diffusion weighted imaging (DWI) and perfusion weighted imaging (PWI) in MRI of stroke patients has led to the creation of the so called ‘mismatch’ concept for identifying tissue at risk of infarction [20]. PWI is a marker for tissue with reduced blood flow [21], while DWI detects the restricted motion of water molecules [22], which approximately correlates with infarct tissue (although DWI lesions can also contain regions of benign oligemia [23]). Both scans are run in series and the spatial difference between the two scans, known as the diffusion-perfusion mismatch, corresponds to the ischaemic penumbra (Figure 1.1).

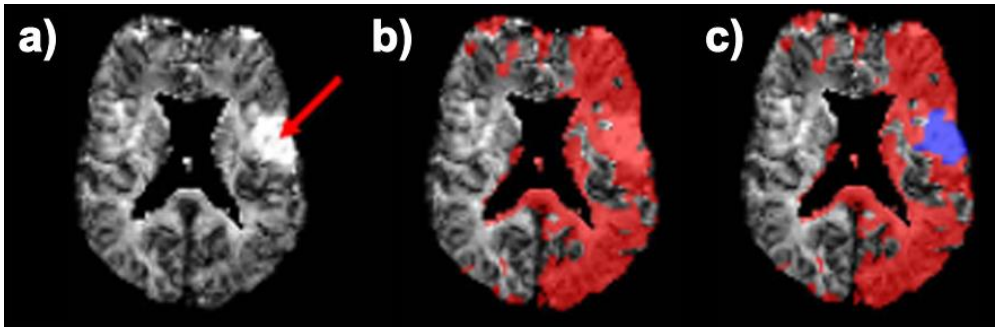

Figure 1.1: Imaging the ischaemic penumbra in acute stroke with MRI (image adapted from [19]). (a) DWI hyperintensity (red arrow) corresponds to the infarct core. (b) PWI shows regions of reduced blood flow (red region). (c) Subtracting the DWI infarct region (blue) from the PWI produces a diffusion-perfusion mismatch image, showing ischaemic penumbra. The red region now corresponds to potentially salvageable tissue.

Treatment of acute stroke aims to restore blood flow to the ischaemic region. The primary method of intervention is thrombolysis, using tissue plasminogen activator (t-PA) drugs to remove the occluding embolism. NICE recommends that t-PA must be administered within 4.5 hours of the onset of stroke symptoms for effective treatment, otherwise the benefits are limited. The majority of patients reach hospital 12-24 hours following a stroke and as a result less than 5% receive thrombolytic treatment [24]. Treatment for patients who miss the opportunity of thrombolysis includes administration of aspirin and, if appropriate, anticoagulants to reduce the possibility of further blood clot formation.

1.2.4 Rat models of stroke – middle cerebral artery occlusion surgery

The experiments in this thesis are all conducted on a pre-clinical 9.4T MRI scanner, often involving imaging of rodents. Animal models of stroke are used to provide a better understanding of the pathological mechanisms underlying the disease and for the development of treatments which can be translated into patients.

In this thesis, a rat model of ischaemic stroke is used. In this model, surgery is performed – by Mrs Valerie Taylor, typically 24-48 hours prior to imaging – with the aim of generating a reproducible infarct and ischaemic region. Surgery is conducted in a controlled, sterile surgical suite with aseptic operating practices. Anaesthesia is induced and then maintained in the rats using 4% and 2% isoflurane in 1.5 l/min oxygen, respectively. Neck and throat regions are shaved and skin is disinfected using Betadine. The animal is placed supine on a heating mat to maintain physiological body temperature, which is monitored via rectal probe. Using a microscope, a ventral midline incision is performed and superficial tissue is

dissected. Further careful dissection is performed to expose the common carotid artery (CCA), external carotid artery (ECA) and internal carotid artery (ICA).

Figure 1.2 shows a schematic of the arterial vasculature supplying a rat brain illustrating how the middle cerebral artery (MCA) is occluded to induce a stroke. Two loops of suture are tied around the CCA. One loop is tightened to prevent unwanted blood flow during surgery, while the second loop is left loose before tightening later on. After a small incision in the CCA, a 2.2-3.0 cm length of silicone rubber-coated monofilament (4-0 Doccol) is inserted into the CCA and pushed to the origin of the MCA. As visualisation of the monofilament inside the vasculature is not possible, a small mark on the monofilament indicates insertion depth, which is used to determine successful middle cerebral artery occlusion (MCAO). Then the second loop of suture is tied to maintain monofilament position. After successful implantation of the monofilament, a microvascular clip is placed on the contralateral CCA to ensure ischaemia. For a 60 minute MCAO, the vascular clip is removed after 30 minutes, while the monofilament is left in place for the full 60 minutes. Finally, the monofilament is removed, all surgical openings are closed and the rat is recovered.

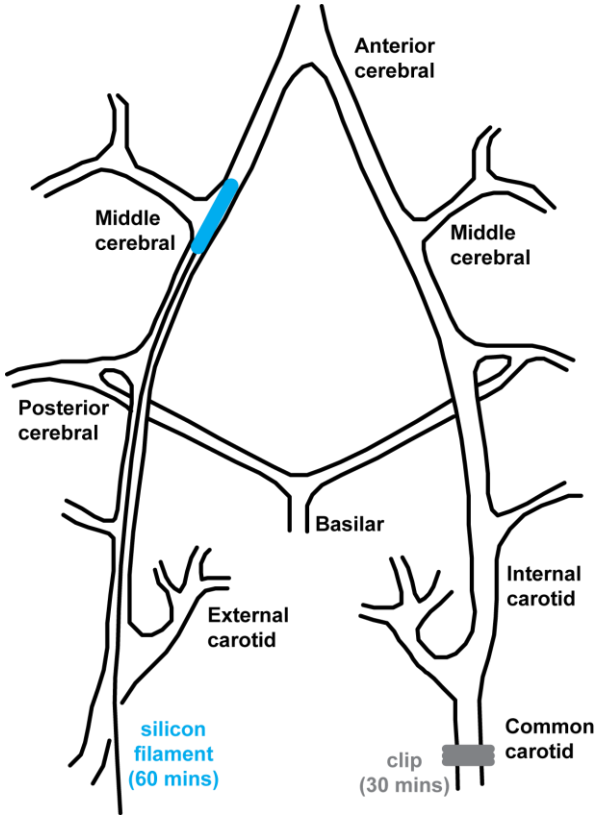

Figure 1.2: Schematic of middle cerebral artery (MCA) occlusion in a rat brain to induce a stroke. A silicon monofilament (blue) attached to a thin wire is inserted into the common carotid artery (CCA) and pushed to the origin of the MCA. The monofilament is kept in place for 60 minutes. At the same time, a microvascular clip (grey) is placed on the contralateral CCA for 30 minutes.

1.2.5 Aetiology of myocardial infarction

Myocardial infarction is the end result of coronary heart disease (CHD). Atherosclerosis within the coronary arteries can cause plaques to develop which rupture and form a thrombus, consequently blocking blood flow and causing myocyte cell death if the thrombus is not removed. Following ischaemia, myocyte cell death can take as little as 20 minutes, while extensive necrosis within the myocardium takes at least 2-4 hours, or longer [25]. The pathophysiology of myocardial infarction is described in greater detail in section 1.2.7, but first a knowledge of normal heart physiology is required to understand how heart disease affects cardiac function.

1.2.6 The physiology of a normal heart

The purpose of the heart is to pump blood through the circulatory system – a vast network of blood vessels linked to the heart and separated into two distinct circuits. The pulmonary circulatory system is responsible for transporting blood to the lungs for oxygenation before returning to the heart. The systemic circulatory system carries blood around the body, delivering oxygen and nutrients before returning deoxygenated blood to the heart.

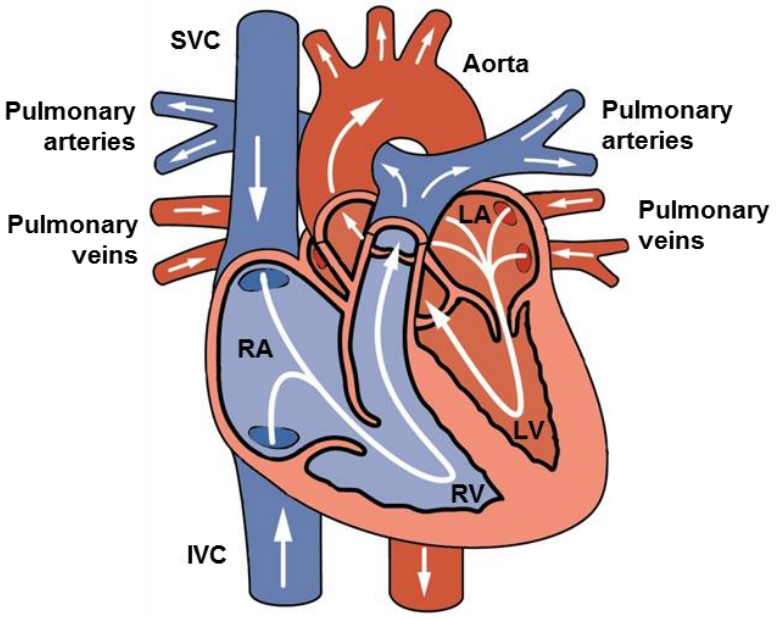

Figure 1.3: Illustration of the heart showing the direction of blood flow through the four chambers (image adapted from Wikipedia.org). Red shading represents oxygenated blood. Blue shading represents deoxygenated blood.

The heart itself is a muscular pump comprising four chambers, surrounded by muscular walls known as the myocardium. The chambers are two atria, responsible for collecting blood, and two ventricles, responsible for pumping blood (Figure 1.3). The right ventricle (RV) pumps deoxygenated blood to the lungs for oxygenation, which is returned to the heart via the left atrium (LA). The left ventricle (LV) then pumps the oxygenated blood around the systemic circulatory system before it is returned to the heart via the right atrium (RA). The LA and LV are separated by the mitral valve, while the RA and RV are separated by the tricuspid valve. The LV and aorta are separated by the aortic valve, while the RV and pulmonary artery are separated by the pulmonary valve. The valves function to prevent retrograde blood flow.

Pumping of the heart is initiated by an electrical impulse which propagates through the heart causing a series of contractions, first in the atrial myocardium and then the ventricular myocardium. The contraction phase of the cardiac cycle is known as systole, where blood is pumped out of the heart. The filling phase of the heart is known as diastole, where blood enters the heart. The extremes of these phases are known as end systole (ES) and end diastole (ED), where the volume of blood in the ventricles is at its minimum and maximum, respectively. A schematic of changing blood volume throughout the cardiac cycle is illustrated in Figure 1.4. The performance of the heart can be assessed by imaging during the systolic and diastolic phases of the cardiac cycle for the diagnosis of heart failure, which will be discussed further in section 2.7.1.

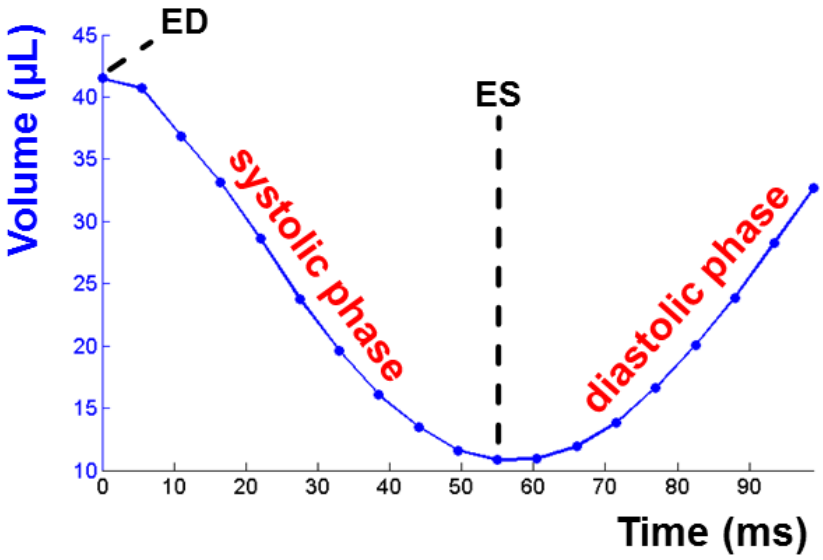

Figure 1.4: Schematic blood pool volume curve generated using standard CINE MRI (see section 2.7) in a normal mouse heart showing the systolic and diastolic filling phases of the cardiac cycle.

The electrical activity of the heart can be detected and recorded by electrocardiography (ECG), typically using electrodes attached to the surface of the skin. Electrical activity is measured as the changing voltage between the electrodes, which represents ionic exchange across the membranes of cardiomyocytes. A normal heart will demonstrate an ECG pattern similar to the schematic pictured in Figure 1.5. The P-wave represents atrial depolarization where the atria contract, the QRS-complex corresponds to ventricular depolarization where the ventricles contract (systole begins) and the T-wave represents repolarization of the ventricles causing them to relax (diastole begins). The QRS-complex has the largest change in voltage throughout the cardiac cycle, hence it is exploited and used for triggering in cardiac MRI (see section 2.6).

The duration of time between consecutive QRS-complexes is known as the R-R interval, measured from R-wave to R-wave. The human heart rate is 50-100 beats per minute (bpm), whereas the mouse heart can be 10 times faster, between 450-700 beats per minute. Hence, the typical R-R interval duration for a mouse is approximately 90-130ms.

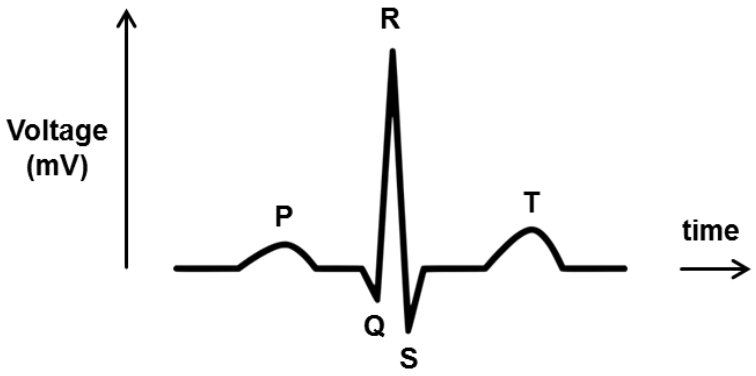

Figure 1.5: Schematic of a QRS complex from an ECG trace of a normal heart. The P-wave represents atrial depolarisation which leads to atrial contraction. Together, the Q-, R- and S-waves form the QRS-complex, which represents the depolarisation of the ventricles and leads to ventricular contraction (systole). The T-wave represents repolarisation of the ventricles, leading to ventricular relaxation (diastole).

1.2.7 Pathophysiology of myocardial infarction

The mechanisms of cell death in myocardial infarction are similar to those in ischaemic stroke. Hypoxia causes myocytes to generate insufficient ATP for normal cellular homeostasis, which results in gradual cell death if blood flow is not restored quickly and cessation of contractile function [26]. On a macroscopic scale, ischaemia leads to what is known as the "wavefront phenomenon" of myocardial infarction [27]. This concept is

similar to the ischaemic penumbra in stroke, as it describes the evolution of an infarct region with time. Following the onset of ischaemia, the region of tissue distal to the occluded coronary artery suffers greatly reduced perfusion, or none at all. This region is now termed the area-at-risk (AAR), as shown in Figure 1.6. Here, cardiomyocytes begin to die within 20 minutes, however, at such a short duration the damage is reversible. After a few hours, a necrotic core begins to form where cell damage cannot be reversed. Throughout this process, the non-infarcted tissue undergoing ischaemia can be salvaged if the occluded coronary artery is reperfused. However, without reperfusion the infarct region typically progresses from the endocardium towards the epicardium as the wavefront of necrosis gradually spreads through viable tissue within the AAR.

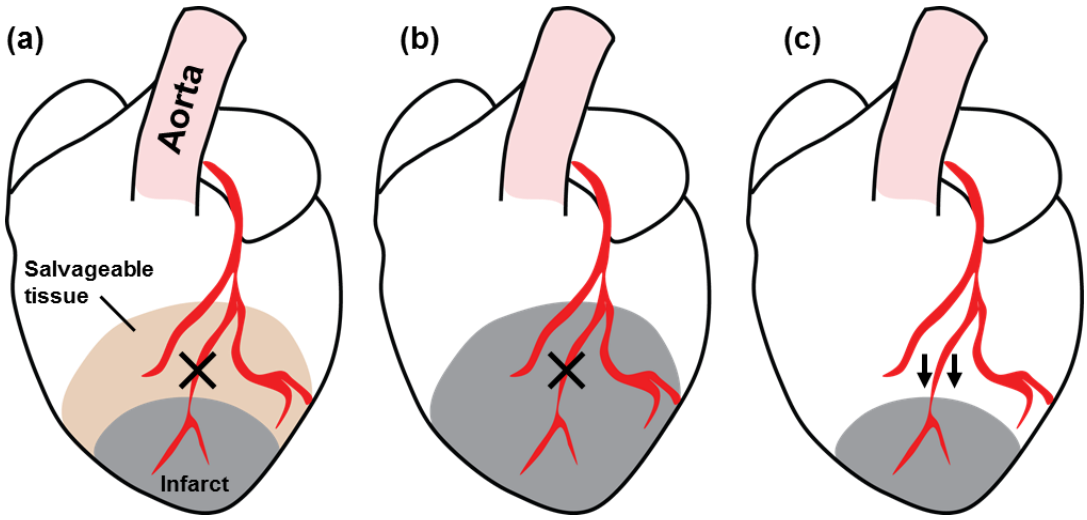

Figure 1.6: Schematic illustrating the concept of area-at-risk (AAR) following myocardial infarction. (a) Coronary artery blockage (×) leads to myocardial hypoxia. The region of myocardium previously perfused by the occluded artery is defined as the AAR (orange + grey). Gradually, the AAR risk turns into infarcted tissue (grey). (b) If the occlusion remains, the entire AAR eventually becomes infarcted, however, (c) if the coronary artery is unblocked, the myocardium becomes reperfused, limiting the size of the infarct region.

1.2.8 Myocardial infarction in the clinical setting – treatment and imaging

Diagnosis of suspected myocardial infarction in the clinic is most often carried out by immediate assessment of ECG [25]. If a coronary artery is blocked, the ECG will often present with an elevated signal between the S- and T-waves of the recorded trace. This is known as STEMI: ST segment elevation in myocardial infarction [28]. Partial blockage of the coronary artery often results in an NSTEMI, non-ST segment elevation in myocardial infarction, ECG waveform. If acute STEMI is diagnosed, the patient is admitted for coronary reperfusion therapy as quickly as possible.

The majority of myocardial infarction imaging in an acute setting is carried out using ultrasound owing to its availability and real-time imaging capabilities. Cardiac MRI has excellent spatial resolution, it is the gold-standard technique for evaluating myocardial function and it offers strong temporal resolution, however, it is less commonly used for assessment of acute myocardial infarction because of its cost and cumbersome form [25]. Nonetheless, MRI offers a wealth of information about contractile performance (systolic and diastolic function – see section 2.7.1), myocardium morphology, myocardial tissue status, perfusion, metabolism, great vessel blood flow, and more [29], particularly in the healing phase following myocardial infarction.

1.2.9 Mouse models of myocardial infarction

Animal models of myocardial infarction play an important role in the prevention, diagnosis and development of therapeutics for human myocardial infarction [30]. In this thesis, two surgical models of myocardial infarction were used. The first model was a reperfused mouse model of myocardial infarction, where the left anterior descending (LAD) coronary artery was occluded for a fixed period of time (typically 15 to 90 minutes) before the ligature was released and the vessel was reperfused. The duration of occlusion ultimately determined the sizes of the infarct and salvageable tissue regions within the AAR. The second model was a permanent occlusion model of myocardial infarction. In this case, the ligature used to occlude the LAD was not released, therefore reperfusion was prevented.

All reperfused surgeries in this thesis were carried out by Dr. Rachel Dongworth, while all permanent occlusion surgeries were conducted by Ms. Valerie Taylor. Surgery was conducted in a controlled, sterile surgical suite with aseptic operating practices. Anaesthesia was induced and maintained in the mice using isoflurane anaesthetic at 4% and 1.5%, respectively, in 1.5l/min. Analgesia was provided using a 0.1mg/kg intramuscular injection of buprenorphine at the beginning of surgery, and both 6- and 24-hours post-surgery. Mice were positioned supine on a heated operating table to maintain physiological body temperature, which was monitored using a rectal thermometer. ECG was recorded with subcutaneous electrodes (Powerlab coupled to Chart7 software, AD Instruments, USA). Artificial respiration was provided by a ventilator (MiniVent Type 845, Hugo Sachs Electronik, Germany) via oral intubation with a stroke volume of 200µL. Open-chest surgery was performed to gain access to the heart. The LAD was identified and a suture was placed under the vessel approximately 2mm below the tip of the left atrium. A custom-made

snare system, created using plastic tubing, was used to occlude the LAD, which was confirmed by ST-elevation on the ECG recording.

At this point in the permanent occlusion model, the ligature was left in place, all surgical openings were closed and the animal was recovered. In the reperfused model, after 30 minutes of occlusion the snare was released to allow for reperfusion of the myocardium. Reperfusion was confirmed by a return to baseline of the ECG signal. Then, the snare system was removed, but the suture was left in place for re-occlusion later on during histology. All surgical openings were closed and the animal was recovered.

1.3 Summary

This chapter has discussed the medical implications and pertinent biology of the CVDs which will be studied in the rest of this thesis, namely stroke and myocardial infarction. The methodologies for creating animal models of these diseases were also described. In the next chapter, the theory behind MRI will be described, with particular reference to the physics and pulse sequences that will be used in the experimental chapters.

1.4 References

1. World Health Organization. *Fact File No. 310: The top 10 causes of death*. August 2014.
2. Mathers CD, Loncar D. *Projections of global mortality and burden of disease from 2002 to 2030.* PLoS medicine, 2006. **3**(11): p. e442.
3. Basson M. *Cardiovascular disease.* Nature, 2008. **451**(7181): p. 903-903.
4. Centers for Disease Control Prevention. *Heart disease and stroke prevention: Addressing the nation's leading killers. At a glance 2011*, (2013).
5. Nichols M, et al. *European Cardiovascular Disease Statistics 2012.* European Heart Network, Brussels, European Society of Cardiology, Sophia Antipolis, (2012).
6. Roehrig C, et al. *National health spending by medical condition, 1996–2005*. Health Affairs, 2009. **28**(2): p. w358-w367.
7. Heidenreich PA, et al. *Forecasting the future of cardiovascular disease in the United States. A policy statement from the American Heart Association.* Circulation, 2011. **123**(8): p. 933-944.
8. Libby P. *Inflammation and cardiovascular disease mechanisms.* The American Journal of Clinical Nutrition, 2006. **83**(2): p. 456S-460S.
9. Singh RB, et al. *Pathogenesis of atherosclerosis: a multifactorial process.* Experimental & Clinical Cardiology, 2002. **7**(1): p. 40.
10. Sherer Y, Shoenfeld Y. *Mechanisms of disease: atherosclerosis in autoimmune diseases.* Nature Clinical Practice Rheumatology, 2006. **2**(2): p. 99-106.
11. Galkina E and Ley K. *Immune and inflammatory mechanisms of atherosclerosis.* Annual Review of Immunology, 2009. **27**: p. 165.
12. Sanz J and Fayad AZ, *Imaging of atherosclerotic cardiovascular disease.* Nature, 2008. **451**(7181): p. 953-957.
13. Go AS, et al. *Heart disease and stroke statistics -- 2013 update: a report from the American Heart Association.* Circulation, 2013. **127**(1): p. e6.
14. Iadecola C and Anrather J. *The immunology of stroke: from mechanisms to translation.* Nature Medicine, 2011. **17**(7): p. 796-808.

15. Lo EH, Dalkara T and Moskowitz MA. *Mechanisms, challenges and opportunities in stroke.* Nature Reviews Neuroscience, 2003. **4**(5): p. 399-414.

16. Moskowitz MA, Lo EH and Iadecola C. *The science of stroke: mechanisms in search of treatments.* Neuron, 2010. **67**(2): p. 181-198.

17. NICE Guidelines [CG68]. *Stroke: Diagnosis and initial management of acute stroke and transient ischaemic attack (TIA).* 2008.

18. Farr TD and Wegener S. *Use of magnetic resonance imaging to predict outcome after stroke: a review of experimental and clinical evidence.* Journal of Cerebral Blood Flow & Metabolism, 2010. **30**(4): p. 703-717.

19. Ebinger M, et al. *Imaging the penumbra–strategies to detect tissue at risk after ischemic stroke.* Journal of Clinical Neuroscience, 2009. **16**(2): p. 178-187.

20. Baird AE, et al. *Enlargement of human cerebral ischemic lesion volumes measured by diffusion-weighted magnetic resonance imaging.* Annals of Neurology, 1997. **41**(5): p. 581-589.

21. Neumann-Haefelin T, et al. *Diffusion-and perfusion-weighted MRI The DWI/PWI mismatch region in acute stroke.* Stroke, 1999. **30**(8): p. 1591-1597.

22. Schaefer PW, Grant PE and Gonzalez RG. *Diffusion-weighted MR imaging of the brain.* Radiology, 2000. **217**(2): p. 331-345.

23. Kidwell CS, Alger JR and Saver JL. *Beyond mismatch evolving paradigms in imaging the ischemic penumbra with multimodal magnetic resonance imaging.* Stroke, 2003. **34**(11): p. 2729-2735.

24. Green A. *Pharmacological approaches to acute ischaemic stroke: reperfusion certainly, neuroprotection possibly.* British Journal of Pharmacology, 2008. **153**(S1): p. S325-S338.

25. Thygesen K, et al. *Third universal definition of myocardial infarction.* Journal of the American College of Cardiology, 2012. **60**(16): p. 1581-1598.

26. Jennings RB and KA Reimer. *Lethal myocardial ischemic injury.* The American Journal of Pathology, 1981. **102**(2): p. 241.

27. Reimer KA, et al. *The wavefront phenomenon of ischemic cell death. 1. Myocardial infarct size vs duration of coronary occlusion in dogs.* Circulation, 1977. **56**(5): p. 786-794.

28. Antman EM, et al., *ACC/AHA guidelines for the management of patients with ST-elevation myocardial infarction—executive summary: a report of the American College of Cardiology/American Heart Association Task Force on Practice Guidelines (Writing Committee to Revise the 1999 Guidelines for the Management of Patients With Acute Myocardial Infarction).* Journal of the American College of Cardiology, 2004. **44**(3): p. 671-719.

29. Marra MP, Lima JA and Iliceto S. *MRI in acute myocardial infarction.* European Heart Journal, 2011. **32**(3): p. 284-293.

30. Wang J, et al. *A simple and fast experimental model of myocardial infarction in the mouse.* Texas Heart Institute Journal, 2006. **33**(3): p. 290.

CHAPTER 2: MRI THEORY, BACKGROUND, PULSE SEQUENCES AND HARDWARE

This chapter is intended to provide an overview of the physics behind the research presented in the rest of the thesis. The fundamental principles underlying the MRI signal and how an image is generated are outlined. Pulse sequence design is discussed with particular reference to the sequences used in the rest of the thesis, and finally, the hardware used for the studies in the following three experimental chapters is described.

2.1 Fundamental physics of MRI

To understand the contents of this thesis, a working understanding of the physical principles underlying MRI is required. Many of the concepts in this chapter have been written about extensively in the past [1-4], so the present chapter will be only a brief discussion. This section (2.1) will start by describing the magnetic field generated by spinning charged nuclei. This will be followed by a discussion of magnetic spin states and how the spin density of a sample is changed when placed in a magnetic field. Next spin relaxation will be covered and finally image generation will be described.

2.1.1 Nuclear spin and the Larmor frequency

All subatomic particles, such as electrons, protons and neutrons can be visualised as spinning on an axis. They possess an intrinsic form of angular momentum known as spin. Atomic nuclei, behave as a single entity with collective nuclear spin, I. In 1924, Otto Stern and Walther Gerlach demonstrated that nuclear spin is quantised, rather than having a continuous distribution of possible momenta [5]. By passing silver atoms through a non-uniform magnetic field, they observed that the atoms were deflected along one of two paths, implying that the atoms had two possible angular momentum states.

MRI is primarily concerned with the hydrogen nucleus (a single proton) which is found abundantly throughout the body in water and fat. Quantum theory dictates that the angular momentum of atomic nuclei is constrained to $2I + 1$ possible spin states. A single proton has spin = ½, therefore the hydrogen nucleus has two possible spin states (2.(½) + 1). In the presence of a magnetic field, the spin states correspond to alignment or anti-alignment of the protons with the magnetic field (Figure 2.1). The two spin states have different energy levels, separated by an energy difference $\Delta E = \hbar\omega$.

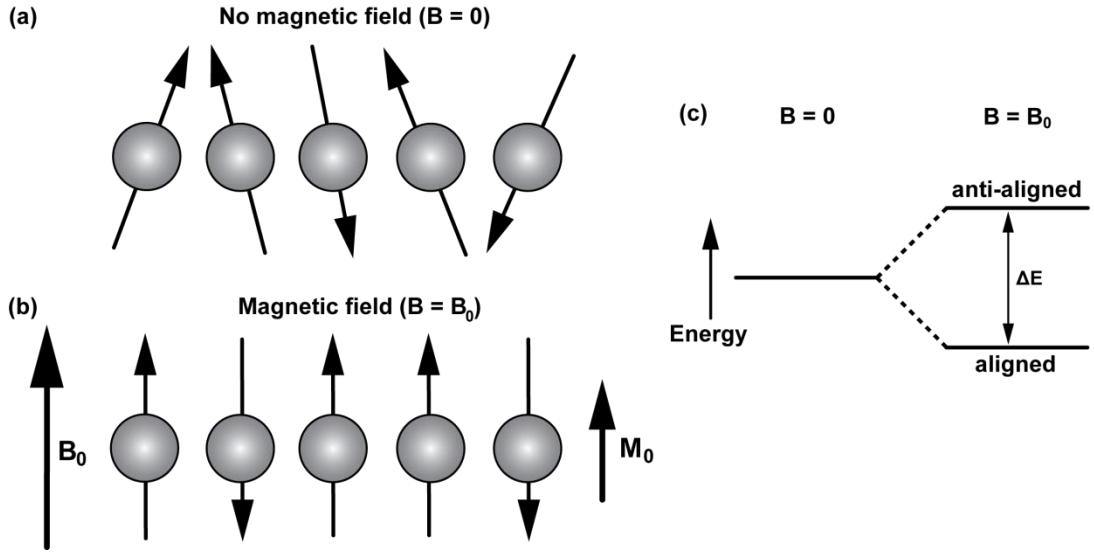

Figure 2.1: Nuclei in the absence of a magnetic field (a) are randomly orientated and there is no net magnetisation. In the presence of a magnetic field (b), the nuclei occupy one of two possible spin states (c). The nuclei are either aligned or anti-aligned with the magnetic field. Overall there is an excess of nuclei which align with the magnetic field as it is energetically favourable.

The magnetic field also causes the nuclei to precess around the direction of the magnetic field. This phenomenon was first described by Sir Joseph Larmor in the early 1900s [6]. He stated that nuclei with non-zero spin placed within a magnetic field will possess a magnetic moment and therefore experience a torque. The rate, or frequency (ω_0), with which the nuclei precess around the magnetic field is determined by the nuclear gyromagnetic ratio (γ) and the strength of the magnetic field (B_0), as described by the now ubiquitous Larmor equation:

$$\omega = \gamma B_0 \qquad \textbf{EQ 2.1}$$

For hydrogen protons $\gamma(H)$ = 42.6 MHz/T. In a typical clinical 1.5T MRI scanner the precessional frequency, ω, of hydrogen protons is therefore approximately 64 MHz. In a 9.4T pre-clinical scanner this increases to 400 MHz. Both values fall within the radiofrequency (RF) range of the electromagnetic spectrum, which is crucial for signal generation in MRI and will be discussed further in the next section.

2.1.2 Resonance, Excitation and Relaxation

When nuclei are placed in a magnetic field, they either align or anti-align with the direction of the magnetic field. The population of these spin states is governed by the Boltzmann distribution:

$$\frac{N_u}{N_d} = e^{-\frac{\Delta E}{kT}} \qquad \textbf{EQ 2.2}$$

where N_u and N_d represent the number of nuclei in the upper and lower spin states, respectively, ΔE is the energy difference between the two spin states, k is Boltzmann's constant and T is temperature. As it is energetically favourable for the nuclei to occupy the lower energy state, a small excess align with the magnetic field. This imbalance in populations results in a small net magnetisation vector, M_0, in the direction of B_0 (Figure 2.1b).

In 1946, Felix Bloch and Edward Purcell discovered the phenomenon of nuclear magnetic resonance (NMR), whereby nuclei placed in a magnetic field absorb and re-emit RF energy at the resonance (Larmor) frequency of the nuclei when they transition between spin states. The pair measured – independently of each other – the precessional signals from water and paraffin molecules in a magnetic field [7, 8].

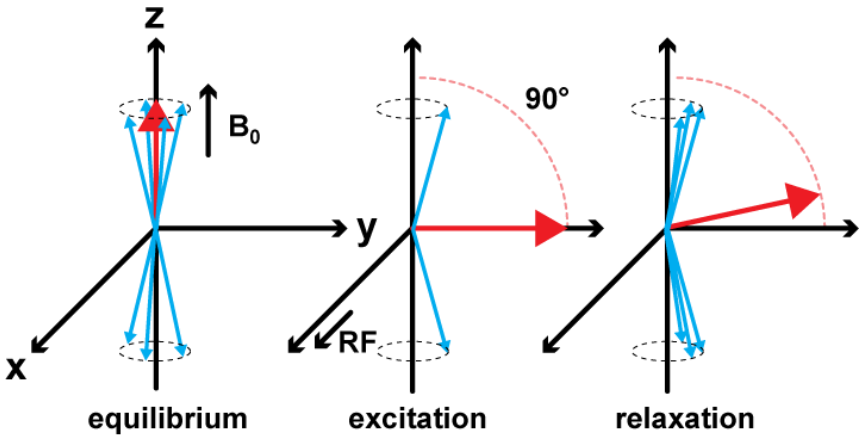

Figure 2.2: The excitation and relaxation of magnetisation in a reference frame rotating at the Larmor frequency. At equilibrium the spins (blue) are aligned or anti-aligned with the magnetic field. A 90° RF pulse excites the spins, causing them to gain phase coherence and the net magnetisation vector (red) to point in the transverse plane. During relaxation, the spins dephase and the net magnetisation vector recovers to the align with the magnetic field.

In the absence of an RF pulse, the nuclei possess no phase coherence and the individual protons rotate out of phase with each other. The application of an RF pulse causes two

important phenomena to occur: firstly, phase coherence is induced between the nuclei causing them to rotate in synchrony, and secondly, the nuclei are excited to transition between the two spin states. Following the RF pulse, relaxation occurs where the nuclei simultaneously lose phase coherence (dephase) and transition between energy levels, returning to their original spin states and re-emitting RF pulses in the process. Diagrammatically, this process is most commonly conceptualised using a coordinate system which rotates at the Larmor frequency (Figure 2.2). Effectively, the observer sees an arc of motion as the net magnetisation is flipped into the x-y plane. After excitation, the nuclei both dephase and relax back to their original spin states. During this period, the transverse component of the magnetisation vector rotating in the x-y plane is detected by Faraday induction in the RF receiver coil of the MRI scanner.

2.1.3 Mechanisms of Relaxation

As mentioned in the previous section (2.1.2), the NMR phenomenon involves two forms of energetic relaxation following excitation of nuclei in a magnetic field. There are two main types known as T1 and T2 relaxation, which represent time constants inherent to different types of media or tissue type.

T1, or spin-lattice relaxation, refers to the time taken for energised nuclei to return to their equilibrium state. T1 is also known as the longitudinal relaxation time because diagrammatically it represents the time taken for the net magnetisation vector, M_0, to return to the B_0 direction following excitation. The mechanism underlying T1 relaxation is thermal transferral of energy from the spins to their surrounding lattice. Nuclei residing within a sample are held in a lattice. The nuclei in the lattice are subject to vibrational and rotational motion, which creates a separate, complex, magnetic field. This magnetic field can share frequency and phase equal to the Larmor frequency of the nuclei, causing the nuclei to lose energy and return to the lower spin state. This is a thermal process because every transferral of energy causes a very small temperature rise in the sample.

T2, or spin-spin relaxation, is a much more rapid process which refers to the time taken for coherent nuclei to dephase. T2 is also known as transverse relaxation because diagrammatically it represents the time for the transverse magnetisation vector M_{xy} to reduce to zero. The mechanism underlying T2 relaxation is the interaction of magnetic fields between neighbouring nuclei. For example, a proton aligned with B_0 exerts a slightly higher magnetic field on its neighbour ($B_0 + \Delta B$) than an anti-aligned proton which exerts a magnetic field on its neighbour slightly weaker ($B_0 - \Delta B$) than the B0 field. As a result of the

Larmor equation (equation 2.1), nuclei residing closest to the aligned proton will have a faster precessional frequency. Similarly, nuclei in the vicinity of the anti-aligned proton will have a slower precessional frequency. Thus, the sample is no longer perfectly coherent and on a macroscopic scale the sample dephases.

The rapidity of T2 relaxation is further increased by inhomogeneities which are present in all magnetic fields. Fluctuations in the magnetic field at different locations cause nuclei within a sample to precess at different frequencies, causing increased dephasing. This is also known as T2* relaxation, to distinguish it from T2 relaxation which is caused purely by spin-spin interactions.

2.1.4 Spatial Encoding

The signal received by an RF receiver originates from the entire sample. To construct an image, spatial information must be encoded into the signal. Spatial encoding is carried out by an additional set of resistive magnets within the MRI scanner known as the gradients. Three gradients (G_x, G_y, G_z) are used to encode spatial information in each Cartesian direction. Depending on the orientation of the desired imaging plane, the gradients perform one of three functions: slice selection, frequency encoding or phase encoding.

For slice selection, a linear gradient (typically G_z) is applied to create a linear distribution of Larmor frequencies through the sample ($B_0 - G_z < \omega_0 < B_0 + G_z$). As resonance only occurs when the frequency of the incident RF pulse matches the Larmor frequency, the frequency of the RF pulse is specified to correspond to a slice of interest. By adjusting the centre frequency of the RF pulse different slices can be spatially encoded. The thickness of the slice can be controlled either by adjusting the bandwidth of the RF pulse, or by changing the strength of the slice selection gradient.

In a similar manner, frequency encoding uses another linear gradient (typically G_x) so that the nuclei possess a Larmor frequency dependency in the direction of the frequency encoding gradient. Combined with the slice selection gradient, frequency encoding effectively enables spatial encoding of columns within the plane of interest.

Finally, a phase encoding gradient (typically G_y) is required to spatially encode pixels. A third linear magnetic field is momentarily applied generating a linear phase dependency in the direction of the phase encode gradient. Nuclei either increase or decrease in phase depending on their location in the sample. After a series of phase encoding steps, typically of

incremental gradient strength, the multiple signals collected are spatially decoded to produce an image.

2.1.5 Basic Pulse Sequences

The ordering and timing of the RF pulses and gradients collectively forms a pulse sequence. 'Gradient echo' and 'spin echo' are the main types of pulse sequence in MRI (Figure 2.3 and Figure 2.4). Many more complicated pulse sequences are built upon these basic sequences. The term 'echo' refers to the emission of energy generated following excitation and refocussing of a sample, which is measured by the RF receiver.

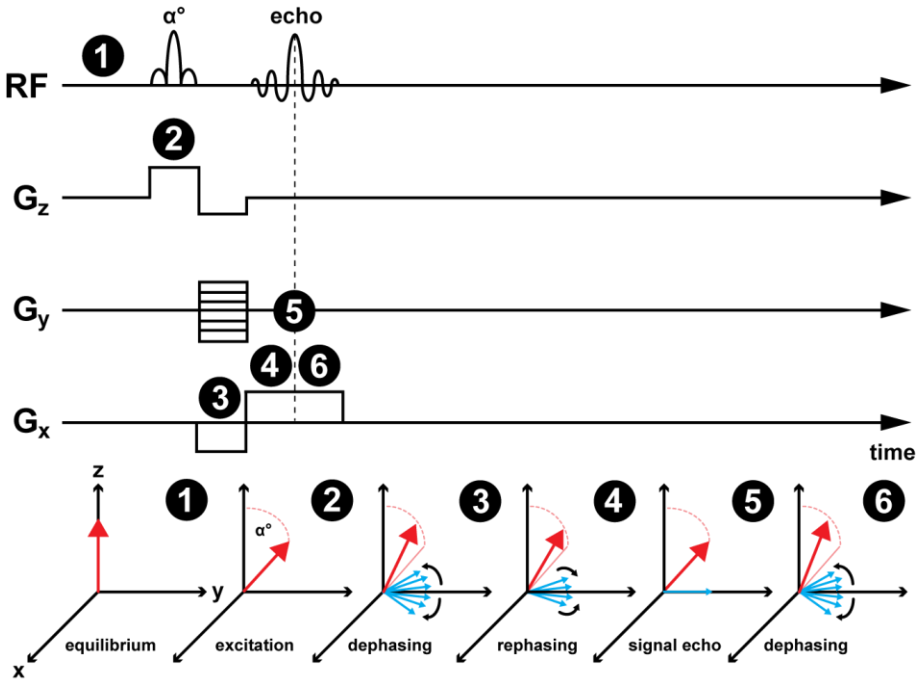

Figure 2.3: Gradient echo pulse sequence timing diagram in the rotating frame showing the ordering of RF pulses and gradient waveforms and the corresponding effects on net spin magnetisation (red) and individual spins (blue). (1) Equilibrium: the net magnetisation aligns with the B_0 field. (2) Spins excited by arbitrary α° RF pulse. (3) Spins dephased by gradients. (4) Spins rephased by readout gradient, G_x. (5) Signal echo coincides with centre of readout gradient. (6) Spins continue to dephase.

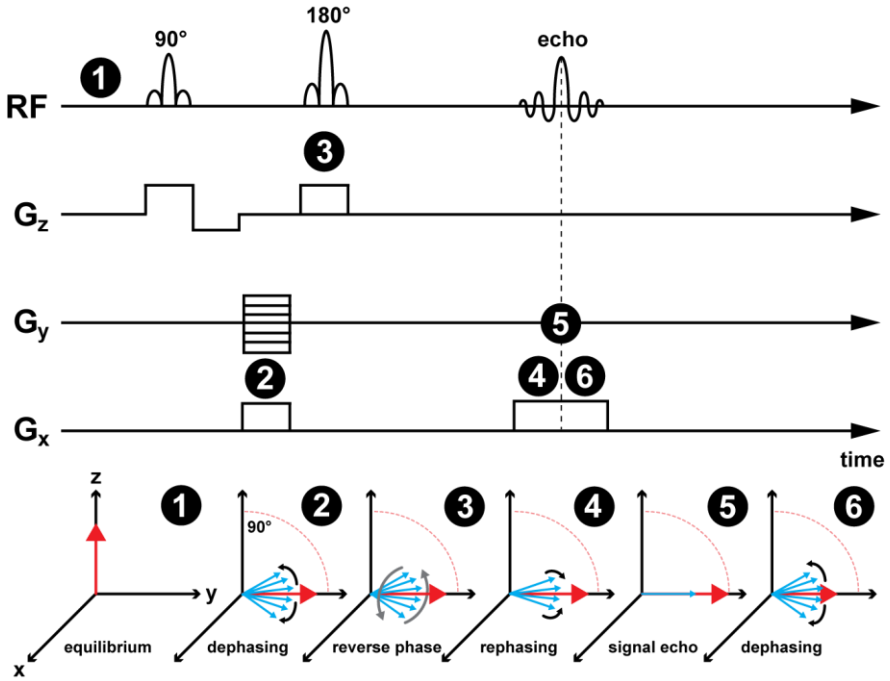

Figure 2.4: Spin echo pulse sequence timing diagram in the rotating frame showing the ordering of RF pulses and gradient waveforms and the corresponding effects on spin magnetisation (red) and individual spins (blue). (1) Equilibrium. (2) Following excitation (omitted), spins dephased by gradients. (3) Spin phase reversed by 180° refocusing pulse. (4) Spins rephased by readout gradient, G_x. (5) Signal echo coincides with centre of readout gradient. (6) Spins continue to dephase.

Both sequences share common features, such as slice selection, frequency encoding and phase encoding gradients as well as a slice select RF pulse. The two pulse sequences are distinguished by different methods of echo formation. In a gradient echo sequence, the echo is formed by rephasing the spins with a gradient waveform of negative polarity. In a spin echo sequence, a second (180°) RF pulse is used to rephase the spins and form an echo. Waveform-by-waveform descriptions of both pulse sequences are given in Figure 2.3 and Figure 2.4. Both sequences are advantageous for different purposes. Gradient echo sequences are generally faster whereas spin echo sequences often have higher a signal-to-noise ratio because the refocusing RF pulse rephases spins, lessening the T2* effect.

2.1.6 k-space and image generation

k-space is a 2D or 3D mathematical matrix in the spatial frequency domain which contains the digitised signals received during an MRI scan (Figure 2.5). In 2D k-space, each row of k-space represents the time course of one digitally sampled echo at a single phase encode value. Typically, there may be 64-256 echoes, each acquired with a unique phase encoding value. Performing a two-dimensional fast Fourier transform (2D FFT) of k-space converts

the spatial frequency data into image data of complex type. The signal detected by the receiver during an MRI scan is an oscillating circularly polarised magnetic field which can be decomposed into real and imaginary components. Two different images can be generated: magnitude images are generated by taking the modulus of the real and imaginary data, according to equation 2.3, and phase images are generated by taking the complex argument of the data, according to equation 2.4.

$$Magnitude = \sqrt{Real^2 + Imag^2} \quad \textbf{EQ 2.3}$$

$$Phase = arctan\left(\frac{Imag}{Real}\right) \quad \textbf{EQ 2.4}$$

Both image types have a different utility. Magnitude images are often used for structural visualisation, while phase images can contain information about magnetic field homogeneity or fluid flow.

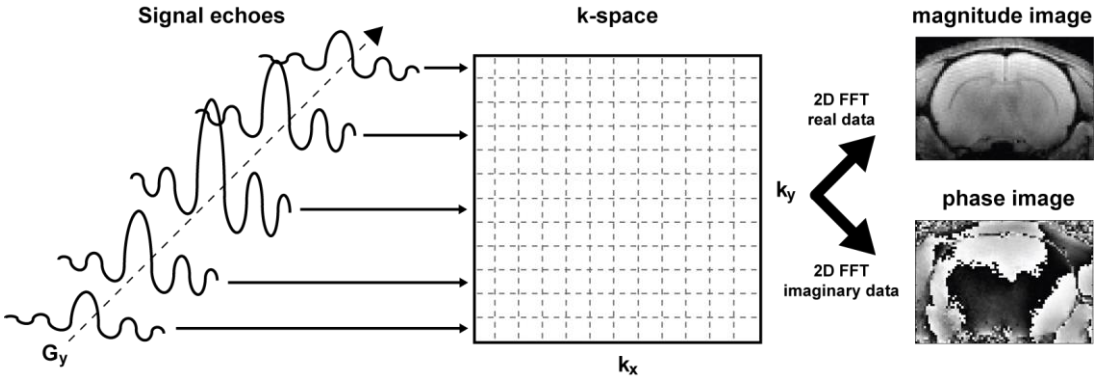

Figure 2.5: Converting echoes into images. Echoes are acquired at incremented phase encode gradient values. Echoes are stored in k-space following analogue to digital conversion. Magnitude and phase images are generated by manipulation of the real and imaginary parts of the signal.

2.2 Velocity-encoded MRI

MRI is a versatile imaging modality because – in addition to its excellent soft tissue contrast and high resolution structural imaging capabilities – pulse sequences can be programmed to enable sensitivity to the direction of motion. Erwin Hahn was the first person to suggest using MRI to detect the motion of water in 1960 [9]. One decade later, the first measurement of blood velocity in humans was carried out [10]. Since then, velocity-encoded MRI has found many applications, primarily in vascular flow studies [11], but also cerebrospinal fluid flow studies [12] and myocardial tissue tracking [13].

MRI velocity-encoding is based on the principle that a sample (blood flow, contracting myocardium, etc.) gains phase proportional to its velocity when moving during a gradient waveform. The phase, ϕ, of nuclei in a magnetic field is the time integral of the Larmor frequency:

$$\phi = \int \omega_0 \, dt \qquad \textbf{EQ 2.5}$$

In the presence of an additional magnetic field gradient, G_x, this phase shift becomes:

$$\phi = \gamma \int (B_0 + G_x x) \, dt \qquad \textbf{EQ 2.6}$$

For moving nuclei with constant velocity, v, traveling in the x direction, this phase shift can be recast as:

$$\phi = \gamma \int (B_0 + G_x(x + vt)) \, dt \qquad \textbf{EQ 2.7}$$

Expanding this equation gives:

$$\phi = \phi_0 + \gamma x \int G_x \, dt + \gamma v \int G_x t \, dt \qquad \textbf{EQ 2.8}$$

where the first term corresponds to background phase from the main magnetic field, the second term corresponds to the zeroth magnetic moment, M_0, or phase due to static spins, and the third term corresponds to the first magnetic moment, M_1, or phase shift due to moving nuclei.

There are various MR velocity-encoding strategies [14], but the most common methods use bipolar gradients pulses to encode phase into the moving spins. Figure 2.6 shows a typical

velocity-encoded gradient echo sequence. The sequence is run twice. For the second acquisition, the polarity of the bipolar gradients is reversed. Thus, the phase difference, $\Delta\phi$, between the two acquisitions can be calculated according to:

$$\Delta\phi = \phi_1 - \phi_2 \qquad \textbf{EQ 2.9}$$

As the background magnetic field and static nuclei contribute the same phase during both orientations of the bipolar gradients, it follows that the first two terms in equation 2.8 contribute zero to the phase difference. Therefore, the phase shift due to moving nuclei with a positive bipolar gradient of duration, *T*, and amplitude, *G*, gives a phase shift:

$$\phi = \gamma \int_0^T Gvt\, dt = \frac{1}{2}\gamma v G T^2 \qquad \textbf{EQ 2.10}$$

For the repeat acquisition, the bipolar gradient amplitude is reversed to –*G*. Therefore, combining equations 2.9 and 2.10 gives:

$$\Delta\phi = \gamma v \Delta M_1 \qquad \textbf{EQ 2.11}$$

where $\Delta M_1 = \frac{1}{2}GT^2 - (-\frac{1}{2}GT^2)$. Finally, the velocity encoding parameter, *VENC*, is defined as the velocity of a moving spin that produces a phase shift of π radians:

$$\pi = \gamma . VENC . \Delta M_1 \qquad \textbf{EQ 2.12}$$

In practice, VENC is a tuneable parameter on the MRI scanner chosen by the operator, therefore equation 2.12 is recast as:

$$VENC = \frac{\pi}{\gamma \Delta M_1} \qquad \textbf{EQ 2.13}$$

The VENC represents the maximum encodable velocity before aliasing occurs; speeds greater than VENC cause phase wrapping [2, 15].

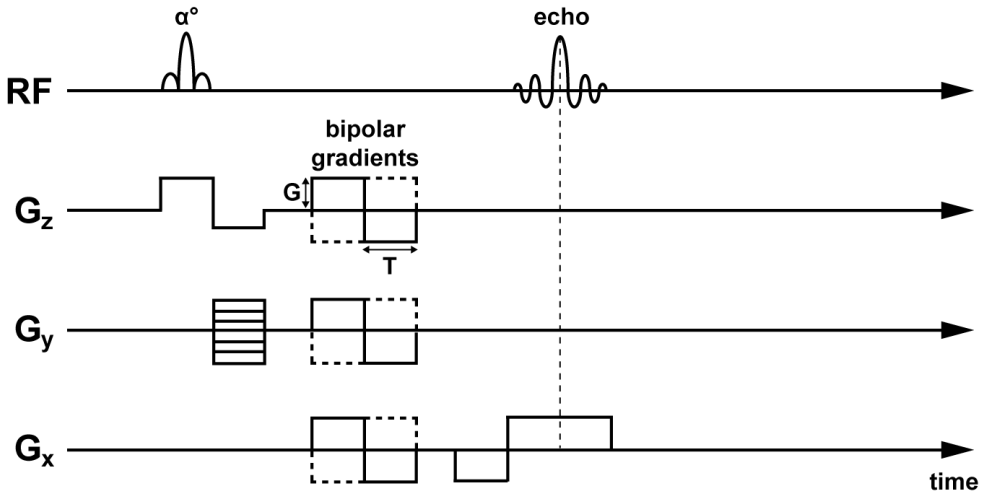

Figure 2.6: Velocity-encoded gradient echo pulse sequence. Flowing nuclei are sensitised by the bipolar gradients. The pulse sequence is run twice with the polarity of the velocity encoding gradients reversed (dashed lines) during the second acquisition. By calculating the phase difference between the two acquisitions, a velocity-encoded image can be generated.

2.3 Inversion recovery MRI

For many MRI studies, it can be advantageous to null the signal from specific regions of the image. Inversion recovery (IR) pulse sequences enable the suppression of signal from tissues of a specific T1, thus making the tissue appear hypointense in the final image. This can reveal and facilitate the delineation of certain tissues or structures that would otherwise be masked in conventional T1- or T2-weighted images.

IR pulse sequences (Figure 2.7a) typically involve applying a 180° RF pulse before waiting a period of time – known as the inversion time, *TI* – when a 90° RF pulse is applied and the magnetisation is measured. If the duration of *TI* is chosen appropriately, it is possible to suppress the signal from a specific tissue. Normally, the choice of *TI* requires some *a priori* knowledge of the tissue relaxation times within the sample.

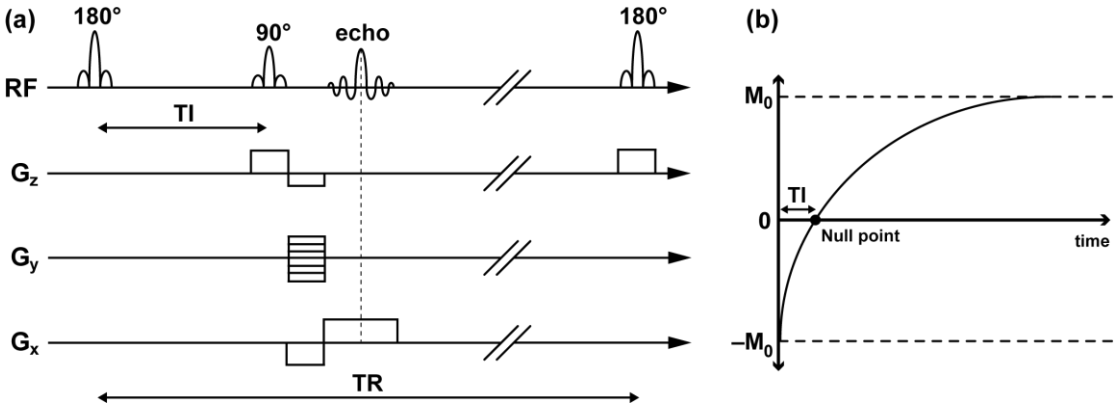

Figure 2.7: (a) Inversion recovery pulse sequence diagram. A 180° RF pulse is added before the gradient echo readout to (b) invert the sample magnetisation which subsequently recovers according to T1 relaxation, passing through a null point corresponding to zero magnetisation at time, TI.

Figure 2.7b shows a relaxation curve during an IR pulse sequence. The 180° RF pulse causes the sample magnetisation to flip along the z-axis so that the initial magnetisation is equal to $-M_0$, equivalent to all the nuclei within a sample swapping spin states from aligned to anti-aligned, and vice versa. Following this, the sample recovers according to T1 relaxation and grows exponentially according the equation:

$$M_z = M_0(1 - 2e^{\frac{-TI}{TR}}) \qquad \textbf{EQ 2.14}$$

In the heart, it is often necessary to null the myocardial signal to facilitate the delineation of infarcted regions (see section 2.7.3). In this case, *TI* is chosen so that the recovery curve of the myocardium passes through zero magnetisation ($M_0 = 0$), at which point the 90° RF pulse and subsequent gradients play out. As blood has a longer T1 duration it recovers more slowly and has non-zero magnetisation at $t = TI$, resulting in a hyperintense blood pool surrounded by hypointense myocardium.

2.4 Double inversion recovery MRI

Double inversion recovery (DIR) MRI pulse sequences extend the concepts underlying IR sequences, discussed in the previous section. In a standard IR sequence, the 180° RF pulse is a global pulse which inverts the spins of the entire sample including those external to the imaging plane. In a DIR sequence, this global inversion pulse is immediately followed by a second, slice-selective 180° RF pulse (Figure 2.8), which returns the nuclei within the slice

back to equilibrium magnetisation. Following the double inversion, the magnetisation of the slice is allowed to recover according to T1 relaxation.

DIR sequences exploit the fact that during T1 recovery the nulled blood external to the imaging slice flows into the slice, while simultaneously, any blood which experienced both inversion pulses exits the slice. In an ideal scenario, this exchange of equilibrated blood and recovering blood means that any signal remaining in the slice must be due to static tissue, which experienced both 180° RF pulses. For this reason, DIR sequences are often referred to as 'black blood' sequences because the blood has little or no signal.

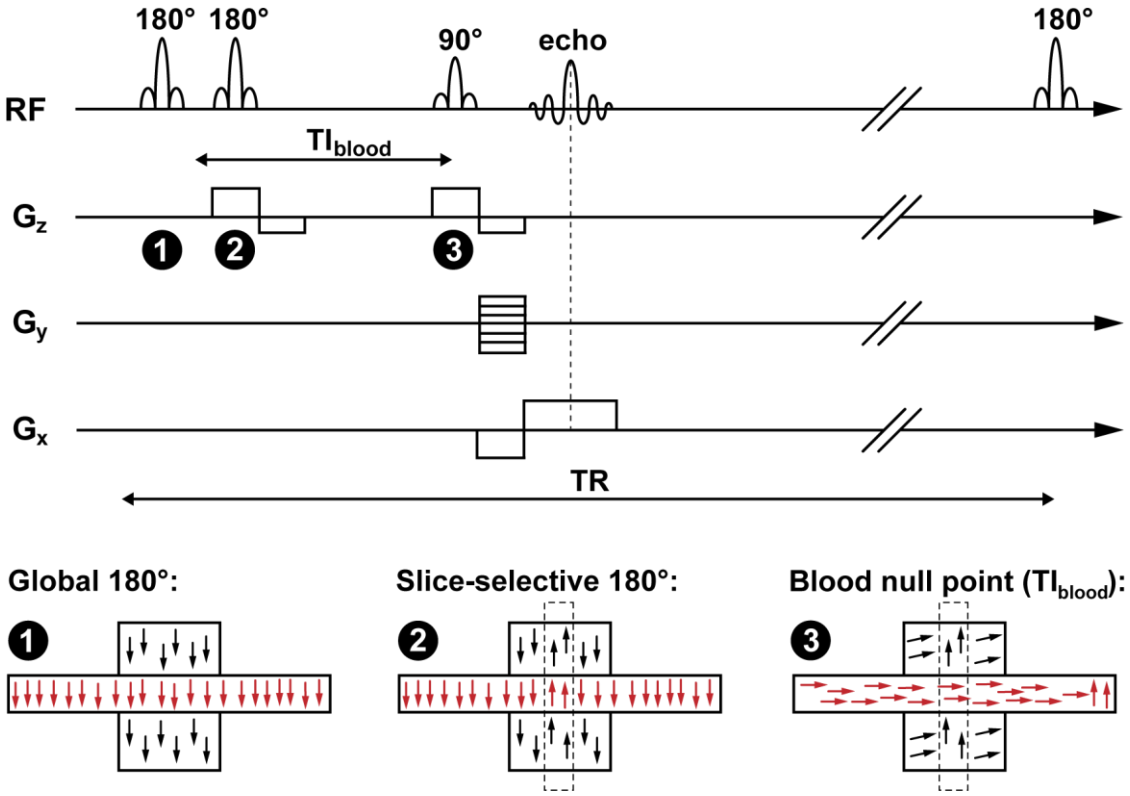

Figure 2.8: Double inversion recovery pulse sequence diagram and illustrations showing the effects of the inversion pulses on spin magnetisation in a flowing blood vessel surrounded by static tissue. (1) Global 180° RF pulse: the magnetisation of all spins is inverted. (2) Slice-selective 180° RF pulse (dashed line): spins within the slice are returned to equilibrium. (3) Blood null point, TI: equilibrated blood flows out of the slice and is replaced by inverted blood undergoing T1 recovery. TI is chosen to coincide with the null point of blood, so that there is no contribution to the signal from blood.

2.5 The challenges of cardiac MRI

Cardiac imaging is a particularly challenging part of MRI due to various types of physiological motion which must be compensated for to produce artefact-free images. MRI sequences must be adjusted to account for respiratory and cardiac motion, as well as high velocity blood flow. These issues are exacerbated in pre-clinical imaging studies because rats, and mice in particular, have very fast heart rates of 330-480 and 450-700 beats per minute, respectively, compared to the human heart rate of 50-100 beats per minute. In mice these values translate to an RR-interval range of 90-150ms. Acquiring a static image of the heart within a single heartbeat is very difficult unless the number of phase encode lines is greatly reduced, therefore most cardiac sequences must be run over multiple heartbeats, often while accounting for respiratory motion at the same time. The following sections describe the theory underlying the basic cardiac MRI techniques used in the rest of the thesis.

2.6 Physiological monitoring and gating in rodent cardiac MRI

For artefact-free cardiac images, animal physiology must be monitored and MRI pulse sequences must be 'gated' or 'triggered' according to the recorded physiological traces. A gated acquisition is one in which specific components of a pulse sequence, such as an RF pulse or gradient waveform, are synchronised to occur in time with a particular physiological event, such as the QRS complex of an ECG trace.

Commonly in pre-clinical imaging, ECG is measured using subcutaneously-inserted electrodes, which translate the electrical impulses of the heart into a continuous voltage waveform. Simultaneously, respiration motion is measured using a small pressure sensitive balloon placed underneath or on the abdomen of the mouse. In addition, body temperature and anaesthesia dose should also be monitored to keep the animal physiologically stable throughout the duration of the imaging session. Moreover, body temperature affects heart rate and parameters of cardiac function, and in turn gating, therefore it should be maintained at between 36.5-37°C for a consistent heart rate. Similarly, anaesthetic has a large impact on respiratory rate and even myocardial perfusion [16], therefore a constant dosage should be maintained as far as possible.

2.7 Cardiac CINE pulse sequences

The most commonly used cardiac MRI sequence is a CINE sequence, shorthand for cinematic, which generates a succession of images – known as frames – throughout the cardiac cycle. The first *in vivo* CINE scan was carried out in rabbits in 1986 [17]. Since then, CINE imaging has become widely used in clinical settings for non-invasively assessing cardiac structure and function. In mice, standard CINE sequences generate in the region of 15-30 frames per cardiac cycle. This gives a 4-8 millisecond temporal resolution, which is sufficient to quantify a host of systolic parameters, detailed further in section 2.7.2.

A number of CINE pulse sequences exist based on different readout strategies including fast-spin echo, gradient echo and steady-state free precession. For pre-clinical imaging, CINE pulse sequences are commonly based on a spoiled gradient echo preparation, also known as a FLASH (fast low-angle shot) sequence. Two gating strategies are possible with CINE methods: either prospective or retrospective, which will be discussed in the rest of this section.

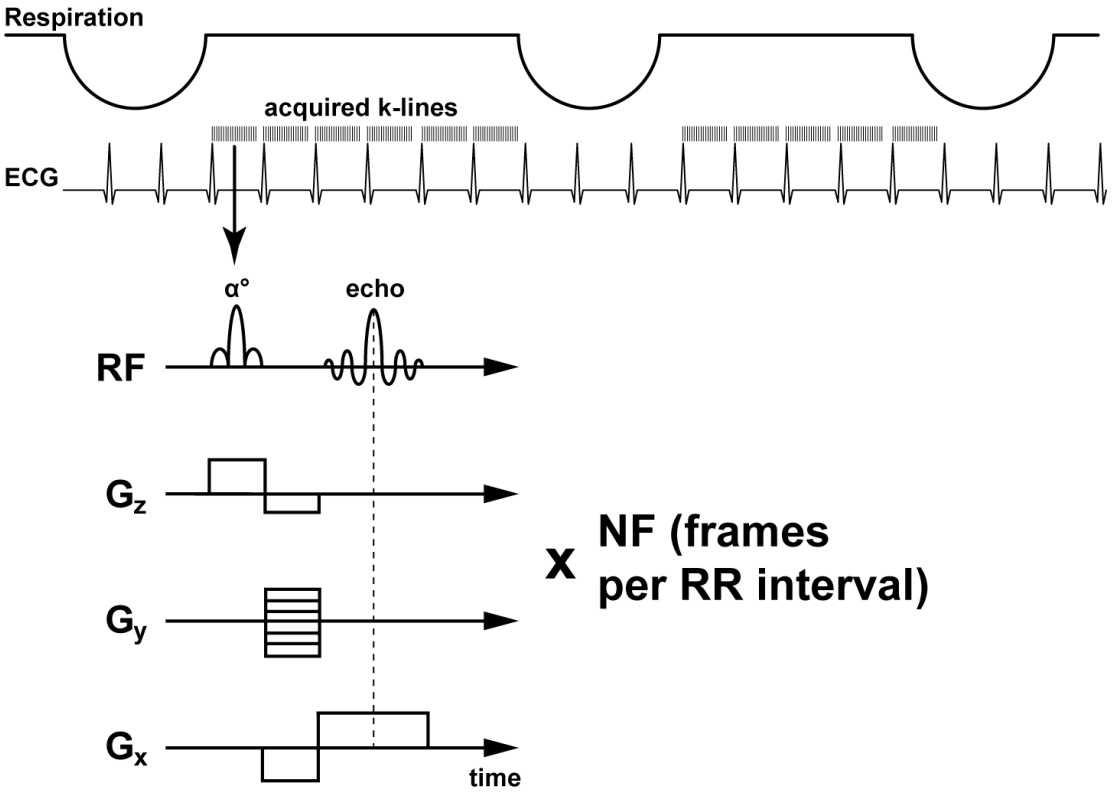

Figure 2.9: Prospectively-gated spoiled gradient echo CINE pulse sequence diagram. The sequence is double-gated to the respiration and ECG traces. Dummy pulses occur during respiration breaths. During the quiescent respiration phases, the sequence is triggered by the R-wave. NF frames, typically 20, are acquired in a single scan. A single line of k-space per frame is acquired with each heartbeat.

Figure 2.9 shows a prospectively-gated spoiled gradient echo CINE pulse sequence diagram. Following R-wave detection, the sequence is repeated *NF* times (*NF* = number of frames, variable depending on the heart rate of the animal). Due to the high heart rate of mice, typically *NF* = 15-30 frames meaning that the repetition time is usually very short (*TR* = 5 ms). In a single heartbeat, one line of k-space is acquired for each frame, therefore it takes 128 or 256 heartbeats to acquire a single slice CINE, depending on resolution. The sequence is simultaneously respiration-gated such that data acquisition is disabled during breaths: the pulse sequence plays-out, however, no lines of k-space are acquired. Such repetitions of the sequence are referred to as dummy pulses and are used to maintain steady state magnetisation. Generally, CINE sequences are run with low flip-angle, slice-selective RF pulses (typically < 30° at 9.4T), which produces bright-blood contrast surrounded by darker myocardium. The RF pulse saturates the in-plane myocardium, whereas inflowing blood is unsaturated because it is unaffected by the RF pulse. The level of contrast between the blood pool and myocardium can be altered by changing the flip angle [18]. Higher flip angles cause greater saturation of the myocardium increasing the contrast, whereas very low flip angles (~5°) homogenise the signals of the blood pool and myocardium.

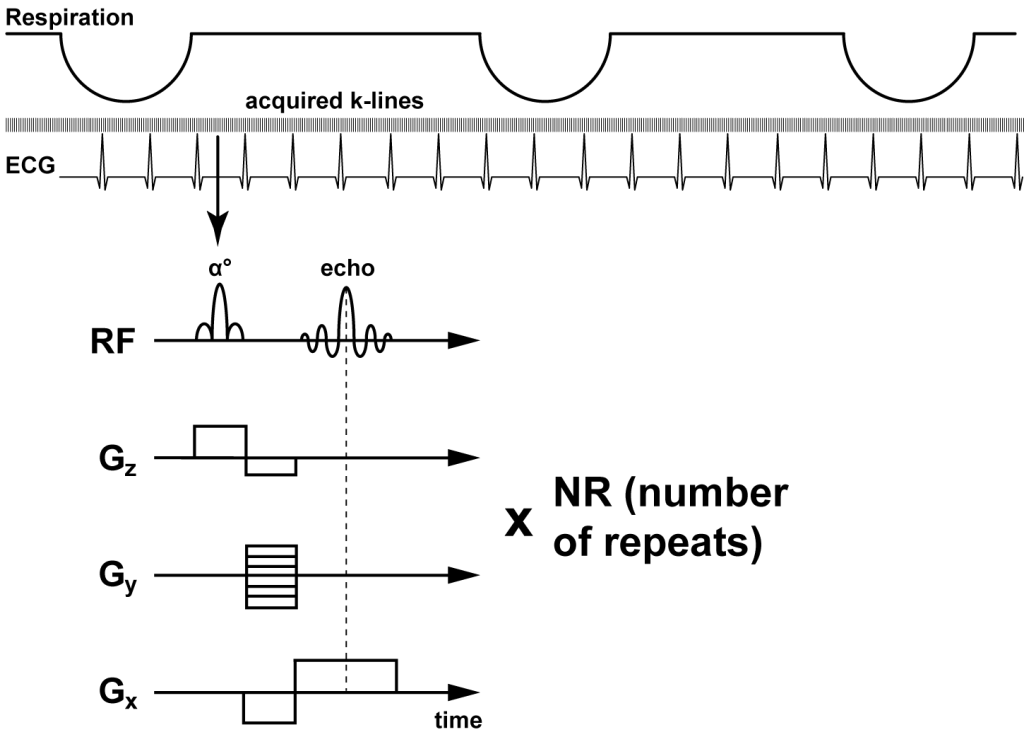

Figure 2.10: Retrospectively-gated spoiled gradient echo CINE pulse sequence diagram. The sequence is run continuously without any gating. Typically, respiration, ECG and RF pulse timestamps are recorded and k-space is reconstructed offline by binning the RF pulses into the appropriate cardiac frames.

Figure 2.10 shows a retrospectively-gated spoiled gradient echo CINE pulse sequence diagram. In this case, the CINE pulse sequence is played continually. Cardiac and respiratory gating are performed offline after completion of data acquisition. Retrospective gating has a number of advantages. The entire cardiac cycle can be imaged including late diastole, which is not possible using a standard prospectively-gated method because the sequence must be stopped during diastole to prevent running into the next heartbeat. Furthermore, retrospective gating is useful in patients and animals with cardiac arrhythmias because lines of k-space can be accepted or rejected depending on the irregularity of certain heartbeats.

In recent years, a variety of retrospective sorting strategies have emerged. Conventionally, cardiac and respiratory traces are recorded using ECG electrodes and respiratory bellows, as in prospective imaging, in parallel with recordings of the signal echo timestamps [19]. Once the acquisition is complete, k-space is sorted based on the timing of these events. This is the method illustrated by the pulse sequence in Figure 2.10. Alternatively, self-gated retrospective pulse sequences [20-22] acquire a 1-dimensional 'navigator' signal from a region which intersects different tissues experiencing both respiratory and cardiac motion. k-space lines are then accepted or rejected, and sorted, based entirely on this signal which is modulated by cardiac and respiratory movement. The advantage of self-gating is that there is no requirement for ECG or respiratory monitoring. In a similar method, cardiac and respiratory motion can be extracted from the echo peak MR signal of an ungated radial acquisition [23] for retrospective reconstruction. Each strategy also has limitations. Retrospective-gating using ECG electrodes suffers from magnetic gradient interference [24], which can make the ECG signal very noisy, and electrode positioning can also be an issue. Self-gating strategies are also imperfect, as in pathological mouse models turbulent blood flow can cause poor periodicity in the navigator signal [25].

2.7.1 Images generated by a standard CINE protocol

A routine CINE protocol will image the heart in three different orientations, as shown in Figure 2.11. When a patient or animal is placed in an MRI scanner, the heart lies obliquely in the chest relative to the imaging gradients. Therefore, cardiac imaging initially requires the acquisition of pilot scans to accurately determine the cardiac axes. After this, two long-axis views of the heart are acquired with a CINE sequence. From this pair of images, a short-axis CINE stack is acquired from the apex to the base of the heart. In a mouse heart, with 1mm slice thickness, this typically corresponds to 9-12 slices for full heart coverage.

The 4-chamber CINE depicts the two ventricles, the two atria and the aorta. Chamber valves can also be observed depending on resolution. The 2-chamber CINE shows the left ventricle and left atrium. The short axis view shows the left ventricle and right ventricle, as well as the atria and great vessels in the higher slices. Standard spoiled gradient echo CINE scans have bright blood (hyperintense) which allows easy delineation of the blood pool against the darker, grey, myocardium. However, all views are affected by fast inflow artefacts to some extent, which cause signal dropout.

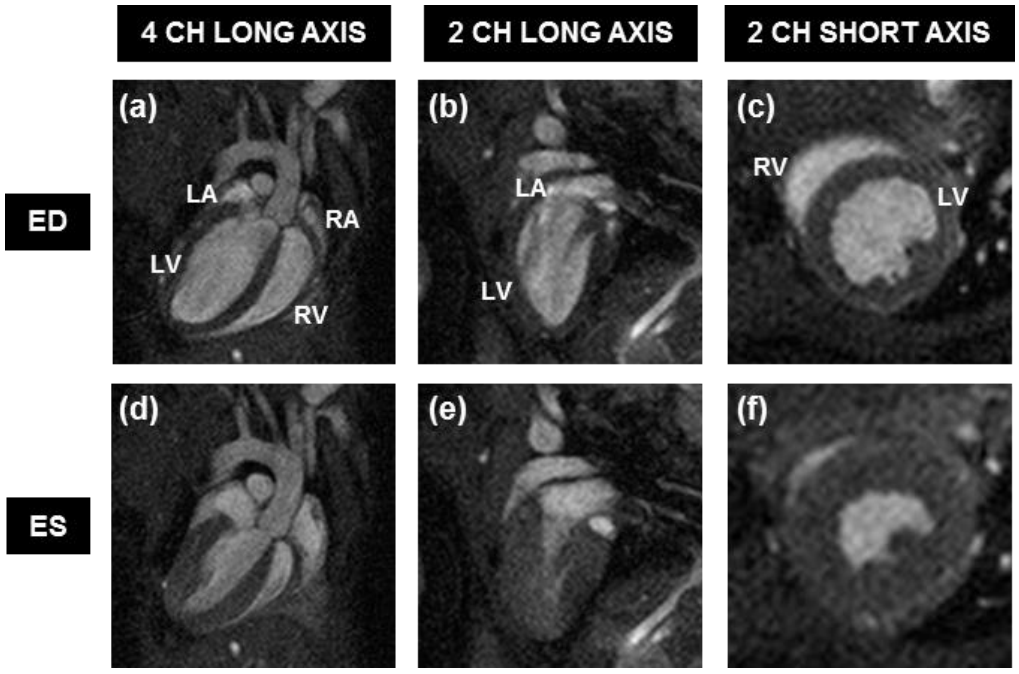

Figure 2.11: CINE frames from a mouse heart in the three cardiac axes. Top row shows views at end diastole (ED). Bottom row shows views at end systole (ES). The 4-chamber long axis views show the left atria (LA), right atria (RA), left ventricle (LV) and right ventricle (RV). The 2-chamber long axis view shows the LA and LV. The 2-chamber short axis images show a mid-ventricle slice.

2.7.2 CINE image analysis

CINE images contain a wealth of information. Structural assessment of the great vessels, myocardial thickness and contractility can all be observed at a glance. However, more thorough, quantitative analysis of CINE images enables the assessment of a host of functional parameters, which help determine cardiac performance and health.

Systolic cardiac parameters – which indicate the performance of the heart during the contracting phase of the cardiac cycle – are assessed by segmentation of the left ventricle endocardium and epicardium at two time points in the cardiac cycle: end diastole and end systole. In this thesis, semi-automatic segmentation was carried out using the software package Segment (Medviso, Sweden), unless stated otherwise. Figure 2.12 shows an

example of a segmented CINE stack. The software package applies an automatic segmentation algorithm to the images. If the automated segmentation is inaccurate, the user can correct the regions manually. Segmentation of the left ventricle endocardium in all ED slices gives end diastolic volume (EDV). Similarly, endocardial segmentation in all ES slices gives end systolic volume (ESV). From these two sets of measurements, various systolic parameters can be calculated, as detailed in Table 2.1. Additional segmentation of the epicardium enables calculation of left ventricular mass (LVM). The average of two epicardial measures at ED and ES, matched to within 2% error of each other, gives a final measure of LVM.

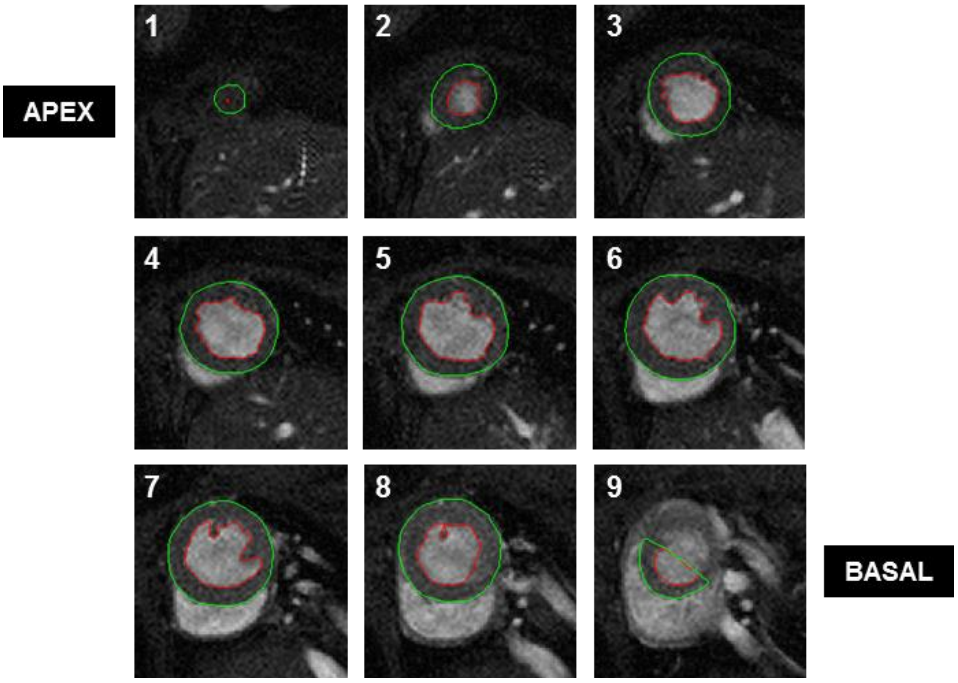

Figure 2.12: Short-axis CINE stack segmentation of the left ventricle blood pool (red) and left ventricle epicardium (green) at end diastole for calculating systolic functional parameters. In the most basal slice (9), the segmentation intersects the ventricular and atrial tissue and blood. For analysis of functional parameters, the CINE stack is also segmented at end systole.

Parameter	**Method of calculation**	**Functional relevance**
Stroke volume (SV)	ESV – EDV	Volume of blood ejected from the LV within a heartbeat
Ejection fraction (EF)	SV/EDV × 100%	Percentage of blood ejected from the LV within a heart beat
Left ventricular mass (LVM)	myocardial volume × 1.05 g/ml [26]	Mass of the left ventricular tissue

Table 2.1: Cardiac systolic functional and morphological parameters, which can be determined by segmentation of standard CINE images.

2.7.3 Late gadolinium enhanced MRI

Assessment of scar tissue size following myocardial infarction is widely visualised both clinically and pre-clinically using gadolinium-based contrast agents during MRI scans, such as gadolinium diethylenetriaminepentaacetic acid (Gd-DTPA). Gadolinium contrast agents are non-targeted and therefore distribute passively throughout the blood and extracellular space [27]. In an infarcted region of myocardium, gadolinium contrast agent exhibits delayed accumulation and longer retention [28] due to decreased tissue perfusion and increased extracellular volume compared to healthy myocardium, as well as an increase in total accumulation due to tissue necrosis. This mismatch in kinetics between healthy and infarcted tissue is exploited for the purposes of late gadolinium enhancement (LGE) MRI. Gadolinium is a T1 shortening contrast agent, therefore the increased presence of contrast agent in regions of infarcted tissue causes a signal difference between healthy and infarcted tissue, allowing delineation of scar tissue and quantification of infarct volume.

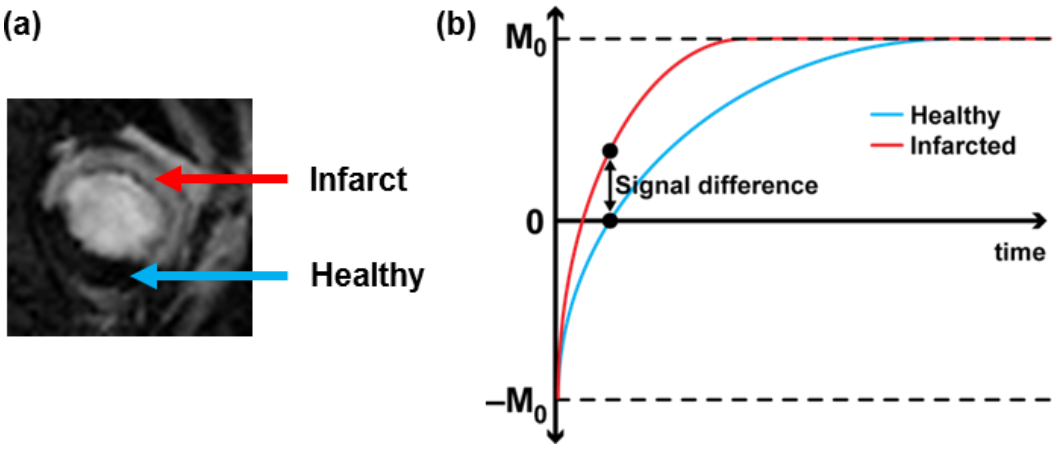

Figure 2.13: T1 relaxation of healthy and scar tissue in an IR late-gadolinium enhanced experiment. (a) 2-chamber short axis slice in a mouse heart showing nulled myocardium and hyperintense infarct tissue. (b) The gadolinium contrast agent preferentially accumulates in the infarct region, causing faster relaxation in the scar tissue. Images are generated at the null point of the healthy myocardium when the scar tissue has higher signal.

In this thesis, all gadolinium-based myocardial infarction imaging is carried out using a multi-slice, IR late-gadolinium enhanced protocol, originally developed in CABI by Dr Anthony Price [29]. Firstly, Gd-DTPA is injected intraperitoneally 10 minutes prior to imaging. The imaging protocol consists of two pulse sequences. The first sequence is an inversion time sweep to determine the optimum value of *TI* required for nulling of the healthy myocardium and hyperintense signal in scar tissue (Figure 2.13). In mice at 9.4T, generally, *TI* = 300-400 ms. Following this, a multi-slice IR sequence with optimised *TI* is used to generate long-axis and short-axis images of the heart.

2.8 Experimental Hardware in CABI

2.8.1 Pre-clinical MRI hardware

All MRI experiments in this thesis were carried out on the Agilent 9.4T horizontal bore scanner (Agilent Technologies, Santa Clara, USA) in CABI (Figure 2.14) using either 1000mT/m or 400mT/m gradient inserts, with internal diameters of 60mm and 120mm, respectively. The scanner software VNMRJ (versions 2.3A and 3.1) were used for data acquisition. Various different volume RF coils were used throughout the experiments with inner diameters of 26mm, 35mm, 39mm and 72mm (RAPID biomed, Ripmar, Germany). For most rat imaging studies, the 72mm volume RF coil was used for transmission with a 4-channel phased array coil used in receive mode.

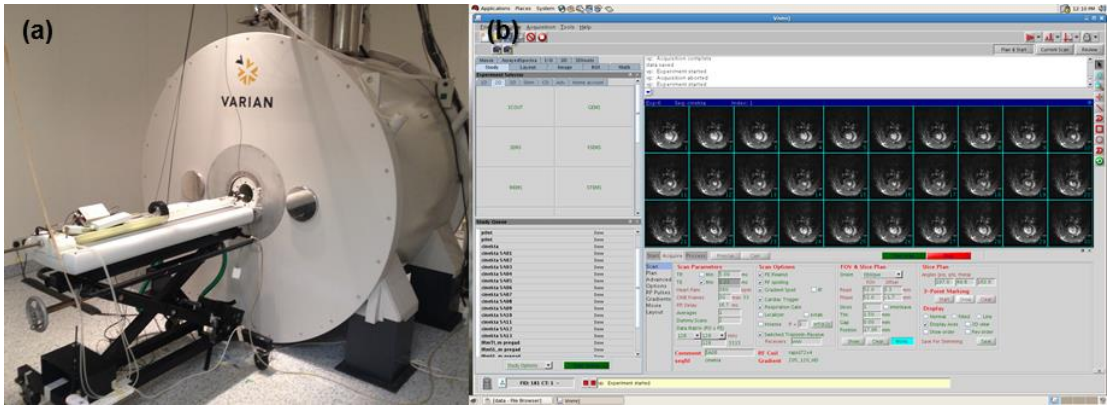

Figure 2.14: (a) The Agilent 9.4T scanner in CABI and (b) a screenshot of the software, VNMRJ, used to control the scanner.

Mice and rats were placed in a cradle which could be positioned in the centre of the MRI scanner bore (Figure 2.15). Generally, mice were positioned supine whereas rats were positioned prone. Animal body temperature was measured using a rectal probe. Temperature was regulated using a hot water system which pumped the water through tubes placed underneath and on top of the animal. Respiration was monitored using a neonatal apnoea pad taped to the abdomen of the animal. For some experiments, a three-lead electrode set was used for monitoring animal ECG. For gadolinium contrast agent-based experiments, an additional infusion line was placed in the cradle.

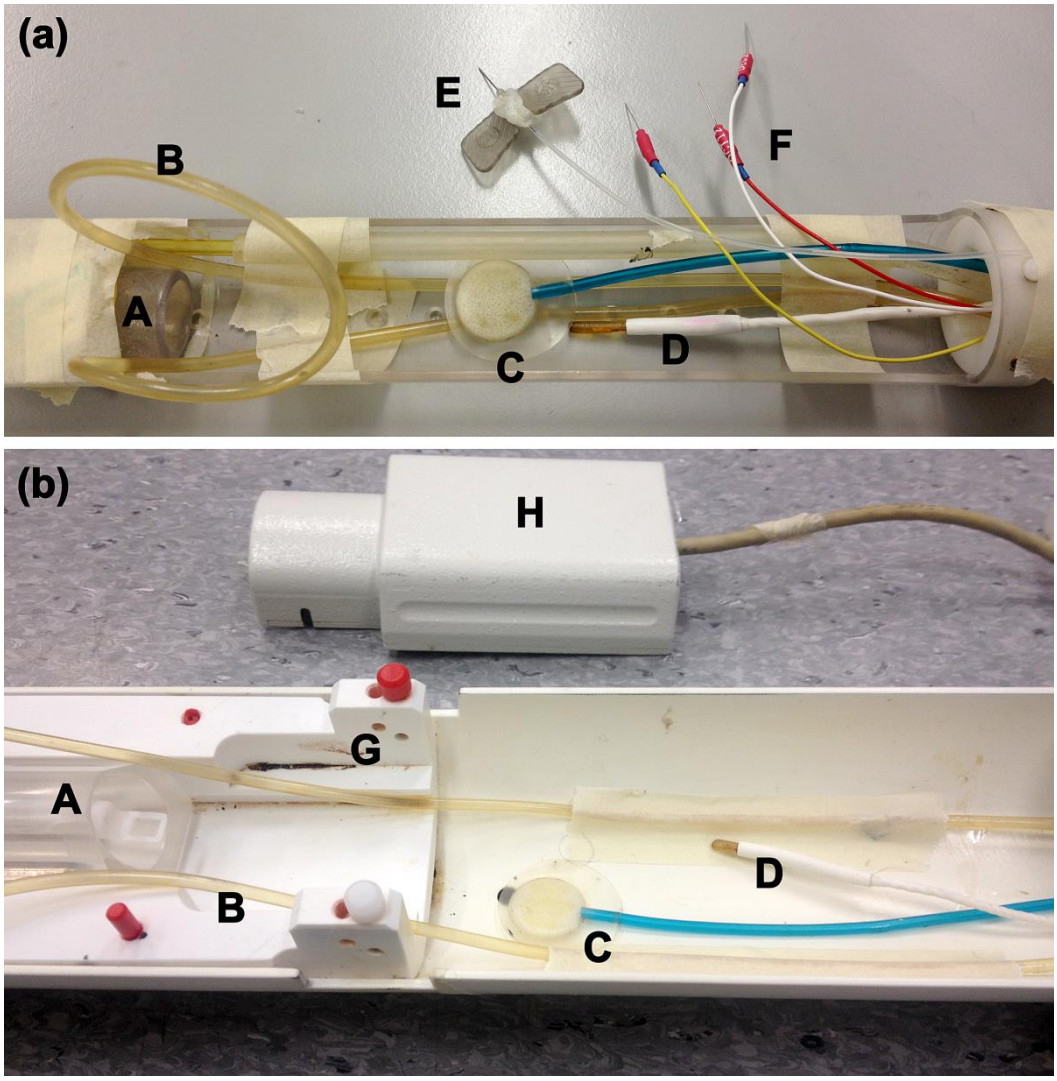

Figure 2.15: Animal cradles used for imaging (a) mice and (b) rats in the MRI scanner. A: anaesthetic nose cone, B: heated water tubes, C: respiration pad, D: rectal temperature probe, E: infusion line, F: three-lead subcutaneous ECG electrodes, G: ear bar holders, H: 4-channel phased array coil.

Software designed by SA Instruments (Stony Brook, NY) was used to monitor animal temperature, respiration and ECG (Figure 2.16a). For most scans the software was also used to control respiration- and ECG-gating. For the retrospective CINE studies in Chapter 5, a Power1401 data logger (Cambridge Electronic Design, Cambridge, UK) was used in conjunction with Spike2 software (Cambridge Electronic Design, Cambridge, UK) for recording respiration, ECG and RF events during the scans (Figure 2.16b). More specific detail on Spike2 will be given in Chapter 5.

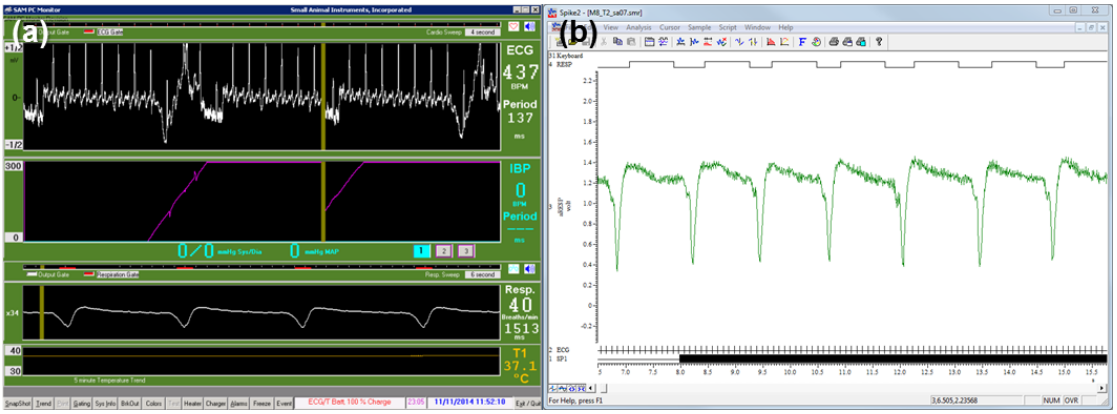

Figure 2.16: (a) SA Instruments animal monitoring software and (b) Spike2 software for recording physiological traces for retrospective image reconstruction.

2.8.2 Pre-clinical ultrasound hardware

All ultrasound imaging in this thesis (see Chapter 5) was carried out on a VisualSonics Vevo 2100 (CA, USA) system (Figure 2.17) using a VisualSonics 550D 30 MHz transducer. Ultrasound was conducted by Dr Daniel Stuckey, a highly experienced ultrasound operator. Mice were positioned supine on a physiological monitoring platform which simultaneously regulated body temperature and measured respiration and ECG traces. Prior to imaging, hair removal cream (Veet, UK) was applied to the chest to reduce attenuation of ultrasound signal.

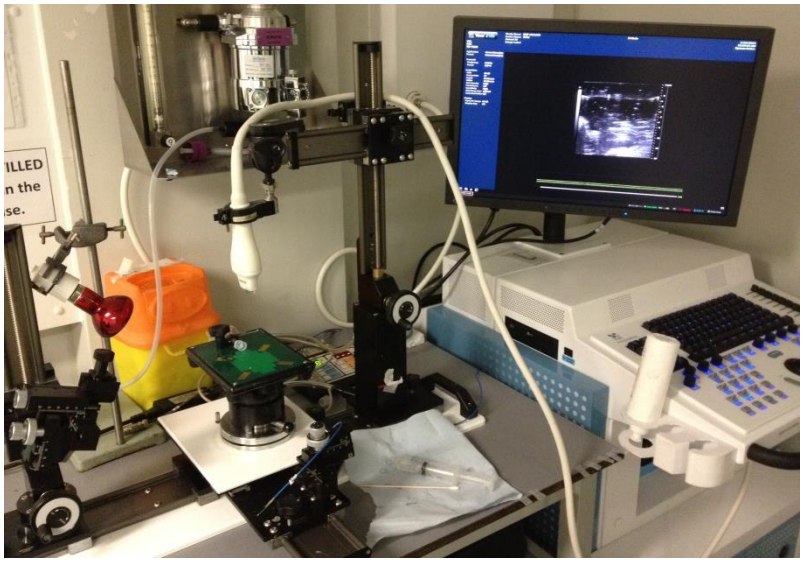

Figure 2.17: The VisualSonics Vevo 2100 ultrasound scanner in CABI showing the animal platform (green), ultrasound probe and hardware to control the system.

2.8.3 Syringe pump

A syringe pump (PHD 2000 Syringe Pump, Harvard Apparatus, Kent, UK) was used for a number experiments (Chapter 3) to drive water through a phantom for the purposes of measuring flow in the MRI scanner (Figure 2.18). The syringe pump console was positioned on a benchtop outside of the MRI scanner room. The syringe driver was positioned on a small platform inside the MRI scanner room. A 50ml syringe was filled with distilled water and connected to the flow phantom inside the scanner bore via plastic tubing. The console allowed the input of precise flow rates down to a minimum of 0.0001µL/hr.

Figure 2.18: The syringe pump used to pass water through a flow phantom within the bore of the MRI scanner.

.

2.9 Summary

In this chapter, the MRI theory and physics underlying the rest of this thesis was described. This included discussion of the basic principles of nuclear magnetic resonance, spatial encoding, data acquisition and fundamental pulse sequence design. Finally, the experimental equipment used in the CABI laboratory was described. The following chapters contain the results of the research performed in this thesis.

2.10 References

1. Haacke EM, et al. *Magnetic Resonance Imaging:* physical principles and sequence design, 1999.
2. Bernstein MA, KF King and XJ Zhou. *Handbook of MRI pulse sequences* Elsevier, 2004.
3. McRobbie DW, et al. *MRI from Picture to Proton*. Cambridge University Press, 2006.
4. Hashemi RH, Bradley WG and Lisanti CJ. *MRI: The Basics.* Lippincott Williams & Wilkins, 2012.
5. Gerlach W and Stern O. *Über die richtungsquantelung im magnetfeld.* Annalen der Physik, 1924. **379**(16): p. 673-699.
6. Geva T. *Magnetic Resonance Imaging: Historical Perspective.* Journal of Cardiovascular Magnetic Resonance, 2006. **8**(4): p. 573-580.
7. Bloch F. *Nuclear Induction.* Physical Review, 1946. **70**(7-8): p. 460.
8. Purcell EM, Torrey H and Pound RV. *Resonance absorption by nuclear magnetic moments in a solid.* Physical Review, 1946. **69**(1-2): p. 37.
9. Hahn E. *Detection of sea-water motion by nuclear precession.* Journal of Geophysical Research, 1960. **65**(2): p. 776-777.
10. Morse O and Singer J. *Blood velocity measurements in intact subjects.* Science, 1970. **170**(3956): p. 440-441.
11. Gatehouse PD, et al. *Applications of phase-contrast flow and velocity imaging in cardiovascular MRI.* European Radiology, 2005. **15**(10): p. 2172-2184.
12. Sweetman B and Linninger AA. *Cerebrospinal fluid flow dynamics in the central nervous system.* Annals of Biomedical Engineering, 2011. **39**(1): p. 484-496.
13. Simpson RM, Keegan J and Firmin DN. *MR assessment of regional myocardial mechanics.* Journal of Magnetic Resonance Imaging, 2013. **37**(3): p. 576-599.
14. Pelc NJ, et al. *Encoding strategies for three-direction phase-contrast MR imaging of flow.* Journal of Magnetic Resonance Imaging, 1991. **1**(4): p. 405-413.

15. Chavez S, Xiang Q-S and An L. *Understanding phase maps in MRI: a new cutline phase unwrapping method.* IEEE Transactions on Medical Imaging, 2002. **21**(8): p. 966-977.

16. Kober F et al. *Myocardial blood flow mapping in mice using high-resolution spin labeling magnetic resonance imaging: Influence of ketamine/xylazine and isoflurane anesthesia.* Magnetic Resonance in Medicine, 2005. **53**(3): p. 601-606.

17. Frahm J, Haase A and Matthaei D. *Rapid NMR imaging of dynamic processes using the FLASII technique.* Magnetic Resonance in Medicine, 1986. **3**(2): p. 321-327.

18. Tyler DJ, et al. *CINE-MR imaging of the normal and infarcted rat heart using an 11.7 T vertical bore MR system.* Journal of Cardiovascular Magnetic Resonance, 2006. **8**(2): p. 327-333.

19. Bishop J, et al. *Retrospective gating for mouse cardiac MRI.* Magnetic Resonance in Medicine, 2006. **55**(3): p. 472-477.

20. Heijman E, et al. *Comparison between prospective and retrospective triggering for mouse cardiac MRI.* NMR in Biomedicine, 2007. **20**(4): p. 439-447.

21. Nieman BJ, Szulc KU and Turnbull DH. *Three-dimensional, in vivo MRI with self-gating and image coregistration in the mouse.* Magnetic Resonance in Medicine, 2009. **61**(5): p. 1148-1157.

22. Bovens SM, et al. *Evaluation of infarcted murine heart function: comparison of prospectively triggered with self-gated MRI.* NMR in Biomedicine, 2011. **24**(3): p. 307-315.

23. Hiba B, et al. *Cardiac and respiratory double self-gated cine MRI in the mouse at 7 T.* Magnetic Resonance in Medicine, 2006. **55**(3): p. 506-513.

24. Polson M, Barker A, and Gardiner S. *The effect of rapid rise-time magnetic fields on the ECG of the rat.* Clinical Physics and Physiological Measurement, 1982. **3**: p. 231-234.

25. Coolen BF, et al. *Contrast-enhanced MRI of murine myocardial infarction–Part II.* NMR in Biomedicine, 2012. **25**(8): p. 969-984.

26. Kani KK, et al. *Problem solving in radiology: cardiovascular imaging.* Academic Radiology, 2014.

27. Weinmann HJ, et al. *Characteristics of gadolinium-DTPA complex: a potential NMR contrast agent.* American Journal of Roentgenology, 1984. **142**(3): p. 619-624.

28. Eichstaedt H, et al. *Magnetic Resonance Imaging (MRI) in different stages of myocardial infarction using the contrast agent gadolinium-DTPA.* Clinical Cardiology, 1986. **9**(11): p. 527-535.

29. Price AN, et al. *Rapid assessment of myocardial infarct size in rodents using multi-slice inversion recovery late gadolinium enhancement CMR at 9.4 T.* Journal of Cardiovascular Magnetic Resonance, 2011. **13**(1): p. 1-9.

CHAPTER 3: IMAGING EXTRACELLULAR AND INTERSTITIAL FLUID FLOW IN EXPERIMENTAL ANIMAL MODELS OF DISEASE WITH EXTRAVASCULAR CONVECTOGRAPHY MRI

Extravascular convectography (EVAC) MRI is a novel imaging sequence designed to image the flow of extracellular fluid, including interstitial and cerebrospinal fluid. Following stroke, intracranial pressure rises causing changes in the extracellular fluid dynamics of the brain. The main objective of the work in this chapter was to use EVAC MRI to image and compare the extracellular fluid dynamics in the normal rat brain and a rat model of stroke. Working towards this aim, a number of validation studies were conducted including flow phantom experiments and some *in vivo* imaging of subcutaneous mouse tumours, where the interaction between interstitial fluid and the tissue microenvironment is relatively well-understood.

Parts of this chapter are contained in the paper: *Imaging tumor interstitial fluid dynamics with MRI.* Simon Walker-Samuel, Thomas Roberts, Rajiv Ramasawmy, Jake Burrell, S. Peter Johnson, Jack Wells, Bernard Siow, Simon Richardson, Miguel Gonçalves, Douglas Pendsé, Simon P. Robinson, R. Barbara Pedley, Mark F. Lythgoe (under review).

3.1 Introduction

Stroke is the second largest cause of death worldwide behind heart disease [1]. In 2012, 6.7 million people died of stroke worldwide. The primary cause of stroke is ischaemia, which accounts for 85% of cases [2], where the blood supply to the brain is blocked by a thrombus. A series of cellular and molecular processes following ischaemia (see section 1.2.2), known as the ischaemic cascade [3], leads to neuronal death and ultimately brain damage. Currently, MRI is widely used for the assessment of the ischaemic penumbra [4] using dual diffusion weighted imaging (DWI) [5] and perfusion weighted imaging (PWI) [6] scans, which generate contrast based on the movement of water molecules and the perfusion state of brain tissue, respectively (section 1.2.3).

Recently in CABI, Dr Simon Walker-Samuel created an MRI pulse sequence for measuring extracellular fluid dynamics [7], known as extravascular convectography (EVAC) MRI. In this sequence, signal generation in phase contrast images comes from the flow of interstitial fluid molecules through the tissue microenvironment. The original application of the sequence was to image interstitial fluid flow in subcutaneous mouse tumours for the purpose of assessing the efficacy of anti-cancer drug delivery techniques. Walker-Samuel et al. showed that interstitial fluid pressure (IFP) maps – derived from interstitial fluid velocity measurements using EVAC – were strongly correlated with gold-standard, invasive, wick-in-needle measures. This demonstrated the potential of EVAC as a non-invasive method for examining IFP, which is a highly important parameter in tumour microbiology.

In stroke, oedema causes severe alterations in brain interstitial fluid and cerebrospinal fluid dynamics. Therefore, the overarching aim of the work in this chapter was to apply EVAC to stroke, to establish whether quantification of brain fluid dynamics could offer some interesting and useful pathological information, potentially beyond the information attainable using well-established DWI/PWI mismatch paradigms.

It should be noted that some of the work by Walker-Samuel et al. fed into this chapter, and conversely some of the work in this chapter contributes to the wider development of the EVAC technique. Where work is not my own, but necessary for discussion, credit will be given to the appropriate author.

In order to follow the experiments in this chapter, an understanding of the EVAC sequence is needed, which is discussed in the next section, 3.1.1. Section 3.2 discusses the aims and objectives of the experiments in this chapter, including a number of preliminary experiments carried out to validate and ensure the robustness of the EVAC sequence. Finally, the results are presented in section 3.4 and discussed in section 3.5.

3.1.1 The EVAC sequence

The EVAC pulse sequence is designed to eliminate any MR signal contributions from blood, while velocity-encoding gradients sensitise moving water molecules. Therefore, the acquired signal comes from only tissue and interstitial fluid, and the resulting phase contrast difference images are proportional to interstitial fluid flow.

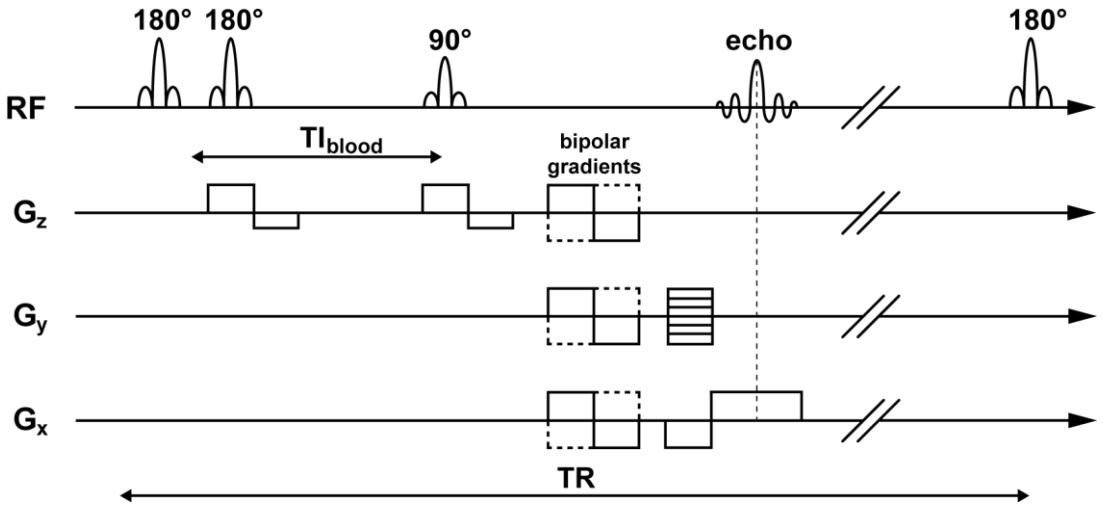

Figure 3.1: The EVAC pulse sequence. The sequence is based on a gradient echo readout containing velocity-encoding bipolar gradients. A double inversion preparation precedes the readout. The double inversion nulls any signal contribution from blood within the slice. The velocity-encoding bipolar gradients are sensitive to any moving nuclei. Therefore, any phase contrast signal caused by flow should originate from interstitial fluid, if imaging tissue.

The pulse sequence (Figure 3.1) combines two MRI concepts discussed in chapter 2, specifically bipolar velocity-encoding gradients and a double inversion recovery (DIR) RF pulse preparation. The double inversion preparation consists of two 180° hyperbolic secant RF pulses. The first RF pulse is applied globally and causes inversion of the entire sample. The second RF pulse is slice selective and reverses the spins within the slice back to equilibrium magnetisation. After a recovery delay, t_{rec}, blood which experienced only the global inversion pulse recovers following T1 recovery to the blood null point. During this time, inverted blood also flows into the imaging slice while unsaturated blood flows out of the slice. In theory, the slice only contains saturated blood which does not contribute to the signal in the final image.

At time, t_{rec}, the gradient echo readout is applied with the additional bipolar velocity-encoding gradients played in either the readout, phase-encode or slice-select direction. The sequence is then repeated with the velocity-encoding gradients inverted. Stationary spins acquire zero net phase from the bipolar gradients. However, if the spins are moving in the

direction of the bipolar gradients while they play, the spins accumulate additional phase, linearly proportional to their velocity. In total, four scans are acquired to construct a single 2D velocity-encoded image: one per spatial encoding direction and one per bipolar gradient polarity.

3.2 Individual study outlines and aims

The main objective of the work in this chapter was to use EVAC for imaging brain fluid dynamics in a rat stroke model. To this end, a number of preliminary studies were carried out to further validate the EVAC technique. This section provides background to each study and details the aim of each one.

3.2.1 Phantom study 1 – establishing the slowest measureable fluid velocity in a flow phantom

The vast majority of MRI phase contrast sequences are applied to imaging fast, bulk blood flow through vasculature, such as the great vessels of the heart [8-11] and the cerebrovascular arteries [12, 13]. Blood flow velocity in these vessels is typically anywhere between 1-150 cm/s. By comparison, interstitial fluid velocity is believed to be several orders of magnitude lower, on the order of microns per second [14]. As a consequence, the magnitude of the velocity-encoding gradients used in a phase contrast MRI sequence must be greatly increased for sensitivity to the slowest flows, according to equation 3.1:

$$VENC = \frac{\pi}{\gamma G T^2} \qquad \textbf{EQ 3.1}$$

where *VENC* is maximum resolvable velocity, γ is the gyromagnetic ratio and *G* and *T* are the velocity-encoding gradient magnitude and duration, respectively. However, the magnitude of the velocity-encoding gradients is limited by the scanner hardware, hence they can only be increased to a certain strength. Furthermore, the maximum duration of the velocity-encoding gradients is also limited, as gradient duration is proportional to signal loss (due to spin dephasing). Therefore, using a water flow phantom, the aims of this study were to establish an optimum VENC for measuring slow flow and to infer the slowest measureable speed using the 9.4T MRI scanner in CABI.

3.2.2 Phantom study 2 – measuring and correcting the phase offset caused by electrical eddy currents

The magnetic fields generated by the G_x, G_y and G_z imaging gradients in an MRI scanner induce electrical eddy currents within the magnet, the imaging gradients themselves and the RF coil, which in turn create small, unwanted magnetic fields that act to degrade image quality [15]. Electrical eddy currents arise according to Faraday's law:

$$\varepsilon = -\frac{d\Phi_m}{dt} \qquad \textbf{EQ 3.2}$$

where ε is the electromotive force, Φm is the magnetic flux and t is time. Equation 3.2 implies that an electric field is generated whenever there is a *change* in magnetic flux. Gradient waveforms in an MRI pulse sequence require a finite ramp-up time, defined by the gradient slew rate, and it is during this period of changing magnetic field that electrical eddy currents are generated, as illustrated in Figure 3.2. A rising ramp generates a negative eddy current magnetic field, and vice versa. The net effect is that the shape of the gradient waveforms is imperfect. Phase contrast velocimetry measurements are particularly prone to electrical eddy current distortion, which leads to phase offset errors causing non-zero quantification of stationary substances and inaccurate measurement of flowing substances [16].

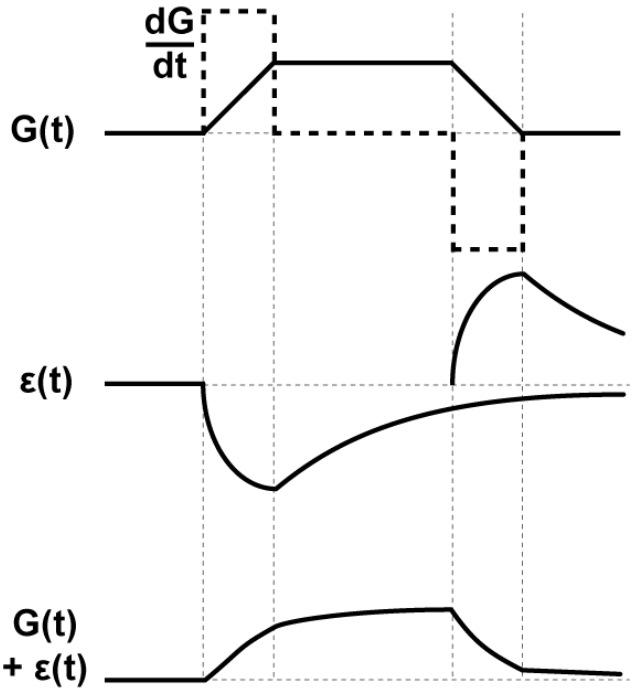

Figure 3.2: The effects of electrical eddy currents on distorting gradient waveforms in an MRI pulse sequence.

Previous vasculature blood flow studies using phase contrast MRI showed improved quantification following phase offset correction [16-18]. It was anticipated that electrical eddy currents may affect our measurements of extracellular fluid flow, therefore, a phantom experiment was performed to assess the effects of electrical eddy currents on our 9.4T MRI scanner. A previous study [17] demonstrated that the phase offset resulting from electrical eddy currents can be estimated by measuring the phase of a stationary sample. Thus, the aim of this study was to measure the phase offset caused by the velocity-encoding bipolar gradients within the EVAC sequence using an agar phantom and use this information to correct inaccuracies in MR measurements of a flow phantom.

3.2.3 Mouse tumour study – Establishing the repeatability and reproducibility of EVAC *in vivo* and applying the phase offset correction method *in vivo*

Prior to stroke imaging, mouse tumour imaging was carried out with EVAC to examine the *in vivo* repeatability and reproducibility of the EVAC sequence, which had not been carried out in previous developmental work by Walker-Samuel et al [7]. Subcutaneous tumours were chosen as a logical starting point for examining the robustness of the sequence *in vivo* because the interstitial fluid dynamics of the tumour microenvironment have been studied extensively [19-25]. Further to this, tumour imaging allowed the opportunity to investigate the effect of applying the eddy current correction method *in vivo*, which had also not been carried out previously.

Therefore, the aims of this study were 1) to examine the within- and between-session variability of interstitial fluid measurements using EVAC and 2) to see how improvements in velocity measurements using the eddy current correction method compared with the inherent *in vivo* variability of the EVAC sequence.

3.2.4 Stroke rat study – Imaging extracellular fluid dynamics in an experimental rat stroke model

Finally EVAC was applied to imaging extracellular fluid dynamics (brain interstitial fluid and cerebrospinal fluid) in an experimental rat stroke model. Compared to our knowledge of tumour interstitial fluid dynamics, brain fluid dynamics remain relatively poorly understood despite more than 100 years of research [26, 27]. It is well-established that stroke induces cytotoxic oedema causing brain water content to increase rapidly, resulting in a significant elevation in intracranial pressure (ICP) [28, 29]. Based on this knowledge, it was

hypothesised that brain fluid pressure gradients would form in the ipsilateral hemisphere of the stroke brain, potentially altering the brain fluid dynamics, as illustrated in Figure 3.3. Therefore, the aim of this experiment was to test this hypothesis by visualising the fluid dynamics in stroke rat brains using EVAC and compare with normal, healthily functioning brains.

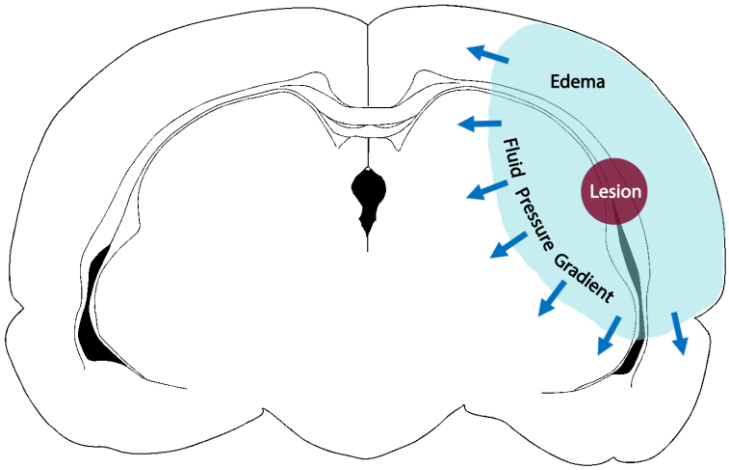

Figure 3.3: Illustration showing hypothesised fluid pressure gradients following stroke in a rat brain. Oedema (light blue) in the ipsilateral hemisphere of the brain causes an increase in intracranial pressure leading to the formation of pressure gradients which disrupt the flow of extravascular fluid in the brain.

3.3 Methods

3.3.1 EVAC velocity map pipeline

All EVAC velocity maps contained in the results section of this chapter were generated using the phase contrast reconstruction pipeline outlined below.

Velocity-encoding in a single dimension requires two repetitions of the EVAC sequence, one per bipolar gradient polarity. Thus, two magnitude and two phase images are generated. Fluid velocity in one dimension, *v*, is proportional to the difference in the phase shift, $\Delta\phi$, induced in the spins by the two bipolar gradients given by:

$$v = \frac{\Delta\phi}{\gamma \Delta M_1} \qquad \textbf{EQ 3.3}$$

where γ is the proton gyromagnetic ratio (267.513 × 106 rad s^{-1} T^{-1}) and ΔM_1 is the difference in first order velocity gradient moments, as described in section 2.2. For in-plane 2D measurements, *x*- and *y*-velocity components were encoded by the readout and phase encoding imaging gradients. Therefore, four phase contrast images were required to generate a single velocity map. Phase difference maps ($\Delta\phi$) were calculated according to Bernstein et al. (2004) [15]:

$$\Delta\phi = ATAN2\left(Im\sum_j \frac{Z_{+j}Z^*_{-j}}{\sigma_j^2}, Re\sum_j \frac{Z_{+j}Z^*_{-j}}{\sigma_j^2} \right) \qquad \textbf{EQ 3.4}$$

where *ATAN2* is the arctangent2 operator, Z_+ is the complex image acquired with a positive-negative polarity bipolar gradient (Z_- is negative-positive polarity), index *j* corresponds to the *j*th receiver channel (if using a multichannel phased-array) and σ_j^2 is the measured noise variance in the *j*th receiver.

In practice, the measureable range of velocities is determined by the operator by tuning the change in first order gradient moment, ΔM_1, according to the equation:

$$VENC = \frac{\pi}{\gamma \Delta M_1} \qquad \textbf{EQ 3.5}$$

The VENC value represents the maximum encodable speed before aliasing occurs. Speeds greater than VENC cause phase wrapping, therefore a trade-off is required: lowering the VENC increases the sensitivity of the velocity-encoding to slower flows, but increases the prospect of wrapping. Any flows that cause a phase change greater than ±2π cannot be unwrapped using the *ATAN2* operator.

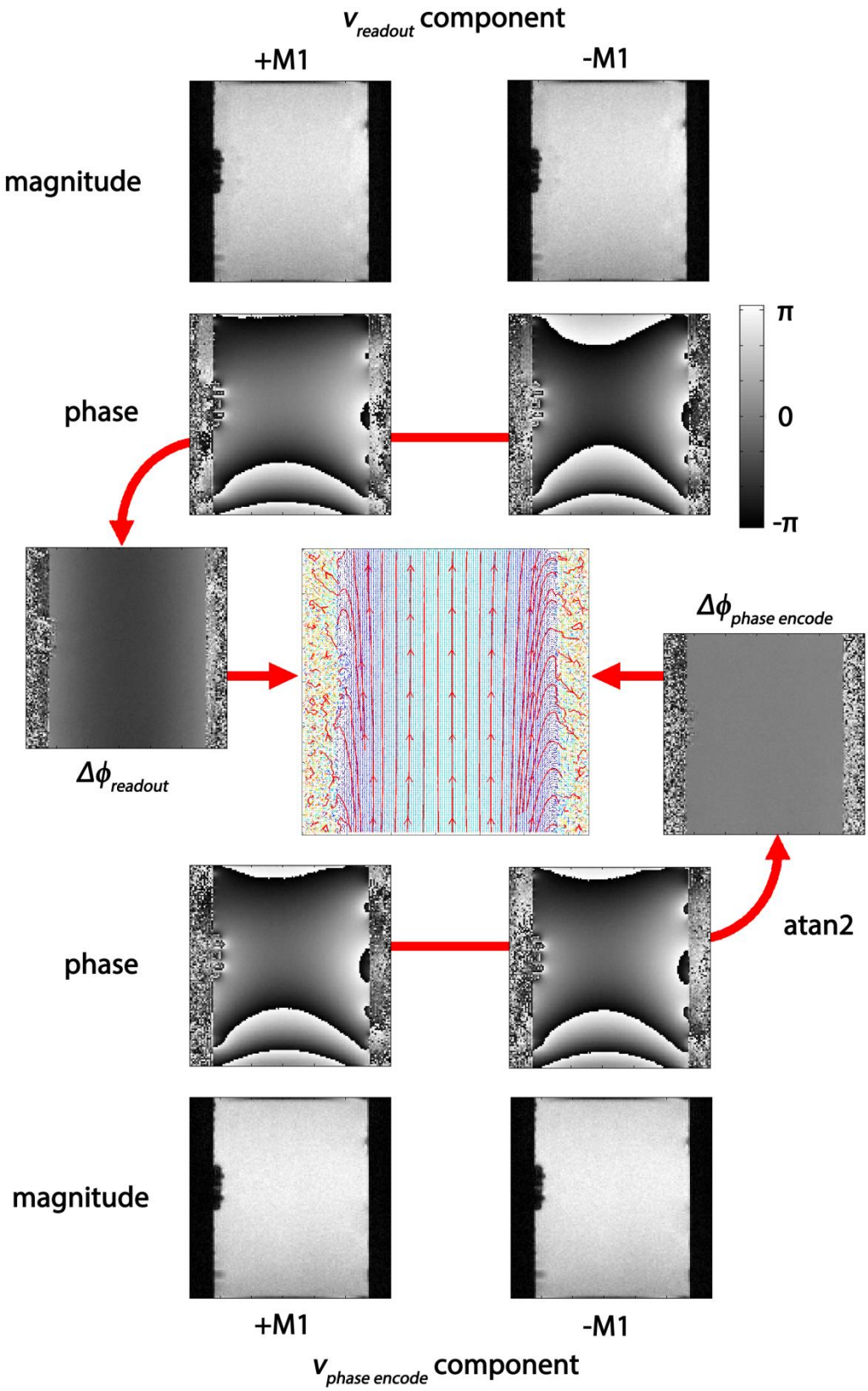

Figure 3.4: Schematic illustrating the pipeline for generating EVAC velocity maps. Data from flow phantom experiments are shown. Four phase contrast images are required for 2-dimensional velocity-encoding: one per bipolar gradient and one per gradient direction. Phase wrapping – regions that suddenly change from black to white, or vice versa – can be observed in the raw phase contrast images. The ATAN2 operator unwraps any phase wrapping. The $\Delta\phi$ maps are combined and scaled to produce an EVAC velocity vector map.

3.3.2 *In vivo* MRI setup

All *in vivo* studies were performed in accordance with the local ethical review panel, the UK Home Office Animals Scientific Procedures Act, 1986 and UKCCCR guidelines. For all *in vivo* experiments, mice and rats were monitored and imaged using the MRI equipment described in Chapter 2. Briefly, animals were anesthetised with 1.5-2.0% isoflurane in 2 l/min O_2 and positioned in a cradle which could be positioned in the middle of the scanner bore. Temperature was monitored and maintained at physiological temperature. Respiration was monitored using a neonatal apnea pad. Mouse imaging was conducted using 1000mT/m gradient inserts and a 39mm volume RF coil (RAPID). Rat imaging was conducted using 400 mT/m gradients and a 72mm volume RF coil (RAPID) for transmission with a 4-channel rat head phased-array coil (RAPID) for reception.

3.3.3 Phantom study 1 – establishing the slowest measureable fluid velocity in a flow phantom

In this study, a custom-built flow phantom was constructed out of a 5ml syringe (internal diameter 12.06mm) and rubber tubing connected to a PHD 2000 Syringe Pump (Harvard Apparatus, UK). Water was pumped through the phantom at a range of pre-determined inflow rates (0.069 to 3.43 ml/min, equivalent to theoretical peak fluid velocities in the range: 10µm/s to 500µm/s) according to:

$$F = \frac{Av_p}{2} \qquad \textbf{EQ 3.6}$$

where F is in the inflow rate on the syringe pump, A is the cross-sectional area of the phantom and v_p is the peak velocity assuming laminar flow. For each flow rate, EVAC was used to measure the fluid velocity inside the phantom. The double inversion recovery preparation in the EVAC sequence was switched off to save time since nulling was not required. Surfactant was used to minimise the formation of air bubbles inside the phantom which could cause susceptibility artefacts.

Imaging was carried out using a 26mm volume RF coil (Rapid MR International, Ohio, US). The phantom was positioned in the isocentre of the scanner and was encased in paper towel to minimise any bulk motion caused by imaging gradients.

EVAC scans: The double inversion preparation was switched-off. Therefore, the single-slice gradient echo readout was acquired with the following parameters: *TR* = 250 ms, *TE* = 3ms,

flip angle = 30°, averages = 1, slice thickness = 1 mm, FOV = 30mm^2, matrix size = 128^2. The gradient amplitude, G_0, and gradient duration, Δt, were varied to establish the optimum VENC for maximum flow sensitivity whilst retaining sufficient signal for imaging.

Statistics: Regression analysis was performed to assess the relationship between pump inflow rate and measuring velocity. Statistical significance was assigned at $p < 0.05$.

3.3.4 Phantom study 2 – measuring and correcting the phase offset caused by electrical eddy currents

In this study, the effects of electrical eddy currents on phase measurements were investigated. An agar phantom was created using 1% agarose powder dissolved in distilled water, which was left to set within a 50ml centrifuge tube. A 39mm volume RF coil (Rapid MR International, Ohio, US) was used for imaging. The agar phantom was imaged using the EVAC sequence. Immediately after this, the agar phantom was removed and replaced with the flow phantom described in the previous section (3.3.3). The flow phantom was driven at a range of inflow rates (0.069 to 1.71 ml/min) using the syringe pump and imaged with EVAC, maintaining exactly the same pulse sequence parameters that were used to image the agar phantom, to ensure consistent gradient waveform shapes.

EVAC scans: The double inversion preparation was switched-off. Therefore, the single-slice gradient echo readout was acquired with the following parameters: *TR* = 250 ms, *TE* = 3ms, flip angle = 30°, averages = 1, slice thickness = 1 mm, FOV = 30mm^2, matrix size = 128^2. The VENC was set to 0.2cm/s (gradient amplitude, G_0 = 30 G/cm; gradient duration, Δt = 3 ms).

Image analysis: All images were reconstructed according to the velocity map pipeline outlined in section 3.3.1, with one additional step. To estimate the phase offset due to electrical eddy currents in the EVAC sequence, the phase data in the agar phantom image was subtracted on a pixel-wise basis from the phase data in the flow phantom images [17, 30, 31] according to the following equation:

$$\phi_{corrected} = \phi_{flow\ phantom} - \phi_{agar\ phantom} \qquad \textbf{EQ 3.7}$$

where ϕ represents the phase of a pixel in the flow phantom and agar phantom images.

Repeatability and reproducibility study: To establish how much within-session and between-session variability there was in the EVAC measurements, both with and without the phase

offset correct, the flow phantom was imaged multiple times. For repeatability analysis, the flow phantom was imaged three times at each inflow rate on the same day. For reproducibility analysis, a single trial of the flow phantom experiment was repeated five times over the course of six months.

Statistics: Regression analysis was performed to assess the relationship between pump inflow rate and measuring velocity. The coefficient of determination (r^2) was used to compare the accuracy of phase corrected and phase uncorrected velocity measurements.

3.3.5 Mouse tumour study – Imaging interstitial fluid dynamics in an experimental mouse tumour model

Following the flow phantom studies, a cohort of mice with subcutaneous tumours was imaged to establish the *in vivo* repeatability and reproducibility of the EVAC sequence. As part of the study, the electrical eddy current phase offset correction method described in the previous section (3.3.4) was also applied *in vivo* to examine how it affected measures of interstitial fluid flow.

Animal preparation: Female MF1 *nu/nu* mice (n = 4) were injected subcutaneously into the right flank with 5×10^6 LS174T human colorectal carcinoma cells. Injections were carried out by Dr Sean Peter Johnson.

Imaging preparation: Following a minimum 10 days of tumour growth, mice were ready for imaging. All mice were anaesthetised and animal physiology was monitored and maintained. Imaging was conducted using a 39mm volume RF coil. Manual shimming of the magnetic field was conducted using a local shim voxel located in the subcutaneous tumour. Typical linewidths achieved following shimming were between 30 and 70Hz.

A set of multi-slice fast spin echo images, which covered the entire tumour volume, were used to pilot to the correct location and orientation within the tumour. The final, ideal slice projection through the tumour was a coronal slice which covered the largest possible extent of the tumour. This slice was used for positioning of the subsequent EVAC scans.

EVAC scans: The double inversion recovery preparation consisted of two hyperbolic secant pulses with thicknesses of 200mm (global) and 3mm (slice-selective). The T1 of blood was taken to be 1900ms at 9.4T, based on measurements in a previous study [32]. Hence, t_{rec} was set to 1317ms according to the relationship $t_{rec} = ln(2)\times T_{1,blood}$. The VENC was set to 0.2cm/s (gradient amplitude, G_0 = 30 G/cm; gradient duration, Δt = 3 ms). The single-slice

gradient echo readout was acquired with the following parameters: *TR* = 3000 ms, *TE* = 3ms, flip angle = 30°, averages = 1, slice thickness = 1 mm, FOV = 30mm^2, matrix size = 128^2.

EVAC blood nulling scan: To investigate the blood nulling capability of the EVAC sequence in the tumours, a further scan was acquired with the double inversion preparation switched off, while keeping all other parameters identical. The difference between two images with and without the double inversion preparation gave an estimate of the fractional blood volume within the tumour, according to the following equation:

$$V_B = \frac{S_{non-nulled} - S_{nulled}}{S_{non-nulled}} \qquad \textbf{EQ 3.8}$$

where V_B is the fractional blood volume and S is the magnitude signal in the non-nulled (no DIR) and nulled (with DIR) images.

Repeatability and reproducibility study design: The tumour mice were studied over the course of two days, for the purposes of repeatability and reproducibility analysis. Therefore, all animals were imaged with the following protocol:

Day 1:

– Animal setup and scanner calibration (10-15 minutes)
– Tumour piloting using multi-slice fast spin echo scans (10 minutes)
– 3 × consecutive EVAC scans (60 minutes)
– 1 × non-nulled EVAC scan (20 minutes)
– Remove and recover animal (5 minutes)

Day 2:

– Animal setup and scanner calibration (10-15 minutes)
– Tumour piloting using multi-slice fast spin echo scans (10 minutes)
– 3 × consecutive EVAC scans (60 minutes)
– 1 × non-nulled EVAC scan (20 minutes)
– Remove and recover animal (5 minutes)

Phase offset correction study design: The phase offset correction method devised during the flow phantom experiments was applied *in vivo*. A separate cohort of female MF1 *nu/nu* mice (n = 6) with subcutaneous tumours were imaged with the following protocol:

– Animal setup and scanner calibration (10-15 minutes)
– Tumour piloting using multi-slice fast spin echo scans (10 minutes)

– 1 × EVAC scan (20 minutes)
– 1 × non-nulled EVAC scan (20 minutes)
– Remove and recover animal (5 minutes)
– Replace animal with agar phantom (5 minutes)
– 1 × EVAC scan using identical parameters and slice profile (20 minutes)

Statistics: Box-whisker and Bland-Altman plots were used to assess repeatability and reproducibility of EVAC velocity measurements in the tumours; Mann-Whitney-U tests were used to test for statistical significance. A Wilcoxon paired rank test was used to test the statistical significance of velocity measurements before and after phase offset correction. In all cases, statistical significance was assigned at $p < 0.05$.

3.3.6 Stroke rat study – Imaging extracellular fluid dynamics in an experimental rat stroke model

In this study, 3 normal rats and 3 stroke rats (male, Sprague-Dawley) were scanned using EVAC to study extracellular fluid dynamics in the brain, along with a host of other common stroke imaging sequences for comparison.

Animal preparation: Surgeries were carried out by Mrs. Valerie Taylor. Ischaemic strokes were induced in three rats as described in section 1.2.4. In brief, stroke rats were anaesthetised using 2-2.5% isoflurane in oxygen. Core body temperature was monitored with a rectal temperature probe and maintained with a heating pad. Ischaemic stroke was induced by simultaneous surgical occlusion of the middle cerebral artery using a silicone rubber-coated monofilament nylon suture (Doccol) and clamped ligation of the contralateral common carotid artery. After 30 minutes, the clamp on the contralateral common carotid artery was released. After a further 30 minutes, the filament occluding the middle cerebral artery occlusion was removed to permit reperfusion.

Imaging preparation: Stroke rats were imaged 24 hours post-surgery. All rats were anaesthetised and animal physiology was monitored and maintained. Ear bars were used to minimise any bulk motion due to respiration. Imaging was conducted using a 72mm volume RF coil with a 4-channel rat head phased-array coil. Manual shimming of the magnetic field was conducted using a local shim voxel located in the rat brain. Typical linewidths achieved following manual shimming were between 30 and 50Hz. A multi-slice axial pilot scan was used to define the slice of interest for EVAC. A mid-brain slice with minimally-sized air pockets below the brain was chosen to lessen susceptibility artefacts.

EVAC scans: The double inversion recovery preparation consisted of two hyperbolic secant pulses with thicknesses of 200mm (global) and 3mm (slice-selective). The T1 of blood was taken to be 1900ms at 9.4T, based on measurements in a previous study [32]. Hence, t_{rec} was set to 1317ms according to the relationship $t_{rec} = ln(2) \times T_{1,blood}$. The VENC was set to 0.2cm/s (gradient amplitude, G_0 = 30 G/cm; gradient duration, Δt = 3 ms). The single-slice gradient echo readout was acquired with the following parameters: *TR* = 3000 ms, *TE* = 3ms, flip angle = 30°, averages = 1, slice thickness = 1 mm, FOV = 30mm^2, matrix size = 128^2.

EVAC blood nulling scan: To investigate the blood nulling capability of the EVAC sequence in the rat brain, a further scan was acquired with the double inversion preparation switched off, while keeping all other parameters identical. The difference between two images with and without the double inversion preparation gave an estimate of nulling efficiency, as described in the previous section (3.3.5), according to equation 3.8.

T2-weighted fast spin echo scans: A multi-slice T2-weighted FSEMS sequence was acquired with the following parameters: *TR* = 4000 ms, *ETE/ESP/ETL* = 48/12/8 ms, k_0 = 4, averages = 3, slice thickness = 1mm, FOV = 30 mm^2, data matrix = 256^2.

Perfusion weighted imaging: A multi-slice echo planar imaging flow-sensitive alternating inversion recovery arterial spin labelling (EPI FAIR ASL) sequence was acquired with the following parameters: TR = 4500ms, TE = 13.5ms, k_0 = 8, shots = 4, repetitions = 10, slices = 5, slice thickness = 1mm, FOV = 30 mm^2, data matrix = 64^2, slice selective inversion pulse width = 12mm, TI = 1500ms. Repetitions were averaged together to generate the final perfusion weighted images. The middle slice was aligned to match the EVAC slice.

Diffusion weighted scans: A multi-slice spin echo EPI DTI sequence was acquired with the following parameters: TR = 4000ms, TE = 25ms, k_0 = 8, shots = 4, averages = 3, slices = 20, slice thickness = 1mm, FOV = 30 mm^2, data matrix = 64^2. Diffusion gradients were applied in 3 directions with the following parameters: amplitude = 19.7 G/cm, duration = 6 ms, Separation = 12 ms, b-value = 1030.5 s/mm^2. In addition, a single unweighted B0 image was acquired.

Histology: Following imaging, rats were sacrificed. Whole brains were extracted and sectioned into 10-14 1mm coronal slices using a McIlwain tissue cutter. Slices were immersed in 2,3,5-triphenylterazoliumchloride (TTC) at 37°C for staining. TTC was drained and slices were immersed in 4% paraformaldehyde (PFA) for 30 minutes. Excess PFA was removed and then slices were scanned at 300 DPI resolution using a desktop scanner (Canon Pixma MX700).

Statistics: Mann-Whitney-U tests were used to test for statistical significance between measurements of the nulling ratio and mean interstitial fluid velocity in normal and stroke brains. Statistical significance was assigned at $p < 0.05$.

3.4 Results

3.4.1 Phantom study 1 – establishing the slowest measureable fluid velocity in a flow phantom

The main aim of this study was to establish the slowest measureable fluid velocity in a flow phantom using the 9.4T MRI scanner in CABI. Figure 3.5 shows the central component of the custom-built flow phantom, which was placed inside the RF coil and MRI scanner. The flow phantom was constructed using a 5ml syringe connected via rubber tubing to a tuneable pump. Distilled water was driven through the flow phantom into a water bath situated at the rear of the scanner bore.

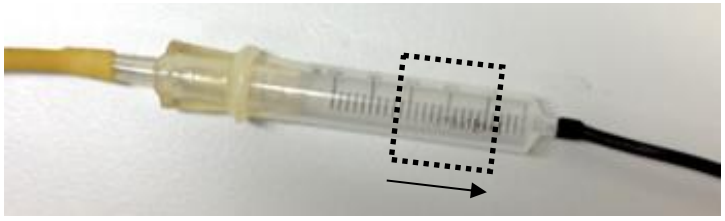

Figure 3.5: Photograph of the custom-built flow phantom. The phantom was constructed using a 5ml syringe. Water was driven (in the direction of the black arrow) by a syringe pump via rubber tubing through the phantom and into a water reservoir at the rear of the MRI scanner. The dotted line represents the approximate location of the imaging slice.

First, the flow phantom was imaged at a range of VENC values to examine the effects of increasing the magnitude and duration of the bipolar gradients on the signal loss. Figure 3.6 shows coronal slices through the flow phantom, where the hyperintense signal comes from the water. A small collection of hypointense air bubbles can be seen along the left edge of the flow phantom.

The duration, T, of the bipolar gradients had a greater effect on signal loss than the size of the bipolar gradients, as expected, due to the inverse-square relationship between *VENC* and T (Equation 3.1). Scanner hardware constraints meant that the magnitude of the bipolar gradients, G, could not be increased beyond approximately 60 G/cm. The water signal in the flow phantom was markedly noisier with bipolar gradient values greater than $G = 30$ G/cm

and T = 3ms. This was determined to be the optimum combination of parameters corresponding to VENC = 0.2cm/s. Averaging multiple EVAC acquisitions was investigated as a method for recovering signal loss, thereby permitting a lower VENC, however, the increased scan duration was prohibitive for *in vivo* imaging (> 20 minutes for a single slice).

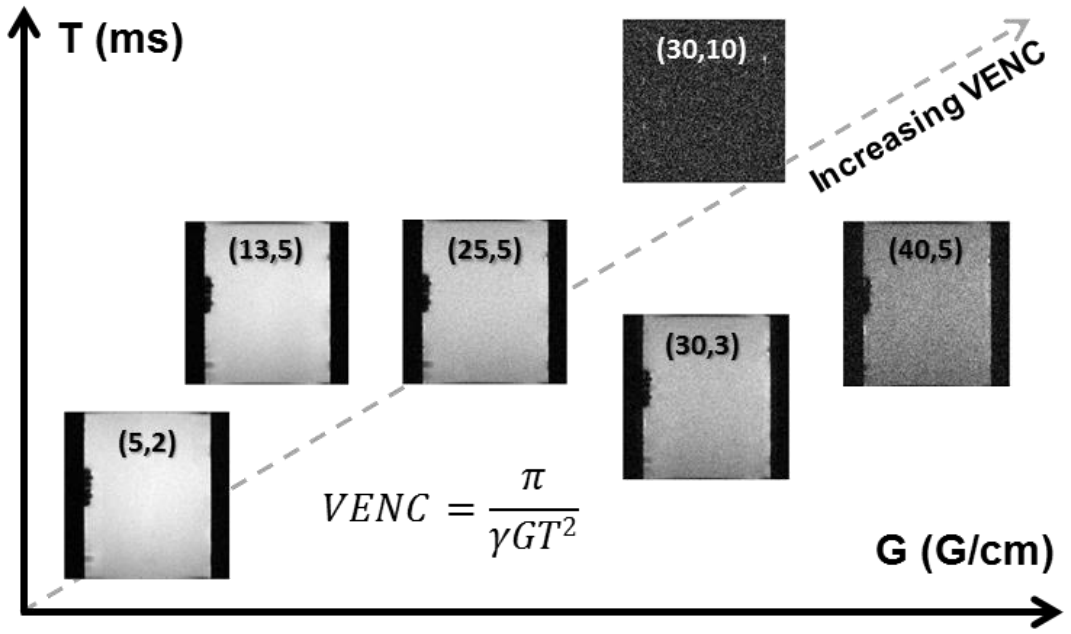

Figure 3.6: Schematic illustrating the effects of changing the magnitude (G) and duration (T) of the velocity-encoding bipolar gradients in the EVAC sequence. Numbers in brackets indicate (G, T). The velocity-encoding parameter, VENC, is inversely proportional to G and T. Hence, increasing the size of the bipolar gradients makes the sequence more sensitive to slower flow velocities. But, signal loss increases with increasing VENC.

Water was passed through the flow phantom at a range of flow rates from 0 to 3.43 ml/min and imaged using EVAC (with the double inversion preparation switched off to save time). The velocity maps are shown in Figure 3.7. Every pixel in each plot contains a vector corresponding to the greatest component of fluid flow within that region. Streamlines (red) were generated and overlaid using the "streamslice" function in MATLAB, which connects the underlying velocity vectors to show bulk flow directionality. In Figure 3.7a, the air space outside the flow phantom has been retained in the image to demonstrate the appearance of noise in a velocity map. For clarity, this region has been segmented from subsequent images

At flow rates higher than 0.069 ml/min, water flowed from the point of inflow towards the point of outflow (a-d). At 3.43ml/min water flow exhibited a laminar profile with the greatest flow in a central channel through the flow phantom (a). Towards the periphery of

the flow phantom the streamlines curl towards the plastic boundary indicating the effects of friction and turbulent flow. This effect was more pronounced at increasingly slow flow rates (b-d). At the slowest flow rate of 0.069 ml/min, the greatest component of flow was backwards (e). A similar flow pattern was observed when the syringe pump driving the water was switched off, suggesting the possibility of a systemic suction effect which overcame very slow flows, or that the noise floor had been reached.

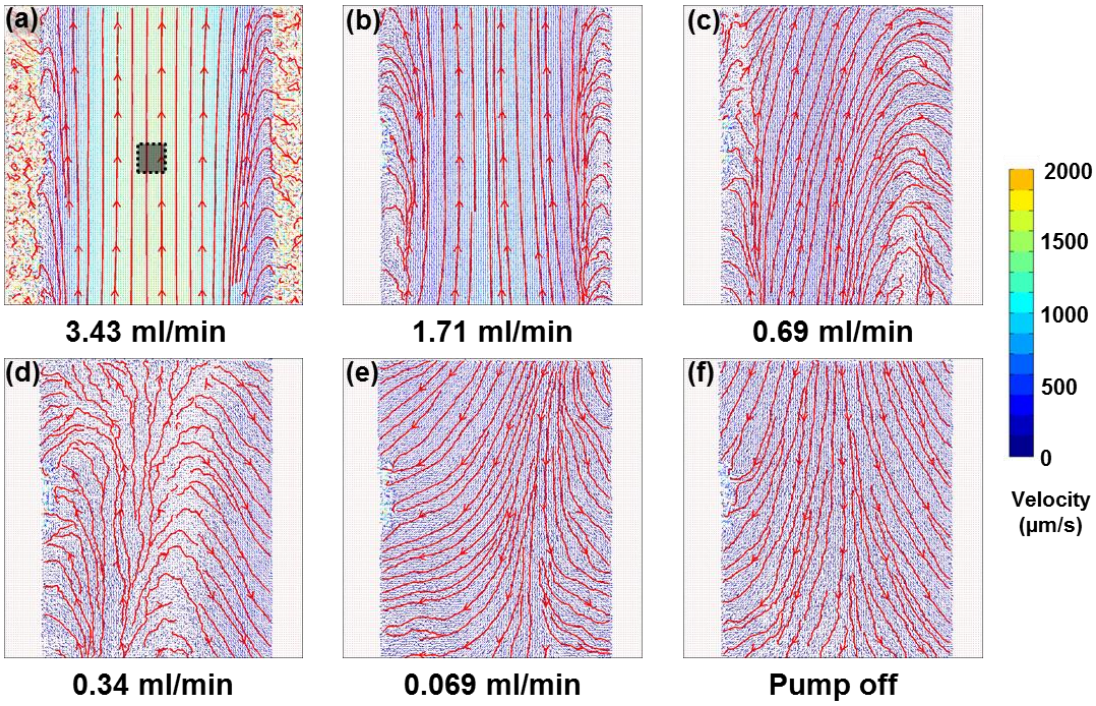

Figure 3.7: EVAC velocity maps showing measurements of water velocity through the flow phantom at variable flow rates. All maps were measured with the same VENC (=0.2cm/s). The streamlines in red connect the underlying velocity vectors showing the macroscopic flow patterns. The black box in (a) shows the region used for calculations of peak velocity, V_p. At faster flow rates, the flow profiles are laminar (a, b, c). As the fluid velocity decreased, turbulent effects became more apparent (c, d). At the slowest flow rate (e), 0.069 ml/min, the fluid appear to flow in the reverse direction. A similar pattern of backwards flow was also observed even with the pump switched off (f).

Figure 3.8a shows 1-dimensional flow profiles taken across a central line in the flow phantom. Again, at the highest inflow rates the water exhibits a laminar flow profile. The peak flow velocity through the water phantom was determined at each flow rate by averaging the velocities in a central 6x6 pixel region within the centre of each image, as demonstrated by the black box in Figure 3.7a. A strong linear correlation ($r^2 = 0.98$, $p = 0.0002$) was observed between the inflow rate and measured peak velocity, as shown in Figure 3.8b. However, at the slowest inflow rate of 0.069 ml/min, or with the pump switched off, the peak velocity was higher than that measured with a faster flow rate of 0.34 ml/min, reflecting that the noise floor had been approached.

The slowest measureable velocity on the scanner was determined to be 44 ± 5 µm/s based on the velocity map of the slowest inflow rate which exhibited a forward flowing velocity pattern (0.34 ml/min, Figure 3.7d).

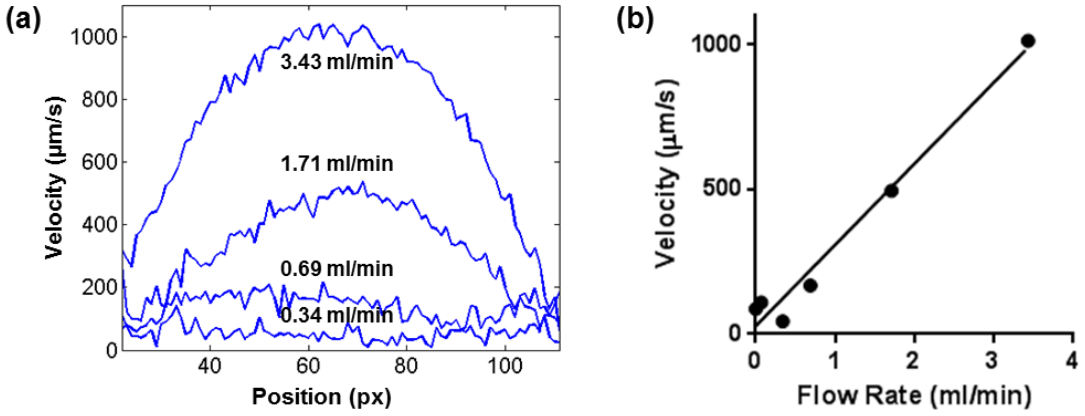

Figure 3.8: (a) 1-dimensional laminar flow profiles across the flow phantom. (b) Flow rate plotted against the peak velocity, V_p, in the flow phantom measured using EVAC. V_p was calculated using a small 6x6 voxel region in the centre of each velocity map. Error bars corresponding to the standard deviation across the 6x6 voxel are too small for visualisation. There was a significant linear correlation between the inflow rate and measured peak velocities ($r^2 = 0.98$, $p = 0.0002$).

3.4.2 Phantom study 2 – measuring and correcting the phase offset caused by electrical eddy currents

Electrical eddy currents created during a pulse sequence result in additional magnetic fields which alter the shape of the gradient waveforms, ultimately affecting the phase of the MRI signals. The aim of this study was to measure the phase offset resulting from these magnetic fields in a static agar phantom and then use this information to correct the phase offset in velocity-encoded MRI phase contrast data of a flow phantom.

The EVAC velocity map phase offset correction process is demonstrated in Figure 3.9. All images were obtained using identical scan parameters (except for alternating the bipolar gradients) and slice locations to ensure eddy current effects were consistent between flow phantom and agar scans. The top row shows images from the flow phantom including the raw magnitude image (a) and two maps showing the difference in phase, $\Delta\phi$, between the bipolar gradients for each velocity-encoding direction (b, c). The bottom row shows the equivalent images taken in an agar phantom (d, e, f). Note, the agar phantom was deliberately made larger than the flow phantom and large enough to fill the majority of the RF coil so that the agar phantom always spatially overlapped with the flow phantom. All images are from a trial with a flow rate of 1.71 ml/min. With the bipolar gradients orientated in the readout direction (RO), a laminar gradient of phase change can be observed in the

phase difference image of the flow phantom (b). This is caused by the flowing water which accumulates phase as the bipolar gradients play out. The same profile is not observed in the agar phantom (e) as there is no flow. With the bipolar gradients orientated in the phase encode direction (PE), a subtle linear change in phase difference can be observed in the flow phantom (c), changing from negative phase on the left edge to positive phase on the right edge. This linear gradient represents a phase offset, which is not flow related as it is also observed in the static agar phantom (f). Combining the flow phantom phase difference maps according to Equation 3.1 produces a raw, uncorrected EVAC velocity map (g). By subtracting the agar phase difference images from the flow phantom phase difference images before combining the phase difference maps results in a corrected EVAC velocity map (h).

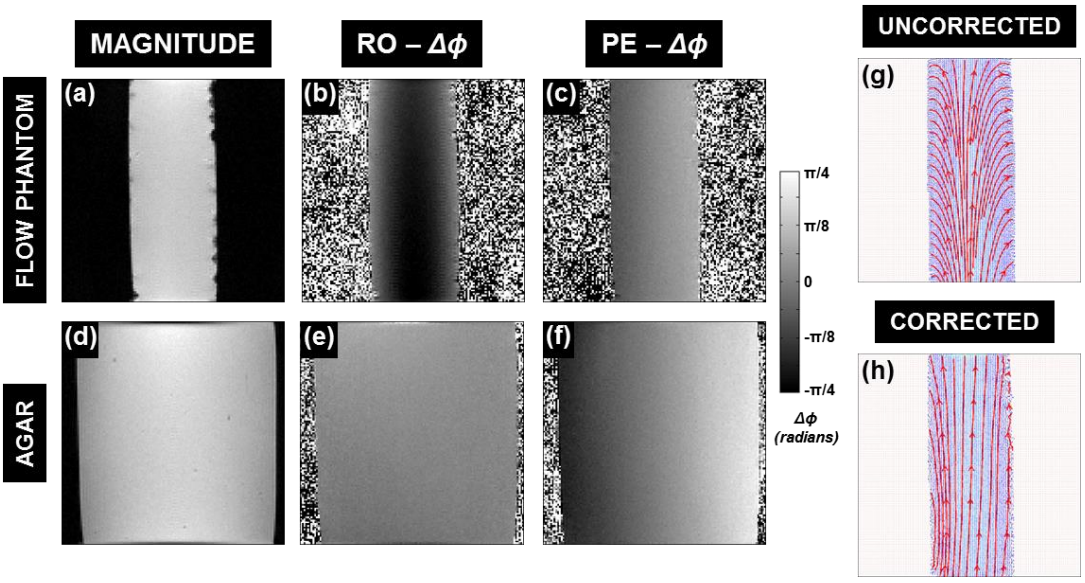

Figure 3.9: Phase offset determination in an agar phantom and application to correcting flow measurements in a flow phantom. The top row shows (a) magnitude and (b,c) phase difference images from a flow phantom. The bottom row shows (d) magnitude and (e,f) phase difference images from a an agar phantom. The uncorrected EVAC velocity map (g) is created by combining the two raw phase difference maps. The corrected EVAC velocity map (h) is created by subtracting the phase difference contributions measured in the agar phantom from the flow phantom measurements.

The phase offset correction method was applied to a range of inflow rates from 0 to 1.71 ml/min. The uncorrected and corrected EVAC velocity maps are shown in Figure 3.10. At the highest flow rate of 1.71 ml/min (a), the uncorrected velocity map exhibits a broadly laminar profile with distinct edge effects along the edges of the flow phantom. In the corrected image (e) the streamlines become more parallel with the edge of the flow phantom. At a flow rate of 0.34 ml/min, the flow pattern in the uncorrected image (b) is mostly forwards, however, at the outflow end of the image the streamlines have a larger component orientated backwards. In the corrected version (f) the streamlines flow forwards through the

entirety of the flow phantom. At the slowest flow rate of 0.069 ml/min (c), halfway through the phantom the streamlines flow backwards. In the corrected image (g), the largest component of flow is forwards, although, the streamlines are not parallel to the edge of the flow phantom. With the flow phantom switched off, the uncorrected image (d) shows apparent backwards flow, however, in the corrected image (h) the streamlines are not connected and there is no clear directionality to the flow pattern.

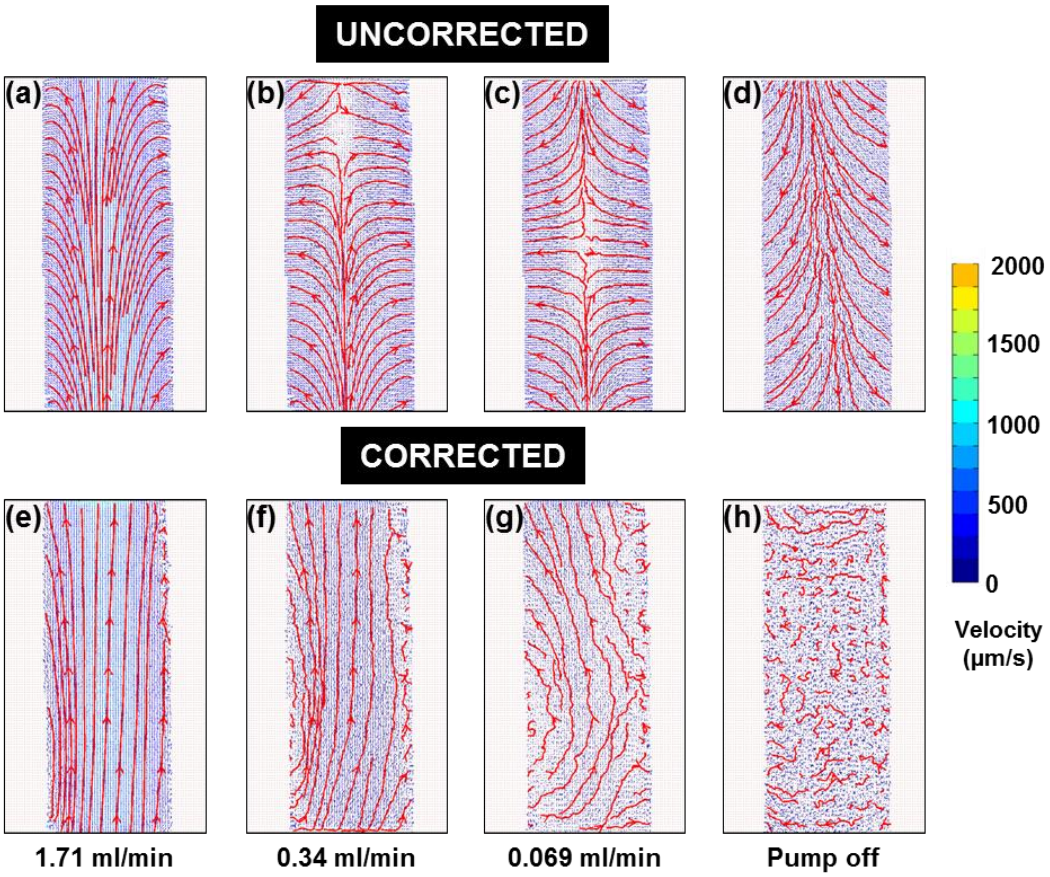

Figure 3.10: Representative EVAC velocity maps of the flow before (uncorrected) and after (corrected) the electrical eddy current phase offset correction was applied. All maps were measured with the same VENC (=0.2cm/s). The streamlines in red connect the underlying velocity vectors showing the macroscopic flow patterns. At the faster flow rates, the electrical eddy current correction has the effect of straightening the streamlines towards the edge of the flow phantom (a,b), producing a more laminar flow profile than in the uncorrected images (e,f). At the slowest flow rate of 0.069 ml/min, applying the eddy current correction produces a turbulent, but broadly forward flowing velocity pattern (g), unlike the uncorrected velocity map which has components of apparent backwards flow (c). With the pump switched off, the flow pattern in the corrected image is heterogeneous, with no clear component of flow (h), unlike the uncorrected image which appears to show backwards flow (d).

To examine the stability of flow quantification using the phase offset correction method, repeatability and reproducibility experiments were undertaken. Figure 3.11a shows the repeatability of three consecutive flow phantom trials using multiple flow rates conducted on

the same day (within-session). Figure 3.11b shows the reproducibility of five separate flow phantom experiments conducted over the course of six months (between-session). In both plots, the dashed grey line represents the theoretical peak velocity in the centre of the flow phantom assuming a laminar flow profile (calculated according to equation 3.6). Repeatability of the EVAC sequence was very strong in both the uncorrected data and corrected data: both showed a strong, significant correlation between the inflow rate and the measured peak velocities (uncorrected: $r^2 = 0.98$, $p = < 0.0001$ and corrected: $r^2 = 0.99$, $p < 0.0001$). Reproducibility of the EVAC sequence showed greater variation, as evidenced by the much larger error bars in Figure 3.11. There was a marked difference between the measured peak velocities with and without the phase offset correction. The corrected data demonstrated a stronger, significant correlation ($r^2 = 0.87$, $p < 0.0001$) than the uncorrected data ($r^2 = 0.61$, $p < 0.0001$). Furthermore, the corrected data (blue curve) was more closely aligned to the theoretical data (dashed grey curve) compared to the uncorrected data (red curve).

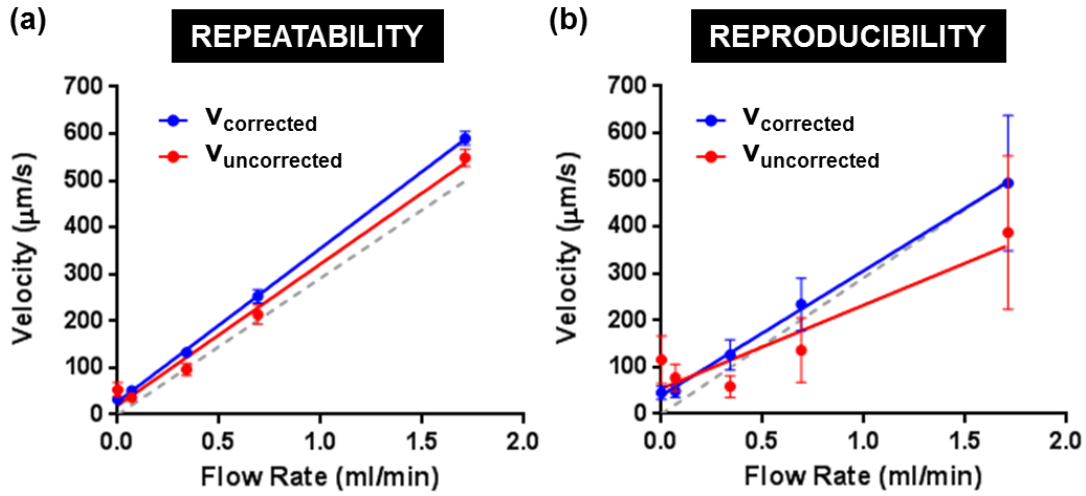

Figure 3.11: Repeatability and reproducibility of slow flow velocity measurements in a flow phantom using the EVAC sequence. (a) Repeatability values consist of three consecutive within-session measurements of the flow phantom. (b) Reproducibility values consist of five between-session measurements of the flow phantom on different days. The accuracy of velocity measurements was improved with the electrical eddy current phase offset correction (blue curve, $r^2 = 0.87$) compared to the raw, uncorrected velocity data (red curve, $r^2 = 0.61$). Dashed grey line represents the theoretical water flow velocity through the phantom.

Overall, the phase offset correction had the effect of raising the measured peak velocity values at higher flow rates (≥ 0.34 ml/min) and lowering them at slower flow rates. The average peak velocity measured at a flow rate of 0.069 ml/min was 48 ± 29µm/s with the phase offset correction, compared to 78 ± 13µm/s without the phase offset correction.

3.4.3 Mouse tumour study – Imaging interstitial fluid dynamics in an experimental mouse tumour model

The aim of this study was to examine the repeatability and reproducibility of the EVAC sequence *in vivo*, using an experimental subcutaneous mouse tumour model. Four mice were imaged across two days with three consecutive repeats of the EVAC sequence.

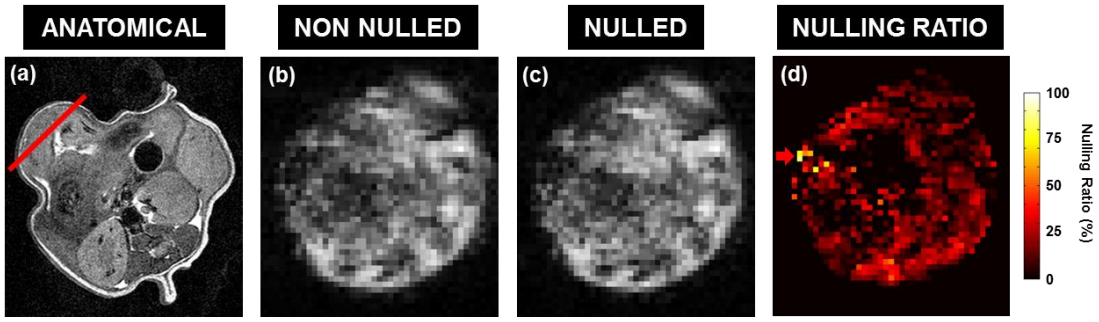

Figure 3.12: Evaluating the blood nulling ratio in a subcutaneous mouse tumour. (a) Axial anatomical image showing the tumour imaging plane (red line). (b) Non-nulled image acquired with the double-inversion preparation in the EVAC sequence switched-off. (c) Blood nulled image acquired using the full EVAC sequence. The two magnitude images appear broadly the same. (d) The nulling ratio image reveals the difference in signal between the nulled and non-nulled images. A localised region of high nulling is visible on the left of the tumour, potentially corresponding to a large tumour blood vessel (red arrow).

Firstly, the efficiency of the blood nulling double inversion preparation was investigated. Taking the ratio of a slice acquired with the double inversion preparation to a slice with the nulling preparation switched off gave the nulling ratio (Equation 3.8), which is a first order estimate of the fractional blood volume. Figure 3.12 shows this process applied to a tumour. The signal in the non-nulled magnitude image (b) is heterogeneous, typical of a tumour image, which could feature regions of necrosis alongside viable tissue. The EVAC, or nulled, magnitude image (c) shows a similar, albeit subtly reduced signal distribution. Calculation of the blood nulling ratio (d) revealed further information on the heterogeneous blood content within the tumour. The nulling ratio ranged from 0 to 80%. Pixels with the highest nulling ratio (yellow) containing the largest volume of blood corresponded to regions in which vasculature is known to be most dense such as at the periphery of the tumour (red arrow). The mean nulling ratio based on a single slice measurement in each of the tumours across the two days (n = 8) was 9.4 ± 3.7 %, which is in agreement with previous data on microvascular density in LS147T tumours [33].

When EVAC was applied to the mouse tumours, three different types of interstitial fluid flow pattern were broadly observed, as shown in Figure 3.13. These included a radial pattern where interstitial fluid flowed from the centre of the tumour towards the periphery (a), a laminar flow profile where fluid travelled laterally across the tumour and (c) a combination of both.

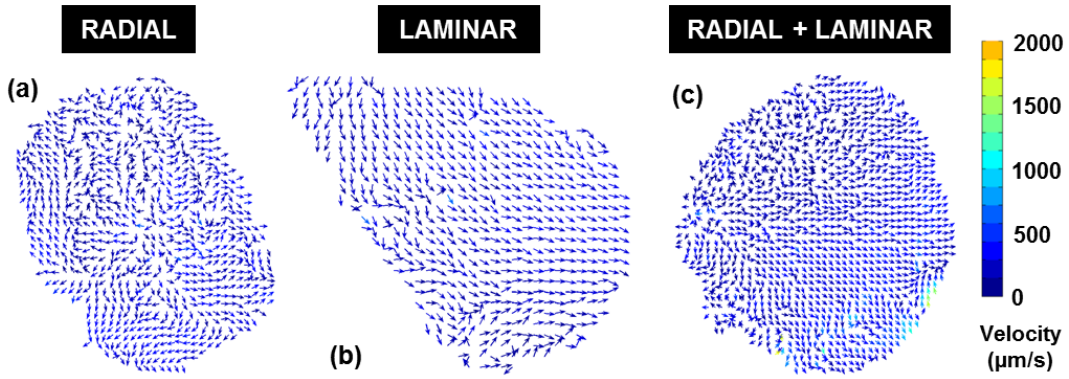

Figure 3.13: EVAC velocity maps in three different mouse tumours showing three different types of interstitial fluid flow pattern. (a) Radial flow from the centre of the tumour, outwards. (b) Laminar flow, where the largest component of flow is laterally across the tumour. (c) A combination of both radial and laminar flow.

The *in vivo* repeatability of the EVAC sequence was investigated by imaging the cohort of mice three times consecutively in the same imaging session. Reproducibility was examined by repeating the experiment on the following day. Repeatability was strong as EVAC velocity maps showed similar interstitial fluid flow patterns within-session, as illustrated in Figure 3.14a. On the left edge of the tumour, there was a small region of high, randomly-orientated velocity vectors (red arrow). This corresponded to tumour vasculature (also visualised in the blood nulling ratio map in Figure 3.12d) containing fast-flowing blood, above the VENC, hence the random orientation of vectors due to phase wrapping. The interstitial fluid emanated from this region, flowing across the tumour towards the periphery. This pattern was broadly consistent across within-session scans. Reproducibility was also strong, as shown in Figure 3.14b. Once again, the small region of blood flow was visible on the left edge of the tumour (red arrow), from which the interstitial fluid flowed across the tumour towards the periphery.

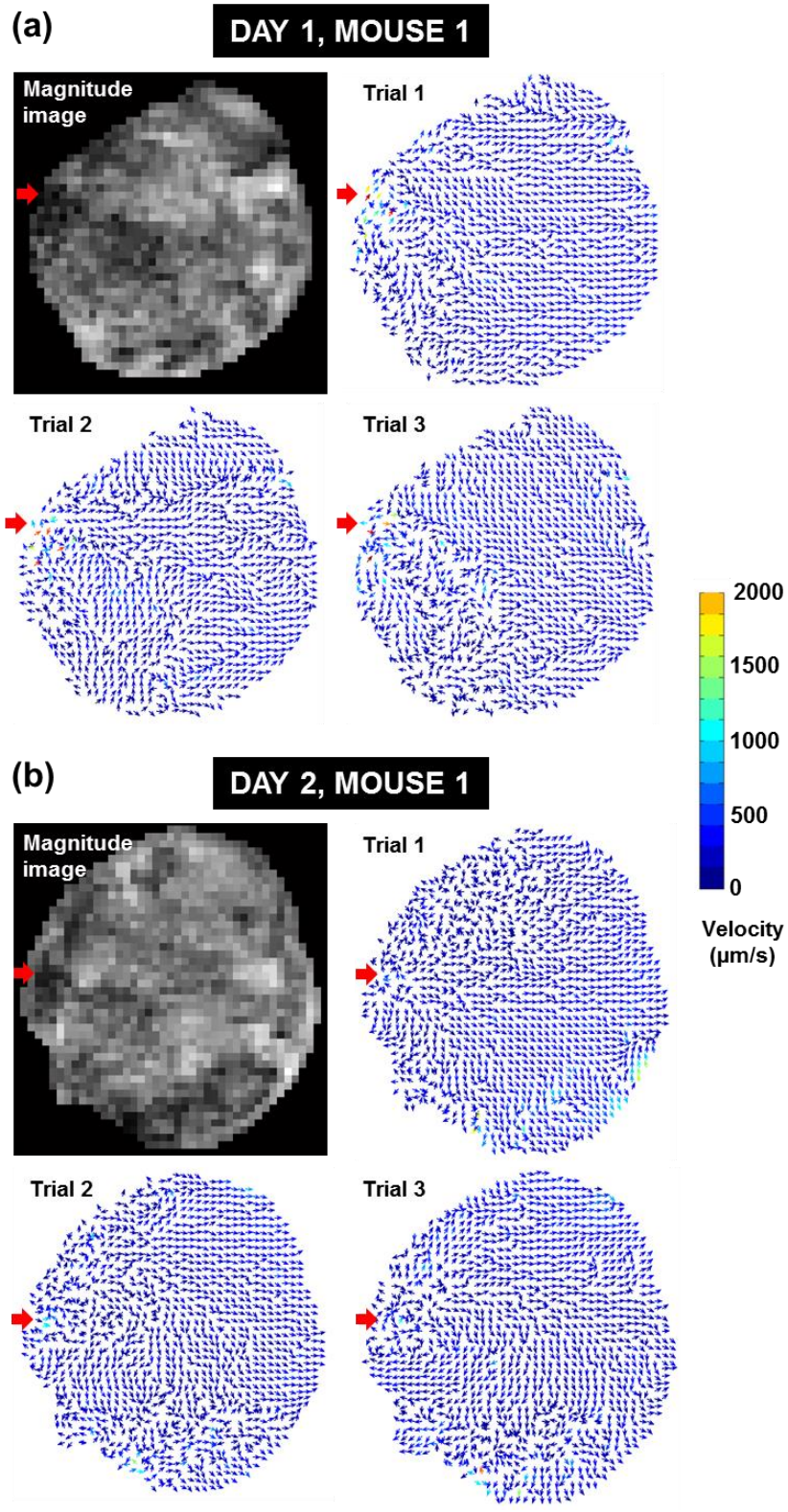

Figure 3.14: Repeatability and reproducibility of EVAC in a mouse tumour. (a) On day 1, the three trials show similar interstitial fluid flow patterns. (b) Reproducibility is also strong, as on day 2 the interstitial fluid flow patterns are broadly consistent with those on day 1. In this tumour, much of the interstitial fluid appears to emanate from a large blood vessel on the left edge of tumour (see Figure 3.12), which then flows from left-to-right across the tumour towards the periphery.

Quantitative repeatability and reproducibility analysis of the EVAC sequence was also conducted. Box plots of the mean interstitial fluid velocity measured across all tumours in all trials is shown in Figure 3.15a, as well as Bland-Altman plots of repeatability (b) and reproducibility (c). The mean interstitial fluid velocity on Day 1 was 206 ± 126 µm/s. On Day 2 the mean interstitial fluid velocity decreased to 188 ± 126 µm/s. Within-session repeatability, calculated by comparing all data from trials 1 and trial 2, was non-significantly different (p = 0.2, Mann-Whitney-U) with a SD_{repeat} = 17.9%. Between-session reproducibility, calculated by comparing all trials between days, was also non-significantly different (p = 0.34, Mann-Whitney-U) with a SD_{reprod} = 26.6%. Note, the two outliers seen on Day 2 were caused by scanner instability which partially corrupted the magnitude and phase images.

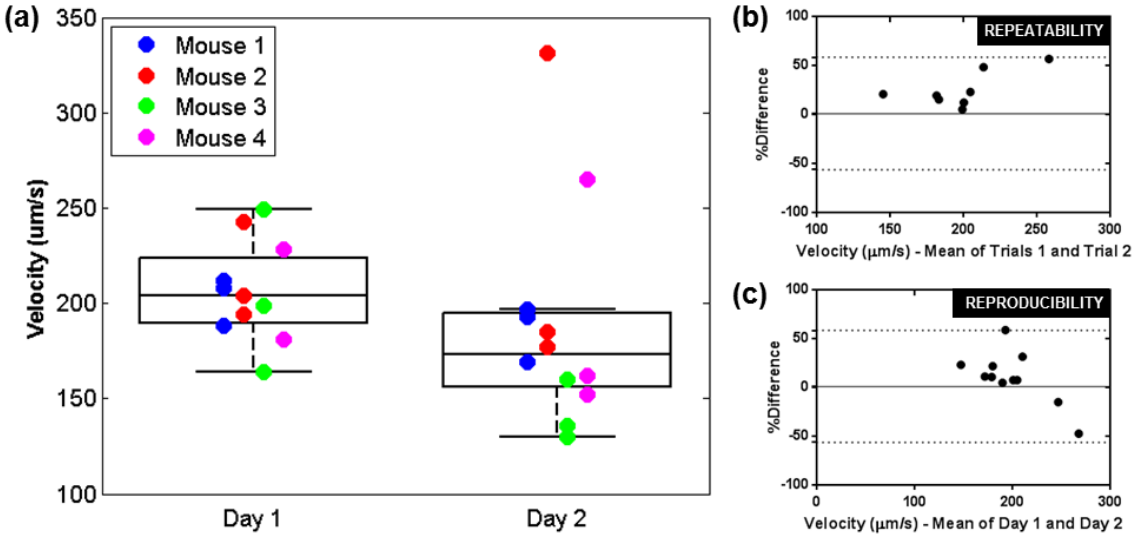

Figure 3.15: Repeatability and reproducibility of in vivo EVAC velocity measurements of interstitial fluid flow in subcutaneous tumours. (a) In the box plots, each point represents the mean velocity across a single slice EVAC velocity map during one of the trials. Mean tumour velocities were lower on Day 2, however, the overall between-session difference was non-significant (p = 0.34, Mann-Whitney-U). Similarly, the within-session difference was also non-significant (p = 0.2, Mann-Whitney-U). (b) Bland-Altman plots of within-session repeatability, SD_{repeat} = 17.9%, and (c) between-session reproducibility, SD_{reprod} = 26.6%.

In a separate cohort of subcutaneous tumour mice (n = 6), the phase offset correction method developed in the flow phantom was applied to examine its effect on imaging tumour interstitial fluid dynamics. Firstly, the mouse tumour was imaged using EVAC, as shown in Figure 3.16b. Following this, the mouse was removed and replaced with an agar phantom which filled the majority of the RF coil. The agar phantom was imaged again using exactly the same EVAC sequence and scan parameters that were used for *in vivo* imaging. Figure 3.16c shows an axial view of the agar phantom, where the red line corresponds to the slice

location of the EVAC scan. The corresponding in-plane image is shown in Figure 3.16d, showing where the tumour was located (dashed blue line).

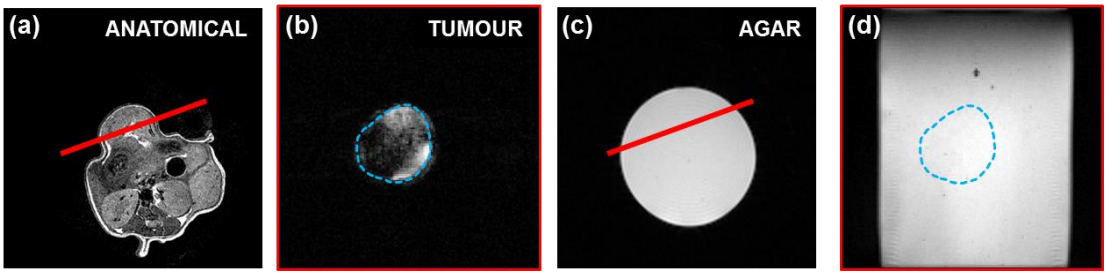

Figure 3.16: Schematic illustrating how the phase offset region within an agar phantom is delineated. (a) Axial anatomical image showing the tumour imaging plane (red line). (b) Coronal slice (FOV = 25.6mm^2) through the tumour, in the same orientation used for the EVAC velocity maps. A region of interest (blue) was drawn around the tumour boundary. (c) Axial image of the agar phantom (FOV = 50mm^2), placed in the scanner following tumour imaging. The red line indicates the slice orientation used for tumour imaging. (d) The agar phantom imaged using exactly the same slice orientation as the tumour slice. The blue dashed line now represents the location of where the tumour occupied the scanner. The phase data within the blue region of interest is used in the electrical eddy current correction procedure.

As before, the phase signals measured in agar were subtracted from the EVAC tumour data to produce phase offset corrected velocity maps. Uncorrected and corrected EVAC velocity maps from two subcutaneous tumours are shown in Figure 3.17. In both mice, the uncorrected and corrected velocity maps demonstrated similar interstitial fluid flow patterns. Mouse 1 appeared to have a large region of potential necrosis (a), which had randomly orientated velocity vectors in the corresponding EVAC velocity maps (b,c). Outside of this region the interstitial fluid appeared to flow towards the tumour periphery. In the uncorrected image, the major component of flow was towards the right edge of the tumour (b), whereas in the corrected image the flow was towards the upper edge of the tumour (c). In mouse 2, the flow patterns within the uncorrected and corrected EVAC velocity maps were even more similar, suggesting that the phase offset correction had little effect on the tumour EVAC velocity maps.

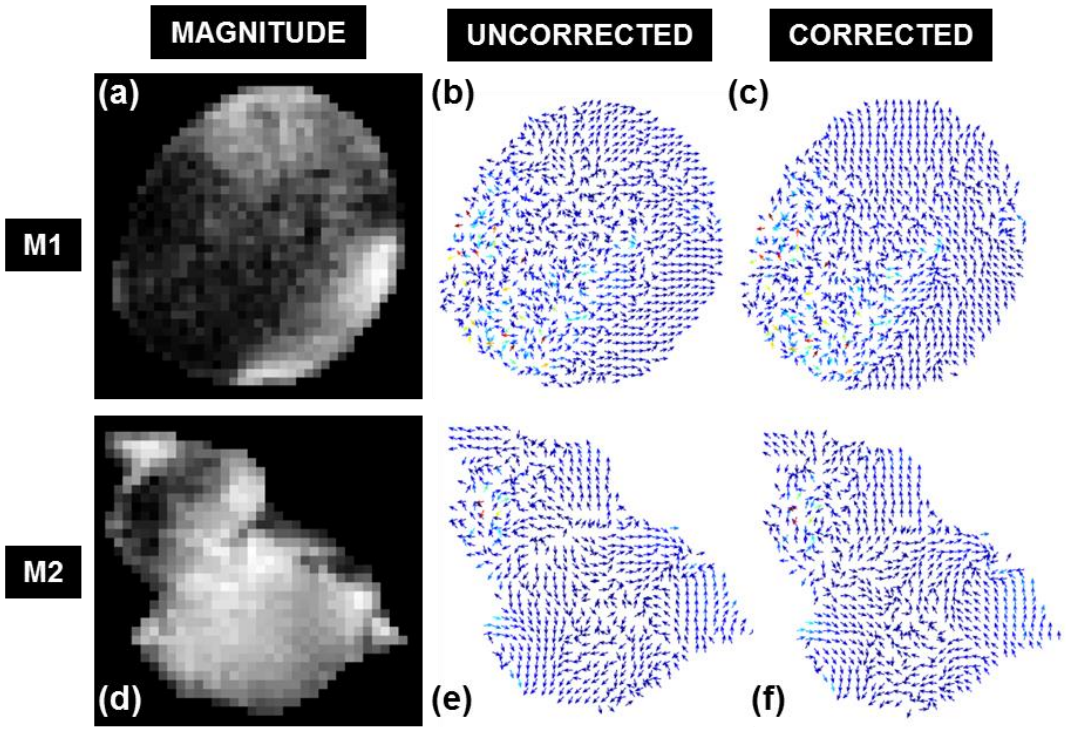

Figure 3.17: Applying the electrical eddy current correction in vivo to mouse tumours. Data from two animals are shown. (a) The tumour in Mouse 1 has a large area of signal hypointensity covering the left hand side of the tumour, possibly corresponding to necrotic tissue. (d) By comparison, the tumour in Mouse 2 has a smaller area of potential necrosis towards the top of the tumour. (e, f) The corrected EVAC velocity maps show some differences in vector directionality compared to the uncorrected maps (b, c), however, the overall interstitial fluid flow patterns remain very similar.

The difference in measured mean velocities across the tumours, before and after phase offset correction, is shown in Figure 3.18. The mean velocity of the corrected data (235 ± 45 μm/s) was marginally lower than the uncorrected data (259 ± 58 μm/s), however, this difference was non-significant ($p = 0.44$, Mann-Whitney-U).

Overall, the phase offset correction method did not show any definitive improvements to the data over the standard EVAC protocol. There was no notable difference in vector directionality or significant difference in velocity magnitude, therefore, the phase offset correction method was not implemented in the stroke imaging study, described in the following section.

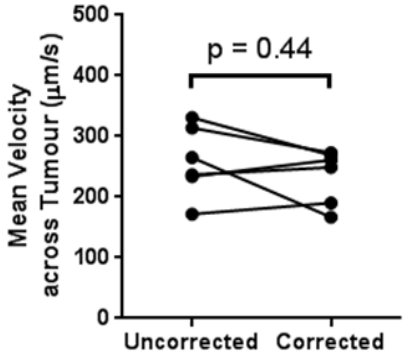

Figure 3.18: Mean velocities across six tumours before (uncorrected) and after (corrected) application of the phase offset correction method. There was no significant difference between velocity values before or after the correction was applied (p = 0.44, Wilcoxon paired rank test).

3.4.4 Stroke rat study – Imaging extracellular fluid dynamics in an experimental rat stroke model

The aim of this study was to image the extracellular brain fluid dynamics in normal rats and a rat model of stroke using the EVAC sequence. A multi-parametric protocol of sequences commonly used in stroke imaging, including T2-weighted imaging, perfusion weighted imaging (PWI) and diffusion weighted imaging (DWI) was acquired for comparison with the EVAC results. Representative images from each of these modalities are shown in Figure 3.19. The T2-weighted images showed hyperintensity in the ipsilateral hemispheres of the stroke rats (e), whereas in normal rats signal intensity was uniform across hemispheres (a). PW images showed a distinct region of perfusion deficit in stroke rats (f) and similarly there was a marked reduction in ADC in stroke rats (g). These results were consistent with histology where TTC-staining showed a significant infarct region, which covered the majority of the ipsilateral hemisphere (g).

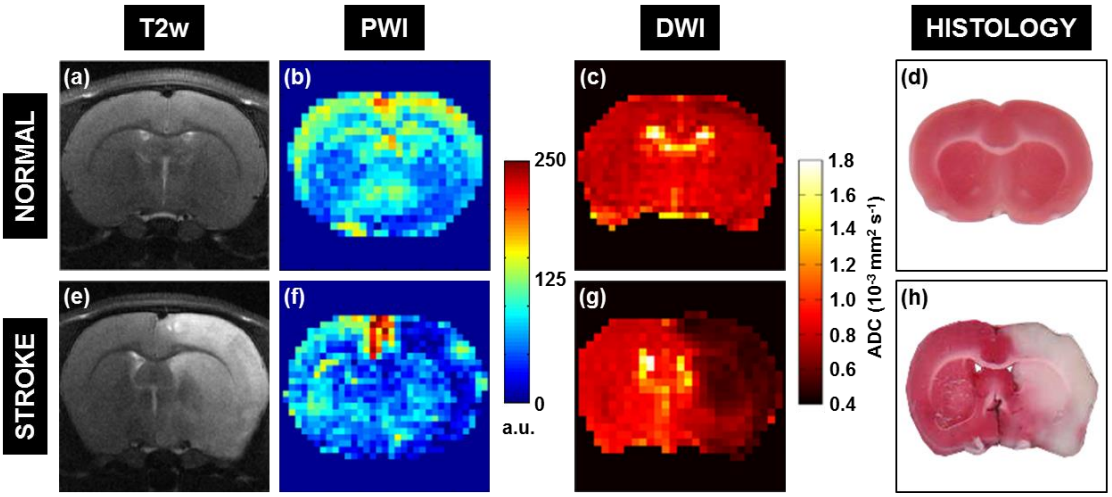

Figure 3.19: Representative images from conventional multi-parametric MRI sequences used in stroke imaging. The top row shows images from a normal rat. The bottom row shows images from a stroke rat imaged 24 hours post-surgery. (a,e) T2-weighted imaging sensitises oedema, which is hyperintense in the stroke animal. (b,f) Perfusion weighted imaging shows perfusion deficits, which are marked by dark blue regions in the stroke animal. (c,g) Diffusion weighted imaging is a marker of infarcted tissue, which is hypointense on ADC maps corresponding to the restricted motion of water molecules. (d,h) TTC-stained histology confirmed that the stroke rats had extensive infarct lesions.

Prior to EVAC imaging, the efficiency of the blood nulling double inversion preparation was investigated in the rat brains, as shown in Figure 3.20. Taking the ratio of a slice acquired with the double inversion preparation to the same slice with the nulling preparation switched off gave the nulling ratio (Equation 3.8), which is a first order estimate of the fractional blood volume. As in the tumour study, the non-nulled and nulled images had similar, but subtly different contrast (a, b, d, e). The blood nulling ratio maps in the normal rat brains (c) were largely homogenous across both hemispheres. Small regions of high intensity (yellow) corresponded to the carotid arteries (red arrows). In the stroke rats, there was a clear difference between the two hemispheres (f). The ipsilateral hemisphere had a markedly lower nulling ratio corresponding to lower fractional blood volume in the infarcted tissue, which agreed with the perfusion deficit seen in the earlier PWI images (Figure 3.19). Across all pixels the nulling ratio ranged from 0 to 85%. The mean nulling ratio across the slice for the normal rats was 12.5 ± 4.6%. In the stroke rats, the mean nulling ratio decreased by more than half to 5.4 ± 3.7%, although this difference was insignificant ($p = 0.2$, Mann-Whitney-U). The nulling ratio in the normal rats was higher than similar measurements of cerebral blood volume reported in the literature (5%) [34], but values were of the same order.

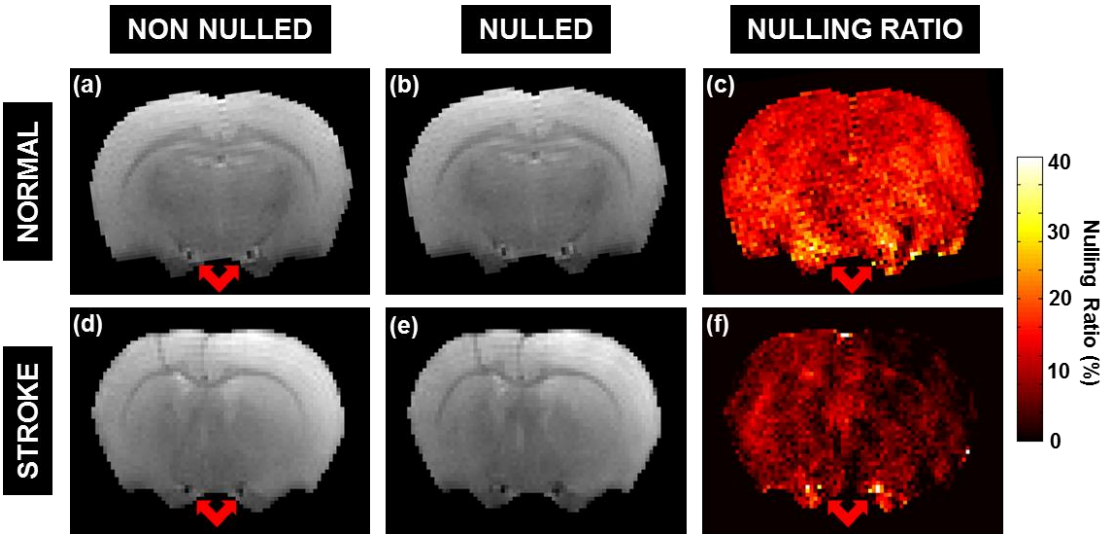

Figure 3.20: Evaluating the blood nulling ratio in normal and stroke rat brains. The top row shows images from a normal rat. The bottom row shows images from a stroke rat. (a, d) Non-nulled images acquired with the double-inversion preparation in the EVAC sequence switched off. (b, e) Blood nulled images acquired using the full EVAC sequence. (c, f) Nulling ratio maps showing the difference in signal between the non-nulled and nulled scans due to fractional blood volume.

Next, the cohort of rats was imaged with EVAC. The magnitude, phase and phase difference images generated during the EVAC velocity map image processing pipeline are shown in Figure 3.21. Only data with the velocity encoding bipolar gradients applied in the readout direction are shown. Two phase images were generated to measure one velocity component, one with a negative bipolar gradient (b) and one with a positive bipolar gradient (c). Both images contain phase wrapping where the phase suddenly jumps from π to $-\pi$, however, the discontinuities were successfully unwrapped by the ATAN2 operator used in the calculation of the phase difference maps (d). The phase difference map is smooth across the brain tissue. The carotid arteries show a large change in phase, consistent with phase wrapping due to high velocity blood flow.

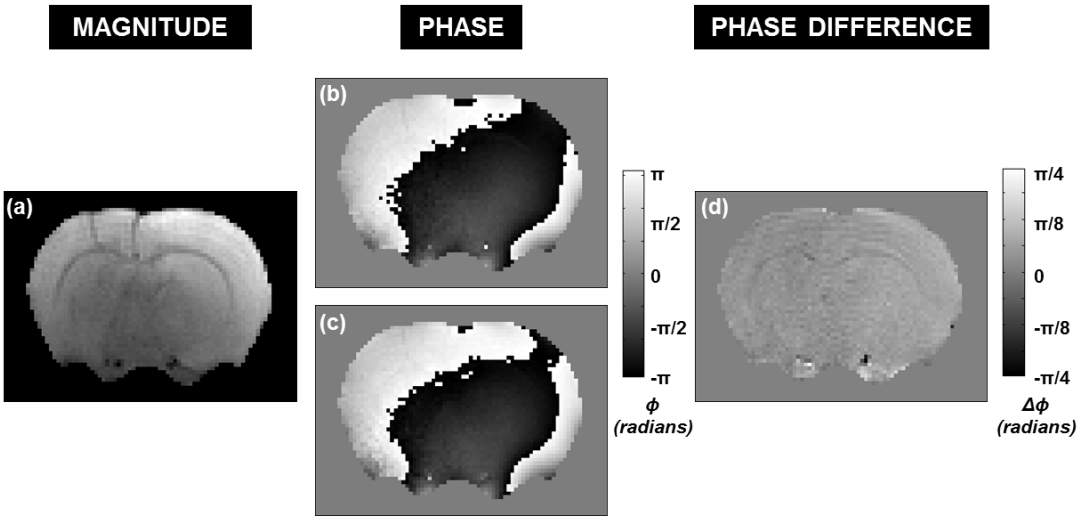

Figure 3.21: Image processing schematic illustrating the steps involved in generating an EVAC velocity map in a rat brain. All images are from a scan acquired with bipolar gradients orientated in the readout direction. (a) Magnitude image, (b) negative bipolar gradient polarity phase image, (c) positive bipolar gradient polarity phase image and (d) phase difference image. The phase wrap present in the phase maps is unwrapped in the phase difference data.

Representative EVAC velocity maps from a normal and a stroke rat are shown in Figure 3.22. The interstitial fluid flow patterns were unexpectedly uniform and broadly unidirectional. In both the normal and stroke rats, the velocity vectors were directed laterally across the brain, from the left hemisphere to the right, ipsilateral hemisphere. This directionality, or vice versa (right to left), was observed in the rest of the cohort.

Measured velocities ranged from 300 to 1000 μm/s, which was much higher than tumour measurements of interstitial fluid flow. Average velocity magnitude across the entire brain region was reduced in stroke rats (507 ± 160 μm/s) compared to normal rats (897 ± 90 μm/s), however this difference was non-significant ($p = 0.10$), as shown in Figure 3.23. The induced strokes were clearly extensive based on the multi-parametric imaging and histology (Figure 3.19), so it was unexpected to observe no obvious hemispheric differences in the EVAC velocity maps of the stroke animals. There was no obvious change in vector directionality or vector magnitude between the two hemispheres. In the region of the carotid arteries, the magnitude of the velocity vectors was very different to the surrounding tissue, reflecting the phase wrapping due to fast blood flow.

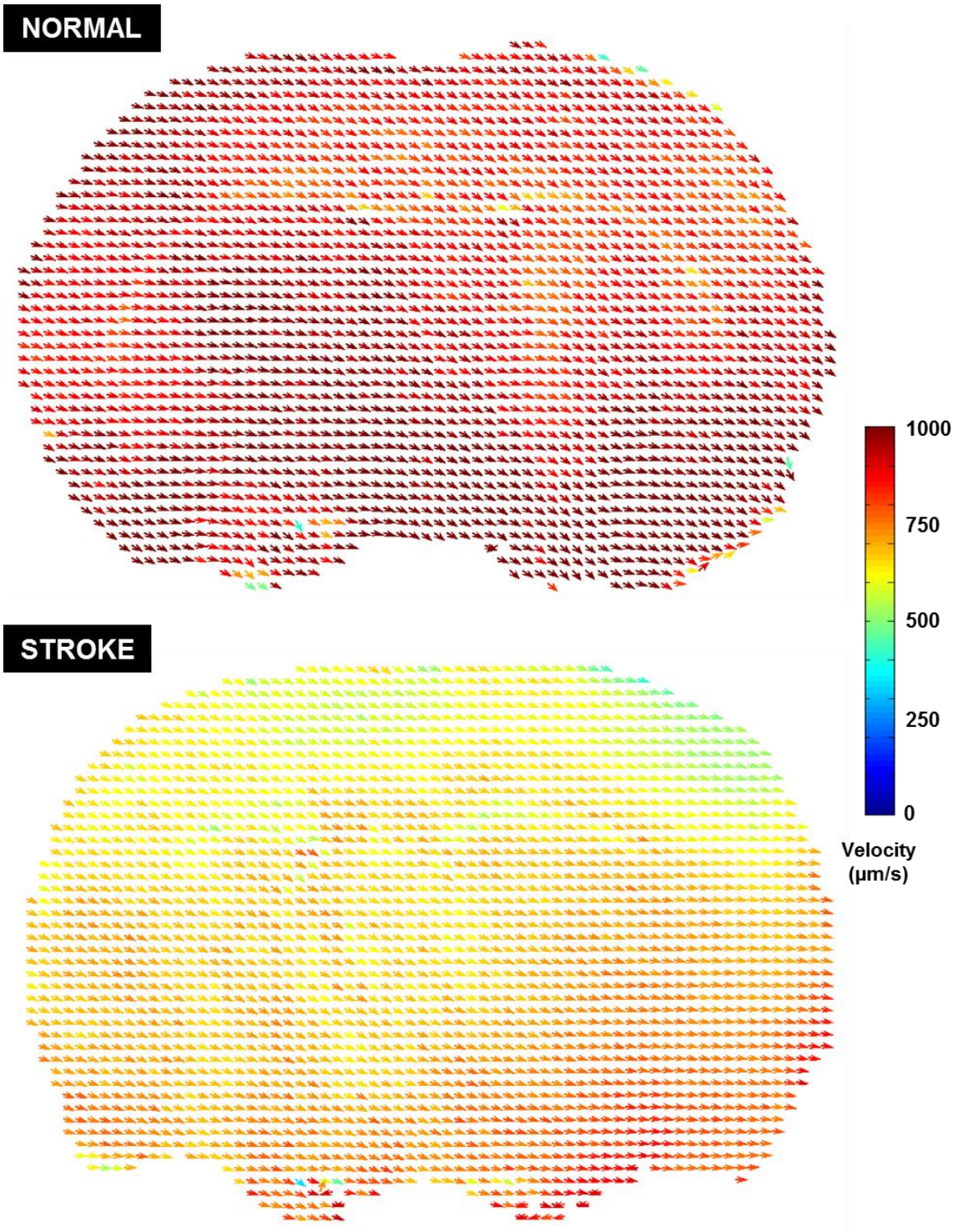

Figure 3.22: Representative EVAC velocity maps in a (a) normal rat brain and a (b) stroke rat brain. Each voxel contains an individual vector, which is supposed to represent interstitial fluid flow within that region. In both the normal and stroke brains, the vast majority of the vectors point laterally across the brain, from left to right. Across the entire brain, the mean velocity magnitude is higher in the normal brain than the stroke brain, which was observed across the entire cohort.

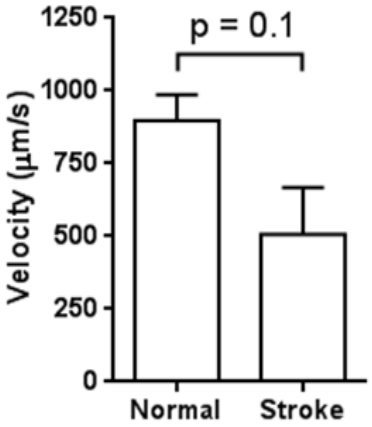

Figure 3.23: Mean interstitial fluid velocity measured across the brains of the normal and stroke rats. Velocities were lower in the stroke rats, however, the difference was insignificant (p = 0.10, Mann-Whitney-U).

3.5 Discussion

In this chapter, further development was conducted on an in-house MRI sequence known as EVAC, designed to image the flow of extracellular fluid. The primary objective of the work in this chapter was to image the flow of extracellular fluid in a rat brain following stroke. To this end, a number of preliminary experiments were undertaken for the purpose of validating the measurements obtained with EVAC. Flow phantom experiments were conducted to establish the slowest measureable flow velocity on the CABI 9.4T MRI scanner and to study the effects of electrical eddy currents on phase measurements. For *in vivo* validation, interstitial fluid flow in mouse tumours was imaged as the underlying physiology is relatively well understood compared to brain fluid dynamics. Finally, the EVAC sequence was applied to rat brains.

Velocity-encoded phase contrast MRI has been predominantly applied to measuring blood flow in major vasculature such as the great vessels [8-11] and the carotid arteries [12, 13] where the flow is constrained and fast. Aortic blood flow in mice can be greater than 100 cm/s [35], while carotid blood flow in mice can reach almost 50cm/s [13]. Measuring very slow flows with MRI is novel in itself, hence a flow phantom experiment was conceived to measure the slowest measurable speed on our 9.4T scanner. The flow resolution was ultimately limited by the size of the velocity encoding gradients. It was demonstrated how smaller VENC values, which require increasingly large gradients, crush out the signal. Averaging and other SNR boosting methods could be used to recover the lost signal, but the increase in sequence duration would be prohibitive for *in vivo* studies.

Fluid speeds lower than 50μm/s were determined to be resolvable while retaining accurate directionality. The flow phantom study was partially limited by the design of the flow phantom because at very slow inflow rates (0.34 ml/min) – and even with the inflow turned off – the direction of flow appeared to be backwards. This was possibly a real effect caused by some form of low-level suction, but more likely it was an artefact related to reaching the noise floor of the phase contrast measurements. Another limitation of the flow phantom was its simplicity compared to interstitial fluid flow in real biological systems: the flow phantom contained only water and fluid motion was broadly unidirectional and non-pulsatile. Nonetheless, the study was important for establishing a baseline measurement under idealised conditions.

Gradient interference due to electrical eddy currents was anticipated to potentially affect the phase contrast measurements in the EVAC sequence [15, 36]. The phase data subtraction process used to create EVAC plots could not compensate for electrical eddy currents

because alternating the polarity of the bipolar gradients also alternates the sign of the eddy currents, hence they become additive in the phase difference image during the image processing pipeline [15]. Previous studies have described two main electrical eddy current correction methods for phase contrast measurements. One common technique is to measure phase in a 'static' region of an image and use this information to correct phase offsets in measures of high speed vascular flow [37]. However, this technique is difficult to implement with EVAC because the sequence is intended to image very slow flows within tissues that would be regarded as "static" for phase correction purposes in vascular flow studies. Instead, the phase offset was measured in a stationary agar phantom after flow imaging, similar to the study by Chernobelsky et al. [17].

When the phase offset correction was applied to the flow phantom, the accuracy of the flow measurements appeared to improve. At higher flow rates, the streamlines representing the underlying velocity vectors became straighter in the direction of flow. At slower flow rates, vector directionality also appeared to improve. Notably, at a flow rate of 0.34 ml/min – where the direction of flow was backwards in the uncorrected EVAC velocity maps – the phase offset correction resulted in the velocity vectors pointing in the correct direction of flow. Furthermore, with the pump switched off, the flow pattern had no clear directionality, instead appearing static, thus resembling stationary water. The reproducibility experiment demonstrated that the phase offset correction method resulted in more accurate measures of fluid velocity in the flow phantom, compared to the standard, uncorrected approach. However, as the correlation plot of repeatability showed (Figure 3.11a), sometimes EVAC yielded accurate velocity measurements, in line with theoretical values, without the need for phase offset correction. In general, however, applying the phase offset correction appeared to be beneficial, especially at the slowest flow rate (0.069 ml/min) where the average measured velocity was approximately 48 μm/s compared to 78 μm/s without the correction.

The first *in vivo* application of EVAC was in subcutaneous mouse tumours, as the fluid dynamics within the tumour microenvironment have been studied widely [22, 23, 25]. The experiments in this chapter and work previously conducted by Simon Walker Samuel et al. [7] imply that EVAC velocity maps accurately and reproducibly reflect interstitial fluid flow patterns in tumours. Tumour blood nulling percentages agreed with previous reports on microvascular density, suggesting that the double inversion preparation functioned correctly. EVAC velocity maps showed a range of interstitial fluid patterns broadly demonstrating either outward, radial flow towards the tumour periphery; laminar flow across the tumour; or a combination of both. These patterns were consistent with interstitial fluid flow from regions of high pressure, such as tumour vasculature, to regions of low pressure, such as the tumour boundary at the intersection with normal tissue. The repeatability and reproducibility

studies demonstrated that EVAC velocity maps showed both low within- and between-session variability. This was further reflected in the mean tumour velocities, where there was no significant difference between trials or days.

One issue apparent in the tumour results was that the magnitudes of the measured interstitial fluid velocity vectors were much higher than reports of interstitial fluid flow in the literature. Interstitial fluid velocity is typically reported between 0.1 and 10 μm/s. These reports include mathematical models of tumour interstitial fluid dynamics [38-41], fluorescence recovery measurements after photobleaching [42], in vitro studies of interstitial fluid flow in glioma cell invasion [43] and dynamic contrast-enhanced MRI-based experiments [44]. One more recent report suggested interstitial fluid velocity could be up to 55 μm/s [14]. The measurements in tumours using EVAC averaged approximately 200 μm/s, an order of magnitude, or more, higher than the aforementioned reports. The phase offset correction method was applied to the EVAC tumour measurements to examine whether this velocity disparity might be caused by the effects of electrical eddy currents. Despite having a clear effect in the flow phantom experiments, the phase offset correction appeared to make little difference to the tumour data. The EVAC velocity maps looked very similar between the corrected and uncorrected data, and although there was an average decrease in the velocities when the phase offset correction method was applied, the difference was non-significant.

Another reason for the velocity disparity could be the incorrect assumption that data acquired with EVAC was completely blood nulled. Simulations carried out by Simon Walker-Samuel (unpublished) suggest that non-nulled blood could contribute to elevating measured interstitial fluid velocity values (Figure 3.24). If this is true, then it is likely that the tumour nulling ratio measurements include some percentage of interstitial fluid or tissue nulling, rather than solely blood nulling.

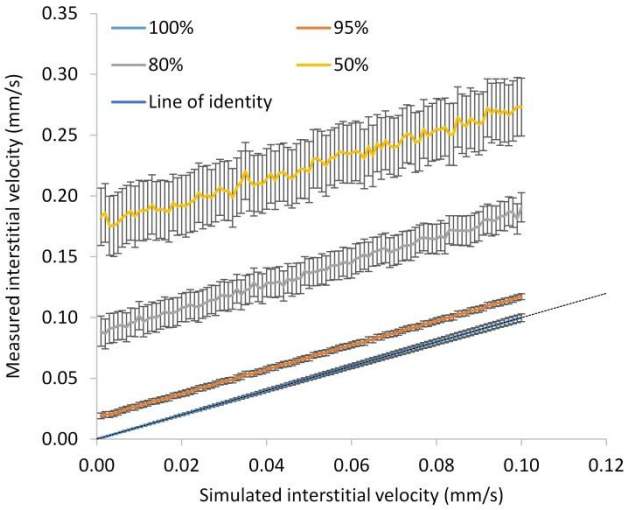

Figure 3.24: Simulations showing the effect of imperfect blood nulling on EVAC measurements of interstitial fluid velocity (figure created and supplied by Simon Walker-Samuel). Measured interstitial fluid velocities become increasingly large as the blood nulling efficiency decreases (100, 95, 80 and 50%). Error bars show the standard error in the mean.

Although it is difficult to definitively account for the disparity in velocities between EVAC measurements and literature values, the robustness of the interstitial fluid flow patterns observed in the repeatability and reproducibility studies offer compelling evidence that the EVAC velocity maps reflect the underlying tumour fluid dynamics. Furthermore, gadolinium infusion studies conducted by Simon Walker-Samuel (unpublished) showed that the contrast agent collected in regions downstream of the EVAC velocity vectors (Figure 3.25), reinforcing the notion that the directionality of the vectors in EVAC tumour measurements appears to be accurate, even if the absolute values are overestimated.

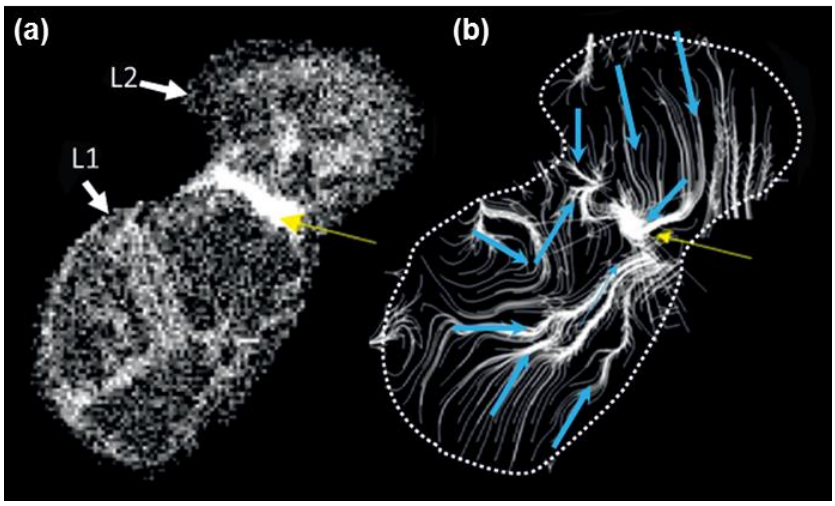

Figure 3.25: Comparison between a subcutaneous mouse tumour (a) infused with a gadolinium contrast agent and an (b) EVAC velocity map (images created and supplied by Simon Walker-Samuel). The gadolinium collects in regions downstream of the velocity vectors in the EVAC map.

Following tumour imaging, EVAC was applied to a rat model of stroke to examine the alterations in brain fluid dynamics post-infarction. The blood nulling percentage in the normal rat brains was 12.5%, higher than the tumour values and previously reported values of cerebral blood volume [34], perhaps reflecting that more than just blood was nulled. In the stroke rats, this value decreased to 5.4% reflecting the infarcted region devoid of perfused tissue.

The multi-parametric imaging sequences all performed as expected. T2-weighting, PWI and DWI were all consistent with histology in showing a large infarcted region in the ipsilateral hemisphere of the stroke animals. Hence, it was very surprising to see no immediate differences between the hemispheres of the stroke animals with EVAC. In normal brains, fluid flow was expected to be approximately random or drain into the ventricles. In stroke brains, extracellular fluid was expected to flow away from the infarcted region due to the build-up of oedema, or at the very least, some form of disruption to vector directionality was expected compared to the healthy hemisphere. Instead, EVAC maps of both normal and stroke brains demonstrated unidirectional flow patterns directed laterally across the brain from one hemisphere to the other. However, this does not make physiological sense as it is impossible for fluid to cross the brain in this way because of the longitudinal fissure which separates the hemispheres. The mean measured extracellular fluid velocities were higher in the brains than the tumours, especially in the normal rats which were more than four times higher, averaging approximately 897 μm/s. Clearly these values were not physiologically accurate, neither was the directionality of the velocity vectors.

The exact cause of the errors in the stroke EVAC data is difficult to determine with certainty. The main hardware differences between the rat brain imaging and the tumour imaging were the use of a larger gradient set (1000mT/m compared to 400mT/m in the mice), a larger RF coil and a 4-channel rat head phased array receiver. A further test was carried out to examine whether the image processing pipeline (section 3.3.1) was correctly reconstructing the 4-channel phased array data, by imaging the flow phantom consecutively in volume receive mode, as in the tumour studies, and then with the same hardware configuration used in the rat studies. The EVAC velocity maps were comparable showing forward flow, both in volume receive mode and 4-channel receive mode (Figure 3.26), indicating that the image processing pipeline was working as intended.

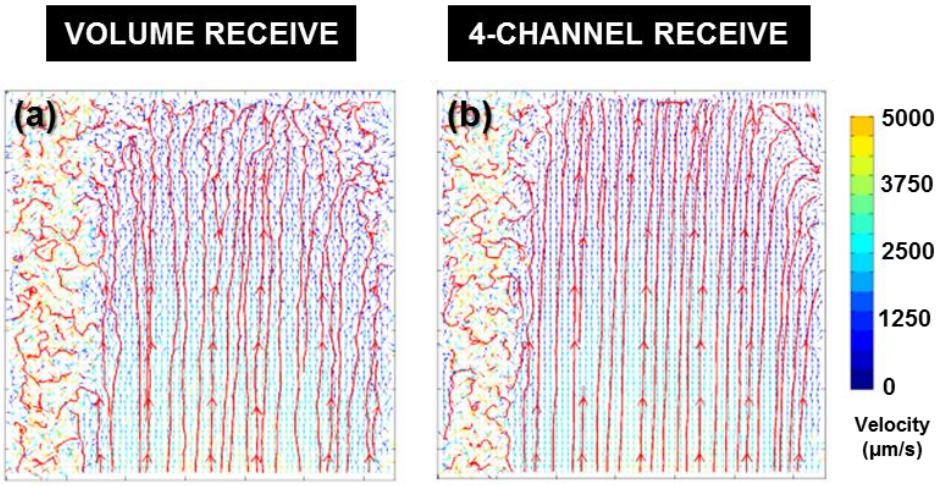

Figure 3.26: Comparing the accuracy of EVAC velocity map reconstruction between a volume receive and a 4-channel receive hardware configuration. (a) The flow phantom imaged using the 72mm diameter RF coil in volume-receive mode. (b) The flow phantom imaged using the 72 mm diameter RF coil in transmit mode and the 4-channel rat head phased array as the receiver. An inflow rate of 1.71 ml/min and a VENC of 0.5cm/s were used in both scans.

Another potential source of error in the measurements may have been motion caused by respiration or scanner vibrations, which masked the very slow interstitial fluid speeds. This may explain why the velocity vectors in the brain images (Figure 3.22) were directed laterally across the brain, reflecting bulk motion of the animal's entire head, although no obvious signs of such motion were observed in the magnitude images. Furthermore, small ear bars were used to tightly secure the heads of the animals to minimise such motion and this exact setup (see section 2.8.1) is routinely used for similarly, motion-susceptible diffusion MRI, without issue.

It is only possible to speculate on the exact cause of the unexpected EVAC velocity maps in the rat brains. Applying EVAC to brains was a natural extension to the tumour imaging work – where the sequence has been more thoroughly validated – however, at present EVAC does not produce physiologically sensible results in brains. More work is required to understand the issues underlying EVAC in the brain, which was not possible to carry out in time for completion of this thesis.

3.6 Summary

In this chapter, further development was conducted of a novel technique for *in vivo* imaging of extracellular fluid flow known as extravascular convectography (EVAC) MRI. A number of validation studies were carried out in a flow phantom and an *in vivo* mouse tumour model to ensure the robustness of the sequence. EVAC was applied to imaging the brain fluid dynamics in a rat model of stroke, however, the results did not reflect the underlying physiology of the brain. EVAC was successful at imaging interstitial fluid dynamics in subcutaneous mouse tumours, but further work is required in the rat brain to establish the sources of error masking the phase contrast extracellular fluid signal.

3.7 References

1. World Heath Organization. *Fact File No. 310: The top 10 causes of death*. August 2014.
2. Go AS, et al. *Heart disease and stroke statistics--2013 update: a report from the American Heart Association.* Circulation, 2013. **127**(1): p. e6.
3. Iadecola C and Anrather J. *The immunology of stroke: from mechanisms to translation.* Nature Medicine, 2011. **17**(7): p. 796-808.
4. Ebinger M, et al. *Imaging the penumbra–strategies to detect tissue at risk after ischemic stroke.* Journal of Clinical Neuroscience, 2009. **16**(2): p. 178-187.
5. Schaefer PW, Grant PE and Gonzalez RG. *Diffusion-weighted MR imaging of the brain 1.* Radiology, 2000. **217**(2): p. 331-345.
6. Neumann-Haefelin T, et al. *Diffusion-and perfusion-weighted MRI The DWI/PWI mismatch region in acute stroke.* Stroke, 1999. **30**(8): p. 1591-1597.
7. Walker-Samuel S, et al. *Investigating tumour interstitial convection currents using extra-vascular convection (EVAC) MRI*. in *Proceedings of the British Chapter of the International Society for Magnetic Resonance in Medicine*. 2011.
8. Gatehouse PD, et al. *Applications of phase-contrast flow and velocity imaging in cardiovascular MRI.* European Radiology, 2005. **15**(10): p. 2172-2184.
9. Markl M, Kilner PJ and Ebbers T. *Comprehensive 4D velocity mapping of the heart and great vessels by cardiovascular magnetic resonance*. J Cardiovasc Magn Reson, 2011. **13**(7): p. 1-22.
10. Joseph A, et al. *Real-time flow MRI of the aorta at a resolution of 40 msec.* Journal of Magnetic Resonance Imaging, 2013.
11. Janiczek RL, et al. *Three-dimensional phase contrast angiography of the mouse aortic arch using spiral MRI.* Magnetic Resonance in Medicine, 2011. **66**(5): p. 1382-1390.

12. Harloff A, et al. *3D blood flow characteristics in the carotid artery bifurcation assessed by flow-sensitive 4D MRI at 3T.* Magnetic Resonance in Medicine, 2009. **61**(1): p. 65-74.

13. van Bochove GS, et al. *MRI-determined carotid artery flow velocities and wall shear stress in a mouse model of vulnerable and stable atherosclerotic plaque.* Magnetic Resonance Materials in Physics, Biology and Medicine, 2010. **23**(2): p. 77-84.

14. Munson JM and Shieh AC. *Interstitial fluid flow in cancer: implications for disease progression and treatment.* Cancer Management and Research, 2014. **6**: p. 317.

15. Bernstein MA, King KF, and Zhou XJ. *Handbook of MRI pulse sequences.* Elsevier, 2004.

16. Lankhaar JW, et al. *Correction of phase offset errors in main pulmonary artery flow quantification.* Journal of Magnetic Resonance Imaging, 2005. **22**(1): p. 73-79.

17. Chernobelsky A, et al. *Baseline correction of phase contrast images improves quantification of blood flow in the great vessels.* Journal of Cardiovascular Magnetic Resonance, 2007. **9**(4): p. 681-685.

18. Gatehouse PD, et al. *Flow measurement by cardiovascular magnetic resonance: a multi-centre multi-vendor study of background phase offset errors that can compromise the accuracy of derived regurgitant or shunt flow measurements.* Journal of Cardiovascular Magnetic Resonance, 2010. **12**(1): p. 1-8.

19. Gullino PM, Clark SH and Grantham FH. *The interstitial fluid of solid tumors.* Cancer Research, 1964. **24**(5): p. 780-797.

20. Rippe B and Haraldsson B. *Transport of macromolecules across microvascular walls: the two-pore theory.* Physiological Reviews, 1994. **74**(1): p. 163-219.

21. Boucher Y and Jain RK. *Microvascular pressure is the principal driving force for interstitial hypertension in solid tumors: implications for vascular collapse.* Cancer Research, 1992. **52**(18): p. 5110-5114.

22. Jain RK. *Transport of molecules in the tumor interstitium: a review.* Cancer Research, 1987. **47**(12): p. 3039-3051.

23. Lunt SJ, et al. *Interstitial fluid pressure in tumors: therapeutic barrier and biomarker of angiogenesis.* Future Oncol., 2008. **4**(6): p. 793-802.

24. Heldin CH, et al. *High interstitial fluid pressure—an obstacle in cancer therapy.* Nature Reviews Cancer, 2004. **4**(10): p. 806-813.

25. Swartz MA and ME Fleury. *Interstitial flow and its effects in soft tissues.* Annu. Rev. Biomed. Eng., 2007. **9**: p. 229-256.

26. Abbott NJ. *Evidence for bulk flow of brain interstitial fluid: significance for physiology and pathology.* Neurochemistry International, 2004. **45**(4): p. 545-552.

27. Pardridge WM, *Drug transport in brain via the cerebrospinal fluid.* 2011.

28. Popovic D, Khoo M, and Lee S. *Noninvasive monitoring of intracranial pressure.* Recent Patents on Biomedical Engineering, 2009. **2**(3): p. 165-179.

29. Kristiansson H, et al. *Measuring elevated intracranial pressure through noninvasive methods: a review of the literature.* Journal of neurosurgical anesthesiology, 2013. **25**(4): p. 372-385.

30. Holland BJ, Printz BF and Lai WW. *Baseline correction of phase-contrast images in congenital cardiovascular magnetic resonance.* J Cardiovasc Magn Reson, 2010. **12**(11).

31. Miller TA, Landes AB and Moran AM. *Improved accuracy in flow mapping of congenital heart disease using stationary phantom technique.* Journal of Cardiovascular Magnetic Resonance, 2009. **11**(1): p. 52.

32. Campbell-Washburn AE, et al. *Cardiac arterial spin labeling using segmented ECG-gated Look-Locker FAIR: Variability and repeatability in preclinical studies.* Magnetic Resonance in Medicine, 2013. **69**(1): p. 238-247.

33. Folarin A, et al., *Three-dimensional analysis of tumour vascular corrosion casts using stereoimaging and micro-computed tomography.* Microvascular Research, 2010. **80**(1): p. 89-98.

34. Lu H, Hua J and Zijl P. *Noninvasive functional imaging of cerebral blood volume with vascular-space-occupancy (VASO) MRI.* NMR in Biomedicine, 2013. **26**(8): p. 932-948.

35. Van Doormaal MA, et al. *Haemodynamics in the mouse aortic arch computed from MRI-derived velocities at the aortic root.* Journal of The Royal Society Interface, 2012: p. rsif20120295.

36. Elkins CJ and Alley MT. *Magnetic resonance velocimetry: applications of magnetic resonance imaging in the measurement of fluid motion.* Experiments in Fluids, 2007. **43**(6): p. 823-858.

37. Walker PG, et al. *Semiautomated method for noise reduction and background phase error correction in MR phase velocity data.* Journal of Magnetic Resonance Imaging, 1993. **3**(3): p. 521-530.

38. Baxter LT and Jain RK. *Transport of fluid and macromolecules in tumors. IV. A microscopic model of the perivascular distribution.* Microvascular Research, 1991. **41**(2): p. 252-272.

39. Zhao J, Salmon H and Sarntinoranont M. *Effect of heterogeneous vasculature on interstitial transport within a solid tumor.* Microvascular Research, 2007. **73**(3): p. 224-236.

40. Soltani M and Chen P. *Numerical modeling of fluid flow in solid tumors.* PLoS One, 2011. **6**(6): p. e20344.

41. Welter M and Rieger H. *Interstitial fluid flow and drug delivery in vascularized tumors: A computational model.* PLoS One, 2013. **8**(8): p. e70395.

42. Chary SR and Jain RK. *Direct measurement of interstitial convection and diffusion of albumin in normal and neoplastic tissues by fluorescence photobleaching.* Proceedings of the National Academy of Sciences, 1989. **86**(14): p. 5385-5389.

43. Munson JM, Bellamkonda RV and Swartz MA., *Interstitial flow in a 3D microenvironment increases glioma invasion by a CXCR4-dependent mechanism.* Cancer Research, 2013. **73**(5): p. 1536-1546.

44. Hompland T et al. *Interstitial fluid pressure and associated lymph node metastasis revealed in tumors by dynamic contrast-enhanced MRI.* Cancer Research, 2012. **72**(19): p. 4899-4908.

CHAPTER 4: ASSESSMENT OF CARDIAC STRUCTURE & FUNCTION USING ADVANCED MRI TECHNIQUES

A breadth of sequences exist for assessing many different aspects of cardiac physiology including morphology, function, myocardial status and the great vessels. This chapter focuses on a pair of studies conducted with cardiac MRI. Firstly, CINE and late gadolinium-enhanced MRI are applied to studying a Prox-1 deficient mouse model of dilated cardiomyopathy, and secondly, the feasibility of using multi-parametric MRI, including T2-mapping, arterial spin labelling and late gadolinium-enhanced MRI, is assessed for quantifying the extent of area-at-risk following myocardial infarction.

Parts of this chapter are contained in the paper: *Loss of Prox1 in striated muscle causes slow to fast skeletal muscle fiber conversion and dilated cardiomyopathy* Louise K. Petchey, Catherine A. Risebro, Joaquim M. Vieira, Tom Roberts, John B. Bryson, Linda Greensmith, Mark F. Lythgoe, Paul R. Riley. *PNAS* (2014) 111 (26) 9515-9520.

4.1 Introduction

Cardiac MR studies were first carried out in the 1970s as a method for assessing myocardial metabolism using phosphorus spectroscopy in isolated, perfused rat hearts [1, 2]. In the 1980s, cardiac MR progressed into clinical imaging where, nowadays, it is routinely carried out. In the past three decades [3], advanced MRI techniques have revolutionised biomedical research by providing novel insights into disease pathophysiology and therapies for treating disease. With cardiac MRI, it is now possible to assess myocardial structure, function, perfusion, metabolism, tissue-status, great vessel blood flow and much more.

In the pre-clinical setting, many surgical and genetic animal models exist which attempt to recreate the pathologies found in humans. Rigorous *in vivo* testing of the pathology underlying these models is crucially important, not only to validate how closely they reflect human conditions, but also to monitor the efficacy of novel therapies and to determine the mechanisms through which such treatments benefit the heart. Imaging plays a significant role in this testing process, as imaging biomarkers can be developed to both characterise these diseases and examine the effects of therapies.

In this chapter, two studies are presented where cardiac MRI is used to assess two different animal models of heart disease. In the first study, a genetic mouse model of dilated cardiomyopathy is assessed using CINE and late gadolinium enhanced MRI. In the second study, multi-parametric cardiac MRI – including T2-mapping and arterial spin labelling (ASL) – is applied to delineate and quantify the size of the area-at-risk following myocardial ischaemia.

4.2 Study 1 – Imaging dilated cardiomyopathy and intracardiac thrombi with MRI

4.2.1 Introduction

Dilated cardiomyopathy (DCM) is a common form of heart disease characterised by an increase in both myocardial mass (hypertrophy) and chamber volume (dilation) [4, 5]. The myocardial walls become stretched, enlarged, or a combination of both, leading to reduced contractility and poor left ventricular function. Key indicators of DCM include reduced ejection fraction (below 40%), increased end diastolic volume and increased left ventricular mass. DCM may occur at any age, but is most common between the ages of 20 and 50 years old. 25-35% of patients that present with DCM have a genetically inherited form of the disease, but there is also a host of non-genetic causes including myocardial ischaemia, viral infections, excessive alcohol consumption, valvular heart disease and hypertension.

At least 50 genes have been linked to causing familial DCM, including numerous mutations in sarcomere genes [6]. Sarcomeres are the basic unit of all muscles. In striated muscle tissue, such as skeletal and cardiac muscle, long myofibrils are formed from repeating sarcomeres. The myofibrils are composed of myosin and actin protein filaments which slide past one another during muscle contraction. Muscle fibres can be categorised based on their 'twitch' capabilities: they are classified as either slow- or fast-twitch fibres depending on their speed of contraction [7]. Fast-twitch fibres contract quickly, but fatigue more easily, whereas slow-twitch fibres have slower contractility but greater endurance. In all muscles, there is a balance between the number of fast- and slow- twitch muscle fibres required for normal function. In the heart, an imbalance in the proportions of these muscle fibres can lead to cardiomyopathy.

Recently, Risebro et al. (2009) demonstrated that the protein Prospero-related homeobox factor 1 (Prox1) is essential for healthy cardiac function and that Prox1 inactivation leads to irregular sarcomere formation and myofibril disarray [8]. Following this study, the same group wanted to probe the exact mechanisms of sarcomere disruption underlying loss of Prox1. In 2014, Petchey et al. demonstrated that Prox1 represses troponin T3, troponin I2 and myosin light chain 1 gene expression, and that the absence of Prox1 causes a switch from the formation of slow- to fast-twitch myofibrils in the heart, which ultimately results in a DCM phenotype [9].

As part of the Petchey et al. (2014) study [9], I imaged adult Prox1-deficient mutant mice *in vivo* to provide functional evidence of a DCM phenotype and to investigate whether it was

caused by myocardial deficiencies associated with the gene knockout rather than structural abnormalities such as aortic stenosis. Preliminary studies had also shown the possibility of intracardiac thrombus formation, which were also visualised using MRI. Three cohorts of mice, including a control cohort, Prox1-deficient mutants at 6-weeks old and Prox1-deficient mutants at 8-weeks old were imaged using CINE imaging for assessment of cardiac function and late gadolinium-enhanced inversion recovery (LGE IR) for thrombus detection.

4.2.2 Methods

Animal strains and cohorts: The mouse strains used for generating mutant mice are described fully in [10, 11]. In short, three cohorts of adult mice were imaged: a six-week old control group (n = 6), a six-week old Prox1-deficient mutant group (n = 6) and an eight-week old Prox1-deficient mutant group (n = 2).

Imaging preparation: All imaging was performed according to the mouse imaging protocol described in section 2.8.1. Briefly, mice were induced and anesthetised with 4% and 1.5-2.0% isoflurane in 2 l/min O_2, respectively. Mice were positioned supine in a cradle which could be positioned in the middle of the scanner bore. Temperature was monitored and maintained at physiological temperature. Respiration was monitored using a neonatal apnea pad and ECG was monitored using three ECG electrodes inserted subcutaneously. For thrombus visualisation experiments, an infusion line was inserted intraperitoneally for injection of gadolinium contrast agent. All imaging was conducted using 1000mT/m gradient inserts and a 39mm volume RF coil (RAPID).

CINE imaging: CINE imaging was conducted according to the protocol outlined in section 2.7.1. Long-axis and short-axis images of the heart were obtained, including full short-axis CINE stacks (9-12 slices). Imaging parameters for all CINE scans were: TR = 5 ms, TE = 1.21 ms, FA = 15°, data matrix = 128^2 (zerofilled to 256^2), FOV = 25.6mm^2, slice thickness = 1mm. Cardiac functional and structural parameters (EF, EDV, ESV, SV, LVM) were analysed using Segment, as described in section 2.7.2. LVM measurements were normalised to mouse mass. The degree of left ventricular remodelling was assessed by calculation of relative wall mass (LVM/EDV), according to Nahrendorf et al.[12].

Late-gadolinium inversion recovery imaging: Long-axis and short-axis images of the heart were obtained using LGE IR imaging, which was conducted according to the protocol outlined in section 2.7.3 [13]. In brief, 0.6 mmol/kg Gd-DTPA was injected intraperitoneally. After an 8 minute delay to allow contrast agent to wash out of healthy

tissue, an IR gradient echo sequence was used for high SNR between the blood pool and thrombi. Imaging parameters were: TR = 3.1ms, TE = 1.21ms, FA = 90°, TI = ~4 x RR-interval (~400ms), data matrix = 128^2 (zerofilled to 256^2), FOV = 25.6mm^2, slice thickness = 1mm.

Aortic stenosis analysis: Four measurements of aortic diameter (in pixels) were made using short-axis CINE images located at the base of the aorta for consistency. Pixel measurements were converted to mm based on a resolution of 100μm/px. The mean aortic diameter was calculated from the average of the four measurements for cohort comparisons.

Statistics: Mann-Whitney-U tests were performed to test for significance between measurements of cardiac parameters in control and mutant mice. Statistical significance was assigned at $p < 0.05$.

4.2.3 Results

CINE imaging: Visual inspection of Prox1-deficient mutant mice showed marked ventricular dilation and atrial dilation in both the 6-week old (Figure 4.1c and Figure 4.1d) and 8-week old cohorts (Figure 4.1e and Figure 4.1f) compared to control mice. Mutant mouse hearts grew progressively larger with time. CINE movies showed abnormal blood flow patterns – particularly in the left ventricle – in the mutant mice visualised as distinct regions of turbulent hypointensity (red arrows, Figure 4.1d).

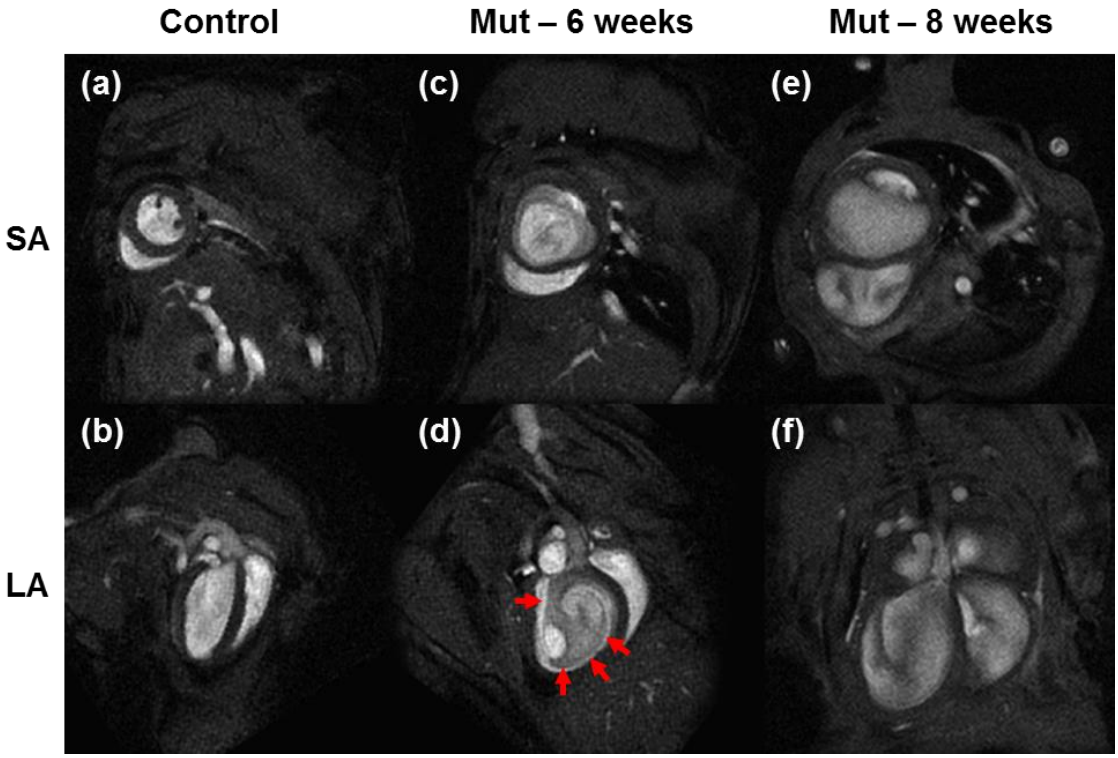

Figure 4.1: Short axis and long axis CINE frames at end diastole from (a-b) a control mouse, (c-d) a 6-week old Prox1 mutant mouse and (e-f) an 8-week old Prox1 mutant mouse. At 6 weeks, the mutant mice exhibit atrial and ventricular dilatation. At 8 weeks, the hearts have grown even further. Abnormal flow patterns can be observed in the mutant hearts, particularly in the long-axis views (red arrows).

Cardiac parameters including EF, EDV, ESV, SV, LVM and LVM/EDV were assessed by segmentation of the CINE images (Figure 4.2 and Table 4.2). EF and SV were significantly reduced in the 6-week old cohort of mutant mice ($p = 0.002$ and $p = 0.02$, respectively) indicating marked impairment of cardiac contractility. Mean EF in the mutant 6-week old cohort was 27.8 ± 6.2%, well below the 40% threshold of DCM. Both EDV and ESV were significantly increased in the mutants compared to control animals ($p = 0.009$ and $p = 0.002$, respectively), reflecting ventricular dilation. LVM was also significantly larger in mutants than control animals reflecting myocardial hypertrophy ($p = 0.004$). LVM/EDV was significantly lower in the mutant animals, decreasing from 1.44 ± 0.05 mg/µl in the control animals to 1.11 ± 0.08 mg/µl in the mutants ($p = 0.008$), in keeping with both left ventricle dilatation and hypertrophy.

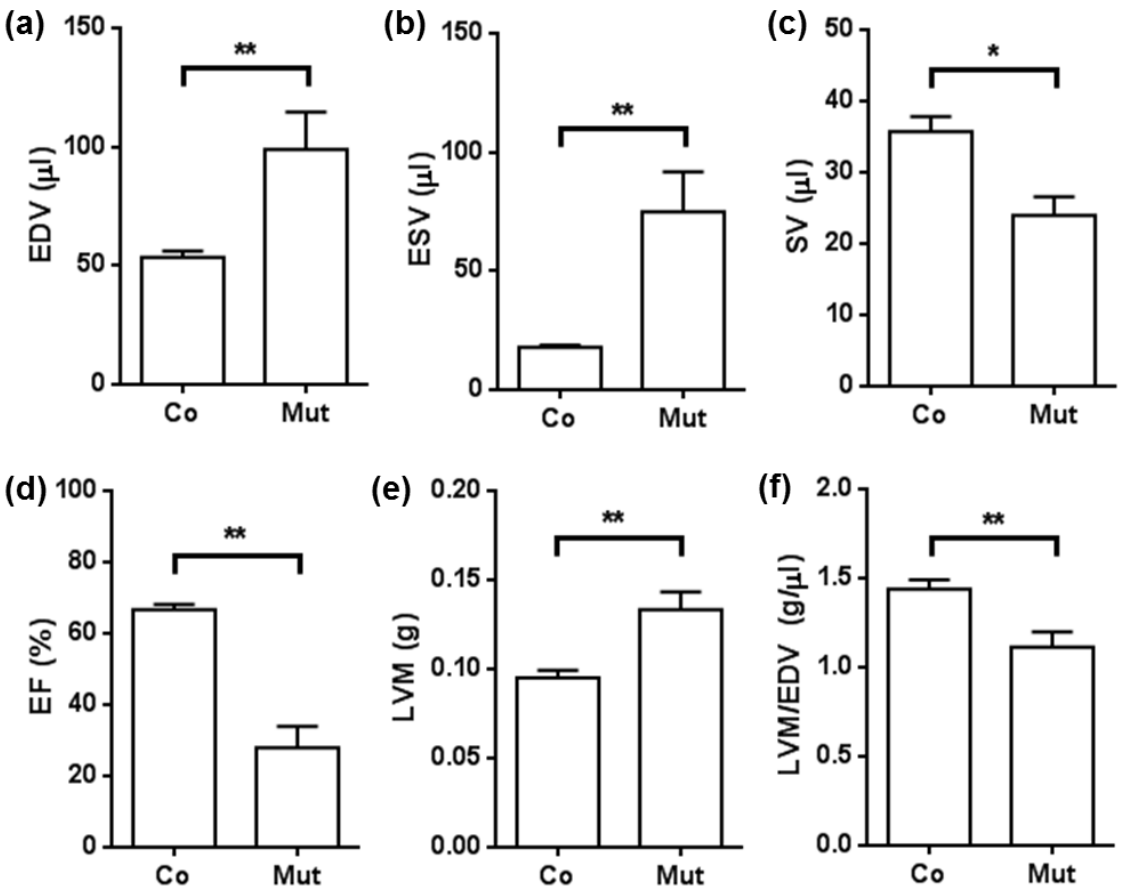

*Figure 4.2: Measurements of cardiac function and structure in control mice and the 6-week old cohort determined by CINE segmentation of the left ventricle. All differences tested using Mann-Whitney-U statistics: *p < 0.05, **p< 0.01.*

	Control	**Mutant – 6 weeks**
n	6	6
EDV (µl)	53.5 ± 2.7	99.0 ± 15.6
ESV (µl)	17.8 ± 1.0	75.0 ± 16.7
SV (µl)	35.7 ± 2.1	24.0 ± 2.6
EF (%)	66.6 ± 1.5	27.8 ± 6.2
LVM (g)	0.095 ± 0.004	0.133 ± 0.010
LVM/EDV (mg/µl)	1.44 ± 0.05	1.11 ± 0.08

Table 4.2: Measurements of cardiac function and structure determined by CINE segmentation of the left ventricle in the control and 6-week old mutant cohorts. Values represent mean ± SEM.

Late gadolinium-enhanced imaging: LGE IR imaging improved visualisation of left ventricular dilation in the mutant mice compared to CINE images because of superior contrast between the nulled myocardium and hyperintense blood pool (Figure 4.3b and Figure 4.3c). Short-axis LGE IR images (not shown) were inspected for signs of diffuse signal hyperintensity indicative of mid wall fibrosis, however, little evidence was observed in either the control or mutant cohorts. The primary purpose for running the LGE IR sequence was thrombus visualisation. Thrombi were not detected in control mice or 6-week old mutant mice. However, a region of hypointensity corresponding to a large thrombus was observed in the right atrium of one 8-week old mutant mouse, pictured in Figure 4.3c. The thrombus was not readily visible with CINE imaging in the same mouse, with the same slice orientation (Figure 4.1f).

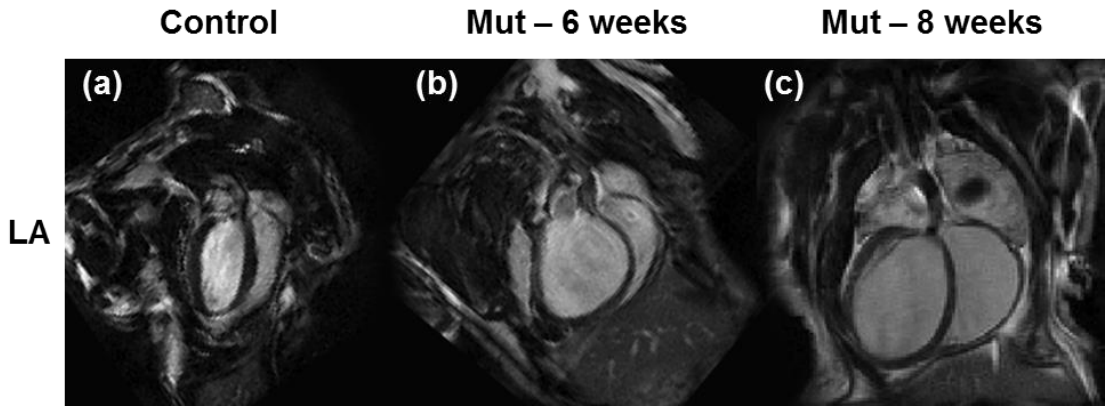

Figure 4.3: Long axis late gadolinium-enhanced inversion recovery images from (a) a control mouse, (b) a 6-week old mutant mouse and (c) an 8-week old Prox1 mutant mouse. The addition of contrast agent enables the visualisation of a large thrombus in the right atrium of the 8-week old mutant, which was not previously visible using a standard CINE sequence.

Aortic stenosis analysis: To determine whether aortic stenosis, rather than the genetic ablation, may have caused the reduction in cardiac function, the diameter of the aorta was examined in the 6-week old cohort. There was no significant difference in the aortic diameter of the control and 6-week old Prox1 mutant mice ($p = 0.31$) based on analysis of short-axis CINE slices located at the base of the aorta (Figure 4.4).

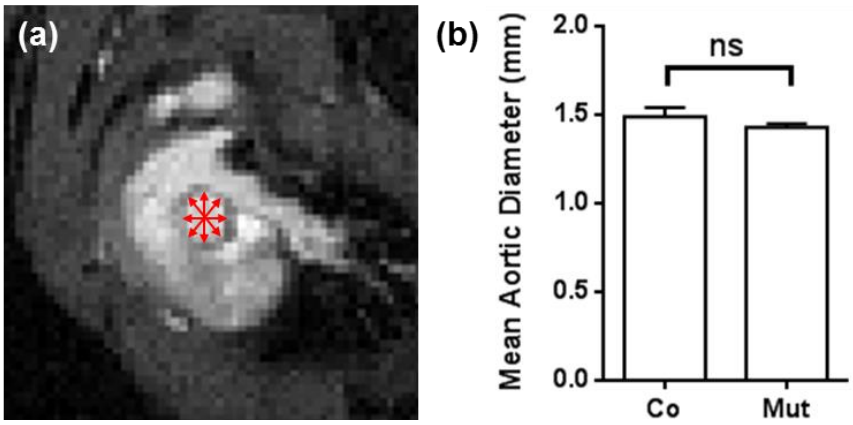

Figure 4.4: Measuring aortic diameter for evidence of aortic stenosis. (a) Diameter was measured at four locations in the aorta (red arrows) of every mouse using a short axis view of the heart. (b) The mean aortic diameter (+ SEM) was non-significantly different between the control and mutant mouse groups (p = 0.31, MWU), indicating no evidence of aortic stenosis.

4.2.4 Discussion

Prox1 plays an essential role in the development of a normal heart by regulating fast-twitch gene expression within the sarcomeres of the cardiac muscle. In the absence of Prox1, normal cardiac muscle structure and growth is severely disrupted. The primary aim of this study was to measure *in vivo* cardiac function in a Prox1 mutant mouse model and to demonstrate the presentation of a DCM phenotype.

CINE and LGE IR imaging of the mutant mice indicated severe left ventricular chamber dilation and increased myocardial mass, consistent with eccentric hypertrophy. This observation was validated by assessment of cardiac function in control, 6-week and 8-week old mutant mice. 6-week old mutant mice exhibited severe cardiac impairment in the form of greatly reduced EF, well below the 40% threshold indicative of DCM. EDV increased by 85% indicating severe left ventricle dilation and LVM increased by 40% indicating LV hypertrophy. Although only two mutant mice were observed at the 8-week timepoint (due to phenotype lethality and death upon anaesthetic inducement), it was clear from visual inspection of the images that the degree of eccentric hypertrophy was even more pronounced.

LGE IR imaging of one mutant mouse from the 8-week old cohort revealed the presence of a very large atrial thrombus, once again consistent with DCM [4]. The thrombus was dark against the hyperintense, gadolinium-enhanced blood pool. This pattern of contrast was likely caused by the inability of gadolinium to accumulate in the avascular thrombus, which has also been observed in images from patients [14]. Considering the size of the thrombus, it

is perhaps surprising that detection was not possible in the standard CINE images. This may be due to a combination of flow artefacts masking the presence of the thrombus and similar T2* times between the blood pool and thrombus. Whereas, the T1 times between the regions are much different in the presence of gadolinium, hence there is contrast in the inversion recovery image, but not the CINE image. This experiment demonstrated the added utility of administering gadolinium contrast agent beyond its most conventional use of visualising scarring following myocardial infarction. Unfortunately, histology was not performed on the thrombotic heart, however, separate histological experiments carried out in 8-week, 12-week and 14-week old Prox1-deficient mutant mice also revealed thrombi in the left ventricle and the atria [9], reinforcing the MRI finding. Thrombi were not detected using LGE IR MRI in the 6-week old cohort, either because the blood clots had not formed at this timepoint, or because only small mural thrombi were present, which were isointense with the myocardium.

Finally, the aortic diameter was measured in all control and 6-week old mutant mice. No significant difference was measured, providing supporting evidence that the DCM phenotype was caused by muscular abnormalities rather than aortic stenosis, which is also known to cause DCM.

In summary, the Prox1 knockout mouse model used in this study has a clear and very severe DCM phenotype, as demonstrated by CINE and LGE IR MRI. The onset of DCM and manifestation of DCM in this mouse model shares many hallmarks with the human condition including dilated cardiac chambers, myocardial hypertrophy, thrombus and impaired cardiac function. This mouse model may be of significant value in future prognostic studies of DCM. Furthermore, the imaging carried out in this study demonstrates the validity of using these techniques to follow disease progression and response to therapy.

4.3 Study 2 – Imaging the area-at-risk in myocardial infarction with multi-parametric MRI

4.3.1 Introduction

Coronary heart disease (CHD) is the leading cause of death worldwide. In 2012, 7.4 million deaths were associated with CHD across the globe [15]. In ischaemic CHD, atherosclerosis leads to the blockage of the coronary arteries resulting in myocardial infarction. The region of myocardial tissue normally perfused by the affected coronary artery, known as the area-at-risk (AAR), experiences hypoxia, ATP generation falls and gradually cell death sweeps through the cells of the myocardium [16].

The extent of irreversible cell death within the AAR is determined by the duration of ischaemia in a process known as the "wavefront concept" [16]. In the absence of reperfusion, the entire AAR will evolve into necrotic tissue. However, with reperfusion – following therapeutic intervention, for example – blood flow is restored to the occluded vessel and a proportion of the AAR may be salvaged. The extent of myocardial salvage depends on a host of factors including the duration of ischaemia to reperfusion, amount of tissue perfusion from collateral vessels and reperfusion injury following restoration of blood flow [17].

Accurate visualisation and quantification of AAR size in patients is an ongoing area of research [18-21]. The extent of myocardial salvage is an important determinant of final infarct size, therefore, quantitative assessment of AAR offers great potential for the development of therapeutics targeted at reducing ischaemic damage [22, 23].

Currently, the most widely used method for assessing AAR in the clinic is single-photon emission tomography (SPECT) imaging of technetium (Tc99m) [18, 19, 24]. However, SPECT requires the injection of a radiotracer before reperfusion therapy can be performed, which is suboptimal for patient recovery, as reperfusion therapy needs to be conducted as quickly as possible. An alternative method for measuring AAR is by calculating the Bypass Angioplasty Revascularization Investigation Myocardial Jeopardy Index (BARI score) using angiography [25, 26]. However, this method does not directly measure the size of the AAR, instead, the lengths and calibre of the coronary arteries are scored and a percentage is calculated as a proxy for AAR size [27]. More recently, T2-weighted (T2w) MRI has emerged as a viable alternative [28-30] for assessing AAR in patients who have already undergone reperfusion therapy. During the acute phase of myocardial infarction, cellular oedema causes increased T2 signal, which can be used to retrospectively quantify the size of

the AAR several days after reperfusion therapy. T2w-imaging has been carried out in mouse models of myocardial ischaemia [31], but it is an inherently low SNR technique requiring long echo times to produce oedema contrast. T2-mapping has emerged as an alternative to T2w-imaging in clinical studies [32, 33], as it circumvents issues of low signal through quantification of absolute T2 values. But, currently only one small T2-mapping study exists in an animal model of myocardial infarction [34].

In this study, a T2-mapping sequence was used to assess the size of the AAR in the myocardium of mice which underwent myocardial ischaemia reperfusion surgery 72 hours prior to imaging. Infarct size (IS) was also assessed using the late-gadolinium enhanced inversion recovery (LGE IR) sequence [13] described in section 2.7.3. Together, these two measures were used to quantify the volumetric extent of irreversibly damaged myocardium and potentially salvageable tissue. In addition, myocardial perfusion in the AAR was also quantified for comparison using a multi-slice arterial spin labelling (ASL) technique recently developed in CABI [35, 36]. To establish the accuracy of the multi-parametric MRI, images were compared with gold-standard histological assessment of AAR and infarct size.

The work in this study was highly collaborative, conducted in partnership with Dr. Rachel Dongworth, who carried out the animal surgery, histology and histological analysis, and Dr Adrienne Campbell-Washburn, who created the T2-mapping and ASL sequences [35, 36], as well as carrying out some of the imaging and much of the data analysis. I contributed to the study by carrying out large amounts of imaging, parts of the data analysis, as well as presenting the work at various conferences.

In summary, the aim of the present study was to assess and quantify AAR in a reperfused experimental mouse model of myocardial infarction using multi-parametric MRI, including T2-mapping, ASL and LGE IR and compare with gold-standard histological staining of excised hearts.

4.3.2 Methods

Study design: B6Sv129 mice (n = 6) underwent myocardial ischaemia reperfusion surgery, as described in section 1.2.9. All surgery was carried out by Dr Rachel Dongworth. In brief, mice were anaesthetised with 2% isoflurane in 1.5 l/min oxygen. Animals were positioned supine on a heated operating table to maintain physiological body temperature. ECG was monitored with subcutaneous electrodes. Artificial respiration was provided by a ventilator. Open-chest surgery was performed to gain access to the heart. The lower anterior descending

(LAD) artery was identified and a suture was placed under the vessel approximately 2mm below the tip of the left atrium. A custom-made snare system was used to occlude the LAD for 30 minutes, after which the snare was released to allow for reperfusion of the myocardium. The snare system was removed, but the suture was left in place for re-occlusion later on during histology. The chest cavity was closed and the animal was recovered. 72 hours after surgery, mice were imaged using the following MRI sequences, before histology was performed:

- CINE MRI for slice localisation (20 minutes)
- T2-mapping for assessment of oedema (40 minutes)
- ASL for assessment of perfusion (30 minutes)
- LGE IR for assessment of infarct size (20 minutes)

Imaging preparation: All imaging was performed according to the mouse imaging protocol described in section 2.8.1. Briefly, mice were induced and anesthetised with 4% and 1.5-2.0% isoflurane in 2 l/min O_2, respectively. Mice were positioned supine in a cradle which could be positioned in the middle of the scanner bore. Temperature was monitored and maintained at physiological temperature. Respiration was monitored using a neonatal apnea pad and ECG was monitored using three ECG electrodes inserted subcutaneously. For late gadolinium enhancement experiments, an infusion line was inserted intraperitoneally for injection of contrast agent. All imaging was conducted using 1000mT/m gradient inserts and a 35mm volume RF coil (RAPID).

T2-mapping: The T2-mapping protocol was designed by Dr. Adrienne Campbell-Washburn. A standard spin echo sequence was modified to be both cardiac- and respiration-gated, as illustrated in Figure 4.5. For each respiration trigger, the sequence acquired one line of k-space per ECG event in a total of 7 different slices. Therefore, the respiration of the animal was maintained below 60 bpm to ensure there was enough time to acquire one phase encoding line for each slice. The sequence was run with 8 different TE values ranging from 3.5 to 30ms. The sequence parameters were: TR = respiration interval, TE = 3.5, 7, 10, 12, 15, 17, 20, 25 and 30ms, matrix size = 128mm^2, slice thickness = 1mm, FOV = 25.6mm^2.

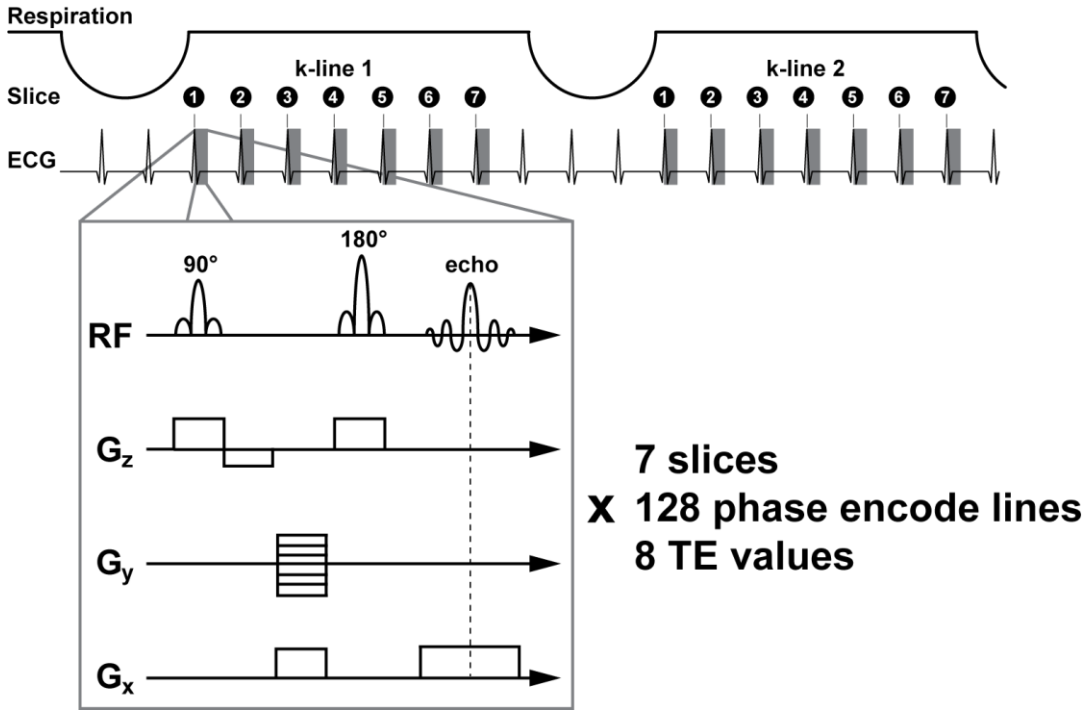

Figure 4.5: Doubled-gated T2-mapping pulse sequence diagram. The T2-mapping sequence is based on a spin echo readout. When the respiration window opens, the pulse sequence is triggered by the next seven ECG R-waves. For each R-wave, a single line of k-space for each slice is obtained at the current TE value. The sequence is repeated for multiple TE values to construct a T2-map.

T2 maps were generated by fitting the signal in each pixel from each of the 8 TE images to the following model of T2 decay:

$$S(t) = S_0 e^{-TE/T2} \qquad \textbf{EQ 4.1}$$

where *S(t)* is the signal at time *t*, S_0 is the signal at equilibrium, *TE* is the echo time and *T2* is the T2 value of the pixel.

To determine which pixels in the T2 maps of the myocardium corresponded to oedematous tissue, a threshold was determined to classify tissue with elevated T2, as in [34]. The T2 value of normal tissue was calculated by averaging over an ROI drawn in the septal region of the myocardium in the most basal slice, as this region of the heart was assumed to be unaffected following surgery. Based on this, the threshold for elevated T2 values, $T2_e$, was defined as:

$$T2_e = mean\left(T2_{septal}\right) + (1 \times SD) \qquad \textbf{EQ 4.2}$$

Finally, the total size of the AAR as a percentage of LV volume was calculated according to:

$$T2_e/LV(\%) = \frac{number\ of\ T2_e\ pixels}{number\ of\ pixels\ in\ LV} \qquad \textbf{EQ 4.3}$$

Perfusion mapping: Perfusion mapping was performed using a multi-slice ASL sequence designed by Adrienne Campbell-Washburn [35, 36], as illustrated in Figure 4.6. The sequence uses a doubled-gated Look-Locker T1 mapping technique [37] following a 180° inversion pulse to gradually build up a series of images at different inversion times during the course of T1 recovery. T1 mapping begins with a 180° inversion pulse triggered to occur at the start of the first quiescent respiration phase. Following this, T1 recovery is sampled in the following 50 heart beats. With each ECG trigger, 4 lines of k-space are acquired in 3 different slices using gradient echo readouts. The entire sequence is repeated (or segmented) 32 times to produce an entire dataset consisting of 50 images throughout the course of T1 recovery.

To measure perfusion in a single slice, the sequence is run twice using a flow alternating inversion recovery (FAIR) technique [38], first with a global 180° inversion pulse and then with a slice selective 180° inversion pulse centred on, but slightly wider than the imaging plane (Figure 4.7). With the global inversion pulse, both the in-plane myocardium and inflowing blood are inverted, and both recover according to T1 relaxation. With the slice selective inversion pulse, the in-plane myocardium is inverted, but any inflowing blood which originated from outside of the inversion slab is assumed to be completely relaxed. This has the net effect of causing accelerated T1 relaxation of myocardium in the imaging plane. Hence, the difference between the global and slice selective T1 recovery curves gives an estimation of perfusion.

For multi-slice acquisition, the sequence is modified to include a larger slice-selective inversion slab, which is required to measure T1 in each slice. However, moving to a larger slice-selective pulse causes more of the blood in the heart and lungs to be inverted. As a result, some of the blood pumped through the coronary arteries into the myocardium now retains a significant amount of magnetisation – compared to single-slice ASL – such that there is an underestimation in T1 relaxation times. To correct for this, the magnetisation of the LV blood pool is measured and accounted for in a method known as the bpMBF quantification method, described in [36].

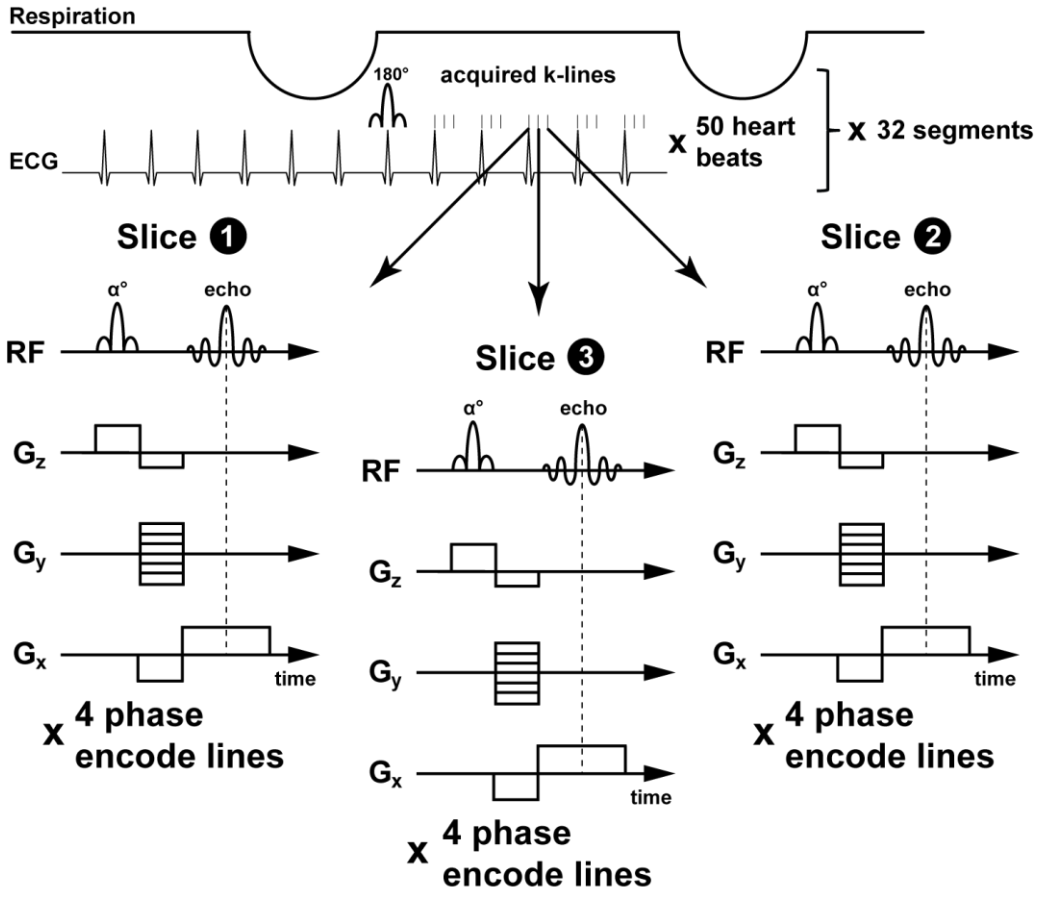

Figure 4.6: Multi-slice perfusion mapping ASL pulse sequence diagram. A 180° inversion pulse is triggered to occur on the first R-wave after a breath. The myocardium recovers with T1 relaxation during which time a multi-slice, ECG-gated Look-Locker readout is acquired. 12 lines of k-space are acquired for each heart beat, 4 per slice. The sequence runs for 50 heart beats, approximately 5-6 seconds, allowing time for T1 recovery. The 180° inversion pulse is repeated for each k-space segment. In total, 32 segments are acquired for full k-space coverage at every timepoint in the T1 recovery curve.

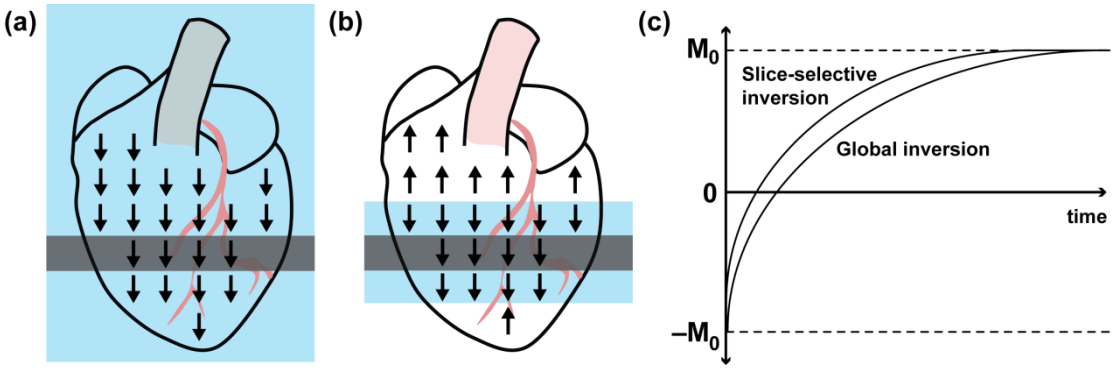

Figure 4.7: Single-slice FAIR ASL in the mouse heart. (a) A global inversion pulse (blue) inverts all blood in the heart. Blood entering the in-plane myocardium (grey) relaxes according to the T1 of blood. (b) A slice-selective pulse inverts the in-plane myocardium, but not the inflowing blood which remains at equilibrium magnetisation. (c) Therefore, the non-inverted blood accelerates T1 recovery. The difference between the two T1 recovery curves gives an estimate of myocardial tissue perfusion.

The ASL sequence was performed with the following parameters: TR(180°) = 13.5s, recovery delay = 8s, TR(RF) = 3ms, TE = 1.18ms, flip angle = 5°, matrix size = 128mm^2, slice thickness = 1mm, FOV = 25.6mm^2, global inversion slab thickness = 100 × slice thickness, slice selective slab thickness = 3 × slice thickness, timepoints on inversion recovery curve = 50.

Perfusion maps were generated based on the Belle model of myocardial perfusion given in equation 4.4. The full quantification method is described in [36]. In brief, global and slice-selective T1 maps were generated by fitting the signal in each pixel from each of the 50 inversion images to a mono-exponential model of T1 recovery. T1 values were derived from curve fitting to generate an estimate of perfusion based on:

$$MBF = \frac{\lambda}{T1_{blood}}\left(\frac{T1_{global}}{T1_{slice-selective}} - 1\right) \quad \textbf{EQ 4.4}$$

where λ (the blood-tissue partition coefficient of water) = 0.95 ml/g. To determine the perfusion state of pixels in the myocardium a threshold was determined, below which pixels were classified as having a perfusion deficit. Variation in baseline perfusion between animals precluded perfusion deficit calculation using absolute values. The perfusion value of normal tissue was calculated, once again, by averaging over an ROI drawn in the septal region of the myocardium in the most basal slice. Based on this, the threshold for perfusion deficit, MBF_d, was defined as:

$$MBF_d = mean\left(MBF_{septal}\right) - (1 \times SD) \quad \textbf{EQ 4.5}$$

Finally, the total size of the perfusion deficit region as a percentage of LV volume was calculated according to:

$$MBF_d/LV(\%) = \frac{number\ of\ MBF_d\ pixels}{number\ of\ pixels\ in\ LV} \quad \textbf{EQ 4.6}$$

Infarct imaging: Infarct imaging was performed using the LGE IR pulse sequence protocol outlined in section 2.7.3 [13]. In brief, 0.6 mmol/kg Gd-DTPA was injected intraperitoneally. After an 8 minute delay to allow contrast agent to circulate, an IR gradient echo sequence was used for high SNR between the blood pool and infarct tissue. Imaging parameters were: TR = 3.1ms, TE = 1.21ms, FA = 90°, TI = ~4 x RR-interval (~400ms), data matrix = 128^2, FOV = 25.6mm^2, slice thickness = 1mm. 9-11 short-axis images of the heart were obtained.

To determine infarct size, manual segmentation was performed using Segment to delineate the hyperintense scar tissue within the myocardium. The region of late gadolinium enhancement (LGE) as a percentage of LV volume was calculated according to:

$$LGE/LV(\%) = \frac{number\ of\ enhanced\ pixels}{number\ of\ pixels\ in\ LV} \qquad \textbf{EQ 4.7}$$

Histology: Immediately after imaging, animals were anaesthetised with a mixture of ketamine (100mg/kg), xylazine (20 mg/kg) and atropine (0.6 mg/kg) and the heart was excised. The aorta was cannulated and first it was washed with 1 ml saline to remove the residual blood from the coronary system. Next, the heart was stained with 2,3,5-triphenylterazoliumchloride (TTC) to delineate the infarct region. The LAD suture retained during the previous surgery session was tightened to re-occlude the vessel and Evans Blue dye was perfused while the heart was submerged in water (to prevent myocardial surface staining) to delineate the healthy tissue and AAR. Following staining, hearts were stored at -20°C for 1 to 2 days. Frozen hearts were then sliced free-hand through to produce short axis views of the heart. Seven or eight slices were taken from the apex towards the base of the heart. Slices were fixed in 10% formalin for 2 hours, then the right ventricle myocardium was removed and all slices were scanned (Epson Scanner, 1200 dpi).

Histology volume analysis: Quantification of infarct size and AAR was performed using ImageJ. Raw images were split into separate colour channels. The AAR region was delineated by choosing a threshold of pixel intensity within the red channel image which matched the AAR in the raw image. The infarct size (IS) was delineated by choosing a threshold of pixel intensity within the blue channel image which matched the infarcted tissue in the raw image. Excised hearts were sliced to match the MR images as closely as possible, including removing right ventricle myocardium. The number of pixels contained in both the AAR and the infarct region were calculated as a percentage of total the pixels in the slice, across all slices. Hence, final values of AAR/LV(%) and IS/LV(%) are presented in the results section (4.3.3).

Statistics: Mann-Whitney-U tests were performed to test for significance between histological and MRI-based measurements of volume. Statistical significance was assigned at $p < 0.05$. Bland-Altman analysis was used to examine the spread the spread of the data.

4.3.3 Results

A complete representative multi-parametric MRI dataset from a single mouse, alongside the corresponding histological slices is shown in Figure 4.8. Seven slices are shown for each modality, apart from ASL where six slices were obtained. Slice 1 represents the most apical slice in the heart. Slice 7 corresponds to a basal slice 6mm higher than slice 1, located approximately below the mitral valve. Slice locations were maintained between MRI sequences.

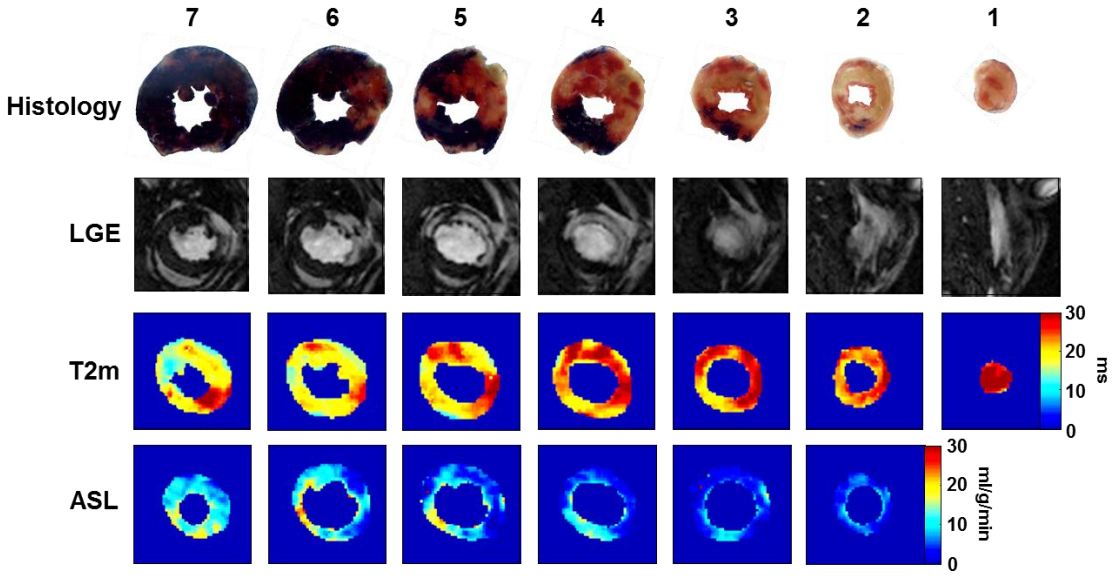

Figure 4.8: Representative multi-parametric MRI and histology dataset of AAR quantification from an infarcted mouse. 7 histology, late gadolinium-enhanced inversion recovery and T2-mapping slices were used for volumetric analysis of AAR and IS. 6 ASL slices were used. TTC and Evans Blue staining of histology shows: dark blue = perfused tissue, red = viable tissue, white = infarcted tissue. Hyperintense regions of myocardium in LGE images show infarcted tissue. Elevated T2-values in T2 maps show the AAR. Perfusion deficit in ASL maps shows another measure of AAR.

The first row in Figure 4.8 shows the histology. The dark blue tissue is stained with Evans Blue, which represents healthy perfused tissue. The red staining corresponds to TTC, which represents ischaemic, but viable tissue within the AAR. The white, unstained tissue is infarcted myocardium. The most basal slices consistently contained the largest proportion of Evans Blue stained, perfused tissue whereas the more apical slices tended to have large regions of infarcted and at-risk tissue. This pattern of infarction was observed through the entire cohort indicating that surgery was successful and consistent. Mean AAR/LV assessed across 7 histology slices was 64.3 ± 6.1%. Mean IS/LV was 32.3 ± 3.7%. On average, the area of salvageable myocardium (100% – IS/AAR) occupied 49.4 ± 6.9% of the area-at-risk.

Infarct regions assessed by LGE IR (Figure 4.8, second row) showed excellent spatial agreement with histology. Hyperintensity in the myocardium closely matched the white, unstained infarct tissue in the histological slices. Mean LGE/LV across 7 slices was 31.7 ± 5.8%, which closely matched IS/LV determined by histology (Figure 4.9a, $p = 0.79$, Mann-Whitney-U).

T2-mapping showed distinct regions of elevated T2 ($T2_e$ > mean septal T2 + 1 SD) which matched the AAR in the histology images. Infarcted tissue was not distinguishable from salvageable tissue using T2 mapping. The mean T2 value of tissue in the 'normal', septal region was 17.9 ± 2.8ms. Regions of elevated T2 increased by approximately 31% to a mean value of 25.8 ± 4.3ms. Mean $T2_e$/LV was 60.4 ± 5.9%, which closely matched AAR/LV determined by histology (Figure 4.9b, $p = 0.24$, Mann-Whitney-U). Based on T2 mapping across 7 slices, the average area of salvageable myocardium (100% – IS/AAR) was determined to be 47.1 ± 11.2% of the area-at-risk, which agreed with histology.

ASL showed very distinct regions of perfusion deficit (MBP_d < mean septal MBF – 1 SD) which also showed excellent spatial agreement with the AAR in histology images. Again, infarcted tissue was not distinguishable from salvageable tissue using perfusion mapping. Mean perfusion in the septal region was 18.2 ± 4.9 ml/g/min. Regions of perfusion deficit decreased by approximately 70% to 5.6 ± 1.5 ml/g/min. Mean MBP_d/LV across 6 slices (rather than 7) was 63.3 ± 9.2%, which closely matched AAR/LV determined by histology (Figure 4.9c, $p = 0.68$, Mann-Whitney-U). Based on perfusion mapping, the average area of salvageable myocardium (100% – IS/AAR) was determined to be 55.1 ± 13.7% of the area-at-risk, which compared to 50.8 ± 5.8% for histology (both analysed across 6 slices).

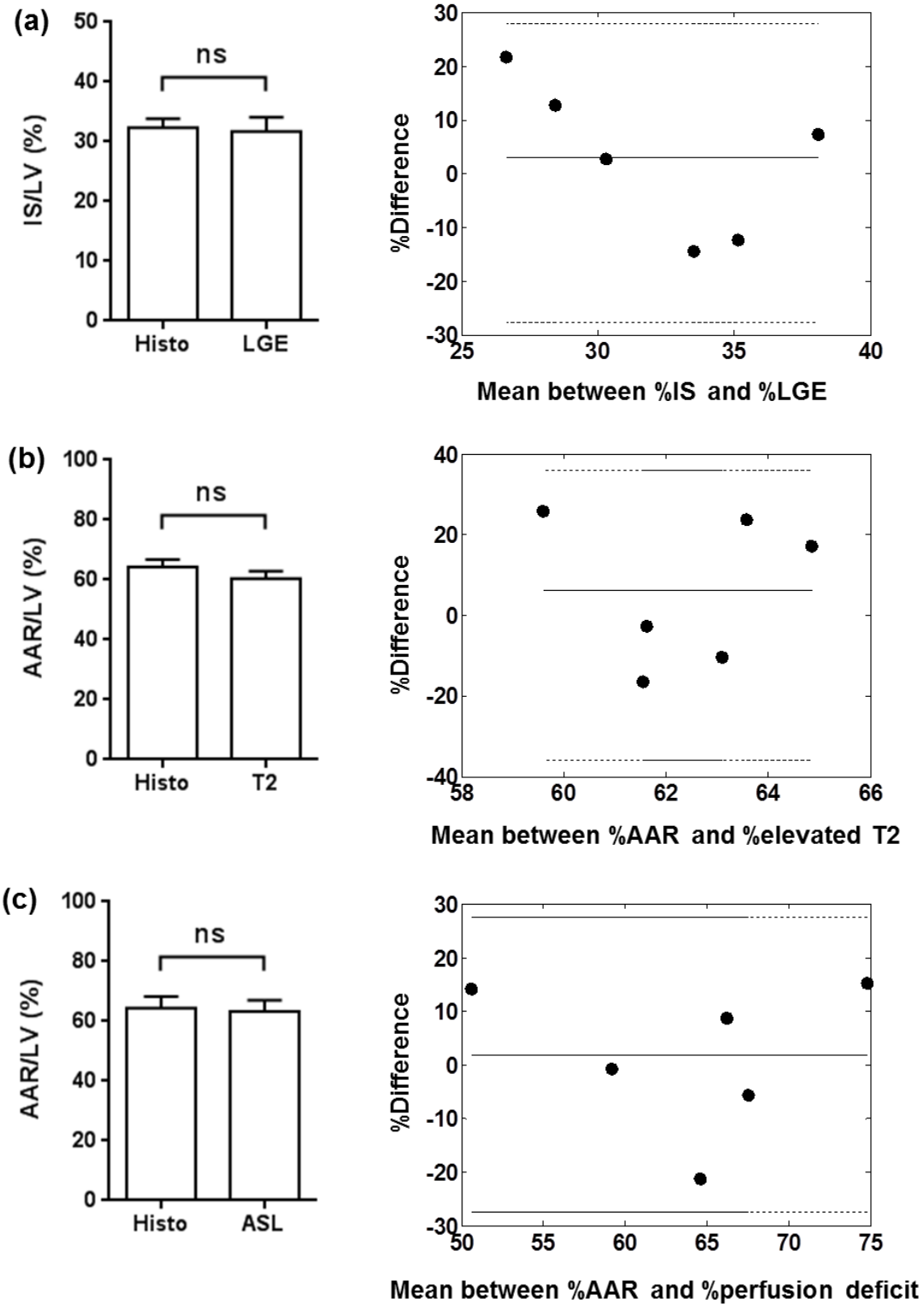

Figure 4.9: Bar charts showing mean infarct size as a percentage of left-ventricle volume (%IS/LV) and area-at-risk values as a percentage of left-ventricle volume (%AAR/LV), and corresponding Bland-Altman plots comparing each MRI sequence with gold-standard histology measurements. (a) Infarct volume assessed by LGE agreed with histology. (b) Elevated regions of T2 matched TTC-stained histological volumes. (c) Perfusion deficit also agreed with TTC-stained histological volumes. All comparisons show no statistical differences (Mann-Whitney-U).

4.3.4 Discussion

There is a clinical need for accurate *in vivo* visualisation and assessment of the AAR following myocardial infarction as the extent of salvageable tissue is an important indicator of final infarct size and it represents a target for therapeutics aimed at reducing ischaemic injury. In this study, the size of the AAR was assessed and quantified in a mouse model of reperfused myocardial infarction, 72 hours post-surgery, using a multi-parametric MRI protocol. The primary aim was to determine how well T2 mapping quantified the size of the AAR, however, perfusion imaging with ASL was also performed. To determine the accuracy of MR-derived regions, gold-standard histology was used for comparison.

Elevated T2 has previously been shown to correspond to myocardial oedema [38-40]. T2-weighted imaging has been used widely in the clinic to measure oedema, but T2-mapping has had little pre-clinical application and potentially offers a more robust alternative, as it is less susceptible to problems of signal variation [33]. The results from this study suggest that T2-mapping can accurately measure the size of the AAR in a reperfused model of myocardial infarction. The average size of the AAR measured using T2-mapping closely matched the AAR using histology. Volumetric subtraction of infarct regions determined the extent of salvageable tissue within the myocardium, which was also in agreement with histology.

Despite the agreement with histology, there were some limitations to the T2-mapping in this study. Firstly, the T2 maps were reconstructed from images up to 30ms after the R-wave. This corresponds to almost one third of a cardiac cycle, meaning that T2 maps were comprised of images at various stages of myocardial contraction. As a result, it is likely that the T2 fits were biased, although across the entire myocardium the fits were still sufficiently accurate that elevated regions of T2 matched the AAR using histology. Another limitation was the necessity for an internal reference point in the septum to determine elevated T2 values. Ideally, absolute T2 values would have been used to determine AAR, however, inter-animal T2 variation meant that normalisation to septal tissue improved comparisons to histology. Intra-animal thresholding is not a definitive solution either though: in this cohort, the mice did not demonstrate elevated T2 in the septum suggesting the tissue was still normal, however, in animals with more extensive infarcts the septum may be damaged too. Furthermore, studies in humans suggest that the remote region in myocardial infarction patients has a slightly higher T2 value than the myocardium in a normal, healthy patient [41]. The uniformity of T2 elevation between the infarct region and AAR was also perhaps surprising. T2 is thought to increase linearly with oedema and water content within infarcted tissue can be as much as 88% compared to 10% in salvageable tissue [42]. Yet, as in many

other studies [31, 34, 39, 40], there was no clear difference in T2 values between infarcted and salvageable tissue in this study – the infarct region was only distinguishable using LGE IR MRI. In fact, this disparity represents a controversial topic within the field as to whether increased T2 represents acute infarction or the AAR [42]. The present study suggests the latter.

Measurements of AAR based on perfusion deficit in the myocardium using ASL also closely matched histological measurements of AAR. This result was surprising because the AAR was not expected to show such extensive perfusion deficit given that a reperfused myocardial infarction mouse model was used. It was expected that the AAR may have reduced perfusion compared to remote tissue, but not reduced to the extent of the infarcted tissue. Instead the perfusion deficit was indistinguishable between salvageable and infarcted tissue. Two possible explanations for this observation are that some of the myocardium within the AAR may have entered a hibernating state [43] resulting in reduced demand for oxygen, or that some of the blood vessels within the AAR – and not just the infarct region – were damaged following ischaemia, enhancing the perfusion reduction. There is also the possibility that surgery was simply incorrect and reperfusion did not occur, however, this seems unlikely as previous surgeries where permanent coronary occlusions were carried out by Dr Rachel Dongworth demonstrated extensive transmural infarction, with minimal viable tissue within the AAR, following TTC staining.

Overall, the results in this study show that both T2 mapping and ASL can be used to measure the extent of AAR in a mouse model of reperfused myocardial infarction and, when used in conjunction with LGE IR MRI, the area of salvageable tissue can be quantified. This multi-parametric approach has the potential to be highly valuable for developing and assessing the efficacy of therapies targeted at reducing ischaemic injury.

4.4 Overall Discussion

This chapter has demonstrated the broad utility of cardiac MRI and the wealth of information that can be obtained using a selection of different pulse sequences. A Prox1-deficient mouse model was imaged using CINE MRI for functional analysis and LGE IR MRI for thrombus visualisation, and shown to exhibit a severe DCM phenotype, which may offer significant value for future prognostic studies of DCM. In the second study, LGE IR MRI, T2-mapping and ASL, were used for the *in vivo* assessment of area-at-risk following myocardial infarction, which compared favourably with gold-standard histological staining. The imaging methods applied in this chapter enable thorough characterisation of animal models of human CVD and enable the efficacy of novel cardioprotective therapies to be assessed.

4.5 References

1. Gadian D, et al. *Phosphorus nuclear magnetic resonance studies on normoxic and ischemic cardiac tissue.* Proceedings of the National Academy of Sciences, 1976. **73**(12): p. 4446-4448.

2. Jacobus WE, et al. *Phosphorus nuclear magnetic resonance of perfused working rat hearts.* Nature, 1977. 24;**265**(5596): p. 756-8.

3. Pohost GM, *The history of cardiovascular magnetic resonance.* JACC: Cardiovascular Imaging, 2008. **1**(5): p. 672-678.

4. Luk A, et al. *Dilated cardiomyopathy: a review.* Journal of Clinical Pathology, 2009. **62**(3): p. 219-225.

5. Jefferies JL and Towbin JA. *Dilated cardiomyopathy.* The Lancet, 2010. **375**(9716): p. 752-762.

6. McNally EM, Golbus JR and Puckelwartz MR. *Genetic mutations and mechanisms in dilated cardiomyopathy.* The Journal of Clinical Investigation, 2013. **123**(1): p. 19-26.

7. Eberstein A and Goodgold J. *Slow and fast twitch fibers in human skeletal muscle.* American Journal of Physiology, 1968. **215**(3): p. 535-541.

8. Risebro CA, et al. *Prox1 maintains muscle structure and growth in the developing heart.* Development, 2009. **136**(3): p. 495-505.

9. Petchey LK, et al. *Loss of Prox1 in striated muscle causes slow to fast skeletal muscle fiber conversion and dilated cardiomyopathy.* Proceedings of the National Academy of Sciences, 2014. **111**(26): p. 9515-9520.

10. Harvey NL, et al. *Lymphatic vascular defects promoted by Prox1 haploinsufficiency cause adult-onset obesity.* Nature Genetics, 2005. **37**(10): p. 1072-1081.

11. Moses KA, et al. *Embryonic expression of an Nkx2-5/Cre gene using ROSA26 reporter mice.* Genesis, 2001. **31**(4): p. 176-180.

12. Nahrendorf M, et al. *Serial cine-magnetic resonance imaging of left ventricular remodeling after myocardial infarction in rats.* Journal of Magnetic Resonance Imaging, 2001. **14**(5): p. 547-555.

13. Price AN, et al. *Rapid assessment of myocardial infarct size in rodents using multi-slice inversion recovery late gadolinium enhancement CMR at 9.4 T.* Journal of Cardiovascular Magnetic Resonance, 2011. **13**(1): p. 1-9.

14. Weinsaft JW, et al. *Detection of left ventricular thrombus by delayed-enhancement cardiovascular magnetic resonance: prevalence and markers in patients with systolic dysfunction.* Journal of the American College of Cardiology, 2008. **52**(2): p. 148-157.

15. World Health Organization. *Fact File No. 310: The top 10 causes of death*. August 2014.

16. Reimer KA, et al. *The wavefront phenomenon of ischemic cell death. 1. Myocardial infarct size vs duration of coronary occlusion in dogs.* Circulation, 1977. **56**(5): p. 786-794.

17. Rochitte CE and Azevedo CF. *The myocardial area at risk.* Heart, 2011: p. heartjnl-2011-301332.

18. Gibbons RJ, et al. *Myocardium at risk and infarct size after thrombolytic therapy for acute myocardial infarction: implications for the design of randomized trials of acute intervention.* Journal of the American College of Cardiology, 1994. **24**(3): p. 616-623.

19. Gibbons RJ, et al. *The quantification of infarct size.* Journal of the American College of Cardiology, 2004. **44**(8): p. 1533-1542.

20. Bissing JW, Ryan AJ and Kerber RE. *Coronary risk area measurement by intracardiac echocardiography and ultrasound contrast.* Journal of the American Society of Echocardiography, 2001. **14**(7): p. 706-711.

21. Stéphane Lafitte S, et al. *Contrast echocardiography can assess risk area and infarct size during coronary occlusion and reperfusion: experimental validation.* Journal of the American College of Cardiology, 2002. **39**(9): p. 1546-1554.

22. Kaltoft A, et al. *Routine Thrombectomy in Percutaneous Coronary Intervention for Acute ST-Segment–Elevation Myocardial Infarction A Randomized, Controlled Trial*. Circulation, 2006. **114**(1): p. 40-47.

23. Levine GN, et al. *2011 ACCF/AHA/SCAI Guideline for Percutaneous Coronary Intervention: a report of the American College of Cardiology Foundation/American Heart Association Task Force on Practice Guidelines and the Society for Cardiovascular Angiography and Interventions.* Circulation, 2011. **124**(23): p. e574.

24. Hadamitzky M, et al. *The assessment of area at risk and myocardial salvage after coronary revascularization in acute myocardial infarction: comparison between CMR and SPECT*. JACC: Cardiovascular Imaging, 2013. **6**(3): p. 358-369.

25. Alderman EL and Stadius M. *The angiographie definitions of the bypass angioplasty revascularization investigation.* Coronary Artery Disease, 1992. **3**(12): p. 1189-1208.

26. Wright J, et al. *Quantification of myocardial area at risk with T2-weighted CMR: comparison with contrast-enhanced CMR and coronary angiography.* JACC: Cardiovascular Imaging, 2009. **2**(7): p. 825-831.

27. Moral S, et al. *Quantification of myocardial area at risk: validation of coronary angiographic scores with cardiovascular magnetic resonance methods.* Revista Española de Cardiología (English Edition), 2012. **65**(11): p. 1010-1017.

28. Lønborg J, et al. *Myocardial area at risk and salvage measured by T2-weighted cardiovascular magnetic resonance: Reproducibility and comparison of two T2-weighted protocols.* Journal of Cardiovascular Magnetic Resonance, 2011. **13**(1): p. 1-9.

29. Amano Y, et al. *T2-weighted cardiac magnetic resonance imaging of edema in myocardial diseases.* The Scientific World Journal, 2012. **2012**.

30. Eitel I and Friedrich MG. *T2-weighted cardiovascular magnetic resonance in acute cardiac disease.* J Cardiovasc Magn Reson, 2011. **13**(1): p. 13.

31. Beyers RJ, et al. *T2-weighted MRI of post-infarct myocardial edema in mice.* Magnetic Resonance in Medicine, 2012. **67**(1): p. 201-209.

32. Giri S, et al. *Journal of Cardiovascular Magnetic Resonance.* Journal of Cardiovascular Magnetic Resonance, 2009. **11**: p. 56.

33. Verhaert D, et al. *Direct T2 quantification of myocardial edema in acute ischemic injury.* JACC: Cardiovascular Imaging, 2011. **4**(3): p. 269-278.

34. Bohl S, et al. *T2-mapping of ischaemia/reperfusion-injury in the in vivo mouse heart*. in *13th Annual SCMR Scientific Sessions*. 2010.

35. Campbell-Washburn AE, et al. *Cardiac arterial spin labeling using segmented ECG-gated Look-Locker FAIR: Variability and repeatability in preclinical studies.* Magnetic Resonance in Medicine, 2013. **69**(1): p. 238-247.

36. Campbell-Washburn AE, et al. *Multislice cardiac arterial spin labeling using improved myocardial perfusion quantification with simultaneously measured blood pool input function.* Magnetic Resonance in Medicine, 2013. **70**(4): p. 1125-1136.

37. Kober F, et al. *High-resolution myocardial perfusion mapping in small animals in vivo by spin-labeling gradient-echo imaging.* Magnetic Resonance in Medicine, 2004. **51**(1): p. 62-67.

38. Garcia-Dorado D. et al. *Analysis of myocardial oedema by magnetic resonance imaging early after coronary artery occlusion with or without reperfusion.* Cardiovascular Research, 1993. **27**(8): p. 1462-1469.

39. Aletras AH, et al. *Retrospective determination of the area at risk for reperfused acute myocardial infarction with T2-weighted cardiac magnetic resonance imaging histopathological and displacement encoding with stimulated echoes (DENSE) functional validations.* Circulation, 2006. **113**(15): p. 1865-1870.

40. Tilak GS, et al. *In vivo T2-weighted magnetic resonance imaging can accurately determine the ischemic area at risk for 2-day-old nonreperfused myocardial infarction.* Investigative Radiology, 2008. **43**(1): p. 7-15.

41. Manrique A, et al. *Cardiac magnetic resonance demonstrates myocardial oedema in remote tissue early after reperfused myocardial infarction.* Archives of Cardiovascular Diseases, 2009. **102**(8): p. 633-639.

42. Friedrich MG, Kim HW and Kim RJ. *T2-weighted imaging to assess post-infarct myocardium at risk.* JACC: Cardiovascular Imaging, 2011. **4**(9): p. 1014-1021.

43. Rahimtoola SH. *The hibernating myocardium.* American Heart Journal, 1989. **117**(1): p. 211-221.

CHAPTER 5: HIGH TEMPORAL RESOLUTION RETROSPECTIVE CINE MRI FOR ASSESSING DIASTOLIC FUNCTION IN HEALTHY AND INFARCTED MOUSE HEARTS: COMPARISON WITH ULTRASOUND

Cardiac function is widely assessed in the clinic using quantitative measures of systolic function, however, assessment of diastolic function may offer a more sensitive early indicator of heart failure. This chapter is focussed on the development of a retrospective high-temporal resolution (HTR) CINE sequence for the assessment of diastolic function in mouse hearts. The chapter describes the creation and optimisation of the sequence, development of algorithms to reconstruct the imaging data, repeatability studies to assess the variability of the technique and comparisons with Doppler ultrasound, which is currently the preferred method for in vivo assessment of diastolic function. Finally, the sequence is applied to a mouse model of myocardial infarction.

5.1 Introduction

In the clinic, cardiac function is most commonly assessed using measures of systolic parameters such as ejection fraction and stroke volume. Reduced ejection fraction (< 50%) is a primary indicator of global systolic dysfunction. However, approximately 50% of heart failure patients have normal ejection fraction [1], but present with diastolic dysfunction. This complicates diagnosis of heart failure and has led to the creation of new terminology to categorise these patients: they are said to have heart failure with preserved ejection fraction (HFpEF). A vast body of literature now exists focused on HFpEF [2-8], as it is recognised as a major international public health problem, and one which is growing [4]. While outcomes in heart failure with reduced ejection fraction (HFrEF) have improved in recent years, HFpEF outcomes have not improved [5], underlining the need for further research in this field.

The cardiac cycle is divided into two main phases: systole and diastole. During systole left ventricular contraction pumps blood out of the heart. Contraction is activated by an influx of calcium (Ca^{2+}) ions into the cardiomyocytes [9]. The diastolic phase involves left ventricular filling, which is characterised by two main stages: the early-filling phase (E) where the myocardium actively relaxes by pumping of Ca^{2+} ions into the sarcoplasmic reticulum via energy-dependent SERCA (sarcoplasmic reticulum calcium ATPase) pumps and the atrial-filling phase (A) where the left atrium contracts to push through more blood. Diastolic performance can be quantified by measuring the blood flow velocity across the mitral valve during these two phases to give the E/A ratio [10]. Two main mechanisms contribute to diastolic heart failure, which can be detected by alterations in the E/A ratio. Firstly, abnormalities in calcium homeostasis, such as decreased SERCA function, can cause impaired active relaxation [11]. This results in a mild form of diastolic heart failure where LV relaxation is slowed and atrial contraction is increased to compensate, known as impaired diastolic dysfunction. In this case, E/A is less than 1 (Figure 5.1). The second mechanism is increased myocardial stiffening which causes elevated blood pressure resulting in the early opening of the mitral valve and a faster inflow of blood into the LV [12]. This is a more severe form of diastolic heart failure known as restrictive filling, which results in an E/A ratio greater than 1.7. For healthy individuals, an E/A value between 1.0 and 1.7 is considered normal, however, patients that fall within this range are considered to be transitioning from impaired to restrictive filling [13].

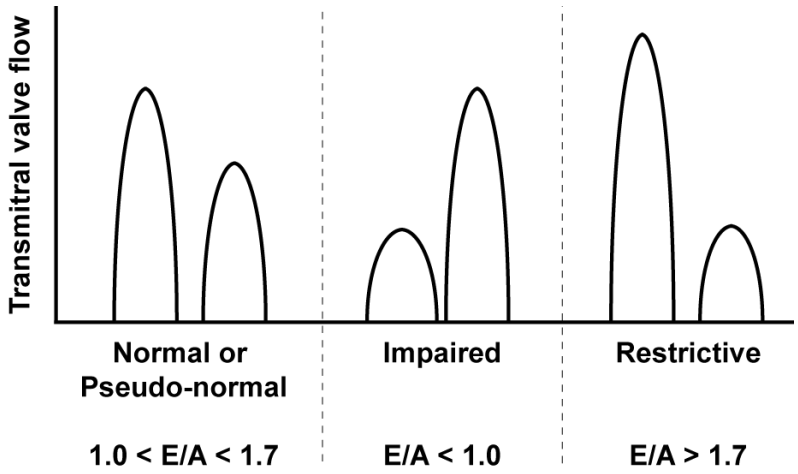

Figure 5.1: Schematic showing different patterns of left ventricular filling by measurement of transmitral valve blood flow. E corresponds to the early-filling phase of diastole and A corresponds to the atrial-filling phase of diastole.

Ultrasound is the "method of choice" for diagnosing heart failure [2, 14] in the clinic and can be used for assessment of both systolic and diastolic dysfunction. It has also been successfully applied to mouse and rat models of heart disease [15-17], however, measures of diastolic dysfunction in particular are limited by difficulties with transducer positioning, the small acoustic window, 1-dimensional acquisition and high heart rates which can lead to the early and atrial filling phases merging together.

MRI is widely recognised as a viable and potentially better alternative for measuring diastolic function [18-20] because of its ability to image the heart in 3D with excellent spatial resolution and tissue contrast. In patients, MRI has been shown to correlate closely with ultrasound measurements of diastolic function [21]. In rodents, where conventional CINE imaging generates 15-30 frames throughout the cardiac cycle, the temporal resolution is only sufficient for analysis of systolic parameters. Assessment of diastolic function requires higher temporal resolution to resolve the subtle filling patterns. Measurements in mice are further complicated by high heart rates and the merging of the E- and A-filling phases, which is not exhibited in human hearts. Ultrasound has the requisite temporal resolution for murine studies, but measurements are often imperfect due to hardware limitations such as those outlined in the previous paragraph. More recently, high temporal resolution, pre-clinical MRI techniques have emerged including a prospective CINE method [22] and a self-gated retrospective method [23] for measuring the E/A ratio in rodents, however none have been directly compared and validated against ultrasound measurements.

Therefore, the aim of this chapter was to develop an ECG-gated retrospective high-temporal resolution (HTR-) CINE sequence for assessing diastolic function in mice by measurement

of E/A ratios and compare the results with ultrasound. The theory behind the retrospective HTR-CINE sequence is discussed in the next section (section 5.1.1). The methods and results begin with some preliminary experiments including phantom scans, early *in vivo* tests and simulations, which all contributed to the optimisation of the sequence. Then, the final image reconstruction pipeline is outlined. Following development of the sequence, an ultrasound versus retrospective HTR-CINE MRI repeatability and variability study is described. Finally, a study applying the HTR-CINE sequence to an experimental mouse model of myocardial infaction (MI) is presented.

5.1.1 Retrospective HTR-CINE sequence theory

The retrospective HTR-CINE sequence developed in this chapter extends the basic idea of a standard retrospective CINE sequence, as described in section 2.7. In a standard retrospective CINE acquisition (Figure 2.10), the sequence is run continuously (~1 minute per slice) with a fixed TR, k-space is sorted depending on ECG and respiration events and then reconstructed offline once all phase encode lines have been acquired. For high temporal resolution, the same sequence is run except the acquisition duration is extended (typically >10 minutes) so that the cardiac cycle is effectively sampled with a high frame rate. Natural fluctuations in heart rate ensure that the cardiac cycle is sampled approximately randomly. Figure 5.2 shows how the retrospective HTR-CINE sequence samples the cardiac cycle at slightly different phases throughout the course of an entire scan.

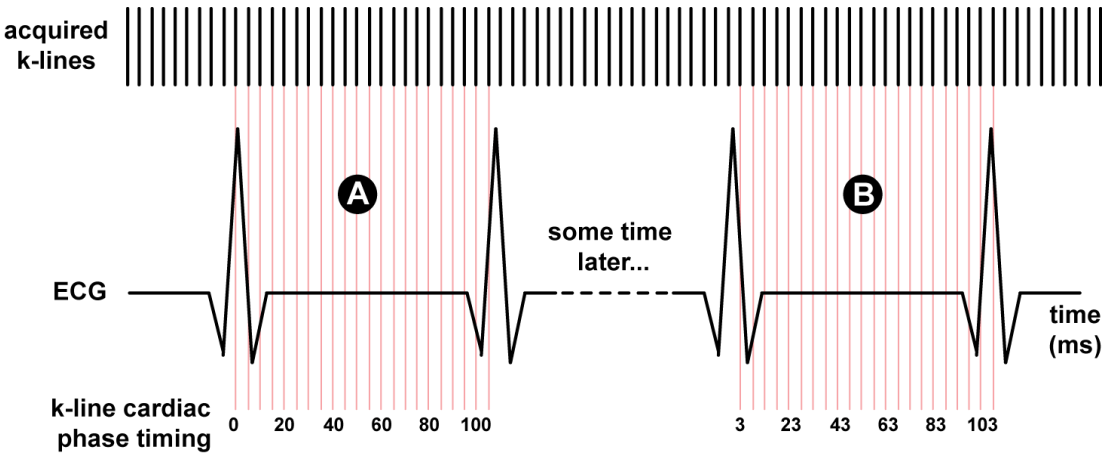

Figure 5.2: Cardiac cycle sampling with a retrospectively-gated HTR-CINE sequence. The red lines show the timing of each k-line acquisition throughout the R-R interval. In this schematic, TR = 5ms for simplicity. The first line acquired in R-R interval (A) coincides with end diastole at 0ms. Later on in the acquisition, the coupling between the sequence and the ECG trace has changed such that the lines acquired in R-R interval (B) are shifted by 3ms through the course of the cardiac cycle.

5.2 Methods

5.2.1 Retrospective HTR-CINE sequence reconstruction

For retrospective reconstruction of the HTR-CINE sequence, a datalogger (see section 2.8) was used to record the exact timings of all RF, ECG and respiration events. These data – along with the raw imaging data – were exported for offline reconstruction of the sequence, as the vendor software on the MRI scanner was incapable of reconstructing retrospectively acquired images.

A reconstruction pipeline was developed in MATLAB to sort the RF events depending on their location within the cardiac cycle and the respiration state of the animal. Data was passed through the pipeline below (see Figure 5.3 for an illustration of this process):

1. All RF events were identified as k_1 to k_{128} depending on their position in the k-space phase encoding table.
2. The period of every cardiac R-R interval was calculated based on the ECG recordings. The ECG trace was passed through the arrthymia correction algorithm described in the next section (5.2.2).
3. Using the corrected ECG trace, every R-R interval was divided into *NF* frames – as defined by the user – of equal duration. For example, an R-R interval of 100ms divided into 20 frames gave a binwidth of 5ms.
4. All RF events were assigned a second number f_1 to f_{NF} depending on where they occurred during each cardiac cycle.
5. Any RF events which occurred during a breath were discarded.
6. k-space for each frame was compiled using the corresponding k-lines k_1 to k_{128}.
7. Lastly, each k-space frame was Fourier transformed to produce a real image.

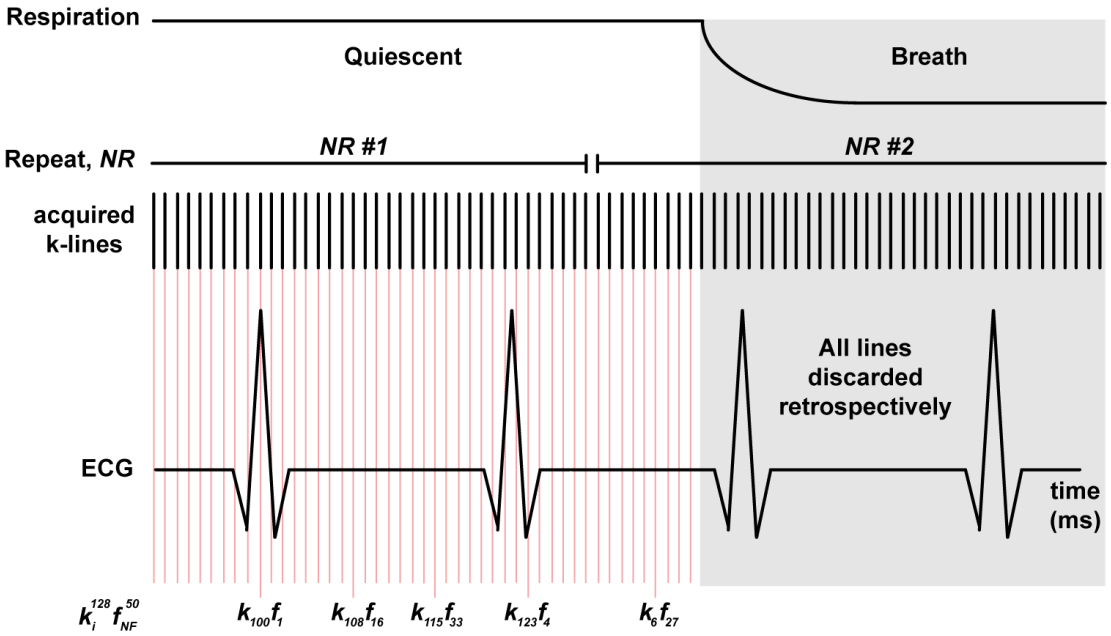

Figure 5.3: Schematic showing RF assignment for retrospective HTR-CINE reconstruction. All k-lines acquired during respiration breaths (grey) are discarded. Each k-line is assigned a number between 1 and 128 (k_i) depending on its location in k-space. The k-lines are also assigned a frame number (f_{NF}) from 1 to NF (= 50 in this diagram) depending on its location in the R-R interval. k-space is reconstructed by sorting the k-lines according to their assigned values.

5.2.2 ECG arrhytmia correction algorithm

There were two main sources of QRS timing error in the ECG recording equipment that were corrected to ensure retrospective reconstruction was as robust as possible (Figure 5.4). Firstly, the SA Instruments software occasionally missed QRS events (a) causing the apparent duration of the R-R interval to double. Secondly, the software sometimes mistakenly recorded spikes of noise in the ECG trace as QRS events causing a shortening of one R-R interval followed by lengthening of the subsequent interval (b).

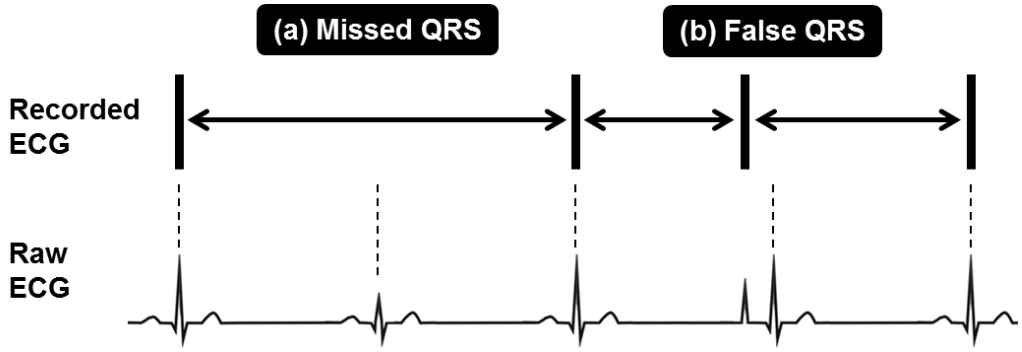

Figure 5.4: Sources of error in ECG recordings. (a) Fluctuating ECG signal would sometimes lead to missed QRS peaks which caused recorded R-R intervals to double in duration. (b) Noise in the ECG signal would also lead to false QRS detection which caused the dual effect of shortening the duration of one interval followed by increasing the duration of the subsequent R-R interval.

Both sources of error caused incorrect assignment of RF events during reconstruction. To account for this, an ECG correction algorithm was developed as part of the reconstruction pipeline in section 5.2.1. The duration of every R-R interval was calculated and the average R-R duration was determined. For missed QRS events, with an R-R interval greater than 175% of the mean R-R duration, a new QRS event was inserted. To account for false QRS detection, all R-R intervals shorter than the mean R-R duration by 2 SD or more were detected and shifted in time to the median R-R duration of the surrounding 10 ECG intervals.

5.2.3 Phantom experiment – retrospective HTR-CINE block acquisition correction

Preliminary *in vivo* images using the retrospective HTR-CINE sequence contained significant flickering artefacts (see Results, Figure 5.8) which needed to be corrected before continuing with the main studies. Therefore, a number of experiments (described in the Results section) in agar phantoms were carried out to determine the source of the artefact. Phantoms were imaged using the retrospective HTR-CINE sequence with the following parameters: TR = 3.15 ms, TE = 1.21 ms, NR = 2500, FA = 15°, data matrix = 128^2, FOV = $20mm^2$, slice thickness = 2mm.

5.2.4 *In vivo* simulations

The majority of preliminary experiments were conducted with NR = 2500, which equated to 20 minutes for a single slice. Therefore, prior to carrying out the main experiments, simulations of typical *in vivo* mouse physiology were programmed and run in MATLAB to determine the optimum scan duration for characterising diastolic function.

Two parameters were varied in the simulations: heart rate and respiration rate. Temperature and isoflurane concentration were assumed constant. An ECG trace was simulated with an R-R interval based on the input heart rate. Gaussian noise was applied to the trace so that ECG events were distributed around the mean R-R interval with a 1ms standard deviation. Similarly, a respiration trace was simulated with a quiescent interval based on the input respiration rate. Breath duration was held constant at 0.25s, based on previous *in vivo* experience, therefore only the quiescent phase was varied in duration. Respiration events were also modelled as a Gaussian distribution with a 0.1s standard deviation. TR was set to be 3.15 ms, in keeping with the minimum duration achievable *in vivo* on the laboratory MRI

scanner. The number of repeats, NR, was set to 2500, equivalent to 320,000 RF events. For analysis, heart rate and respiration rate were varied between 400–650 bpm and 30–90 bpm, respectively, which were rates consistent with previous *in vivo* mouse experiments. All simulations were repeated five times (n = 5) and error bars represent standard error in the mean (SEM).

Previous studies by Coolen et al. (2013) showed that retrospective HTR-CINEs generated from only partially filled k-f spaces were adequate for diastolic function analysis [23]. Thus, the simulations were run to determine the time needed 99% completion of k-f space, and for comparison, 95% and 100% completion of k-f space.

5.2.5 *In vivo* MRI setup

For all *in vivo* experiments, mice were imaged using the standard cardiac MRI setup described in section 2.8.1. Briefly, mice were anesthetised with 1.5-2.0% isoflurane in 2 l/min O_2 and positioned supine in a cradle which could be positioned in the middle of the scanner bore. Temperature was monitored and maintained at physiological temperature. Respiration was monitored using a neonatal apnea pad and ECG was monitored using three ECG electrodes inserted subcutaneously. For myocardial infarction experiments, an infusion line was inserted intraperitoneally for injection of gadolinium contrast agent. All imaging was conducted using 1000mT/m gradient inserts and a 35mm volume RF coil (RAPID).

5.2.6 Study 1: Repeatability of diastolic function measurements using retrospective HTR-CINE MRI vs ultrasound

The aim of this experiment was to establish the repeatability of the retrospective HTR-CINE sequence and validate the results using ultrasound. To this end, (n = 8) naïve mice were scanned twice using both ultrasound and MRI for intra- and inter-modality comparisons. Pulse wave Dopper mode ultrasound was used as a gold-standard estimate of E/A ratios. The retrospective HTR-CINE sequence was performed at three different slice locations within the heart: apical, mid-ventricular and basal, to examine variability due to slice location. A conventional CINE stack was also acquired to serve as a basis for localising the retrospective planes, for estimation of systolic functional parameters and to compare variation in established parameters such as ejection fraction and stroke volume with variation in the diastolic function parameters. Total imaging time was approximately 2.5 hours per animal. All animals were imaged with the following protocol:

1. **Ultrasound scan 1** (15 minutes)
2. **MRI session 1**
   – Animal setup and scanner calibration (15-20 minutes)
   – Prospective CINE stack (10 minutes)
   – Retrospective HTR-CINE
      – single apical slice (11 minutes)
      – single mid-ventricle slice (11 minutes)
      – single basal slice (11 minutes)
3. **MRI session 2**
   – Remove and reposition the animal cradle within the scanner
   – Scanner calibration (5 minutes)
   – Prospective CINE stack (10 minutes)
   – Retrospective HTR-CINE
      – single apical slice (11 minutes)
      – single mid-ventricle slice (11 minutes)
      – single basal slice (11 minutes)
4. **Ultrasound scan 2** (15 minutes)

In vivo ultrasound setup: Ultrasound imaging was carried out on a VisualSonics Vevo 2100 (CA, USA) system using a VisualSonics 550D 30 MHz transducer. Mice were anesthetised with 1.5-2.0% isoflurene in 2 l/min O_2 and positioned supine on a physiological monitoring platform which simultaneously regulated body temperature and measured respiration and ECG traces. Prior to imaging, hair removal cream (Veet, UK) was applied to the chest to reduce attenuation of ultrasound signal.

For the assessment of diastolic function, pulse wave Doppler mode ultrasound was used to measure mitral inflow in an apical four-chamber view of the heart. Early-filling (E) and atrial-filling (A) peaks were measured in three separate heart beats, from which the mean E/A ratio was calculated for each animal.

In vivo MRI setup: Mice were positioned in the scanner as described in section 5.2.5. Global shimming was performed followed by a series of pilot scans to correctly orientate the short axis CINE stack within the heart. The main MRI sequences were acquired with the following imaging parameters:

Prospective CINE imaging: To quantify standard cardiac functional parameters, a standard CINE stack was acquired with the following parameters. TR = 5 ms, TE = 1.21 ms, FA = 15°, data matrix = 128^2, FOV = 25.6mm^2, slice thickness = 1mm, number of slices = 9-12 depending on animal.

Retrospective HTR-CINE imaging: For quantifying diastolic function, the retrospective HTR-CINE sequence was run with the following parameters: TR = 3.15 ms, TE = 1.21 ms, NR = 1400, FA = 15°, data matrix = 128^2, FOV = 25.6mm^2, slice thickness = 1mm. Images were reconstructed according to the pipeline described in section 5.2.1.

Statistics: Bland-Altman analysis was used to assess the repeatability of systolic parameters measured using CINE imaging and the repeatability of E/A parameters. Variability of E/A measurements were compared between imaging modalities using the standard deviation (SD) derived from Bland-Altman plots. Spearman's correlation (ρ_s) was also performed to compare measurements of E/A between MRI and ultrasound. Statistical significance was assigned at $p < 0.05$.

5.2.7 Study 2: Application of HTR-CINE MRI to imaging myocardial infarction

The aim of this study was to examine the performance of the retrospective HTR-CINE sequence in a mouse model of myocardial infarction (n = 14) and compare this to ultrasound. In addition to running prospective and retrospective CINE sequences, a late gadolinium enhanced inversion recovery sequence was performed to characterise infarct volume for comparison.

CINE imaging: The prospective and retrospective HTR-CINE sequences were acquired with the same parameters as described in the previous section.

Late-gadolinium inversion recovery imaging: Long-axis and short-axis images of the heart were obtained using LGE IR imaging, which was conducted according to the protocol outlined in section 2.7.3 [24]. In brief, 0.6 mmol/kg Gd-DTPA was injected intraperitoneally. After an 8 minute delay to allow contrast agent to wash out of healthy tissue, an IR gradient echo sequence was used for high SNR between the infarcted and healthy tissue. Imaging parameters were: TR = 3.1ms, TE = 1.21ms, FA = 90°, TI = ~4 x RR-interval (~400ms), data matrix = 128^2 (zerofilled to 256^2), FOV = 25.6mm^2, slice thickness = 1mm. Note, one mouse died before LGE IR imaging could be performed, hence this data point is omitted from some plots in the Results section.

Statistics: Mann-Whitney-U tests were performed to test for significance between measurements of systolic cardiac parameters. Spearman's correlation (ρ_s) was performed to examine the relationship between infarct size assessed by LGE imaging and measurements

of EF. Mann-Whitney-U tests were also used to compare measurements of mean E/A in naïve and infarcted animals. In all cases, statistical significance was assigned at $p < 0.05$.

5.2.8 Image analysis for determining E/A ratios

Following reconstruction, retrospective HTR-CINE images were exported to Segment (http://segment.heiberg.se/) for segmentation. The endocardial border was semi-automatically delineated in all frames to produce a chamber volume curve. A filling rate curve was calculated from the derivative of the volume curve. Moving average statistics (span = 5: N-2 … N+2) were applied to filling curves to filter noise. From the filling rate curve, E and A peaks were determined and the E/A ratio calculated.

5.3 Results

5.3.1 Preliminary pulse sequence development, reconstruction and implementation

The vendor software on the Agilent MRI scanner did not contain a retrospective CINE sequence, so a custom retrospective CINE sequence was programmed. The sequence was based on a conventional FLASH CINE sequence, but modified to run for a user-defined number of repetitions, NR. TR was set to its minimum of 3.15ms to ensure maximal temporal resolution through the cardiac cycle. *In vivo* scans required retrospective sorting according to animal physiological traces. Figure 5.5 shows RF, ECG and respiration events recorded using the datalogger.

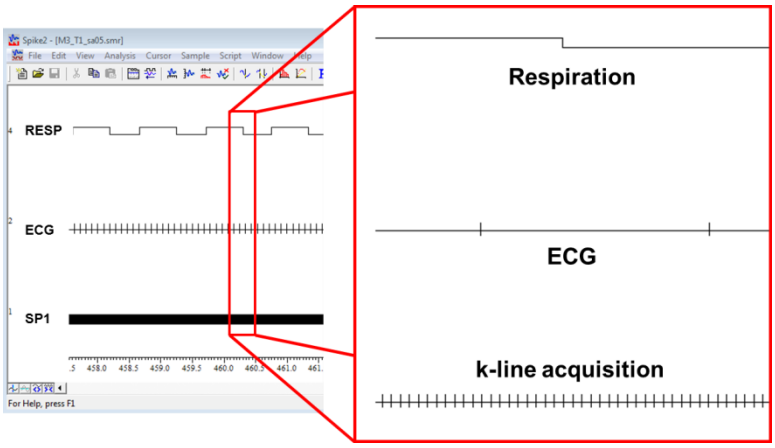

Figure 5.5: Screenshot from the datalogger software, Spike2, showing recordings of mouse respiration, ECG and the k-line RF timestamps.

The imaging data and the traces from the datalogger were passed through the reconstruction pipeline described in the methods (section 5.2.1). Based on recordings of 8 naïve mice, the mean percentage of k-space lines discarded from a scan due to respiration events was 43.3 ± 1.3% and the average R-R interval duration was 100.5 ± 2.5ms.

As discussed in section 5.2.2, there were two main sources of timing error in the datalogger ECG recordings, which caused miscalculated R-R intervals. Figure 5.6a shows a plot of all R-R interval durations from a mouse. The spikes in the plot correspond to missed or incorrectly timed ECG events. On average, there were 6936 ± 165 heart beats during a scan. The mean percentage of incorrectly recorded QRS events in a mouse was 1.5 ± 0.4%. The arrhythmia correction algorithm was effective at detecting and correcting any missed or erroneous ECG timestamps recorded by datalogger (Figure 5.6b).

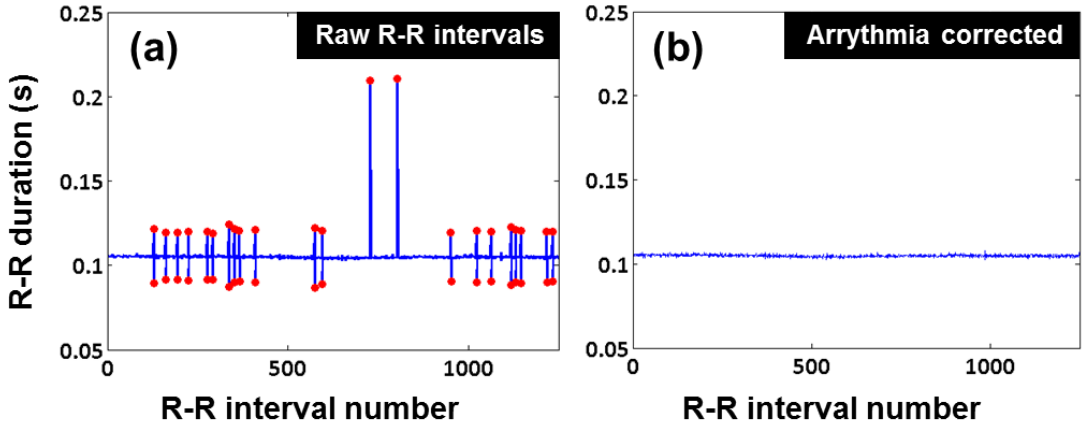

Figure 5.6: Arrhythmia correction in a mouse ECG trace. (a) The raw ECG trace shown has a mean R-R duration of 0.11 ms, however, noise in the ECG traces caused incorrect measurement of QRS events or QRS events to be missed completely. (b) The same ECG trace passed through the arrhythmia correction algorithm shows steady R-R intervals.

Following respiration and arrhythmia correction, the imaging data were retrospectively reconstructed into HTR-CINE movies. Figure 5.7 shows typical k-f space filling patterns in a single mouse. In each plot, the x-axis corresponds to the phase encode lines (or k-lines) in a single image and the y-axis corresponds to the different frames of the cardiac cycle. Every nonzero pixel in the image corresponds to a successfully assigned RF event. The diagrams feature repeating diagonal streaks through k-f space indicative of the animal physiology. The widest regions of unfilled bins correspond to respiration events, during which lines of k-space are discarded. As the number of repeats, NR, increases many bins are filled more than

once before the entirety of k-f space is completely filled. By NR = 1400, the entire acquisition has been completed: the target number of k-lines per bin for the HTR-CINE acquisition was 3 (dark red), which has clearly been achieved in the majority of bins. Any bins which were filled more than three times were automatically reduced to three k-lines, to minimise artefacts in the reconstructed images.

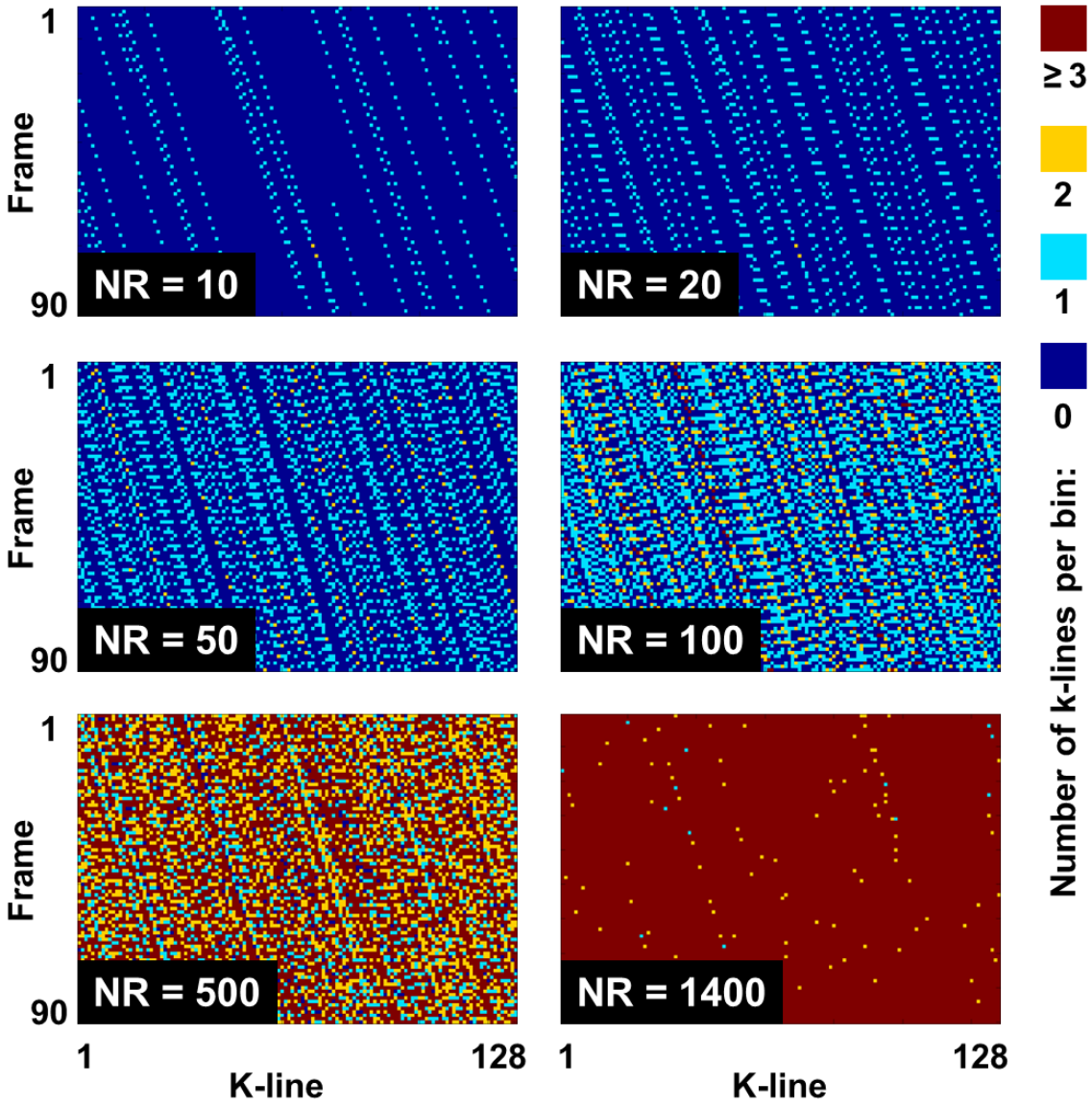

Figure 5.7: Plots showing k-f space filling over the course of an entire acquisition. After 10 repeats (NR = 10), the vast majority of k-f space remains unfilled. The 'zig-zag' pattern reflects animal physiology. The widest sections of unfilled k-f space reflect respiration events. As k-f space filling proceeds, some bins are filled two or three times (yellow and red), while other bins remain unfilled (dark blue). By NR = 500, the majority of bins have been filled at least once. By NR = 1400, most bins have been filled at least three or more times.

Once k-f space was constructed, each frame was fast Fourier transformed to create the HTR-CINE images. Figure 5.8 shows end diastolic frames from a preliminary retrospective HTR-CINE scan, reconstructed using the full pipeline, alongside the equivalent frame from a prospective CINE. The retrospective HTR-CINE images contained flickering artefacts (Figure 5.8a) that were present throughout the entire cardiac cycle, which significantly compromised image quality. The artefacts appeared similar to respiration artefacts manifesting as streaks across the images, however, they were not present in prospective CINE images acquired during the same session (Figure 5.8c) suggesting the problem was isolated to the retrospective HTR-CINE sequence. Closer examination of k-space revealed streaking patterns (Figure 5.8b), which were not present in k-space of the prospective CINE images (Figure 5.8d). This effect was investigated further, and is discussed in the next section.

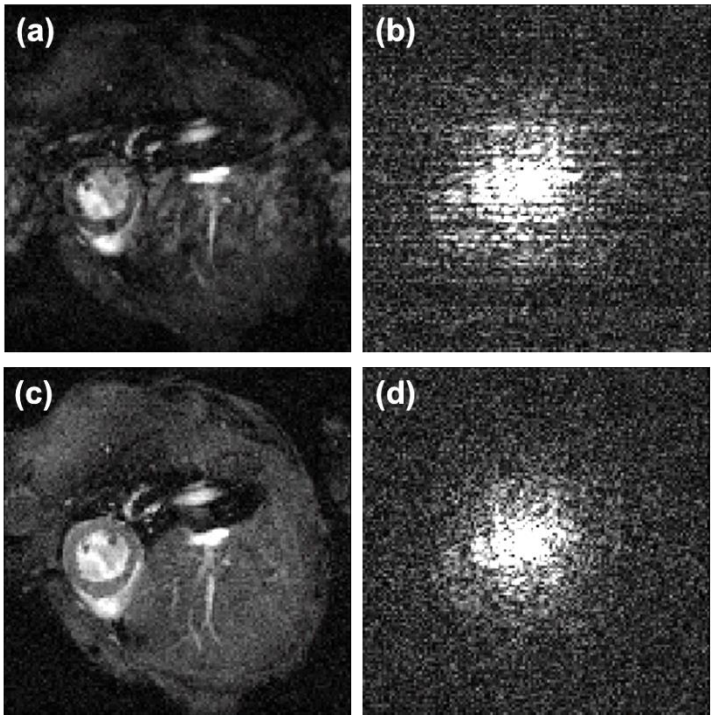

Figure 5.8: Preliminary retrospective HTR-CINE images compared to prospective CINE images. (a) The retrospective HTR-CINE images contained 'flickering' artefacts across the image in the phase encode direction, severely compromising image quality. (b) In k-space, these artefacts appeared as streaks. (c) Prospective CINE images acquired were free from artefacts and (d) k-space was smooth, as expected.

5.3.2 Phantom experiment – retrospective HTR-CINE block acquisition correction

To investigate whether the artefacts observed in the *in vivo* retrospective HTR-CINE images were due to animal physiology or caused by errors in the reconstruction algorithms, the retrospective HTR-CINE sequence was applied to an agar phantom.

Images reconstructed using a block of 128 consecutive lines of k-space, from anywhere during the entire acquisition, resulted in an accurate representation of the phantom (Figure 5.9a). Reconstructing k-space using phase encode lines randomly selected from different repetitions of the sequence resulted in images containing significant artefacts (Figure 5.9b). As observed in the preliminary *in vivo* scans, the artefacts manifested as streaks across the images in the phase encode direction. This suggested that the artefacts observed earlier *in vivo* were not caused by physiological effects.

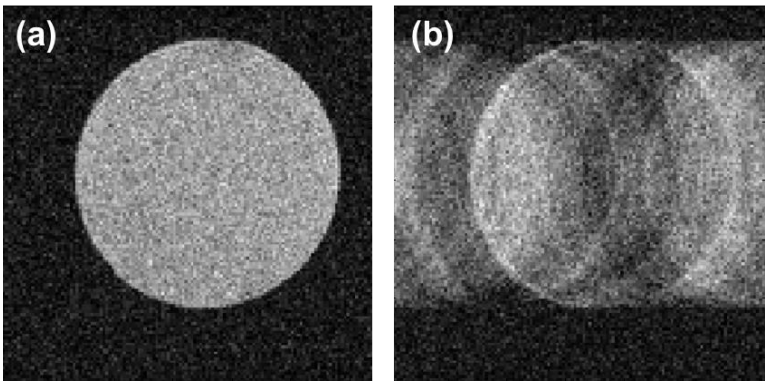

Figure 5.9: Retrospective HTR-CINE images of an agar phantom. (a) Image generated using 128 consecutive lines of k-space. (b) Image generated using phase encode lines selected randomly throughout the entire acquisition. This experiment determined that the cause of the artefact was not physiological.

Further investigation of k-space in the agar phantom experiments demonstrated that a k-space "phase roll" effect was causing the artefacts in the retrospective HTR-CINE images. That is, the signals recorded in k-space would invert – then reinvert – as an increasing number of repetitions (*NR*) were acquired, as shown in Figure 5.10a. The plot shows the maximum signal intensity measured in a 1D profile through the centre of k-space (Figure 5.10b and Figure 5.10c) for every repetition, *NR*, in a single run of the retrospective HTR-CINE sequence. The signal in the centre of k-space (Figure 5.10d) was initially high (> 6000 au) for the first 4 repetitions while the magnetisation reaches a steady state. From NR #5 to approximately NR #250 the signal in the centre of k-space was approximately constant at ~5800 au (red points). After this point, the signal drops sharply, plateauing at ~1200 au (blue

points). A 1D profile through k-space of the blue repetitions showed a negative signal (Figure 5.10e). The signal from the central line of k-space proceeded to oscillate for the duration of the scan, increasing in frequency with NR.

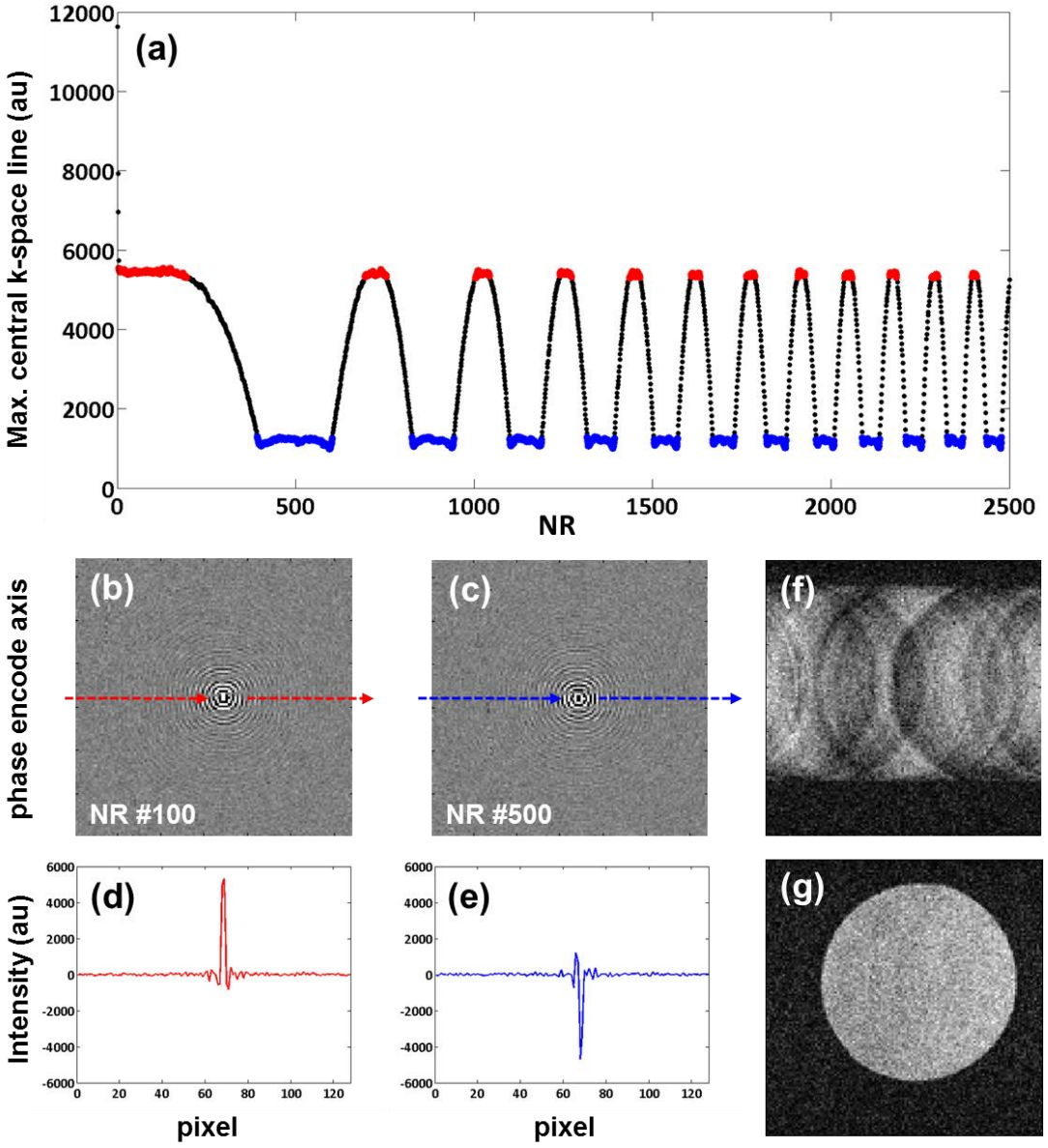

Figure 5.10: k-space phase roll during the retrospective HTR-CINE sequence. (a) The phase of k-space oscillates as the number of sequence repetitions increases. Red points correspond to repetitions where the central line of k-space (b) has positive signal (d).Blue points correspond to repetitions where the central line of k-space (c) has negative signal (e). Corrupt image reconstructed using random phase encode lines from black and blue repetitions only. (f) Image reconstructed using random phase encode lines from red repetitions only.

Images reconstructed using randomly sampled phase encode lines from red repetitions only, (i.e, those with a positive signal in the centre of k-space) produced artefact-free images of the agar phantom (Figure 5.10g). Whereas, images reconstructed using phase encode lines randomly sampled from both blue and black repetitions contained artefacts (Figure 5.10f). Similarly, images reconstructed using only blue repetitions – or only black – also contained artefacts (not shown, but looked very similar to Figure 5.10f).

In an attempt to remedy this issue, large spoiler gradients were implemented into the sequence to test whether it was caused by any residual transverse phase accumulation, but the oscillating phase roll remained. In the end, the issue was circumvented by acquiring consecutive repetitions of shortened acquisitions. The retrospective HTR-CINE sequence was shortened to NR = 200 and immediately restarted once the sequence had finished acquiring. To test the correction method, 5 blocks of 200 repetitions were run for a total NR = 1000. The block-acquisition strategy was carried out in a mouse heart, using the datalogger as normal to record the RF and physiological events. The signal in k-space remained approximately constant throughout the duration of the scan (Figure 5.11). The resultant HTR-CINE images were artefact-free throughout the entire cardiac cycle. This block acquisition approach was implemented in all subsequent studies.

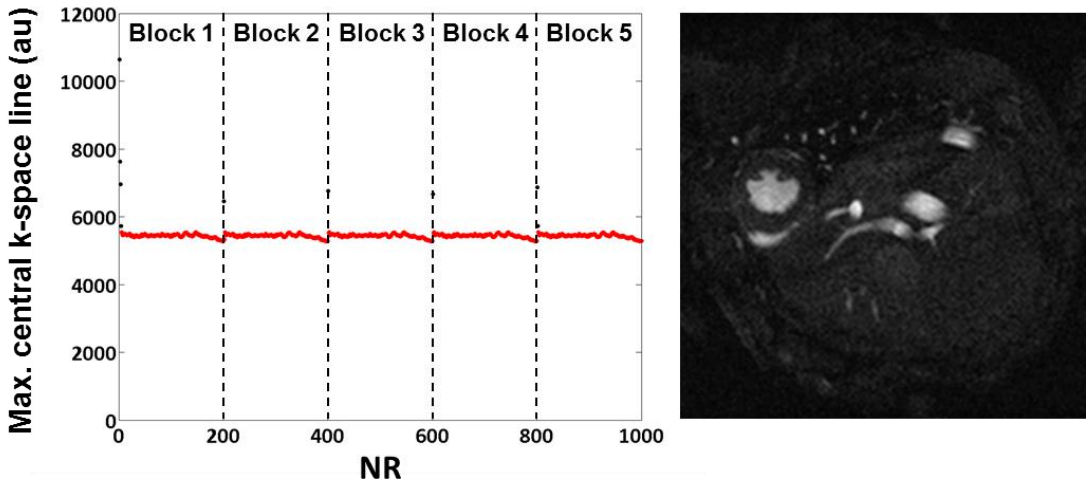

Figure 5.11: The block acquisition strategy for artefact-free retrospective HTR-CINE images. In this example, the full acquisition comprises five blocks of 200 sequence repetitions. The scanner is momentarily stopped in between blocks before resuming. The maximum signal in k-space remains positive throughout the entire duration of the acquisition. Image quality was greatly improved, as shown in an end diastolic frame acquired using the block acquisition strategy.

5.3.3 *In vivo* simulations

Prior to the main animal studies, simulations of *in vivo* mouse physiology were conducted to determine the optimum scan duration required to satisfactorily fill k-f space so that image quality was good enough for reliable segmentation. Simulations were run to determine the time needed for 99% completion of k-f space, and for comparison, 95% and 100% completion of k-f space.

The simulations showed (Figure 5.12a) that the acquisition time required for one complete transient (NT = 1) with 100% filling of k-f space was 11 minutes, with a heart rate of 450 bpm and a respiration rate of 50 bpm, typical of an anesthetised mouse. This equated to three complete transients with 99% filling. Acquisition time was halved for one 99% completed transients of k-f space, which took just over 5 minutes. 95% completion took just under 4 minutes. As k-f filling was a stochastic process, the time taken to acquire transients after completely filling k-f space once was greatly reduced as many phase encode lines had already been acquired multiple times (as shown in Figure 5.7).

Heart rate had little effect on k-f space filling completion times (Figure 5.12b), with respiration set constant at 50 bpm. The time taken to complete one transient with 100% filling (blue curve) was approximately 11 minutes with heart rates between 450 and 650 bpm. However, respiration rate was directly proportional to k-f space completion times (Figure 5.12c), with ECG set constant at 450 bpm. As outlined above, the time taken to complete one transient with 100% filling (blue curve) was approximately 11 minutes. This decreased to less than 9 minutes with a respiration rate of 30 bpm and increased to 14 minutes with a respiration rate of 90 bpm. This result reflects the fact that with faster breathing rates, the duration of the quiescent phase decreases, therefore more lines of k-space must be discarded.

Testing during preliminary experiments determined that creating HTR-CINEs from averages of three 99% complete k-f spaces would be sufficient for determining E/A ratios in the main diastolic function studies. As determined by the simulations, this required imaging for approximately 10 minutes. Therefore, with the addition of a small buffer to allow for some additional respiration variation between animals and imperfect QRS detection *in vivo*, an imaging time of 11 minutes (NR = 1400, 7 blocks) was chosen for subsequent studies to generate retrospective HTR-CINEs with 90 frames per cardiac cycle.

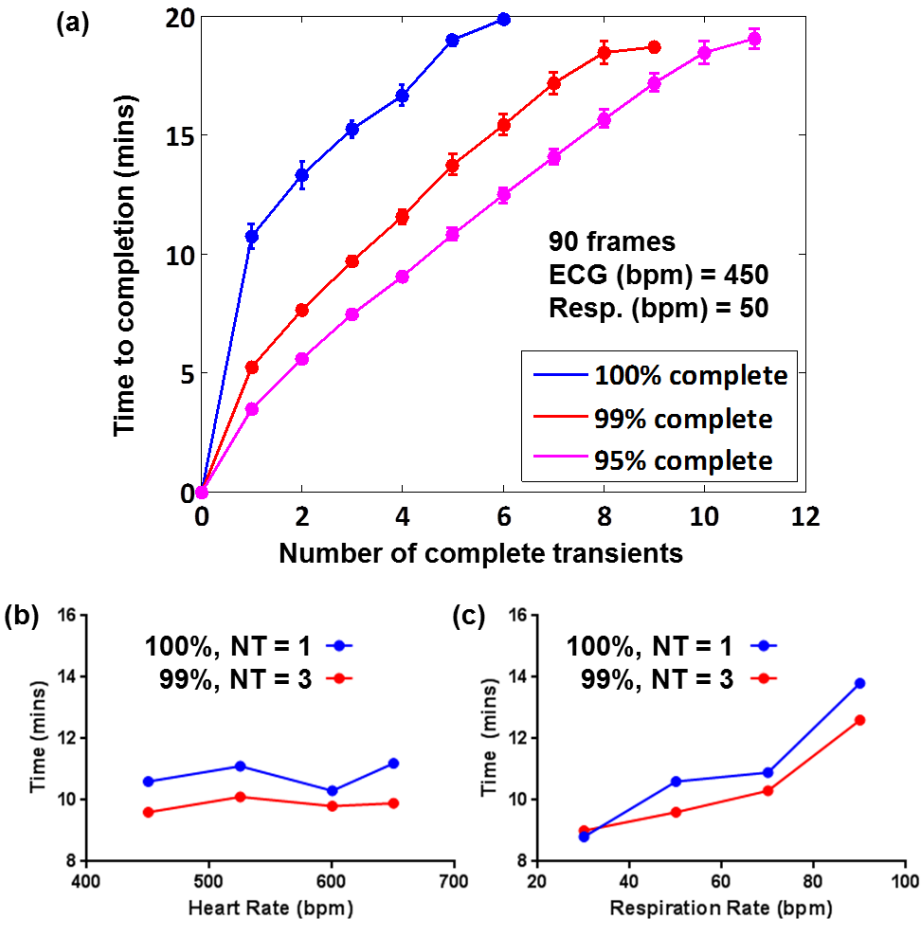

Figure 5.12: In vivo simulations of the retrospective HTR-CINE sequence. (a) The three curves represent the times taken to fill a 90 frame k-f space to 100%, 99% and 95% completion. Each point on a curve represents one 'complete' transient. In this simulation, the mouse heart rate was set to 450 bpm and the respiration rate was set to 50 bpm. (b) The effect of heart rate and (c) the effect of respiration rate on k-f space completion times. The blue curves represent the time taken to complete one transient (NT = 1) with 100% filling. The red curves represent the take taken to complete 3 transients (NT = 3) with 99% filling. Different heart rates have little effect on completion times, whereas completion times take longer with increasing respiration rate.

5.4 Study 1 – Retrospective HTR-CINE MRI vs. ultrasound: repeatability of diastolic function measurements in normal mice

5.4.1 Systolic assessment with retrospective HTR-CINE MRI

Prior to assessment of diastolic function, the repeatability of systolic parameters was determined to examine the variability in the measurements. EF and SV had the lowest variability (Figure 5.13 and Table 5.3) as they depend on two values: EDV and ESV. Measurements of ESV were more variable than EDV because the left ventricle chamber is smaller at end systole making segmentation more difficult. These measurements of systolic variation are discussed further in comparison with variation in diastolic parameters later in the chapter (see section 5.4.4).

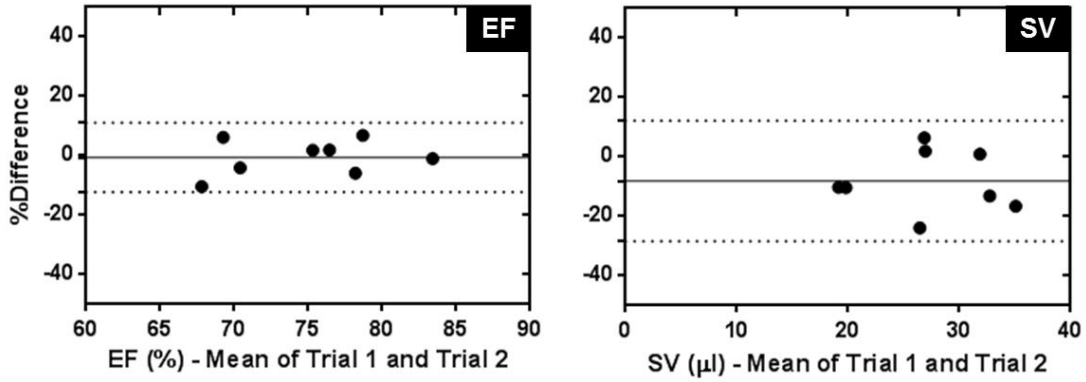

Figure 5.13: Bland-Altman plots showing the repeatability of systolic parameters assessed by segmentation of standard CINE stacks. Solid lines show mean bias, dotted lines show 95% confidence intervals (= 1.96 × SD). EF is highly repeatable with SD = 6.0%. Variability in SV measurements is greater, but still low with SD = 10.4%.

Cardiac Parameter	Bland-Altman SD of %Difference between Trial 1 and Trial 2
EF	6.0 %
EDV	13.6 %
ESV	28.5 %
SV	10.4 %

Table 5.3: Table showing the standard deviation of the percentage difference between two measurements of various cardiac systolic parameters.

5.4.2 Slice selection for diastolic function assessment

Retrospective HTR-CINEs were generated at three separate slice locations in the heart based on standard CINE stacks (Figure 5.14) acquired within the same session. The three separate slice locations were acquired to establish which slice was most closely correlated with ultrasound measurements of E/A ratios. 'Basal' slices were defined as the slices closest to the atria, just below the mitral valve. 'Apical' slices were defined as the most apical slice which still contained papillary muscles. 'Mid-ventricle' slices were defined as a slice in between the Basal and Apical slices. The slices chosen were often contiguous, as shown in Figure 5.14, but in some animals there was a gap equivalent to one slice between the Apical and Mid-Ventricle slices.

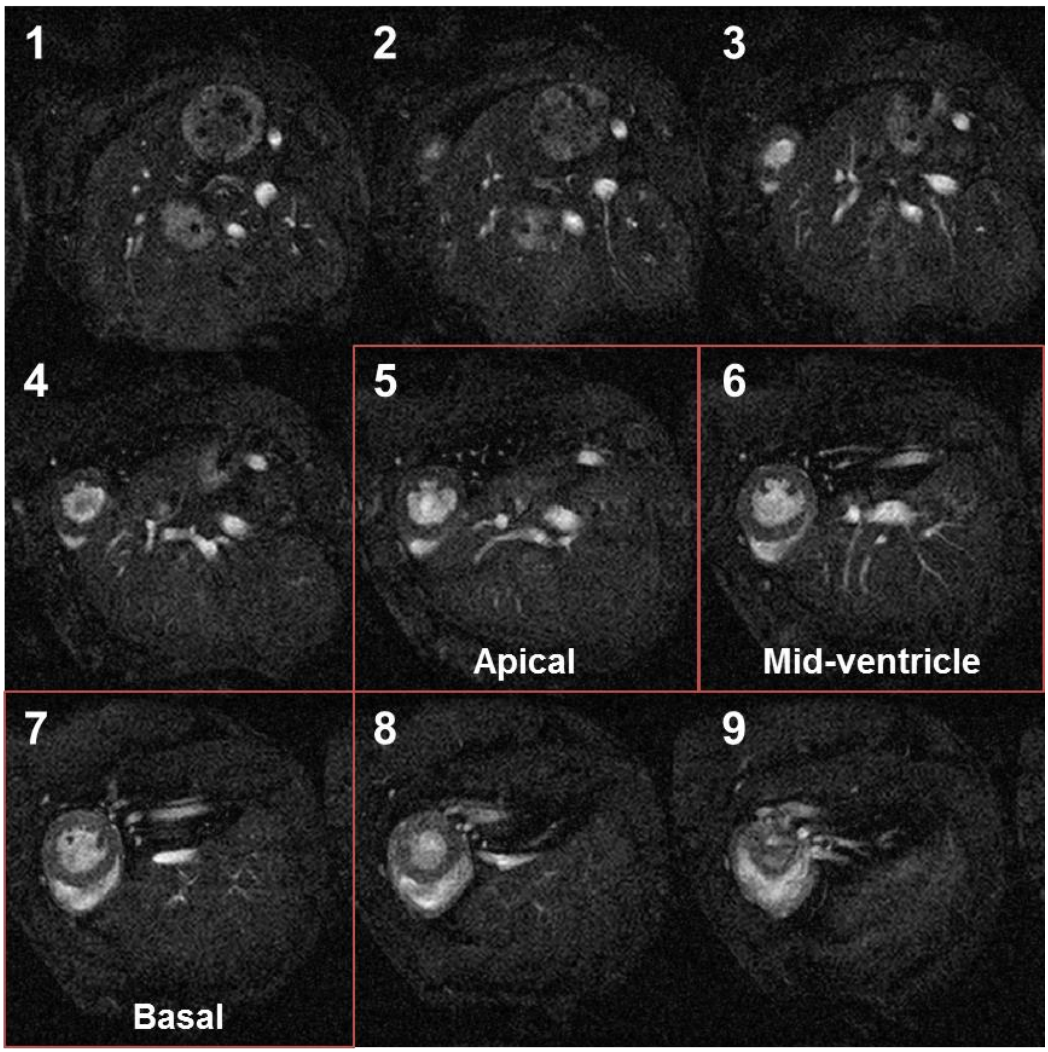

Figure 5.14: Prospective CINE stack showing slices selected for use in retrospective HTR-CINE scans (red boxes). 'Basal' slices were defined as slices closest to – but not including – the atria. 'Apical' slices were defined as the most apical slice which still clearly contained papillary muscles. 'Mid-ventricle' slices were defined as a slice inbetween the Basal and Apical slices.

5.4.3 Diastolic function image analysis – determining E/A ratios from HTR-CINE MRI and ultrasound

Figure 5.15 shows every third image through the cardiac cycle of a naïve mouse from a 90 frames retrospective HTR-CINE acquisition. For comparison, images from a pulsed wave Doppler ultrasound scan are shown in Figure 5.16a. Retrospective HTR-CINEs were exported to Segment for left ventricular segmentation (Figure 5.16c). Every frame in the cardiac cycle was segmented to generate a left ventricular volume curve (blue) (Figure 5.16d). Filling curves (red) were calculated by differentiation of the volume curve. For ultrasound, one filling curve (Figure 5.16b) was acquired for every heartbeat – the average of three consecutive filling curves was taken for final E/A values. Distinct early- and atrial-filling peaks could be resolved using both modalities.

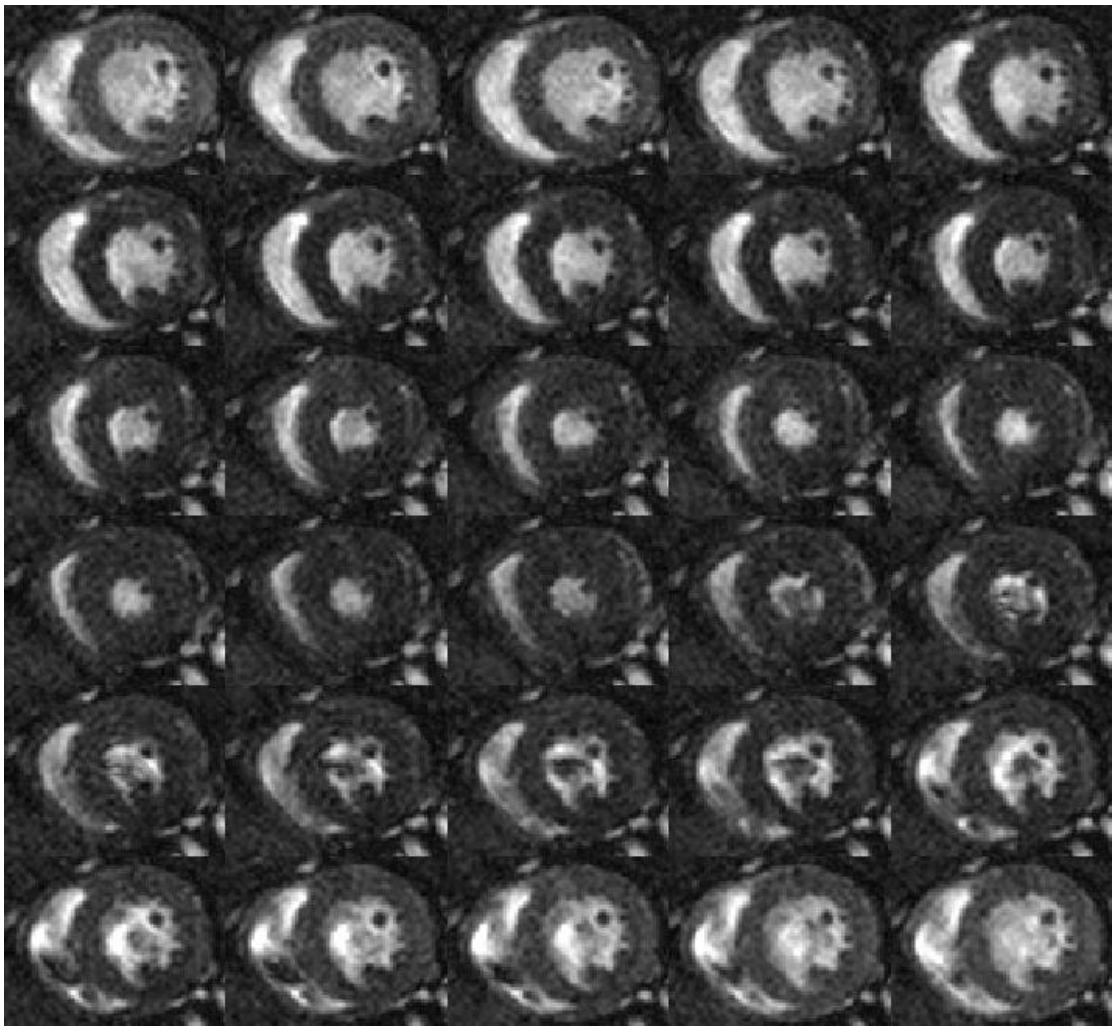

Figure 5.15: 30 images through the cardiac cycle from a 90 frame retrospective HTR-CINE acquisition. Temporal resolution is approximately 1.1-1.3ms depending on heart rate.

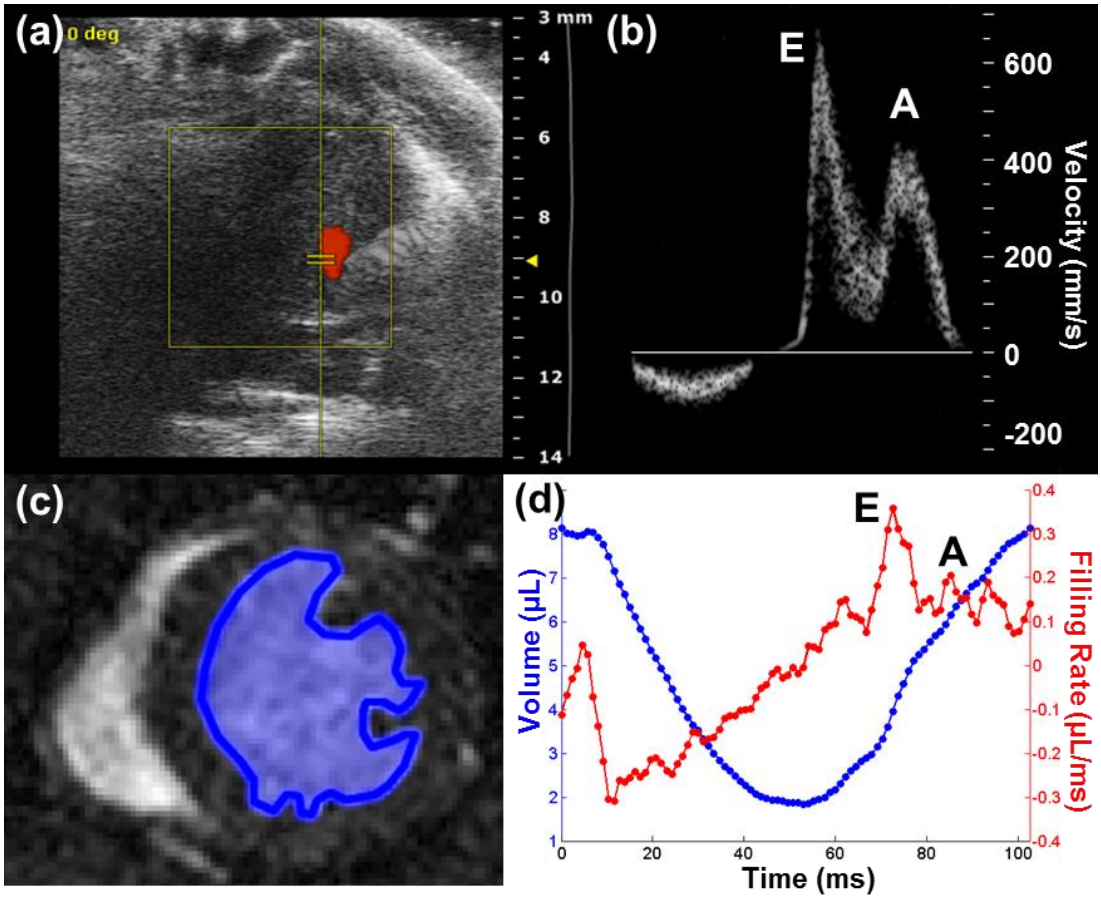

Figure 5.16: Measuring E/A ratios using pulsed wave Doppler ultrasound and retrospective HTR-CINE MRI in naïve mice. (a) Typical ultrasound image of mitral blood flow showing Doppler measurements overlaid. (b) Corresponding ultrasound filling curve. (c) Retrospective HTR-CINE image showing left ventricle blood pool segmentation (blue). (d) Corresponding left ventricle volume curve (blue) and filling rate curve (red). Early- and atrial-filling peaks can be seen clearly with both modalities.

5.4.4 MRI vs. ultrasound – repeatability and correlations

Naïve mice (n = 8) were scanned twice for repeatability using both MRI and ultrasound. Figure 5.17 shows raw measurements of E/A ratios using both modalities. Ultrasound showed no significant difference between measurements in both trials. Similarly, there was no significant difference between any repeated MRI measurements, regardless of slice location.

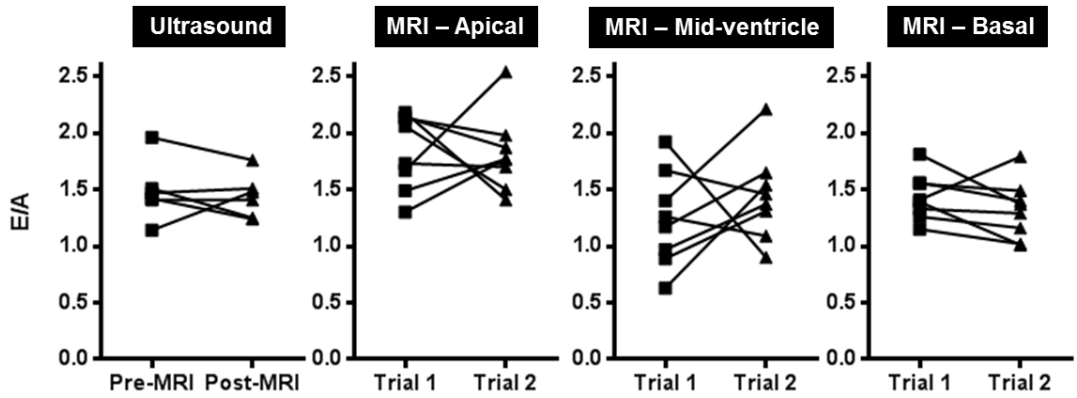

Figure 5.17: Raw data from repeat measurements of E/A ratios using ultrasound and MRI at three different slice locations: Apical, Mid-ventricle and Basal. There were no significant differences observed in any repeat measurements ($p > 0.05$, Mann-Whitney-U test).

Figure 5.18a presents the mean E/A ratios measured using both modalities. The mean E/A ratio (± SEM) measured across all ultrasound scans was 1.42 ± 0.07. The mean E/A ratios measured using MRI were 1.41 ± 0.10 in the Mid-ventricle slices and 1.42 ± 0.07 in the Basal slices, which agreed with ultrasound. These measurements were also within the range (1.0–1.7) of values corresponding to normal heart function. However, the mean E/A ratio measured using Apical slices was 1.84 ± 0.08, which was significantly higher than ultrasound measurements ($p < 0.05$). The coefficient of variation was greatest in MRI measures using Mid-ventricle slices (Figure 5.18b). Apical and Basal slices (16.9% and 16.0%, respectively) were comparable to ultrasound (17.1%).

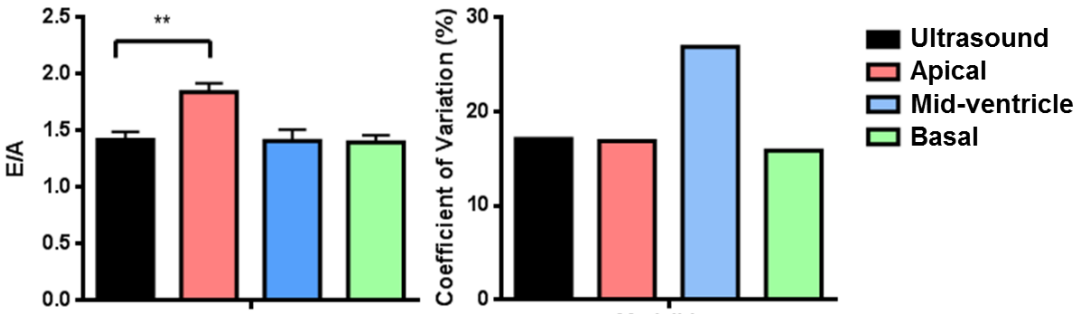

Figure 5.18: (a) Mean E/A ratios and (b) coefficient of variation measured using ultrasound and MRI at three different slice locations in the heart. MRI measures of E/A using Apical slices were significantly different to ultrasound values ($p < 0.05$), whereas Mid-ventricle and Basal slices showed the closest correspondence to ultrasound values. There was most variation in Mid-ventricle measures of E/A, whereas variation in the other two slice positions was comparable to ultrasound.

Bland-Altman analysis of ultrasound and MRI filling ratio measurements was carried out to establish the repeatability of the two modalities and to determine which MRI slice most closely reflected the ultrasound measurements (Figure 5.19). Ultrasound had the smallest standard deviation: SD_{US} = 16.1%. Basal positioning of MRI slices produced the best repeatability in MRI measurements where the standard deviation was comparable to ultrasound at SD_{BASAL} = 16.5%. Variability was much greater in Apical and Mid-Ventricle slice MRI measurements, which had standard deviations of SD_{APICAL} = 29.3% and $SD_{MID\text{-}VEN}$ = 48.1%, respectively.

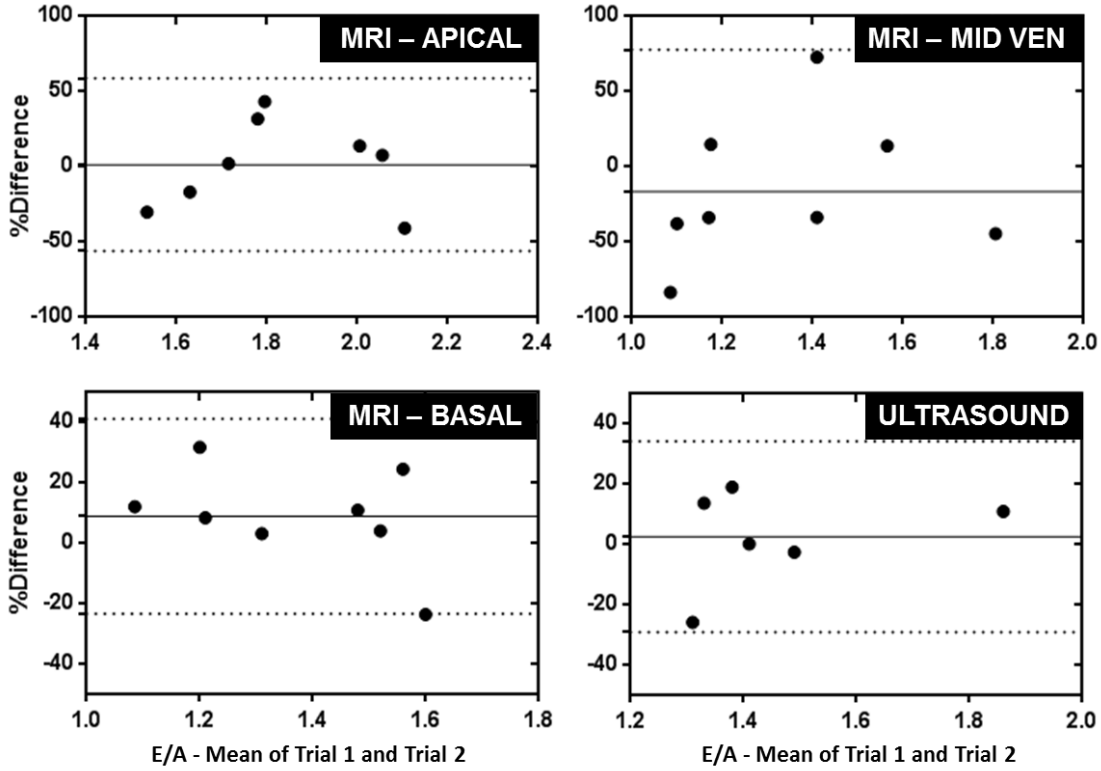

Figure 5.19: Bland-Altman plots of E/A ratios measured using ultrasound and MRI. All plots show the mean difference and percentage differences between two trials within the same mouse. Solid horizontal lines show mean bias, dotted lines show 95% confidence intervals (= 1.96 × SD). Apical and Mid-ventricle MRI measurements showed poor repeatability with standard deviations SD_{APICAL} = 29.3% and $SD_{MID\text{-}VEN}$ = 48.1%, respectively. Repeatability in Basal MRI slices was best: SD_{BASAL} = 16.5%. This was comparable to ultrasound: SD_{US} = 16.1%.

The repeatability measurements of E/A using either ultrasound or Basal MRI were reasonably comparable with repeatability measurements of systolic parameters (previously determined in section 5.4.1). The standard deviations of EF and SV measurements were SD_{EF} = 6.0% and SD_{EF} = 10.4%, respectively. Variability in the Apical and Mid-Ventricle MRI measurements was vastly higher, however, ultrasound and Basal MRI measurements of E/A had much lower and more reasonable standard deviations of 16.1% and 16.5%,

respectively. The increased standard deviation in the E/A measurements reflects the difficulty in measuring subtle diastolic filling patterns compared to systolic function. Furthermore, the MRI measurements of E/A are derived from a single-slice acquisition whereas EF and SV were determined using a CINE stack with whole heart coverage.

Correlation plots between the two modalities in naïve mice (Figure 5.20) showed that only MRI measurements using Basal slices were significantly correlated with ultrasound measurements of E/A ratios (Spearman's correlation coefficient, $\rho_s = 0.54$, $p = 0.04$). Apical and Mid-ventricle MRI measurements were not correlated with ultrasound ($p > 0.05$). Based on the results in this section, Basal slices were chosen for future MRI scans as E/A ratios determined at this location showed the greatest agreement with ultrasound and the variability was smallest compared to Apical and Mid-ventricle locations.

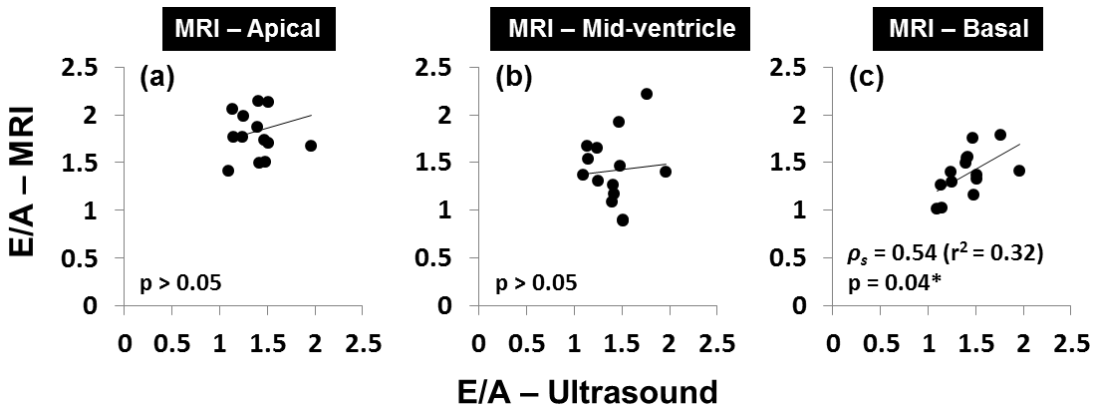

Figure 5.20: Correlations between ultrasound and MRI measurements of E/A ratios. Apical (a) and Mid-ventricle (b) measures of E/A ratios showed no correlation with ultrasound, whereas Basal slice MRI measurements were significantly correlated with ultrasound (Spearman's correlation, $\rho_s = 0.54$, $p = 0.04$).

5.5 Study 2 – Retrospective HTR-CINE MRI vs. ultrasound: assessing diastolic function in a mouse model of myocardial infarction

5.5.1 Systolic function assessment

Cardiac function was assessed in the infarct cohort of mice (n = 14). Figure 5.21 shows systolic parameters in the infarcted mice assessed by segmentation of prospective CINE images and compared with naïve mice from Study 1.

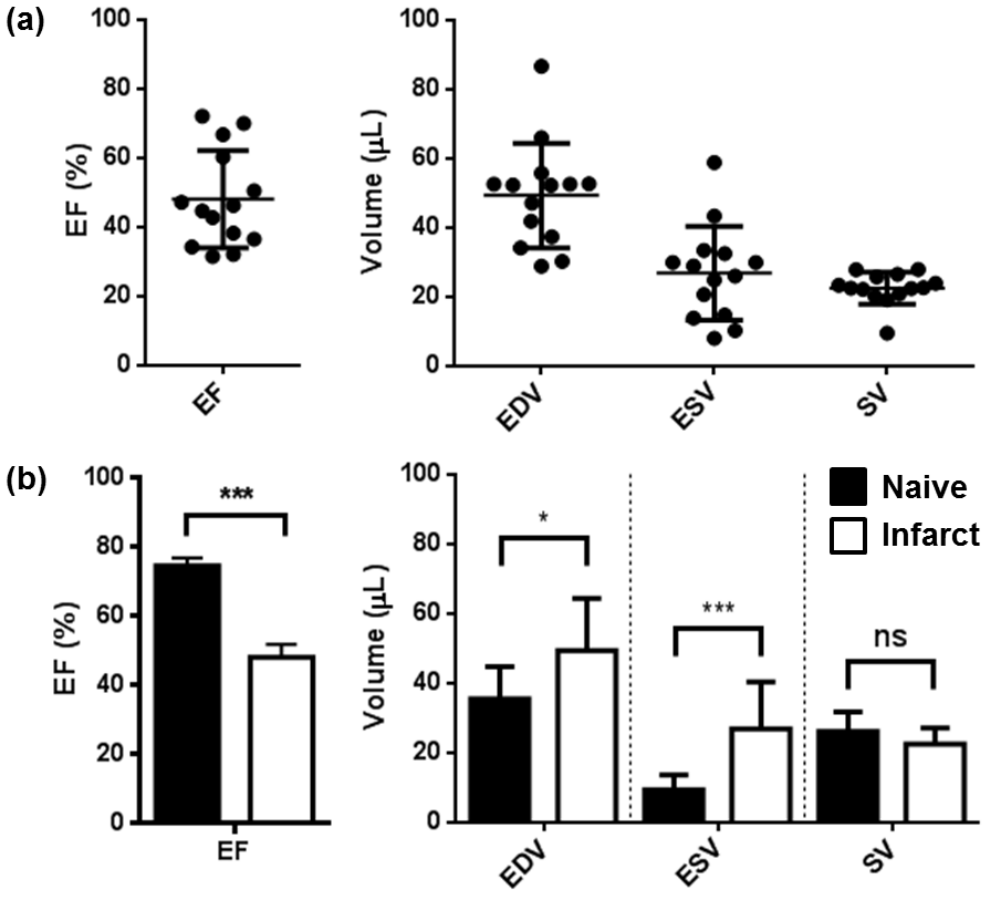

Figure 5.21: (a) Raw data showing systolic parameters in infarcted mice. Lines on plots represent mean and standard deviation. (b) Comparison of systolic parameters between naïve and infarcted mice. Error bars represent SEM. EF was significantly reduced in infarcted mice. EDV and ESV were both significantly increased in infarcted mice. There was no significant difference in SV between groups. All p-values were generated using Mann-Whitney-U tests.

The infarct cohort of mice demonstrated heart failure with varying degrees of severity. EF values ranged from 31.5% indicating severe heart failure to 72.1% suggesting normal cardiac function. Overall, mean EF in infarcted mice was 48.1 ± 3.8% (SEM), which was significantly reduced compared to the naïve cohort. Mean EDV was 49.4 ± 4.0 µL and mean

ESV was 26.8 ± 3.6 µL, both of which were significantly increased compared to the naïve cohort. Mean SV was 22.5 ± 1.2 µL, which was lower than the naïve cohort, but the difference was non-significant.

5.5.2 Myocardial scar tissue volume

Myocardial scar tissue volume was assessed using late-gadolinium enhanced MRI. Figure 5.22a shows a representative stack of images acquired in an infarcted mouse. Normal myocardial tissue is dark. Segmentation of the hyperintense myocardial scar tissue enabled calculation of total infarct volume as a percentage of left ventricle volume (LGE/LV%). Mean total infarct volume across all infarcted mice was 19.4 ± 3.6% (SEM). As expected, ejection fraction decreased with increasing scar volume (Figure 5.22b), showing a significant correlation (Spearman's correlation coefficient, $\rho_s = -0.88$, $p = 0.04$). A broad range of infarct volumes was measured, from 2.8% to 43.3%, reflecting the varying severity of the myocardial impairment.

Due to the wide range of ejection fractions and infarct volumes observed in the cohort, a criterion was devised to create a subset of mice which had marked heart failure, where surgery definitely resulted in ischaemic infarction, rather than just mild damage resulting from the process of undergoing surgery. Infarct mice with EF < 50% and LGE/LV > 10% were included in the group (n = 9), which was used for all subsequent analysis.

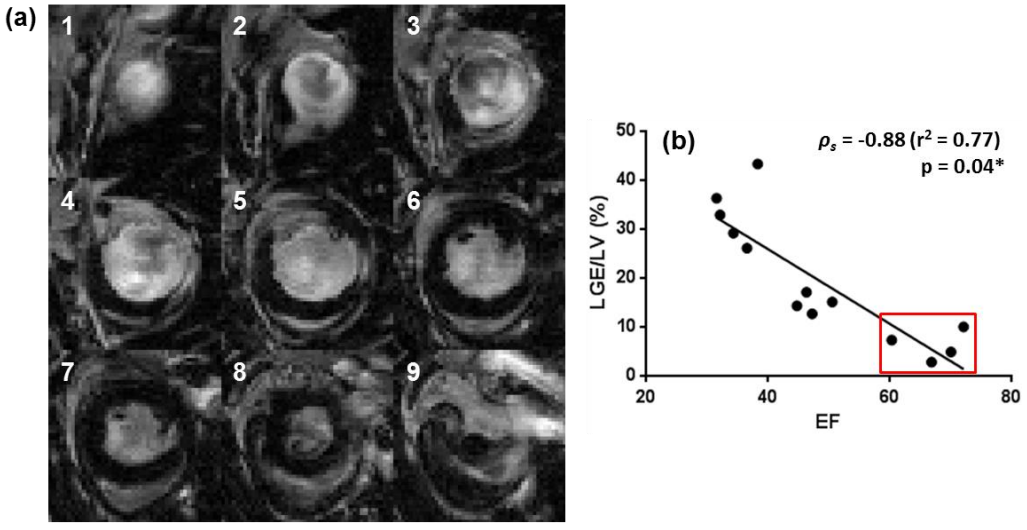

Figure 5.22: Late gadolinium enhanced MRI in an infarcted mouse heart. (a) Stack of slices from the apex (1) towards the base (9) of the heart. Hyperintensity in the myocardium corresponds to accumulation of gadolinium within scar tissue. (b) Correlation of ejection fraction versus scar tissue volume using MRI. EF is reduced with more severe scarring, as expected. The red outline indicates animals with mild cardiac impairment, which were not included in subsequent analysis. Note, n = 13 mice shown in this plot as one animal died before LGE IR imaging was performed.

5.5.3 Diastolic function assessment in infarcted mice using HTR-CINE MRI and ultrasound

E/A ratios were assessed using the method outlined in the repeatability study of naïve mice (section 5.4.3). For infarcted mice, only Basal slices were used to calculate E/A ratios as this slice location was determined to most closely reflect ultrasound measurements. Infarcted mice demonstrated a broader variety of filling rate curves compared to naïve mice. Representative examples are shown in Figure 5.23. Broadly, mice with the largest infarct volumes demonstrated E/A ratios close to or less than 1, as in Figure 5.23a. and Figure 5.23b. Some mice exhibited merged peaks, as in Figure 5.23c. Finally, mice with minor infarcts generally demonstrated filling curves with higher E peaks than A peaks.

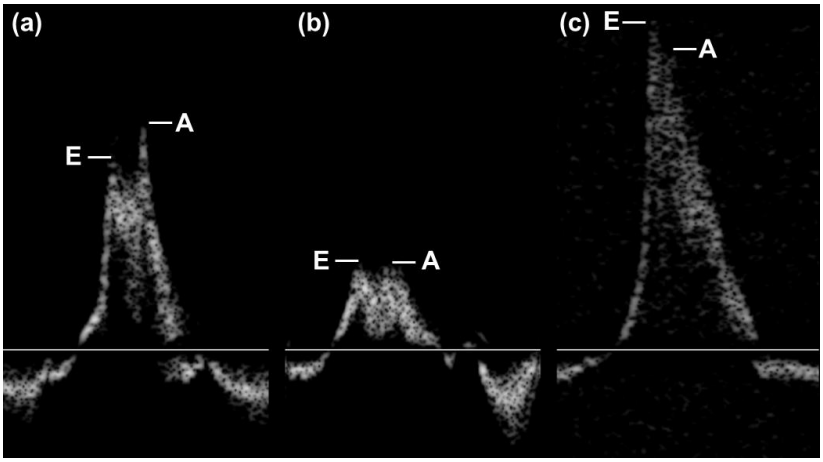

Figure 5.23: Example left ventricular filling curves in infarcted mice showing the broader range of patterns compared to naïve animals. (a) E lower than A, indicating impaired relaxation. (b) E approximately equal A. (c) Merged peaks.

Raw E/A ratios (Figure 5.24a) for *all* (n = 14) animals in the infarct cohort indicated a tendency for MRI to measure lower values than ultrasound. However, statistical analysis showed there was no significant difference in measurements of E/A ratios between MRI and ultrasound (p = 0.09, Mann-Whitney-U).

Overall, E/A values were reduced in the subset of mice with marked heart failure (n = 9, see section 5.5.2) compared to naïve mice according to both modalities (data taken from Pre-MRI ultrasound scans and Trial 1 Basal MRI scans only), as shown in Figure 5.24b. With ultrasound, the mean E/A ratio was reduced from 1.39 ± 0.10 in naïve mice to 1.21 ± 0.11 in the infarct subset of mice, although this difference was non-significant. However, MRI was able to distinguish between the naïve mice and infarcted subset – a reduction in mean E/A was observed from 1.42 ± 0.07 in naïve mice to 0.94 ± 0.11 in the infarcted mice, which was

significantly different (p = 0.006, Mann-Whitney-U). Finally, there was significant difference between modalities in the infarct group (p = 0.04, Mann-Whitney-U), which was not observed in the naïve group.

Linear correlation of E/A ratios between the two modalities in the entire infarct cohort was strongly correlated (Spearman's correlation coefficient, $\rho_s = 0.89$, $r^2 = 0.79$, $p << 0.05$), as shown in Figure 5.24c. The tendency for MRI measures of E/A to be lower than ultrasound can be observed in all but one animal.

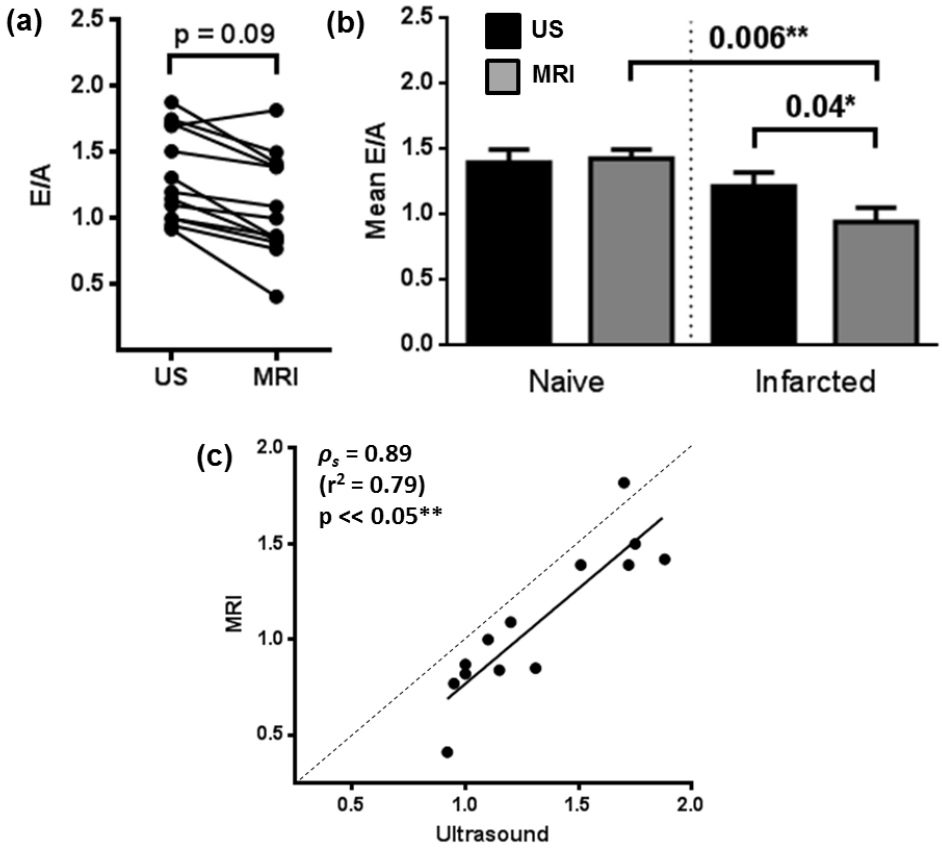

Figure 5.24: E/A ratios in infarcted mice. (a) Raw E/A ratios generated from ultrasound and MRI measurements of all mice in the infarct cohort (n = 14). MRI measures tended to be lower than ultrasound measurements, however the difference between groups was non-significant (p = 0.09, Mann-Whitney-U). (b) Mean E/A ratios in the naïve mice and the subset of mice (n = 9) with marked infarcts (EF < 50%, LGE/LV > 10% – see section 5.5.2), assessed using both modalities. There was a significant difference between naïve and infarct mice using MRI (p = 0.006, Mann-Whitney-U), however, this difference was not significant using ultrasound. (c) Ultrasound and MRI showed a strong, significant correlation across the entire infarct cohort (Spearman's correlation, $\rho_s = 0.89$, $p << 0.05$). E/A values tended to be lower when assessed with MRI compared to ultrasound.

5.6 Discussion

In this chapter a retrospective high temporal resolution CINE MRI sequence has been developed, optimised and applied to mice for the assessment of diastolic function by determination of early- and atrial-filling peaks. The technique was compared to pulsed wave Doppler ultrasound measurements of mitral flow, which is currently the accepted modality for assessing diastolic function. The results presented in this chapter suggest that MRI is more sensitive than ultrasound in detecting heart failure in a mouse model of myocardial infarction compared to naïve animals based on assessment of diastolic function.

The retrospective HTR-CINE sequence developed in this chapter builds upon work conducted by Stuckey et al. and Coolen et al [22, 23]. These studies found that high temporal resolution MRI is able to resolve cardiac filling peaks, however, the study presented here is the first to directly compare MRI with pulsed wave Doppler ultrasound for evaluating diastolic dysfunction in mice. A retrospective acquisition strategy was chosen instead of interleaving multiple prospective CINE [22] scans because there are various advantages to retrospective sequences. Firstly, the temporal resolution can be increased beyond prospective strategies enabling single millisecond resolution. Retrospective acquisition also allows for the entire cardiac cycle to be imaged without having to trigger every second R-wave, reducing acquisition redundancy. In addition, retrospective reconstruction permits the implementation of image artefact correction schemes, such as arrhythmia correction, which are not possible in prospective acquisitions.

Initial *in vivo* studies using the retrospective HTR-CINE pulse sequence produced significant ghosting artefacts. This effect was reproduced in a phantom suggesting that the underlying issue was caused by a problem with the sequence rather than the *in vivo* setup. The ghosting was determined to be caused by k-space gradually changing phase as the sequence was played out. In one preliminary study, large spoiler gradients were inserted into the sequence to test whether the effect was caused by an accumulation of residual transverse phase, however, the phase roll remained unchanged. The cause of the ghosting remains unclear, however, the issue was circumvented by creating a block acquisition strategy where the sequence was acquired using several consecutive repeats of 200 images.

Prior to *in vivo* imaging, simulations were carried out to determine the optimum scan duration needed to acquire a CINE movie with 90 frames. An 11 minute duration was deemed to be sufficient for 99% filling of k-f space with 3 averages. The datalogger used during *in vivo* scans was very good at correctly detecting the ECG events; the imaging gradients were anticipated to significantly interfere with the signal measured by the

subcutaneous electrodes, however, only 1.5% of ECG events were mistimed during a scan, including those discarded during respiration breaths. The arrhythmia correction algorithm successfully corrected these timing issues, however, even without its implementation the datalogger recordings were generally robust enough to produce CINEs with minimal artefacts.

In study 1, repeatability experiments were carried out to test the variability in measurements of E/A ratios using both the retrospective HTR-CINE sequence and the pulsed wave Doppler ultrasound system. A basal slice location in the heart was determined to have the smallest variability compared to more apical slices. Basal slice measurements using HTR-CINE MRI showed comparable mean values and variability with ultrasound, most likely because the basal slices were closest to the mitral valve plane where the ultrasound probe measured inflowing blood. The mean E/A ratio values measured in the naïve mice using basal slices (1.42 ± 0.07) corresponded closely with measurements of non-diabetic control mice in MRI experiments by Coolen et al. [23] (1.51 ± 0.08). However, MRI measurements in non-diabetic control mice by Stuckey et al. were [22] lower (1.06 ± 0.06). Ultrasound measurements of non-diabetic mice by Daniels et al. [25] measured E/A ratios (1.5 ± 0.1) which supported the data obtained in this chapter.

In study 2, the retrospective HTR-CINE sequence was applied to a cohort of infarct mice and compared with pulsed wave Doppler ultrasound to examine the robustness of the sequence to pathology. First, the animals were imaged with standard CINE imaging to determine systolic function parameters and LGE IR to quantify infarct size. The cohort of mice exhibited varying infarct severity, reflected in the range of ejection fractions and infarct volumes observed. Consequently, a broader variety of filling curves was observed in the infarcted mice compared to naïve animals. Both modalities were able to successfully resolve the filling peaks in the majority of mice, however, in some hearts the filling peaks were merged. On average, infarcted mice exhibited reduced E/A ratios compared to healthy mice, as determined using both modalities. However, this reduction was only significant when measured using HTR-CINE MRI, and not with ultrasound. Furthermore, MRI measured a mean E/A ratio = 0.94 ± 0.11, which was below the threshold of healthy diastolic function (less than 1.0). This was not the case with ultrasound, which remained above the threshold (greater than 1.0). These results indicated that MRI was more sensitive for detecting heart failure in mice based on assessment of diastolic function. The reason for this difference may possibly be attributed to the subtly different measurements made by the two techniques: pulsed wave Doppler ultrasound measures blood velocity during inflow, whereas MRI measures volumetric change during diastole. Hence, MRI may be a more direct measure of myocardial relaxation than ultrasound.

5.7 Summary

In this chapter a retrospective HTR-CINE MRI sequence has been developed, implemented and optimised for imaging diastolic function in mouse hearts. Repeatability comparisons between HTR-CINE MRI and pulsed wave Doppler ultrasound – the current-standard for assessing diastolic function – indicated that variability was similar and MRI was robust. Measurement of E/A ratios in infarcted mice using both techniques found that HTR-CINE MRI was more sensitive to detecting diastolic dysfunction compared to ultrasound.

5.8 References

1. Vasan RS and Levy D. *Defining diastolic heart failure a call for standardized diagnostic criteria.* Circulation, 2000. **101**(17): p. 2118-2121.

2. McMurray JJ, et al. *ESC Guidelines for the diagnosis and treatment of acute and chronic heart failure 2012.* European Journal of Heart Failure, 2012. **14**(8): p. 803-869.

3. Garg N, et al. *Heart failure with a normal left ventricular ejection fraction: Epidemiology, pathophysiology, diagnosis and management.* The American Journal of the Medical Sciences, 2013. **346**(2): p. 129-136.

4. Komajda M and Lam CS. *Heart failure with preserved ejection fraction: a clinical dilemma.* European Heart Journal, 2014. **35**(16): p. 1022-1032.

5. Owan TE, et al. *Trends in prevalence and outcome of heart failure with preserved ejection fraction.* New England Journal of Medicine, 2006. **355**(3): p. 251-259.

6. Borlaug BA and Paulus WJ. *Heart failure with preserved ejection fraction: pathophysiology, diagnosis, and treatment.* European Heart Journal, 2011. **32**(6): p. 670-679.

7. Bhatia RS, et al. *Outcome of heart failure with preserved ejection fraction in a population-based study.* New England Journal of Medicine, 2006. **355**(3): p. 260-269.

8. Meyer T, Shih J and Aurigemma G. *Heart failure with preserved ejection fraction (diastolic dysfunction).* Annals of Internal Medicine, 2013. **158**(1): p. ITC1-1.

9. Eisner D, et al. *Calcium flux balance in the heart.* Journal of Molecular and Cellular Cardiology, 2013. **58**: p. 110-117.

10. Aurigemma GP and Gaasch WH. *Diastolic heart failure.* New England Journal of Medicine, 2004. **351**(11): p. 1097-1105.

11. Dostal DE and Watson LE. *Understanding Diastolic Heart Failure With Preserved Ejection Fraction Choosing the Right Model.* Hypertension, 2006. **47**(5): p. 830-832.

12. Mandinov L, et al. *Diastolic Heart Failure.* Cardiovascular Research, 2000. **45**(4): p. 813-825.

13. Frank KF, et al. *Modulation of SERCA: implications for the failing human heart.* Basic Research in Cardiology, 2002. **97**(1): p. I72-I78.

14. Garcia MJ, Thomas JD and Klein AL. *New Doppler echocardiographic applications for the study of diastolic function.* Journal of the American College of Cardiology, 1998. **32**(4): p. 865-875.

15. Stuckey DJ, et al. *Cine-MRI versus two-dimensional echocardiography to measure in vivo left ventricular function in rat heart.* NMR in Biomedicine, 2008. **21**(7): p. 765-772.

16. Hoit BD, et al. *In vivo echocardiographic detection of enhanced left ventricular function in gene-targeted mice with phospholamban deficiency.* Circulation Research, 1995. **77**(3): p. 632-637.

17. Sjaastad I, et al. *Echocardiographic criteria for detection of postinfarction congestive heart failure in rats.* Journal of Applied Physiology, 2000. **89**(4): p. 1445-1454.

18. Daneshvar D, et al. *Diastolic dysfunction: improved understanding using emerging imaging techniques.* American Heart Journal, 2010. **160**(3): p. 394-404.

19. Westenberg JJ, *CMR for assessment of diastolic function.* Current Cardiovascular Imaging Reports, 2011. **4**(2): p. 149-158.

20. Jung B, et al. *Detailed analysis of myocardial motion in volunteers and patients using high-temporal-resolution MR tissue phase mapping.* Journal of Magnetic Resonance Imaging, 2006. **24**(5): p. 1033-1039.

21. Rathi VK, et al. *Routine evaluation of left ventricular diastolic function by cardiovascular magnetic resonance: A practical approach.* Journal of Cardiovascular Magnetic Resonance, 2008. **10**(36): p. 36.

22. Stuckey DJ, et al. *Novel MRI method to detect altered left ventricular ejection and filling patterns in rodent models of disease.* Magnetic Resonance in Medicine, 2008. **60**(3): p. 582-587.

23. Coolen BF, et al. *High frame rate retrospectively triggered Cine MRI for assessment of murine diastolic function.* Magnetic Resonance in Medicine, 2013. **69**(3): p. 648-656.

24. Price AN, et al. *Rapid assessment of myocardial infarct size in rodents using multi-slice inversion recovery late gadolinium enhancement CMR at 9.4 T.* Journal of Cardiovascular Magnetic Resonance, 2011. **13**(1): p. 1-9.

25. Daniels A, et al. *Impaired cardiac functional reserve in type 2 diabetic db/db mice is associated with metabolic, but not structural, remodelling.* Acta Physiologica, 2010. **200**(1): p. 11-22.

CHAPTER 6: FINAL DISCUSSION

Cardiovascular diseases are the number one cause of death worldwide. As the economic burden of CVDs continues to grow, the need to understand and treat these conditions becomes increasingly important. Research into CVDs must be all-encompassing: the basic mechanisms of these diseases must be exhaustively understood, methods of diagnosis and prognosis must be reliable and accurate, and therapies must be thoroughly validated and cost-effective before coming to market. To this end, pre-clinical imaging using animal models plays an extremely valuable role in medical research. Imaging experimental animal models allows observation of biological processes at every scale, from the cellular level to the interaction of whole organs. Pre-clinical imaging allows for the development of sensitive and specific imaging biomarkers which can be translated into the clinic, as new methods for the diagnosis and prognosis of disease. And, pre-clinical imaging facilitates the wider development of therapeutics through the longitudinal characterisation of drugs in relatively low-cost animal models of human disease, prior to proceeding with long and expensive clinical trials. The overall aim of the research in this thesis was the development of pre-clinical MRI techniques for imaging four important areas of CVD including: stroke, dilated cardiomyopathy, myocardial infarction and diastolic heart failure. This chapter summarises the studies carried out throughout the thesis, discusses some of the successes and limitations of each study and outlines potential avenues for future development.

In chapter 3, a novel method for imaging extracellular and interstitial fluid flow *in vivo*, known as extravascular convectography (EVAC) MRI, was applied to imaging brain fluid dynamics following a stroke in a surgical rat model. Stroke is known to cause major alterations to intracranial pressure and intracranial fluid dynamics. Some previous studies have attempted to quantify ICP using MRI [1, 2] as an alternative to highly invasive gold-standard methods [3], however, these methods only result in a global measure of ICP. With EVAC, the aim of the technique was to visualise localised changes in fluid dynamics and to determine if any useful pathological information could be gained beyond simple measures of ICP or other commonly used MRI methods such as diffusion and perfusion imaging.

In the end, the results from applying EVAC to stroke rats were physiologically inaccurate. The EVAC velocity maps of extracellular fluid flow showed lateral movement across the hemispheres, which was not physically possible. The cause of the erroneous measurements was difficult to ascertain. *In vivo* repeatability and reproducibility studies carried out in a subcutaneous mouse tumour model demonstrated meaningful interstitial fluid flow patterns

which agreed with literature descriptions [4] of pressure distribution in tumours. The interstitial fluid flow maps were validated by gadolinium distribution experiments carried out by Walker-Samuel et al., which showed contrast agent accumulation in regions of vector convergence, suggesting that the directionality of the vectors was accurate in the tumour experiments despite high absolute values of interstitial fluid velocity compared to measurements using other techniques [5]. Validation studies were also carried out in a flow phantom to determine if the high interstitial fluid velocity values could be attributed to a phase offset effect, possibly due to electrical eddy currents masking the bipolar gradient velocity-encoded phase changes. A phase offset correction technique was implemented, which showed promise in flow phantom experiments, however, when it was applied *in vivo* the fluid patterns showed minimal changes. This was likely caused by added complications when imaging *in vivo*, such as more complicated fluid dynamics, voxels comprised of flowing and static tissue and a poorer shim, which all contributed to masking the benefits of the phase offset correction. Conversely, the flow phantom experiments were limited because the setup was probably too ideal: the flow was highly coherent and the signal measured was very high compared to *in vivo* imaging.

Establishing and correcting the cause of the error in the brain measurements using EVAC will be a significant challenge. Nonetheless, imaging mouse brains using the same hardware configuration as that used in the tumour imaging studies – to rule out the rat imaging setup as a confounder – may be an informative future study. However, this is likely to result in lower SNR due to volume coil usage rather than a 4-channel receive configuration, which will likely require increased scan duration as a trade-off.

In chapter 4, a pair of studies was carried out using MRI to assess two different animal models of heart disease. In the first study, CINE and LGE IR imaging were used to characterise a novel Prox1-deficient mutant mouse model with a DCM phenotype, in order to investigate the importance of the Prox1 gene in the maintenance of normal cardiac muscle physiology and development. CINE imaging was used to quantify various parameters of cardiac function and to assess changes in myocardial morphology. At 6-weeks old, the mutant mice demonstrated significantly raised left ventricular mass, end diastolic volume and significantly lower ejection fraction, all indicative of DCM. By 8-weeks, the severity of the phenotype increased such that only two mutants survived through to imaging. Despite this, LGE IR MRI indicated a thrombus in the right atrium of one 8-week old mouse, illustrating the versatility of this technique beyond traditional scar tissue visualisation. One limitation of the study was that, unfortunately, the mouse which presented with a thrombus was not taken for histology, which may have provided additional evidence that the hypointensity was definitely a thrombus and not an unusual flow artefact. Despite this,

histology performed in other Prox1-deficient mice also showed thrombi, reinforcing the LGE IR MRI finding. Another limitation of the study was the severity of the animal model: anaesthetising the mice beyond the age of 6-weeks old often resulted in death soon after induction, which restricted the number of animals imaged. Further still, the mutant mice were very weak once anaesthetised and required prompt imaging. For future studies using the model, this would make extensive multi-parametric protocols challenging, although the animals could be imaged at earlier timepoints when the phenotype is less severe. Overall though, the MRI showed that the mouse model shared many of the features present in human DCM, illustrating its importance as a tool for understanding the biological processes underlying the disorder and its utility for future studies investigating prognosis in DCM patients.

In the second study of chapter 4, multi-parametric cardiac MRI techniques were applied to visualising and quantifying the AAR *in vivo* following myocardial infarction. Currently, in the clinic SPECT imaging is most commonly used for assessing the AAR, however, this requires substantial radiation exposure and must take place before reperfusion therapy can be administered, which is detrimental to patient outcome. The most widely used MRI alternative is T2-weighted MRI – which can be used post-reperfusion therapy – however, assessment is based on small signal increases within the myocardium. Hence, in this study T2-mapping was applied as a quantitative alternative for assessing AAR in a reperfused mouse model of myocardial infarction. In addition, perfusion mapping was also carried out for AAR analysis and LGE IR was conducted to calculate scar tissue volume. The MRI images were compared with gold-standard histology to assess the accuracy of the *in vivo* data.

Two main results arose from this study. Firstly, areas of elevated T2 matched closely with volumes measured by histological staining. This demonstrated the potential of T2-mapping as a useful marker of oedema and indicates promise for use in clinical imaging. However, the T2-mapping protocol used in this study was not without its limitations. The sequence was relatively slow, taking approximately 40 minutes to acquire a full dataset necessary for generating the T2 maps. Acquiring less data using fewer echo times would reduce the acquisition time, but at the expense of less accurate T2 fitting. Another issue was the threshold method for determining elevated T2, which makes direct comparison of AAR regions between animals difficult without absolute values. This is less of an issue for volumetric analysis, but absolute quantification would potentially allow for the degree of severity within the AAR to be assessed. This could be useful for therapeutic studies, for instance if there was proportionality between T2 elevation and the potential to reverse the tissue damage, and in conditions where T2 is altered across the whole myocardium, such as

aortic stenosis [6]. Further studies are needed to improve the T2-mapping protocol. A cohort of normal, non-infarcted animals should be studied to gain an understanding of baseline T2 variation in mouse hearts, which would be informative for defining AAR thresholds. In addition, the interplay between oedema and AAR over time would be a valuable area of study, especially in response to therapy, to fully understand T2-mapping as a useful biomarker.

The other main interesting result from this study was more surprising: quantification of AAR using perfusion mapping also showed a very close correspondence to histological measures. Despite reperfusion of the ligated vessel, regions of distinct perfusion deficit were observed in the ASL maps, which corresponded closely with the AAR under histology. The underlying mechanisms causing this perfusion deficit are not entirely clear – the ischaemic injury may have caused capillary damage and impaired microvascular perfusion – and may be of interest in future studies. As with T2-mapping, further studies are needed to understand how perfusion mapping of AAR evolves with time and therapy.

Finally, in chapter 5 a retrospectively-gated HTR-CINE sequence was developed, optimised and compared to pulsed wave Doppler ultrasound for assessing diastolic function in mouse hearts. Diastolic function is believed to be a potentially more sensitive marker for early-stage heart failure and MRI has emerged as an alternative to ultrasound for detecting diastolic dysfunction. Only a few studies exist in this area [7, 8] and none have yet to compare the two techniques directly in mice. A retrospective CINE acquisition was used as it enabled very high temporal resolution sampling of the cardiac cycle. Simulations determined that an 11-minute acquisition was sufficient for 90 frames per cardiac cycle with effectively three averages. A higher frame rate could have been achieved, however, any longer was prohibitive for the repeatability study as a total scan duration of less than 3 hours was required. As MRI measurements of E/A were based on a single-slice MRI acquisition, positioning of the imaging plane was crucial for minimising variation. Slices located just below the mitral valve were determined to have the least variation. In naïve mice, MRI and ultrasound measurements of E/A ratios showed a close correspondence and were determined to have comparable variation. Following validation in naïve mice, the HTR-CINE MRI sequence was applied to a cohort of infarcted mice and compared with ultrasound. Both modalities measured an average reduction in E/A ratios compared to the naïve cohort, but only MRI measured a significant reduction, indicating that MRI may be the more sensitive technique for detecting diastolic dysfunction in mice. The difference in E/A ratios between the modalities is possibly due to the different quantification methods used to calculate the E- and A-peaks. Pulsed wave Doppler ultrasound is a 1-dimensional measurement of blood flow, which is highly dependent on probe positioning whereas MRI is a 2-dimensional

measure of volume change, which is a more direct measure of myocardial relaxation and is more robust to orientation misalignment.

While the results in chapter 5 suggested that MRI may be more sensitive than ultrasound at detecting dysfunction due to myocardial infarction, there was not enough evidence to say whether diastolic function is a more sensitive marker than systolic function for detecting early heart failure. However, this could be a focus of future experiments. For example, one limitation of this study was the wide range of infarct sizes within the infarct cohort; if a more reproducible model of mild heart failure was used – such as caused by a short duration of ischaemia – then it would be possible to test whether assessment of diastolic function is more sensitive that systolic measures. Another limitation to the study was the use of a single-slice acquisition for assessing an inherently 3-dimensional problem. It would be worthwhile comparing the results from a single-slice HTR-CINE acquisition with a multi-slice scan covering the whole left ventricle, which would provide insight into how well the single-slice acquisition represents the entire change in volume of the left ventricle chamber. This experiment would require a scan duration of more than 90 minutes per animal, which is feasible for a validation purposes, but future experiments requiring a full HTR-CINE stack may need to implement MRI undersampling techniques [9] to improve acquisition times. Alternatively, it may be beneficial to evaluate diastolic parameters based on three or four slices rather than an entire stack.

To conclude, in this thesis a number of MRI techniques have been developed and applied to pre-clinical animal models including stroke and various forms of heart disease. These imaging techniques provide valuable insights into the pathological mechanisms underlying CVDs, facilitate the creation of improved, non-invasive biomarkers and contribute to the development of new therapeutic strategies, all of which are crucial in the ongoing effort to tackle the global burden of CVD.

6.1 References

1. Alperin, N., A. Sivaramakrishnan, and T. Lichtor, *Magnetic resonance imaging-based measurements of cerebrospinal fluid and blood flow as indicators of intracranial compliance in patients with Chiari malformation.* J Neurosurg, 2005. **103**(1): p. 46-52.

2. Alperin, N., et al., *From cerebrospinal fluid pulsation to noninvasive intracranial compliance and pressure measured by MRI flow studies.* Current Medical Imaging Reviews, 2006. **2**(1): p. 117-129.

3. Raboel, P., et al., *Intracranial pressure monitoring: invasive versus non-invasive methods—a review.* Critical care research and practice, 2012. **2012**.

4. Lunt, S.J., et al., *Interstitial fluid pressure in tumors: therapeutic barrier and biomarker of angiogenesis.* 2008.

5. Munson, J.M. and A.C. Shieh, *Interstitial fluid flow in cancer: implications for disease progression and treatment.* Cancer management and research, 2014. **6**: p. 317.

6. Jabbour, A., et al., *T2 Mapping by Cardiovascular Magnetic Resonance Reveals Reduced T2 Times in Aortic Stenosis.* Heart, Lung and Circulation, 2011. **20**: p. S192.

7. Stuckey, D.J., et al., *Novel MRI method to detect altered left ventricular ejection and filling patterns in rodent models of disease.* Magnetic Resonance in Medicine, 2008. **60**(3): p. 582-587.

8. Coolen, B.F., et al., *High frame rate retrospectively triggered Cine MRI for assessment of murine diastolic function.* Magnetic Resonance in Medicine, 2013. **69**(3): p. 648-656.

9. Motaal, A.G., et al., *Accelerated high-frame-rate mouse heart cine-MRI using compressed sensing reconstruction.* NMR in Biomedicine, 2013. **26**(4): p. 451-457.